



University
of Glasgow

Minto, James Martin (2014) *Towards a rational design of gravel media water treatment filters: MRI investigation of the spatial heterogeneity in pollutant particle accumulation*. PhD thesis.

<http://theses.gla.ac.uk/5711/>

Copyright and moral rights for this thesis are retained by the author

A copy can be downloaded for personal non-commercial research or study, without prior permission or charge

This thesis cannot be reproduced or quoted extensively from without first obtaining permission in writing from the Author

The content must not be changed in any way or sold commercially in any format or medium without the formal permission of the Author

When referring to this work, full bibliographic details including the author, title, awarding institution and date of the thesis must be given



**Towards A Rational Design of Gravel Media Water Treatment
Filters**

*MRI investigation of the spatial heterogeneity in pollutant particle
accumulation*

James Martin Minto

Submitted in fulfilment of the requirements for
the degree of doctor of philosophy.

Infrastructure and Environment Research Division

School of Engineering

University of Glasgow

October 2014

Abstract

Gravel filters are potentially a low cost, low maintenance water treatment solution. They require no mechanical or electrical parts and can operate without the addition of chemicals or the need for close supervision. As such, they are an appropriate technology for treating road runoff as a component of Sustainable urban Drainage Systems (SuDS) and as an initial stage of drinking water treatment in rural areas. However, the processes by which pollutant particles are removed in gravel filters are poorly understood and practical experience shows that many filters fail long before their expected design life is reached. For this reason gravel filters are little used for drinking water treatment and, when they are incorporated into SuDS, their removal efficiency and maintenance requirements are unpredictable.

The aim of this thesis was to better understand particle removal processes and the implications for gravel filter design. This was achieved through a combination of lab-based experiments and numerical modelling.

- The change in conservative tracer transport characteristics with pollutant particle accumulation was assessed through column experiments.
- The spatial heterogeneity of particle accumulation was measured by collecting 3D data with magnetic resonance imaging (MRI). Multiple scans of filters allowed the temporal evolution of particle accumulation to be assessed. A method for processing the raw MRI data to yield the change in 3D pore geometry was developed, assessed and applied.
- A simple method for extracting and comparing pore network characteristics at different stages of particle accumulation was applied to the MRI derived geometry.
- Direct modelling of the 3D MRI pore geometry with the open source software OpenFOAM allowed correlation of flow velocities with particle accumulation at each point in the pore network. Lagrangian particle tracking was used to simulate the transport of a conservative tracer through the filter.

Key findings were that spatial heterogeneity in particle accumulation was influenced by both initial pore geometry and the temporal evolution of the pore network with

accumulation. This was attributed to the formation of high velocity preferential flow paths that were evident in both the 3D MRI data and the numerical model of that data. Pore networks exhibited a decrease in connectivity with accumulation and this was mirrored by a decrease in the volume of the filter that was accessible to a conservative tracer.

Conclusions of this thesis are that MRI is a useful tool for non-invasively assessing the spatial variability of clogging in gravel filters and, when combined with numerical modelling of the pore geometry, for establishing the link between pore velocity and particle removal. The formation of preferential flow paths is detrimental to the pollutant removal efficiency of a filter and could explain why many filters fail to produce good quality effluent well before their physical pollutant storage capacity is reached.

Keywords: magnetic resonance imaging, pore network, gravel filter, numerical modelling, tracer residence time distribution.

Contents

Abstract	i
Contents	iii
Acknowledgements	vii
Author’s Declaration	viii
Definitions & Abbreviations	ix
Chapter 1 – Introduction	1
1.1 Context	1
1.1.1 Sustainable Drainage Systems	1
1.1.2 Roughing Filtration	4
1.2 Current State of Gravel Filtration Research	5
1.3 Thesis Aims & Layout	7
Chapter 2 – Characterisation of Filter Clogging with Conservative Tracers	9
2.1 Abstract	9
2.2 Introduction	9
2.3 Tracer Theory	10
2.3.1 Tracer Residence Time Distribution	10
2.3.2 Normalising the RTD of Steady-flow Systems.....	11
2.3.3 Hydraulic Efficiency	12
2.3.4 CXTFIT/Excel.....	13
2.4 Kaolin as Surrogate for Road & River Particulate Pollution	13
2.4.1 River Particulate Matter	13
2.4.2 Road Runoff Particulate Matter	14
2.4.3 Kaolin Properties.....	16
2.4.4 Fluid Phase	19
2.5 Hydraulic & Lifetime Sediment Loading on Filters	20
2.5.1 Roughing Filter Hydraulic & Sediment Loading Rates	21
2.5.2 Highway SuDS Gravel Filter Hydraulic & Sediment Loading Rates.....	22
2.6 Gravel Media Physical Characteristics	28
2.7 Experimental Setup & Procedure	30
2.7.1 Phase 1 – Column Preparation & Tracer Characterisation	33
2.7.2 Phase 2, 4 & 6 – Kaolin Removal Efficiency & Size	33
2.7.3 Phases 3 & 5 – Clogging & Tracer Characterisation	34
2.7.4 Phase 7– Mass Balance	35

2.8 Results	35
2.8.1 Kaolin Turbidity/Concentration Relationships	35
2.8.2 Filter Sediment Loading.....	37
2.8.3 Kaolin Removal Efficiency.....	41
2.8.4 Tracer Characteristics & Repeatability	45
2.8.5 Clean Bed Pore Volume Estimation from Tracer RTD	51
2.8.6 Clogged Bed Pore Volume Estimation from Tracer RTD	52
2.8.7 Intermediate Clogged Bed Pore Volume Estimation from Tracer RTD.....	54
2.8.8 Particle Size Breakthrough.....	55
2.9 Discussion	58
2.9.1 Kaolin as Surrogate for Road & River Particulate Pollution	59
2.9.2 Kaolin Turbidity/Concentration Relationship.....	60
2.9.3 Tracers.....	62
2.10 Conclusions	65
Chapter 3 – Magnetic Resonance Imaging: a non-invasive tool to characterise and quantify spatial variation in particle accumulation.....	67
3.1 Abstract	67
3.2 Introduction	68
3.3 Data Collection Methodology	69
3.3.1 Experiment Setup	69
3.3.2 Image Acquisition	72
3.4 MRI Scan Quality	73
3.5 Image Processing	76
3.5.1 Segmentation Quality.....	77
3.5.2 Selection of Image Processing Method.....	83
3.5.3 Sensitivity to Image Stack Processing Direction	84
3.5.4 Optimum Image Processing Method.....	87
3.5.5 Quantification of Error & Uncertainty.....	88
3.6 Image Analysis Results	91
3.6.1 Bulk Porosity, Number of Regions and Surface Area Analysis	92
3.6.2 Slice-by-slice Porosity Analysis	96
3.6.3 3D Region Analysis	103
3.6.4 Summary of Experimental Data.....	107
3.7 Discussion	108
3.7.1 Suitability of MRI	108
3.7.2 Image Processing	110
3.7.3 Results Discussion	112
3.8 Conclusions	119

Chapter 4 – Pore Network Analysis	120
4.1 Abstract	120
4.2 Introduction	120
4.3 Pore Network Analysis	121
4.3.1 Medial Axis Trimming.....	121
4.3.2 Maximal Balls	121
4.3.3 Selection and Implementation of Skeletisation Method	122
4.4 Methodology	124
4.4.1 Quality of Pore Network Medial Axis	124
4.4.2 Bulk Properties of Pore Network	124
4.4.3 Change in Pore Network Properties with Clogging.....	125
4.5 Results	127
4.5.1 Quality of Pore Network Medial Axis	127
4.5.2 Bulk Properties of Pore Network	131
4.5.3 Change in Pore Network Properties with Clogging.....	135
4.6 Discussion	139
4.6.1 Quality of Pore Network Medial Axis	139
4.6.2 Change in Pore Network Diameter	140
4.7 Conclusions	142
Chapter 5 – Numerical Modelling of Flow in MRI Derived Pore Geometry	143
5.1 Abstract	143
5.2 Introduction	143
5.3 Methods and Method Development	145
5.3.1 OpenFOAM Software	145
5.3.2 Geometry.....	146
5.3.3 Eulerian Finite Volume Method.....	150
5.3.4 Lagrangian Particle Tracking.....	156
5.3.5 Case Execution.....	160
5.3.6 Parametric Study & Optimum Parameters	161
5.3.7 Full Volume Cases	164
5.4 Discussion	173
5.4.1 Model Accuracy	173
5.4.2 Eulerian Flow Velocities.....	175
5.4.3 Lagrangian Particle Tracking of Tracer	177
5.5 Limitations and Further Work.....	179
5.6 Conclusions	180
Chapter 6 – Conclusions.....	181

6.1 Chapter 2	181
6.2 Chapter 3	182
6.3 Chapter 4	183
6.4 Chapter 5	184
6.5 Reflection on Gravel Filter Design and Further Research	184
References	187
Appendix A – Glossary of Image Processing	201
A.1 Pre-segmentation Processing	201
A.2 Image Segmentation (Binary Thresholding)	209
A.3 Post-segmentation Processing	218
A.4 Selection of Image Processing Method	220
Appendix B – Parametric Study Results.....	221
B.1 Solution Scheme	225
B.2 Turbulence & Surface Roughness	227
B.3 Mesh Initial Resolution & Surface Refinement	231
B.4 STL generation and Viscosity	237
B.5 Lagrangian Dispersion.....	241
B.6 Discussion.....	242
Appendix C – OpenFOAM Model Files.....	243
C.1 <i>snappyHexMesh</i> Dictionary File	244
C.2 <i>fvSchemes</i> – <i>simpleFoam</i> Solver Finite Volume Schemes.....	246
C.3 <i>fvSolutions</i> – <i>simpleFoam</i> Solver Solution & Algorithm Control.....	247
C.4 <i>kinematicParticleProperties</i> – Lagrangian Particle Properties	249
C.5 Example Bash Script – Eulerian Model	252
C.6 Example Bash Script – Lagrangian Model.....	253

Acknowledgements

I would like to thank my supervisors for their time and support throughout my project, for allowing me the freedom to suspend my studies to volunteer in Ethiopia, and for helping me get back in to the PhD when I returned.

William Holmes and Jim Mullin at the Glasgow Experimental MRI Centre for all their help with the MRI experiments and the technicians Anne, Bobby, Ian, Julie, Stuart and Tim with the experiments in the Department of Civil Engineering.

I would also like to thank Becky and Grainne at the University of Strathclyde for their support, guidance and patience whilst writing up.

Finally, a special thanks to my fellow PhD students at both the University of Glasgow and University of Strathclyde. You made the whole experience that much better.

Author's Declaration

I declare that no portion of the work in this thesis has been submitted in support of any application for any other degree or qualification of this or any other university or institute of learning. I also declare that the work presented in this thesis is entirely my own contribution unless otherwise stated.

James Minto

Definitions & Abbreviations

CFD – Computational Fluid Dynamics

CLAHE – Contrast Limited Adaptive Histogram Equalization

CT – Computer Tomography

DMRB – Design Manual for Roads & Bridges

FVM – Finite Volume Method

GEMRIC – Glasgow Experimental Magnetic Resonance Imaging Centre

LES – Large Eddy Simulation

LPT – Lagrangian Particle Tracking

MRI – Magnetic Resonance Imaging

NTU – Nephelometric Turbidity Units

PAHs – Polycyclic Aromatic Hydrocarbons

PET – Positron Emission Tomography

PSD – Particle Size Distribution

PV – Pore Volume

RARE – Rapid Acquisition Relaxation Enhanced

RAS – Reynold’s Averaged Stress

RANS – Reynold’s Averaged Navier Stokes

RF – Radio Frequency

ROI – Region Of Interest

RPM – Revolutions Per Minute

RTD – Residence Time Distribution

SuDS – Sustainable (urban) Drainage Systems

STL – STereoLithography file format

TIFF – Tagged Image File Format

TSS – Total Suspended Solids

VTK – Visualization ToolKit file format

3D – Three Dimensional

3T – Three Tesla magnetic field strength

Chapter 1 – Introduction

1.1 Context

It is often necessary to remove pollutants such as chemicals, pollutant metals and suspended solids from water either to render it potable, or to reduce the environmental pollution that results from human development. These two applications vary in the quantity of water to be treated, the types of pollutants, what constitutes an acceptable residual pollutant level, and when and where the water need be treated. However, they also share many similarities in terms of the processes that can be utilised to remove pollutants. This thesis considers the use of gravel filtration as a pollutant removal process for both reducing environmental pollution and producing potable water.

1.1.1 Sustainable Drainage Systems

As a region develops and urbanises, permeable soil is replaced with impermeable surfaces such as roads and buildings. This results in a shift in the hydrological balance of a catchment from a system dominated by infiltration and evapo-transpiration to a system dominated by surface runoff, as shown in Figure 1.1. The increased surface runoff is traditionally collected in artificial piped drainage systems and discharged as quickly/efficiently as possible to a watercourse. This has the effect of both increasing the flood hydrograph peak (potentially increasing the risk of flooding) and reducing baseflow which is often detrimental to the ecology of the watercourse.

Increased levels of pollutant are also introduced to the runoff as a result of combustion processes, careless disposal of waste and general wear and deterioration of the built environment. Diffuse pollution is thought to account for 11% of polluted rivers and 31% of seriously polluted rivers in Scotland (D'Arcy et al., 2000).

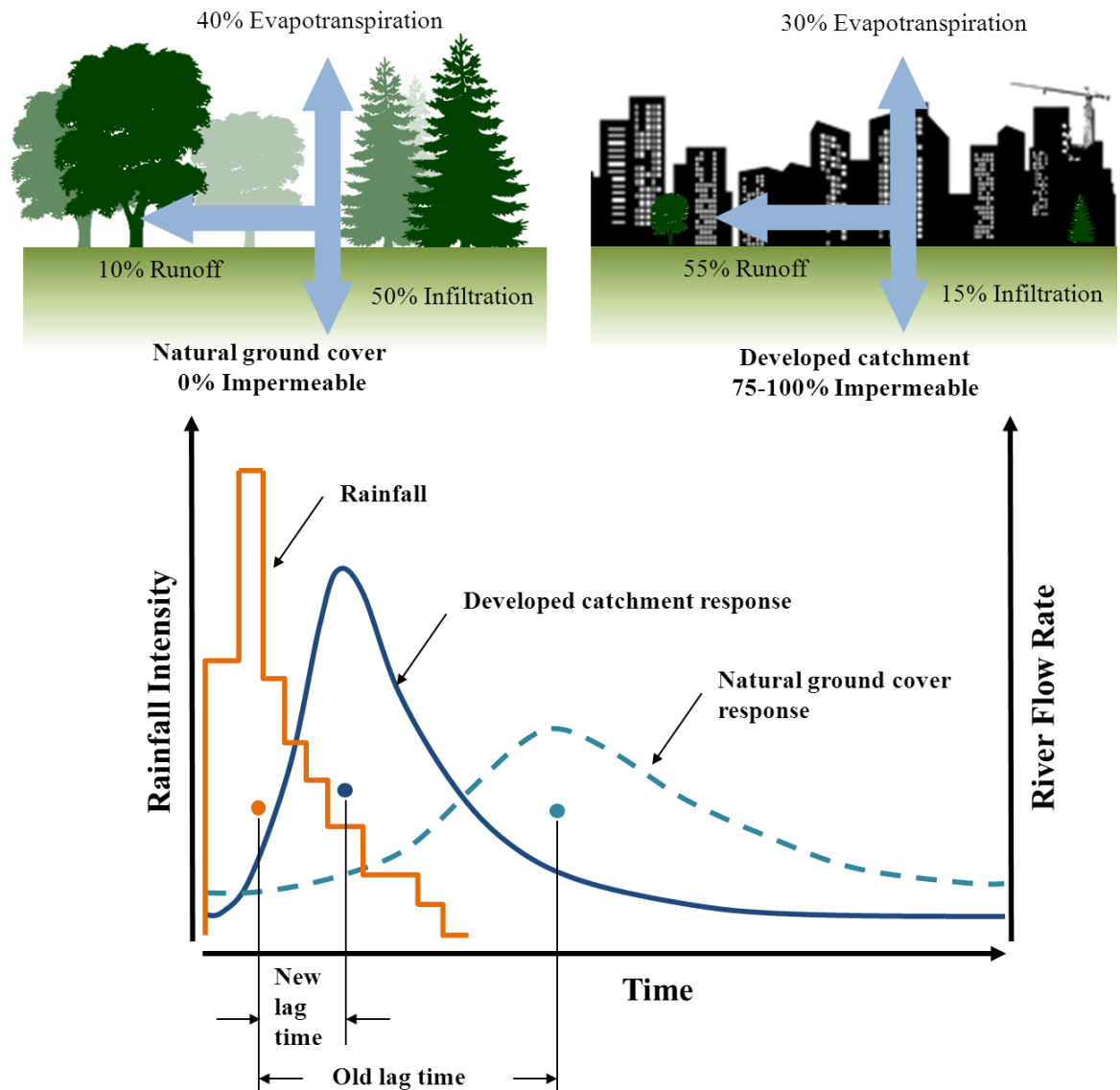


Figure 1.1. Urbanisation results in a shift from permeable ground cover with high infiltration and low runoff to impermeable with low infiltration and high runoff (top left and right, adapted from Arnold & Gibbons (1996)). The consequences of this are illustrated with a river hydrograph: a shorter lag time between rain falling on a catchment and the peak river flow, higher river flow peaks (increasing flood risk) and lower river baseflow (with associated negative ecological impacts).

Roads are the greatest source of polluted runoff (Deletic & Orr, 2005; Grant et al., 2003; Thorpe & Harrison, 2008). Types of pollutants found in road runoff include oils and hydrocarbons leaked from vehicles, pesticides from roadside weed control, pollutant metals from disintegration of vehicle brakes, tyres and body as well as from signs and

street furniture, and sediment washed or blown onto the road surface or created as a result of degradation of the road itself (Campbell et al., 2004). In addition to being a pollutant in its own right, sediments act as a surface onto which other pollutants can adsorb. These pollutants accumulate on the road surface during dry periods and are washed off by suitably intense rainfall (Richardson & Tripp, 2006; Sansalone et al., 1998; Shuster et al., 2008).



Figure 1.2. Typical types of SuDS: A) retention pond, B) detention basin, C) vegetated roadside swale and D) roadside filter trench with coarse gravel overlying finer filter media (to prevent gravel scatter onto the road). The pollutant removal processes that occur in each type of SuDS, to a greater or lesser degree, are sedimentation, filtration, biodegradation, adsorption and uptake by vegetation.

Sustainable Drainage Systems (SuDS) are a method of mitigating the impacts of urbanisation at a catchment level. They attempt to preserve the natural hydrology by attenuating and infiltrating runoff, improving water quality and maximising the amenity

and biodiversity opportunities of the land the SuDS occupy. Figure 1.2 shows several typical types of SuDS.

Under the Water Environment (Controlled Activities) (Scotland) Regulations 2005, the drainage of surface water from all new developments must be to “a SUD system or equivalent equipped to avoid pollution of the water environment” (HMSO, 2005b). Whilst regulation varies from country to country, regulatory requirement for some form of SuD system is becoming increasingly common; most notably in the USA where they are referred to as Best Management Practices (BMPs) and Australia where they are known as Low Impact Designs (LIDs).

1.1.2 Roughing Filtration

For water treatment by chlorination, ultra violet light or by slow sand filtration to be effective, the water must first have low suspended solids content. Roughing filtration has been developed as a means of removing suspended solids prior to further treatment. Roughing filters can operate in both vertical and horizontal flow configurations and generally consist of three or more compartments filled with progressively finer grades of gravel (Wegelin, 1996), as shown in Figure 1.3.

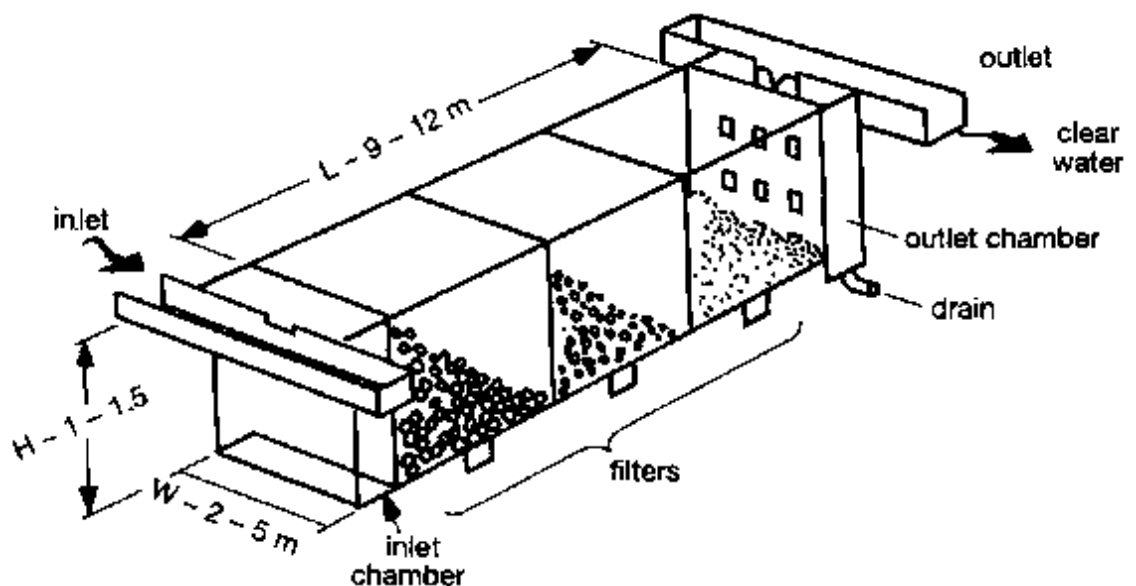


Figure 1.3. Horizontal flow roughing filter with three gravel filled compartments. Reproduced from United Nations High Commissioner for Refugees (1992).

The gravel provides a large surface area onto which suspended solids can attach, reduces the distance a settling particle must travel before encountering such a surface, and provides a large pore volume for storage of removed particles. Due to the presence of the gravel, roughing filters occupy a much smaller land footprint than an equivalent plain settlement/sedimentation tank. Further advantages of roughing filters compared with other sediment removal methods are that they do not require the addition of chemicals such as flocculants (although flocculants have been used to improve performance (Dórea, 2005)), nor regular backwashing to restore permeability, and, where site topography permits, they can be operated entirely under gravity requiring no electricity for pumping. Roughing filters also have few mechanical components resulting in little maintenance or supervision and hence low operational costs. All of these factors increase the suitability of roughing filters for pollutant removal in locations without electricity, where the addition of chemicals is undesirable and where regular supervision and maintenance cannot be guaranteed.

1.2 Current State of Gravel Filtration Research

Both SuDS and roughing filters are established treatment techniques yet there is considerable scope for the performance of both to be improved. It is unclear what level of treatment gravel filter SuDS provide and typically a great variation in removal efficiencies of a variety of pollutants are observed. For instance Claytor & Schueler (1996) found the removal of metals, polycyclic aromatic hydrocarbons and total suspended solids in gravel SuDS filters to be in the range of 40-50%, 85% and 80% respectively whilst in the Design Manual for Roads and Bridges (DMRB), lower removal efficiencies of 7%, 52% and 38% are noted (HMSO, 2006). Possible reasons for such a discrepancy could be the result of different filter designs, hydraulic loading and pollutant characteristics between different countries (USA for Claytor & Schueler (1996), UK for DMRB). Nevertheless, this highlights the uncertainty in SuDS removal efficiency with the result that more modern guidance has moved away from stating percentage removal efficiencies in favour of ranking each different SuDS measure as low, medium or high relative to other SuDS measures (Scholes et al., 2008; Pittner & Allerton, 2010).

Research into gravel filter SuDS has focused on the following areas:

1. The removal of contaminant metals by different filter media such as iron oxide coated gravel (Norris et al., 2013), limestone (Fernández-Barrera et al., 2010), woodchips (Syring et al., 2009) and zeolite (Wu & Zhou, 2009) to name a few.
2. The “clean filter bed” removal efficiency of suspended solids (Barton & Buchberger, 2007).
3. Monitoring of operational gravel filters (Schluter, 2005).
4. Measuring the accumulation of pollutant metals and suspended solids on road surfaces (Herngren et al., 2006; Poletto et al., 2009; Pal et al., 2010).
5. Measuring pollutant metal and suspended solids content of road runoff and rainfall event mean concentrations (Kayhanian et al., 2007; Crabtree & Whitehead, 2006; Lau et al., 2009).

Little research has been carried out into the effects that filter clogging with accumulated sediment has upon filter operation. Siriwardene et al. (2007) attempted to develop a model of removal efficiency with sediment accumulation. The authors note that whilst their model was successful in estimating removal efficiency in clean filters, the model failed to predict sediment removal over time as sediment accumulated.

Understanding filter clogging is crucial as filtration based SuDS are prone to failure within several years, well short of their anticipated 10 year design life (Rowlands & Ellis, 2007; Schluter, 2005). Lindsey et al. (1992) (in Emerson & Traver, 2008) found that, less than two years after installation, 67% of the filtration based SuDS surveyed in Maryland, USA were not functioning properly. After six years a follow up survey identified that 51% were not functioning at all with many of the observed problems relating to accumulated sediment.

Research into roughing filters has progressed along a different route. Pollutant metals are less of a problem and so the main pollutant of concern is suspended solids. Far more progress into a theoretical and conceptual understanding of the transport and removal processes has been made culminating in a collection of approaches known as “filtration

theory” which have been applied to slow sand filters (Iwasaki et al., 1937; Weber-Shirk & Dick, 1997) and to gravel roughing filters (Ahn et al., 2007; Ahsan, 1995; Boller, 1993; Lin et al., 2008; Wegelin et al., 1987). However filtration theory has its limitation: the trajectory approach (a microscopic approach originally developed for air filtration which considers how individual particles collide and adhere to a single collector surface (Yao et al., 1971)) is only valid for clean bed conditions in which no particles have been deposited within the filter (Amirtharajah, 1988). The phenomenological approach (a macroscopic approach that considers bulk filter characteristics) can model the whole filter cycle including clogging, but requires extensive experiments to determine the empirical constants of the model, cannot be used for predicting removal in systems that differ from the experimental setup, and does not provide a fundamental understanding of the mechanisms of deposition.

1.3 Thesis Aims & Layout

Both gravel filter SuDS and roughing filters could benefit from an improved understanding of how sediment accumulation affects filter pollutant removal efficiency. Such information could result in improved filter design (e.g. more efficient at removing pollutants or longer lasting filters), a better understanding of the level and frequency of maintenance required to ensure adequate filter operation, or perhaps a more realistic expectation of filter performance and design life based upon local conditions ensuring that filters are only used where appropriate.

This thesis aims to better understand sediment accumulation within gravel filters through a combination of lab-based experiments and numerical modelling:

- **Chapter 2:** the change in conservative tracer transport characteristics with pollutant particle accumulation was assessed through column experiments.
- **Chapter 3:** the spatial heterogeneity of particle accumulation was measured by collecting 3D data with magnetic resonance imaging (MRI). Multiple scans of filters allowed the temporal evolution of particle accumulation to be assessed. A method for processing the raw MRI data to yield the change in 3D pore geometry was developed, assessed and applied.

- **Chapter 4:** a simple method for extracting and comparing pore network characteristics at different stages of particle accumulation was applied to the MRI derived geometry.
- **Chapter 5:** direct modelling of the 3D MRI pore geometry with the open source software OpenFOAM allowed correlation of computer flow velocities with measured particle accumulation at each point in the pore network. Lagrangian particle tracking was used to simulate the transport of a conservative tracer through the filter.

Chapter 2 – Characterisation of Filter Clogging with Conservative Tracers

2.1 Abstract

Experiments were carried out in which gravel filters, similar to water treatment roughing filters and roadside SuDS filters, were clogged with kaolin clay. The removal efficiency of the kaolin was measured for clean filters prior to any deposition, after sediment loading equivalent to 20 days of roughing filter operation (for a given filter design) and finally after 40 days of operation. Conservative tracers were used to determine the change in filter hydraulics with clogging and it was found that, by fitting a convection-dispersion model to the tracer breakthrough curves, the mobile pore volume of the filter could be estimated to within at least 10% of the independently measured pore volume. With knowledge of filter sediment loading and sediment deposit bulk density, it was possible to estimate sediment removal efficiency from the change in pore volume between two tracers. It is proposed that this may be a useful tool for evaluating laboratory or pilot scale filter performance and as a diagnostic tool to analyse failing or under-performing filters.

It was found that care must be taken when using turbidity as a surrogate for total suspended sediment concentration. Due to the preferential removal of larger particles within the filter, the influent and effluent particle size distributions differ. The kaolin turbidity/TSS relationship derived for the influent kaolin suspension was not appropriate for the effluent suspension. The use of a single turbidity/TSS relationship derived for the influent suspension under-predicted TSS removal efficiency by ~16%. It is therefore recommended that TSS removal efficiency be calculated from TSS measured by filtration through glass fibre filter papers rather than turbidity. In some situations it may be more appropriate to derive separate influent and effluent turbidity/TSS relationships to determine TSS removal efficiency from turbidity measurements.

2.2 Introduction

To understand filter removal efficiency and how it changes over the filter design life, it is necessary to understand how sediment particles are transported through and removed by

the filter and how this is affected by increasing amounts of retained sediment. The aim of this chapter was to evaluate conservative tracers as a monitoring or diagnostic tool to assess the volume of sediment retained within a gravel filter. Additionally, this chapter includes justification for aspects of the experiments used throughout the thesis such as flow rates and concentrations of sediment.

The format of this chapter consists of a brief introduction to tracer theory, justification for the use of kaolin as the model pollutant for removal, justification for kaolin concentrations and experiment flow rates and a description of the gravel filter media. The experimental setup and operation is detailed together with results on filter removal efficiency, tracer transport characteristics and change in suspension particle size distributions. Finally, the utility of tracers as a diagnostic tool for gravel filters is assessed.

2.3 Tracer Theory

Conservative tracers have been used to establish dispersion coefficients in wetlands (Werner & Kadlec, 2000), in saturated soils (Pattanaik et al., 2004) and as tools for monitoring change in granular filter hydraulics with sediment accumulation (Pendse et al., 1978; Rodier et al., 1997). In this thesis I evaluated the use of tracers as tools for measuring the change in pore volume of a gravel filter with sediment deposition and thus, to measure removal efficiency.

2.3.1 Tracer Residence Time Distribution

The residence time is the average time it takes a particle suspended in the flow to travel through the filter. Consequently, the residence time is important for pollutant treatment as longer residence equals longer contact/reaction times for particle removal, chemical degradation, bio-assimilation and adsorption.

Filter residence time is calculated as the first moment of the residence time distribution (RTD) function (Kadlec, 1994). The residence time distribution curve is also known as the tracer breakthrough curve and is calculated by:

$$\tau_a = \frac{M_1}{M_0} = \frac{\int_0^{t_f} t \cdot Q(t) \cdot C(t) \cdot dt}{\int_0^{t_f} Q(t) \cdot C(t) \cdot dt} \quad \text{Equation 2.1}$$

Where $C(t)$ = effluent tracer concentration (kg/m^3),

$Q(t)$ = flow rate (m^3/s),

M_0 = effluent mass of tracer (area under breakthrough curve) (kg/s),

M_1 = first moment of tracer effluent distribution (kg),

t = elapsed time (s),

t_f = total time span of the effluent pulse (s),

τ_a = average (mean) tracer hydraulic residence time determined from RTD (s).

The second moment of the RTD is the variance (the square of the spread of the distribution) and this is a measure of the dispersive processes occurring within the system and is expressed in units of time² (Dierberg & DeBusk, 2005):

$$\sigma^2 = \frac{\int_0^{t_f} t^2 \cdot Q(t) \cdot C(t) \cdot dt}{\int_0^{t_f} Q(t) \cdot C(t) \cdot dt} - \tau_a^2 \quad \text{Equation 2.2}$$

Where σ^2 = the variance (s^2).

The variance can be non-dimensionalised by dividing by the tracer detention time squared:

$$\sigma^2(\varphi) = \frac{\sigma^2}{\tau_a^2} \quad \text{Equation 2.3}$$

Where $\sigma^2(\varphi)$ = the non-dimensionalised variance.

2.3.2 Normalising the RTD of Steady-flow Systems

In order to compare the RTDs between experiments carried out under different conditions, each RTD should be normalised by removing units of flow rate, tracer concentration and the volume of the system (Holland et al., 2004). Volume and flow are commonly used to normalise the time axis into dimensionless units. This is done by replacing the x-axis with dimensionless flow-weighted time, known as pore volumes (PV):

$$PV = \int_{t_0}^t \frac{Q(t)}{V(t)} dt^2 \quad \text{Equation 2.4}$$

where $Q(t)$ = flow rate (m^3/s),

t = time (s),

t_0 = the time of tracer introduction (s),

$V(t)$ = the system volume (m^3),.

For perfect plug flow, the normalised residence time of the filter should occur at one pore volume. Pore volume is simply the total volume of fluid that can be contained within the porous media. If there is significant short-circuiting and regions of immobile pore water, the normalised residence time will occur in less than one pore volume.

The y-axis can be normalised with respect to the concentration of tracer injected and removal of background conductivity.

$$C(t)' = \frac{C(t)}{C_0} - \frac{C_B}{C_0} \quad \text{Equation 2.5}$$

where $C(t)'$ = normalised concentration at time t (dimensionless),

$C(t)$ = concentration at time t (kg/m^3),

C_0 = tracer stock concentration (kg/m^3),

C_B = background concentration of column effluent (kg/m^3).

2.3.3 Hydraulic Efficiency

The hydraulic efficiency is the ability of a system to distribute flow uniformly throughout its volume. This can be used to characterise the systems treatment efficiency as maximising the hydraulic efficiency maximises contact time of pollutants in the system, thus optimising the chance of pollutant removal (Holland et al., 2004).

The theoretical residence time of the system can be calculated from the system pore volume divided by the flow rate (Dierberg & DeBusk, 2005):

$$\tau_T = \frac{PV}{Q} \quad \text{Equation 2.6}$$

Where: τ_T = the theoretical hydraulic residence time (s).

Thackston et al. (1987) (in Holland et al. (2004)) proposed dividing the theoretical residence time by the actual residence time calculated from the RTD curve to give the hydraulic efficiency. This is a measure of what proportion of the filter pore volume was accessible to the tracer.

2.3.4 CXTFIT/Excel

CXTFIT is a computer programme widely used to analyse the transport of solutes in subsurface tracer experiments (Tang et al., 2010; Zhang et al., 2010; Wang et al., 2008). A Microsoft Excel version of the original FORTRAN code, developed by Tang et al. (2010), was used to fit equilibrium and non-equilibrium convection-dispersion models to the tracer RTDs using a nonlinear least squares method. Convection-dispersion model parameters such as dispersivity, mobile water fraction, tracer mass transfer and pore volume can then be estimated for each RTD.

2.4 Kaolin as Surrogate for Road & River Particulate Pollution

When measuring the long-term particle removal efficiency of gravel filters, it is desirable that the particle properties be as consistent as possible during or between experiment runs. Collecting a sufficient quantity of homogenous road runoff and river particulate matter for all experiments would be problematic. In addition, the large variation in particle size and densities that would be present in the road particles would make analysis of the results challenging. Instead, kaolin clay (Imerys Kaolin Supreme™) was used as a surrogate for both river particles and the finer fraction of road runoff particles.

2.4.1 River Particulate Matter

In drinking water treatment studies, kaolin has traditionally been used in place of the colloidal particles suspended in river water. Kaolin is suited to this purpose as it can be obtained in bulk and with a relatively uniform particle size. As both the size and surface charge of kaolin are similar to that of river particles, attachment mechanisms are similar hence removal efficiencies are similar. Researchers who have used kaolin as a surrogate

for river particles for these reasons include Wegelin et al. (1987), Rajapakse & Ives, (1990), Boller (1993), Ahsan (1995), Rooklidge et al. (2002) and Lin et al. (2008).

2.4.2 Road Runoff Particulate Matter

Road runoff particles consist of those blown onto the road surface by wind, washed off vehicles and degradation of the road, road infrastructure and vehicles themselves. As such, road runoff consists of a diverse range of particles with a range of sizes and characteristics. Other pollutants such as polycyclic aromatic hydrocarbons (PAHs), pesticides and herbicides applied to roadside verges, bacteria and pollutant metals are contained within road runoff (Napier et al., 2008). A review of numerous studies from around the world reporting the particle size distribution in road runoff is summarised in Figure 2.1 together with the measurement of a sample collected from Great Western Road, a busy urban dual carriageway in Glasgow.

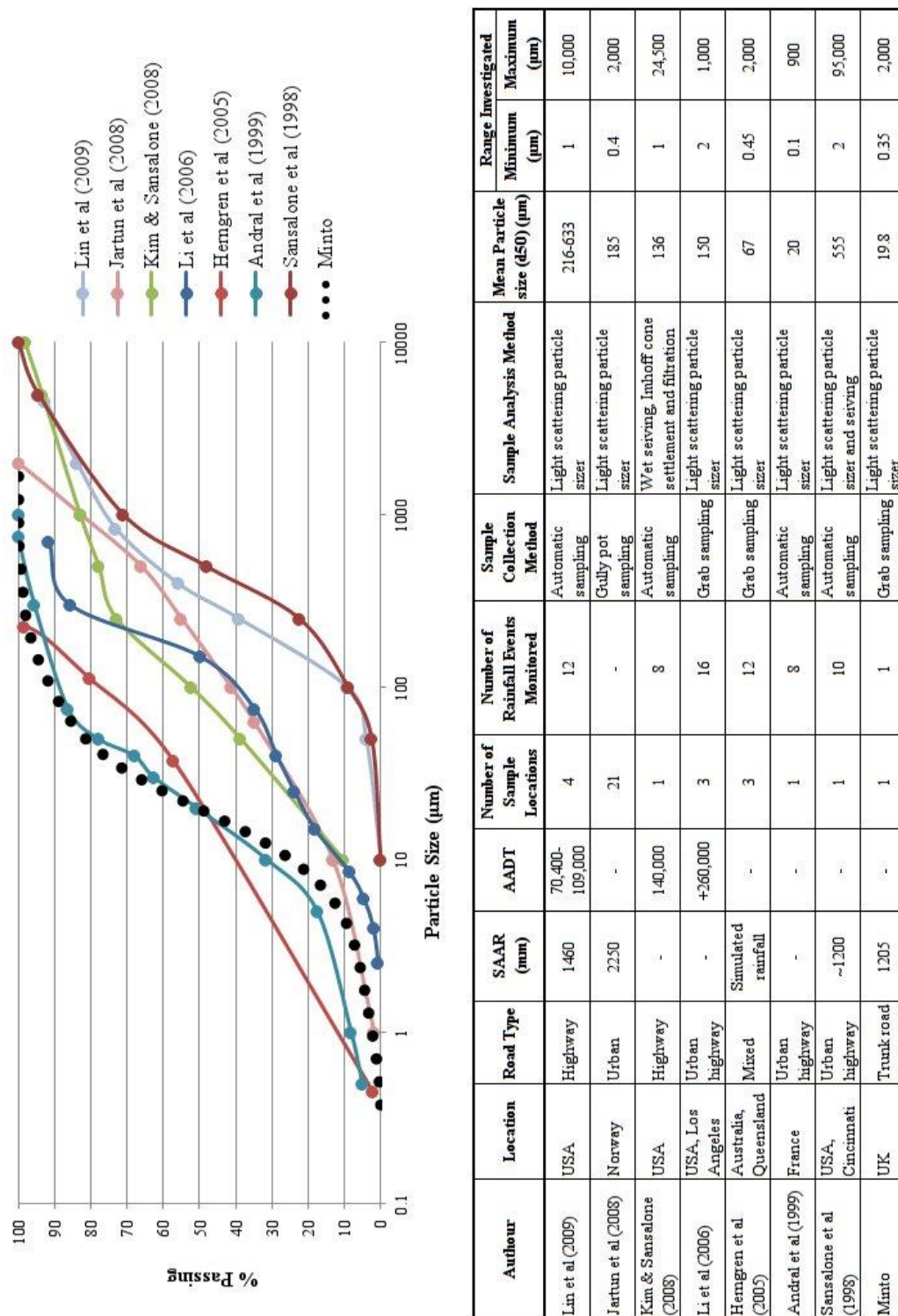


Figure 2.1. Review of reported particle size distributions in road runoff from around the world. Analysis of a single road runoff sample collected from a typical urban trunk road in Glasgow (labelled Minto) is presented for comparison. Specific Annual Average Rainfall (SAAR) is an indicator of average rainfall depth whilst Annual Average Daily Traffic (AADT) is an indicator of average traffic load.

As is evident from Figure 2.1, road runoff particle size typically covers a range from millimetres down to colloidal particles. Median (d_{50}) particle sizes are in the range $19.8\mu\text{m}$ to $633\mu\text{m}$. This highlights the variability in road runoff particle characteristics depending on location, road type, traffic characteristics, climate and geology as well as the intensity of the individual storms producing the runoff and antecedent dry period between rainfall events.

Numerous researchers have reported increased pollutant loading associated with the finer fractions of road runoff particles such as clay sized particles (Bentzen & Larsen, 2009; German & Svensson, 2002; Herngren et al., 2006; McKenzie et al., 2008; Pal et al., 2010). This is most likely because, due to their large surface area and negative surface charge of the clay sized particles, pollutants such as pollutant metals and PAHs adsorb onto their surface (Li et al., 2006). When coupled with the difficulty in removing such fine particles in other SuDS components such as ponds and swales, any improvement in filter drain design so as to retain clay sized particles would reduce the greater volume of pollution passing through a SuD treatment system. As such, it is appropriate to use kaolin as a surrogate for road runoff particles when measuring the removal efficiency of clay sized particles.

2.4.3 Kaolin Properties

The kaolin particle size distribution was measured by dynamic light scattering with a Malvern Zetasizer ZS90 (Malvern Instruments). This instrument records the intensity of light scattered by particles in the suspension over discrete time steps. The change in intensity is a function of particle motion. Provided that temperature and viscosity of the suspension are known and constant, and the particles are small enough that settlement under gravity is not significant, the particle motion can be considered to be from Brownian motion alone. From this Brownian motion, the particle size distribution can be inferred.

To ensure the particle size measurements were representative of the particles entering the gravel filters, multiple samples (totalling 31) were taken throughout the experiments from the kaolin suspension feed tank at the same level as the tank extraction tubes. This sampling method captured the natural flocculation of particles within the tank (i.e. the

flocculation occurring without the addition of a chemical coagulant) and for a change in average particle or particle floc size as the experiment progressed and tank volume decreased, as presented in Figure 2.2.

Ideally particle size would remain constant throughout each experiment; however, despite vigorous mixing of the kaolin suspension feed tank with an overhead stirrer (details of the experimental setup can be found in Section 2.7), differential settlement of the naturally polydisperse kaolin led to a decrease in particle size over time. As shown in Figure 2.2 A), influent median particle size decreases from 1762nm when the tank is full (45 litres) to 1126 when the tank is empty (5 litres remaining below extraction tube level). This change in particle size must be considered when analysing the particle removal efficiency results (Section 2.8.3).

Particle size variation within the first 10 litres is, on average, 4.8% (reducing from 1762nm to 1682nm). The evaluation of size dependent particle breakthrough (Section 2.8.8) was limited to the first 10 litres. It is worth noting that none of the studies identified in the literature review that used a polydisperse particle such as kaolin reported influent particle size variation over time and the effect it may have on removal efficiency.

Kaolin has a dry density of 2600g/l. Settling column tests established that a high concentration (80g/l) kaolin suspension settled with a bulk density of 1178g/l which is similar to the value of 1150g/l determined by Wegelin et al. (1987). It is assumed that the particle-by-particle accumulation of kaolin within the filter would result in a sediment with less trapped water and hence a higher bulk density than that observed in the settling column tests, similar to the values of 1264 and 1340g/l reported in Boller & Kavanaugh (1995) for 3 μ m diameter kaolin deposits. The settled bulk density of kaolin therefore lies within the range of 1178 to 2600g/l and must be determined experimentally.

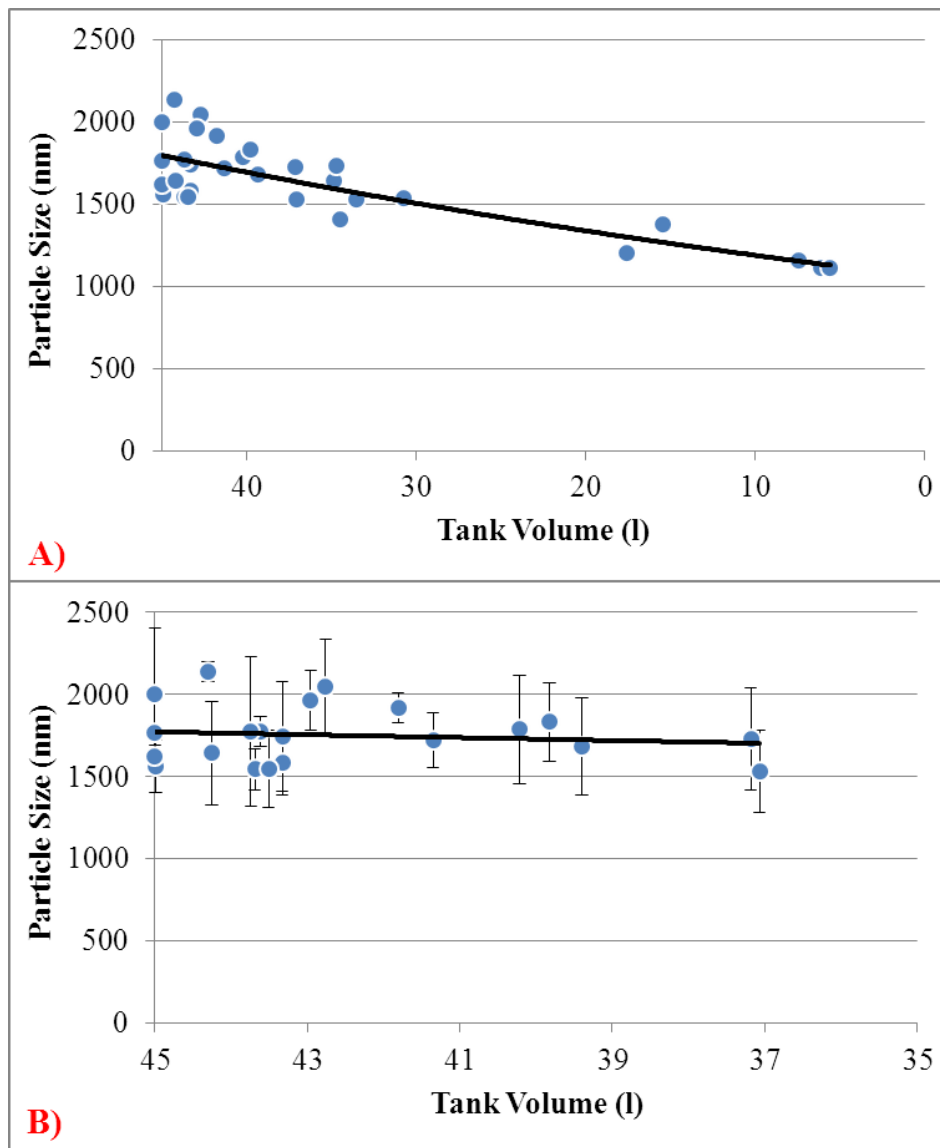


Figure 2.2. Median (d_{50}) size of kaolin particles entering filter over A) the entire removal efficiency measurement period from full tank (45 litres) to empty (0 litres)) and B) the particle size monitoring period (first 10 litres). Vertical bars in B denote range in particle size about the median from 5th to 95th percentile for each measurement. A reduction in median particle size entering the filter is evident when considering the entire removal period, yet is relatively minor when considering the first 10 litres, as shown by the exponential trendlines (solid black lines) fitted to each data set.

The concentration of particles in suspension can be measured gravimetrically following the procedure outlined in standard method 2540D (American Public Health Association, 1999) in which a sample of known volume is filtered through a glass fibre filter of known mass, dried to constant mass and the increase in mass recorded. A far quicker method is to measure the turbidity of each sample.

Turbidity is an optical property of a particle suspension that primarily depends upon particle concentration. However, particle colour and particle size distribution also affect turbidity, as do environmental factors such as temperature (Lin et al., 2008). As such, the relationship between the turbidity and concentration of a kaolin suspension is not quite linear (Lin et al., 2008; Wegelin et al., 1987) and must be established for each batch of kaolin. Results of the turbidity/concentration relationship for the batch of kaolin used in this thesis are presented in Section 2.8.1.

2.4.4 Fluid Phase

Attachment properties of the kaolin particles and the suspension stability depend upon the chemistry of the fluid phase (O'Melia & Stumm, 1967). Measurements of pH and zeta potential were made for three concentrations of kaolin, each suspended in either deionised water (Millipore Milli-Q, 18M Ω /cm resistivity), tap water or SuDS water. The SuDS water was collected from a highway SuDS system (M77, East Ayrshire, UK) between filter drain outflow channel and sedimentation pond during a rainfall event.

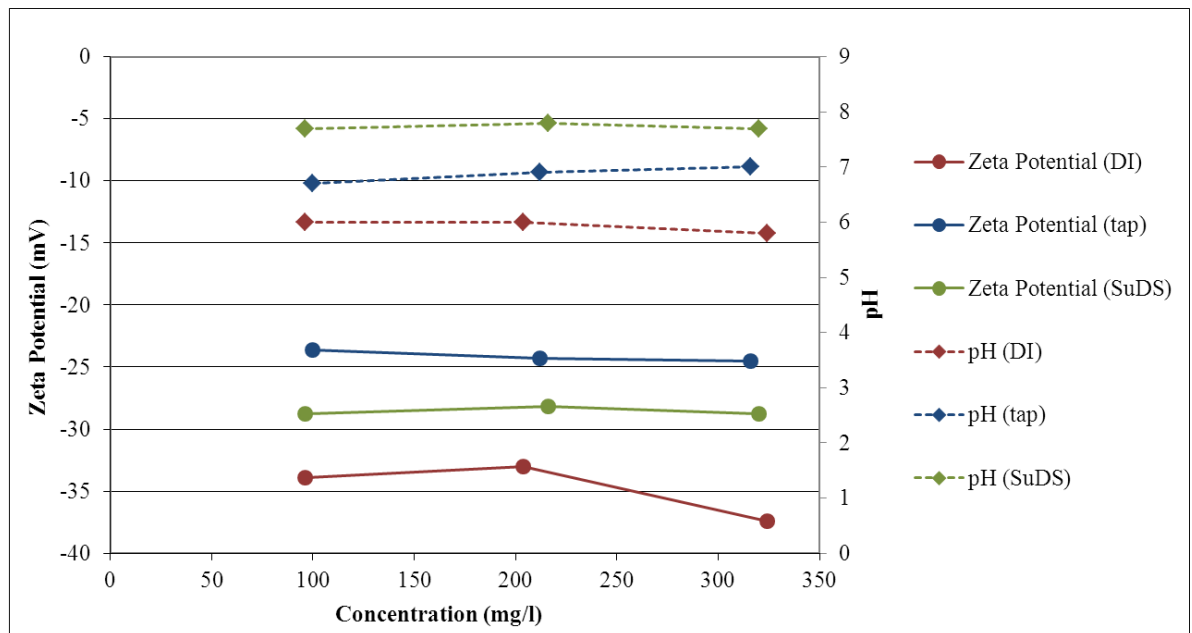


Figure 2.3. Variation in zeta potential and pH with kaolin suspension concentration and fluid type.

Results are presented in Figure 2.3 and show that both zeta potential and pH are independent of particle concentration, but are dependent on the fluid type. Ideally SuDS water or river water would be used in the experiments. However, the properties of the SuDS or river water would vary with each rainfall event and would change with time in storage hence could not reliably be collected and used. The zeta potential and pH of the tap water/kaolin suspensions more closely match those of the SuDS water than does the deionised water, however the difference is minimal. Tap water was chosen for the practicality of obtaining the large volumes (~225 litres) required for each filter run.

2.5 Hydraulic & Lifetime Sediment Loading on Filters

As the aim of this chapter is to evaluate changes in filter hydraulics over the life of a gravel filter as it clogs with sediment, the clogging process must be accelerated to ensure substantial clogging within a feasible timescale for lab based experiments.

In the Trajectory Approach to modelling particle removal proposed by O'Melia & Stumm (1967), three methods by which particles may be transported to the gravel surface are considered: diffusion, interception and sedimentation. Transport by diffusion and sedimentation are both reduced as velocity increases. Velocity therefore cannot be increased so as to deliver a greater quantity of sediment to the filter and accelerate clogging without altering the deposition mechanisms under investigation.

Particle concentration on the other hand should not influence particle transport to the gravel surface. This is provided that the particles can be considered dispersed with a bulk density approximately equal to the fluid density and no particle-particle interactions that would hinder settlement.

Hindered settlement only occurs once the mass of particles in suspension exceeds several kilograms per cubic metre. Clear hindered settlement of kaolin was noted by Dankers & Winterwerp (2007) at concentrations of 27kg/m^3 (2.7% weight for weight) and above whilst Nicholson & O'Connor (1986) used 25kg/m^3 (2.5% w/w) to define the onset of hindered settlement in cohesive sediments based on laboratory studies. The maximum concentration of kaolin used in this study was 200g suspended in 30 litres of tap water

corresponding to a weight for weight ratio of 0.67% and no hindered settlement of the suspension was observed.

Filter clogging was accelerated by increasing the concentration of kaolin entering the filter and, in the case of SuDS gravel filters, duration of flow entering the filter whilst maintaining realistic flow velocities. The influent kaolin concentration and flow duration were chosen to obtain a meaningful degree of clogging based on whether the filter would be operated as a roughing filter for potable water supply or SuDS gravel filter for treating highway runoff.

2.5.1 Roughing Filter Hydraulic & Sediment Loading Rates

2.5.1.1 Hydraulic Loading

The hydraulic loading on roughing filters is normally expressed as a filtration rate which is the inflow rate divided by the cross-sectional area of the filter and is equivalent to the superficial flow velocity through the filter. The volume that must be treated by the roughing filter is determined by the required output of the water treatment works, which is often limited by other components of the treatment system such as slow sand filters. Cross-sectional area of the filter can therefore be chosen to ensure the filtration rate falls within the desired range.

Filtration rates used in pilot studies and full scale roughing filters generally fall within the range of 0.3 to 1.5m/hr (Ahsan, 1995; Sánchez et al., 2006; Nkwonta & Ochieng, 2009) and appear to be based upon the recommendations of Wegelin et al. (1987), perhaps because these are incorporated into the only comprehensive manual for roughing filter design and construction (Wegelin, 1996).

2.5.1.2 Sediment Loading

River water sediment loading varies with climate, geology and season (amongst other factors). Reported raw water concentrations of suspended solids entering roughing filters range from 10 to 800 NTU (nephelometric turbidity units, a standard measure of turbidity) (Wegelin, 1996; Galvis, 1999; Ochieng et al., 2004; Boller, 1993; Ahsan, 1995) under

normal conditions. During high river flows the total suspended solids load can be much greater. Sánchez et al. (2006) report that, over a 10 year period in Peru, peak turbidities exceeded 3600NTU, however 90% of the monitoring samples were below 80NTU whilst in Bolivia peaks of 1350NTU commonly lasted for two or three days.

The sediment loading on a filter over its lifetime can be calculated as the suspended sediment concentration multiplied by the flow rate multiplied by the duration of operation before maintenance. A load factor is necessary to take account of filters that are only in operation for a fraction of a 24 hour period. It is preferable to use the filtration rate in place of flow rate as this way the cross-sectional area of the filter need not be known. The result is Equation 2.7 in which the sediment loading for a given unit of time (for instance 1 day) can be calculated. The units of Equation 2.7 are g/m^2 i.e. the mass of suspended sediment entering each unit of cross-sectional area of the filter over the run duration.

$$\text{sediment load} = \text{TSS} \cdot V_f \cdot T \cdot \text{LF} \quad \text{Equation 2.7}$$

Where TSS = total suspended sediment concentration (g/m^3),

V_f = filtration rate (m/hr) = flow rate divided by filter cross-sectional area,

T = filter run duration (hours),

LF = load factor on filter (dimensionless) = hours of operation per 24 hours.

In the removal efficiency experiments, a known mass of kaolin passed through the filter at each stage of the experiment. Non-dimensionalising this mass by the cross-sectional area of the experimental filter column allows direct comparison with the roughing filter sediment loading in g/m^2 .

2.5.2 Highway SuDS Gravel Filter Hydraulic & Sediment Loading Rates

2.5.2.1 Hydraulic Loading

SUDS for Roads (Pittner & Allerton, 2010) is a guidance manual that aimed to consolidate all the design guidance and information available on road application SuDS, specifically for Scotland. Together with The SUDS Manual (Woods-ballard et al., 2007) and the Design Manual for Roads and Bridges (DMRB) sections relevant to road drainage, these three documents constitute the main design guidance for roadside filters.

The hydraulic loading on roadside gravel SuDS filters is more complicated than for roughing filters. This is because inflow volume is usually not controlled; instead it is determined by the amount of rainfall, the “catchment” size and the design of the SuDS system. Roadside SuDS filters are designed to empty within 24 hours so that they have the capacity to attenuate the runoff from the next rainfall event. The water level in a SuDS filter therefore constantly varies between full and empty in response to rainfall.

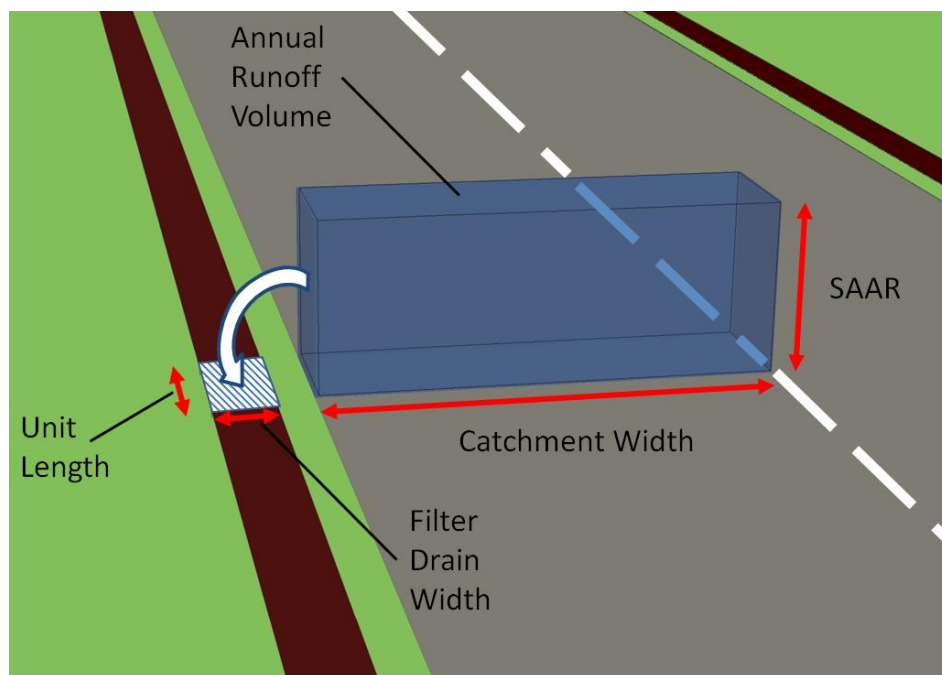


Figure 2.4. Total annual volume of road runoff entering each unit length of roadside filter drain for a single carriageway road. Approximately to scale with specific annual average rainfall (SAAR) of 1400mm (typical of West Scotland), road width of 3.65m and filter drain width of 0.5m.

Roadside filter drains are linear structures that run parallel to the road. The catchment area that is connected to the SuDS can be described per metre length of road regardless of whether the flow enters the SuDS as lateral sheet flow from the road surface directly to the drain, as shown in Figure 2.4, or to kerbside gullies and then into the drain at specific points.

The Scottish trunk road network consists of 3,405km of road, 559km of which is motorway of 2 to 4 lanes, 526km of which is dual carriageway A road and 2,320km of which is single

carriageway A road (National Statistics, 2008). The majority of the trunk road network is therefore single or dual lane. Using the standard lane widths given in the DMRB (HMSO, 2005a) and assuming all roads have a camber that diverts the flow either to the left or the right of the central reservation, the catchment area is between $3.65\text{m}^2/\text{m}$ length for a single lane with no hardshoulder to $10.60\text{m}^2/\text{m}$ length for a dual carriageway with a 3.30m hardshoulder.

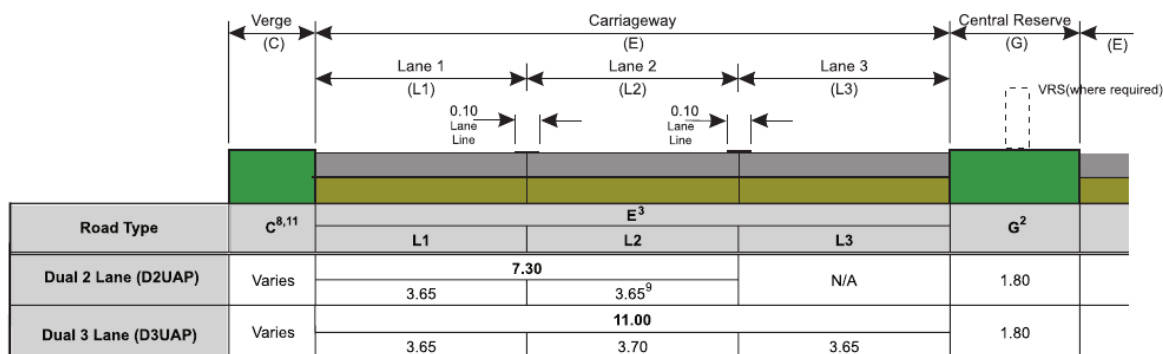


Figure 2.5: Typical cross-section of UK urban dual carriageway road (HMSO, 2005a).

Filter drain widths are a minimum of 0.2m (HMSO, 1998) with no upper limit set in the design guidance. This is because filter drain depth is often constrained by topography yet the filter must have sufficient capacity to attenuate the 1 in 30 year return period flow volume. The filter width, together with the porosity of the gravel media, is chosen to achieve this capacity. In practice they rarely exceed approximately 1m in width.

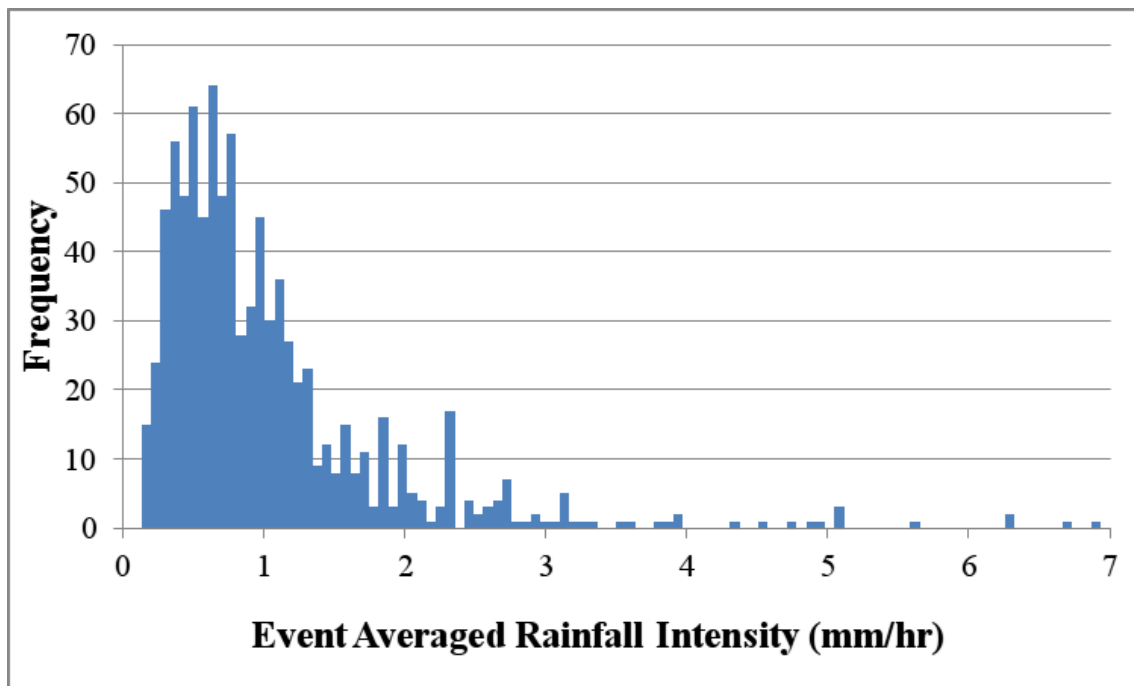


Figure 2.6. Histogram of event averaged rainfall intensities for all events exceeding 1mm total depth within the five year period (886 separate rainfall events). The annual volume of road runoff entering each meter length of filter can be calculated by multiplying the catchment area by the annual rainfall. This volume is useful when calculating the pollutant load on a filter over the course of a year but does not allow the flow rate entering the filter to be calculated as for much of the year there is no rainfall and hence no road runoff. The approach taken in this thesis to determine the range in potential filter flow rates was:

1. use five years of 15 minute interval tipping bucket rain gauge measurements of rainfall at a location in Glasgow (175,000 measurements),
2. divide this data series into discrete rainfall events using an inter-event dry period of three hours to define the end of one rainfall event and the start of a new event,
3. remove all rainfall events with less than 1mm total precipitation as these events are unlikely to produce runoff with most of the rain water stored on the road surface (Ellis et al., 1986; Chin, 2000; Ostendorf et al., 2001),
4. calculate the average intensity of each of the resulting 886 separate rainfall events (see Figure 2.6),

5. calculate the maximum intensity within each rainfall event by multiplying the average intensity by 3.9, termed the 50% summer profile and derived from analysis of UK summer storms (Faulkner, 1999),
6. define five catchments:
 - “best case” filter design with a filter width of 1m, road width of 3.65m (single lane trunk road with no hardshoulder) and over-the-edge inflow;
 - “median case” with filter width of 0.5m, road width of 7.3m (two lane trunk road with no hardshoulder) and over-the-edge inflow;
 - “worst case” with filter width of 0.2m, road width of 10.6m (two lane trunk road with hardshoulder) and over-the-edge inflow;
 - median case with flow entering filter through road gullies spaced at 24m intervals corresponding to a road slope of 0.5° (HMSO, 2000), the minimum slope necessary to ensure drainage of the road surface;
 - median case with flow entering filter through road gullies spaced at 79m intervals corresponding to a road slope of 6° (HMSO, 2000), the maximum slope typically allowed for motorways;
7. each catchment area was divided by the filter drain width and multiplied by both the 886 event averaged rainfall intensities and peak intensities to obtain a range in filtration rates.

The range in average and peak filtration rates for each filter and road design are presented in Figure 2.7. It is apparent that the filtration rates in roadside SuDS filters span several orders of magnitude depending on the design of the filter, the road, the rainfall event and whether peak or average event intensities are considered.

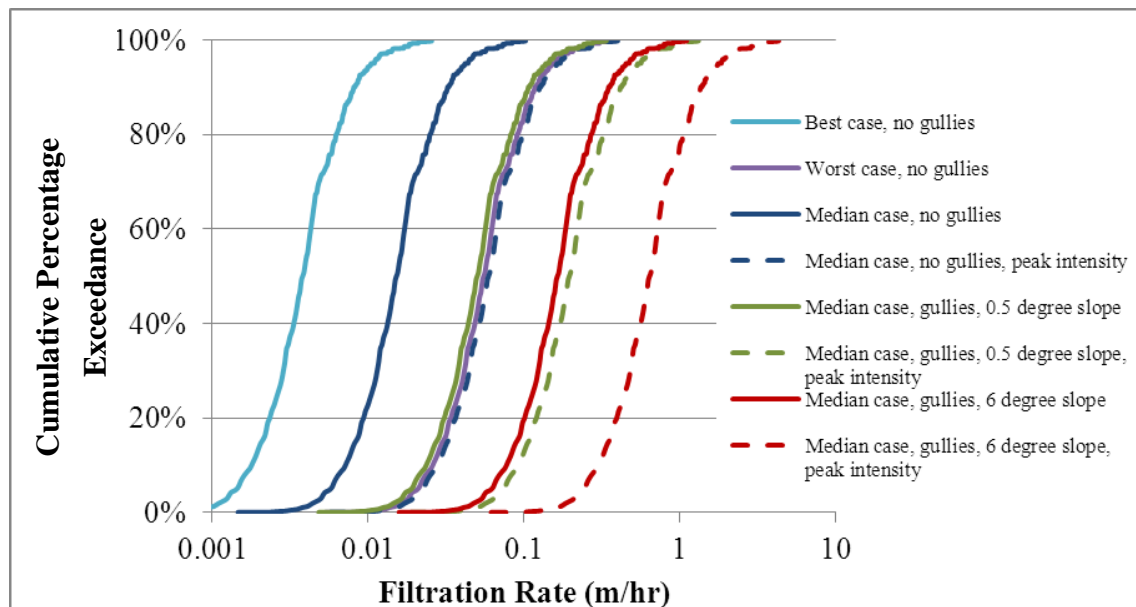


Figure 2.7. The total volume of flow passing through the roadside SuDs filter over the five year period investigated is plotted against the range in filtration rates. Each data series corresponds to different filter widths, road widths, event averaged intensity or peak intensity, and, when flow into the filter is through road gullies, the slope of the road which determines gully spacing and hence catchment area between gullies.

2.5.2.2 Sediment Loading

Duncan (1999) reviewed the concentration of pollutants in urban stormwater runoff from a variety of land uses at locations throughout the world. Suspended solids from 37 locations were evaluated and found to vary between 60mg/l and 720mg/l with a mean of 210mg/l. Duncan (1999) notes a strong correlation between average suspended solids concentration and mean annual rainfall with a higher mean annual rainfall resulting in lower average concentrations leading to the conclusion that the runoff concentration is limited by the availability of sediment.

The annual sediment loading on a roadside SuDS filter can be calculated as the annual average total rainfall depth of runoff producing events (in this case taken to be all events with a total rainfall depth greater than 1mm) multiplied by the average runoff suspended sediment concentration for a range of catchment sizes and filter widths:

$$\text{sediment load} = \frac{\sum D_{>1\text{mm}}}{\text{Years}} \text{TSS} \cdot W_R \cdot \text{Gullies} / A_F \quad \text{Equation 2.8}$$

Where A_F = area of filter drain for a unit length (m^2),

$D_{>1\text{mm}}$ = the depth of rainfall for each event exceeding 1mm (m),

Gullies = spacing between roadside gullies (set as 1 if no gullies) (m),

TSS = total suspended sediment concentration (g/m^3),

W_R = width of road carriageway (including hardshoulder) (m),

Years = number of years of data series from which rainfall depths were evaluated.

2.6 Gravel Media Physical Characteristics

Two types of gravel media were investigated: angular gabbro from a quarry that supplies aggregates for drainage and rounded beach pebbles supplied by Rowebb Garden Aggregates. The angular gabbro was divided into the two size ranges of 4-8mm and 8-11.2mm with standard sieves and mechanical shaker, whilst the rounded beach pebbles were sieved to 8-11.2mm. Average gravel particle sizes were therefore 6mm and ~10mm.

Roughing filters typically consist of several compartments, each filled with a different size of media e.g. 1.5-2mm, 3-5mm, 7-10mm and 15-25mm (Wegelin et al., 1987). For roadside SuDS filters, locally available graded stone/rock is recommended with a nominal size of 40-60mm (Woods-ballard et al., 2007) or locally available Type B (BS EN 13242) 20-40mm gravel (HMSO, 1998).

The average gravel sizes of 6mm and ~10mm used in this study were more appropriate for roughing filters than for roadside SuDS filters. Larger gravel sizes in the range 20-40mm were not investigated because, to avoid significant wall effects, the ratio of the column to the average gravel particle diameter should exceed 10:1. With the 100mm diameter column used, the maximum gravel diameter was 10mm.

To measure the difference in angularity of the two types of gravel, an image-based method that related angularity to the geometry of each gravel grain was used, as described by Janoo (1998). The degree of angularity was calculated for 20 pieces of angular gravel and 20 pieces of rounded gravel with Equation 2.9.

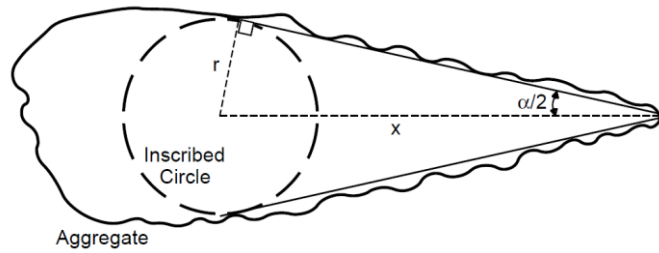


Figure 2.8: Parameters for determining the degree of angularity (Janoo, 1998).

$$A_i = (180^\circ - \alpha) \frac{x}{r} \quad \text{Equation 2.9}$$

where: A_i = degree of angularity (degrees)

α = measured angle (degrees)

r = radius of the maximum inscribed circle (m)

x = distance to the tip or the corner from the centre of the maximum inscribed circle (m)

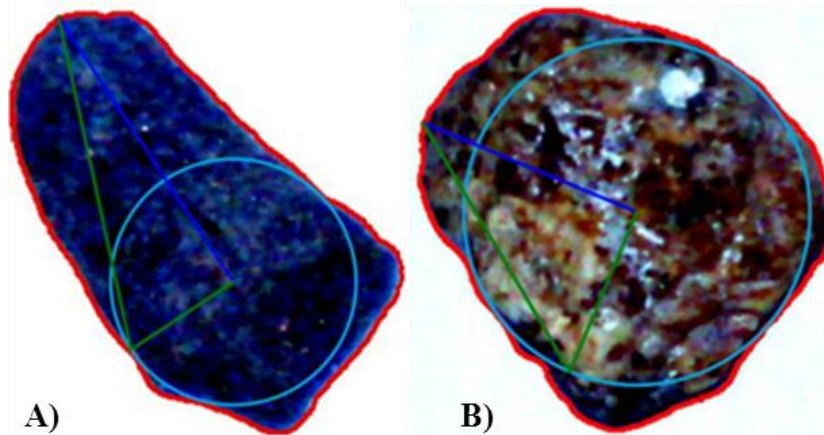


Figure 2.9. A) angular 10mm gravel grain B) rounded 10mm gravel grain.

Average degree of angularity was 316 with a standard deviation of 133 for the angular gravel and 250 with a standard deviation of 81 for the rounded gravel. This shows that the angular gravel is indeed more angular than the rounded, but also is more heterogeneous with implications for gravel packing in the filter, pore throat size distributions, porosity and hence local variations in the interstitial pore velocity.

A standard procedure was adopted for filling each column with gravel so as to minimise variations in porosity due to the placement of the gravel and ensure repeatable and comparable experiments. The procedure is described in Section 2.7.1.

Whilst only the physical properties of the gravel were investigated in this thesis, Norris et al. (2013) have shown that both gravel mineralogy and surface weathering are important for pollutant metal adsorption. Using the same angular gabbro as used in this thesis, they found that scrubbing the gravel clean resulted in removal of a weathered clay layer and a decrease in pollutant metal removal efficiency. It is therefore worth bearing in mind that, when selecting the most appropriate media for a filter, both the physical and mineralogical characteristics of the gravel must be considered.

2.7 Experimental Setup & Procedure

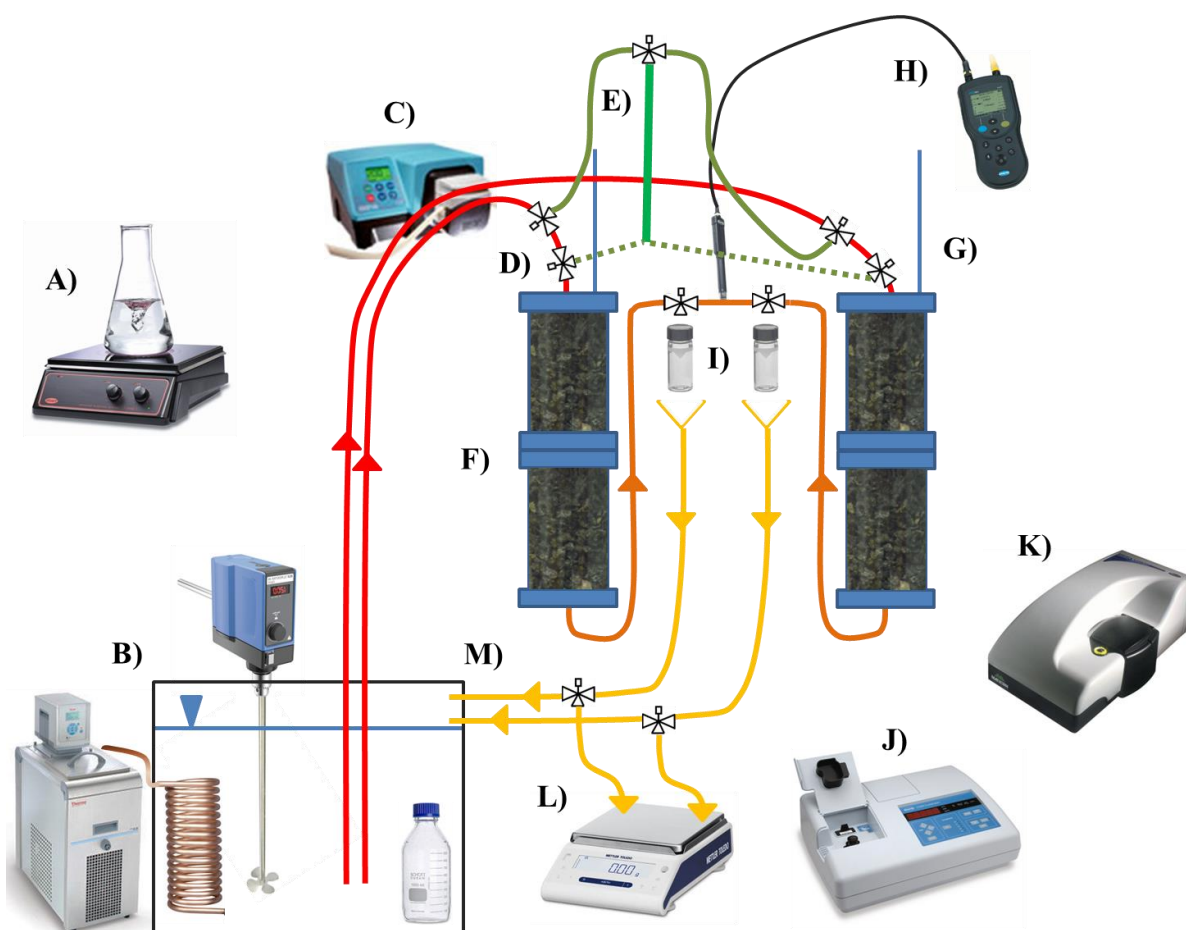


Figure 2.10. Experimental setup for two filter column experiments run in parallel.

Figure 2.10 outlines the experimental setup and equipment used to deliver a kaolin suspension to the two gravel columns, measure removal efficiency, monitor change in particle size and measure conservative tracer breakthrough profiles. The experimental setup consisted of the following components:

- A) Magnetic stirrer to mix stock of concentrated kaolin suspension.
- B) 50litre thermally insulated feed tank filled with 45litre kaolin suspension kept in suspension with an overhead stirrer and at constant temperature with a heater/cooler unit (ThermoFisher) connected to a copper heat exchange coil. Tracer stock kept in bottle in tank prior to tracer injection.
- C) Dual channel peristaltic pump (Watson Marlow 323E).
- D) Three-way valves controlling flow through tracer injector.
- E) Tracer injector system diverting flow from pump to ensure tracer delivered at a constant flow rate. Injector system must be connected directly to either column and alternated between tracer injections.
- F) Gravel filled column composed of sections of clear acrylic, sealed with silicone sealant and thermally insulated.
- G) Piezometer allowing measurement of inlet head.
- H) Multimeter (Hach HQ40D) with conductivity probe (Hach CDC401) allowing on-line measurement of conductivity.
- I) Sample collection area with three-way valves to direct flow to conductivity probe (during tracer breakthrough measurement) or free outflow (during clogging and removal efficiency measurement phases).
- J) Turbidimeter (Hach 2100N) for off-line measurement of kaolin concentration.
- K) Particle sizer (Zetasizer ZS90, Malvern Instruments) for off-line measurement of particle size.
- L) Balance to measure effluent mass per unit of time and hence flow rate.
- M) Return of column effluent to tank during recirculating phases.

The experimental procedure consisted of seven phases outlined graphically in Table 2.1:

1. filling and sealing the gravel column, characterising initial porosity and conservative tracer transport properties,
2. first measurement of kaolin concentration and particle size breakthrough profiles together with removal efficiency from a once through flow of kaolin suspension,

3. first clogging of filter with high concentration kaolin suspension recirculated through tank and followed by a tracer transport measurement,
4. second measurement of kaolin concentration breakthrough profile together with removal efficiency from a once through flow of kaolin suspension,
5. second clogging of filter with high concentration kaolin suspension recirculated through tank and followed by a tracer transport measurement,
6. third and final measurement of kaolin concentration breakthrough profile together with removal efficiency from a once through flow of kaolin suspension,
7. dismantling filter, measuring mass of kaolin retained in gravel, in filter pore water and within the acrylic column.

Table 2.1. Experiment procedure for clogging filter and acquiring measurements.

	Phase 1	Phase 2	Phase 3	Phase 4	Phase 5	Phase 6	Phase 7
Flow	Once through	Once through	Recirculated	Once through	Recirculated	Once through	-
Kaolin	-	667 mg/l	5000 mg/l	667 mg/l	5000 mg/l	667 mg/l	-
Tracer	-	T1	-	T2	-	T3	-
Turbidity Measurement	-						
Size Measurement	-						
Samples for Filtering	-						

Table 2.2. Experiment parameters.

Name	Run Identifier	Parameters			
		Shape	Size	Flow Rate	Length
Standard	S	Angular	8-11 mm	0.35m/hr	2 sections
Fine gravel	FG	Angular	4-8mm	0.35m/hr	2 sections
Layered gravel	LG	Angular	8-11mm, 4-8mm	0.35m/hr	2 sections
Rounded gravel	RG	Rounded	8-11 mm	0.35m/hr	2 sections
Low flow, long	LF	Angular	8-11mm	0.12m/hr	3 sections

Five filter runs were performed, each with two identically prepared columns. The details of each run are provided in Table 2.2. The parameters investigated were gravel size, the effect of layering different sized gravels, gravel shape and the residence time within the column. Residence time (Run LF) was evaluated by reducing the flow rate and increasing the column length. To determine if “filter ripening” occurs during the initial periods of kaolin deposition, run LF was conducted with five once through removal efficiency phases (5x Phase 2) and a lower kaolin loading during clogging (Phases 3 & 5) of 2500mg/l in place of 5000mg/l.

2.7.1 Phase 1 – Column Preparation & Tracer Characterisation

Columns were filled by hand with a known mass of washed and dried gravel. After every handful of gravel was placed in the column, the column was gently tapped to re-arrange and compact the gravel. Once full, silicone sealant was used to ensure a waterproof seal on each section of the column.

The column was initially filled with water by slowly pumping from a container filled with a known mass of room temperature tap water. By filling from the base upwards and recording the change in mass of the container, the volume of water in the tubing and the pore volume of each section of the gravel column could be ascertained.

After switching from upflow to a downflow configuration and running ten pore volumes of temperature regulated tap water through the filter at the experimental flow rate, a pulse of NaCl tracer was injected. The injection system consisted of a 10ml graduated pipette filled with 10ml of tracer (at feed tank temperature) connected at one end to the column influent line and at the other end to the column inlet (see E, Figure 2.10). During tracer injection, three-way valves divert the flow supplied by the peristaltic pump through the pipette forcing the tracer into the column at a constant flow rate. With this system tracer pulse volume and duration were precisely known.

A conductivity probe connected to a meter with time-interval data logging capabilities allowed the conductivity of the column effluent to be measured at ten second intervals. The entire tracer breakthrough profiles were captured together with the volume of the profile and average concentration and was analysed with the Microsoft Excel implementation of CXTFIT.

2.7.2 Phase 2, 4 & 6 – Kaolin Removal Efficiency & Size

To measure kaolin removal efficiency, a constant inflow of kaolin from the feed tank was passed through the filters. Samples were taken from the feed tank and from the column outflow and turbidity was measured with a ratio turbidimeter then converted to a

concentration of kaolin using Equation 2.10 and Equation 2.11 for inflow and effluent respectively (see Section 2.8.1).

Kaolin stock was prepared by adding 30g dry kaolin to 5l of tap water and mixing with a magnetic stirrer for 24 hours. The stock was then added to 40l of tap water in the temperature controlled feed tank and mixed with an overhead stirrer for one hour; enough time for a stable suspension and temperature to be reached.

The peristaltic pump RPM was set to supply the required flow rate through the column. The flow rate was subsequently monitored at regular intervals by collecting the column effluent over a given time period and dividing the volume by the length of time.

Particle size measurement was performed on a selection of the influent and effluent samples used for turbidity measurement. The selection of samples focused on the point of breakthrough so as to establish the change in particle size at breakthrough.

When the kaolin suspension feed tank approached empty, flows were stopped and the remaining kaolin suspension in the feed tank was collected, the volume measured (~5l) and the concentration of kaolin measured by filtration so that a mass balance of kaolin passing through the filter could be calculated.

Phases 4 and 6 were identical to Phase 2, only without the particle size measurement.

2.7.3 Phases 3 & 5 – Clogging & Tracer Characterisation

A kaolin stock of 200g in 5l of tap water was prepared and mixed for 24 hours prior to being added to the feed tank. After thorough mixing in the feed tank with 35l tap water, the clogging phase began in which the concentrated kaolin was re-circulated through the filter for 48 hours.

At the end of the clogging phase, a 10ml tracer pulse was injected to establish the change in filter hydraulics due to the deposition of kaolin within the filter.

2.7.4 Phase 7– Mass Balance

After the final measurement of removal efficiency (Phase 6), the columns were drained by pumping in air at the minimum flow rate of 3 RPM (~5ml/min). The volume of pore water in the columns was measured and the concentration of kaolin measured by filtration. The gravel from each column section was removed and dried at 103-105°C until a constant mass was reached, allowed to cool and then the mass of gravel and attached kaolin was measured. Finally, the acrylic components of the columns were rinsed with tap water. All rinse water was collected, the volume was measured and the concentration of kaolin in the rinse water was measured by filtration through glass fibre filter paper.

As the mass of kaolin attached and retained by the gravel, the concentration of kaolin in the pore water (and washed out of the column during draining) and the amount of kaolin retained on the column itself was known, a mass balance of kaolin retained within the filter could be performed.

2.8 Results

2.8.1 Kaolin Turbidity/Concentration Relationships

The relationship between turbidity and concentration of the kaolin suspension was established by taking 200mg of kaolin, suspending in 200ml of tap water (see Section 2.4.4 for justification of using tap water) to obtain a concentration of 1000mg/l. The suspension was mixed by overhead stirrer for 24 hours to ensure a uniform distribution of kaolin before serial dilutions down to 10mg/l were performed. The turbidity of each dilution was measured using a Hach 2100N ratio turbidimeter with an EPA method 180.1 compliant filter installed and with signal averaging turned on. This created the range of turbidity/concentration values labelled as *Standard* in Figure 2.11 with values from Wegelin et al. (1987) presented for comparison.

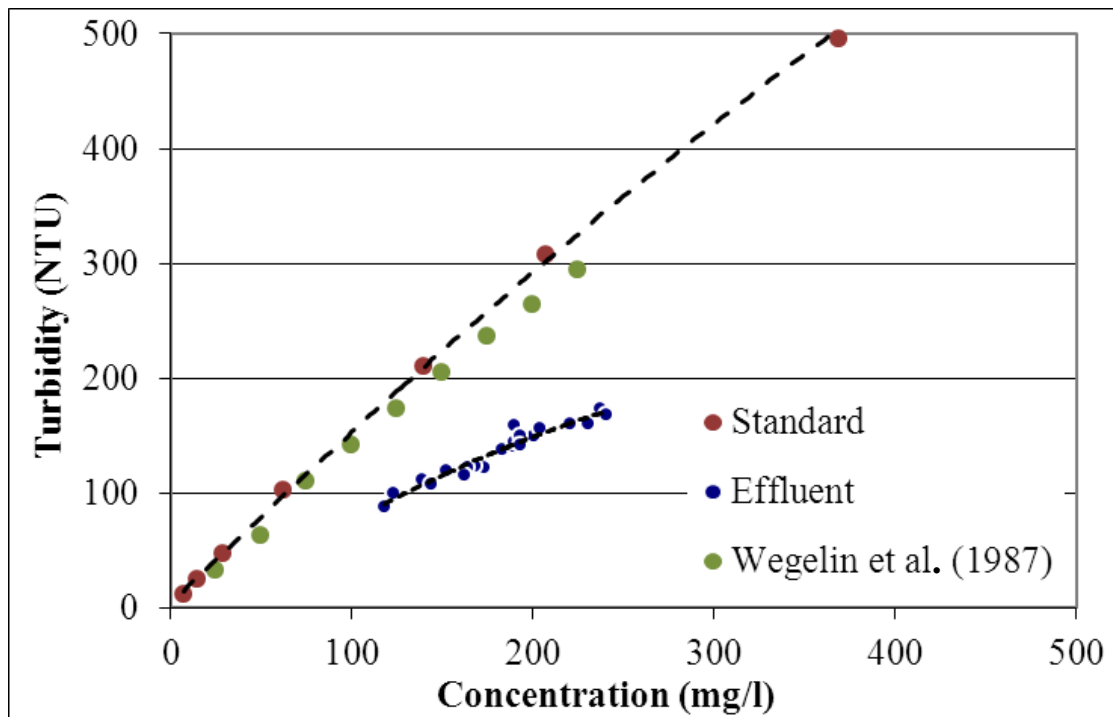


Figure 2.11. Kaolin turbidity/concentration relationship for 1) standards in which known masses of kaolin were suspended in a known volumes of water, 2) the gravel filter effluent concentration measured by filtration through glass fibre filters and 3) the relationship reported by Wegelin et al. (1987). Turbidity was measured in nephelometric turbidity units. Polynomial trend lines were fitted to the *Standard* and *Effluent* data series. The *Standard* data series (and associated trend line) extended to 1000mg/l (947NTU) but is only shown up to 500 for clarity.

The *Standard* turbidity/concentration relationship was best fitted by a second order polynomial equation with an R^2 value of 0.999 (Equation 2.10). This equation was used when determining the mass of kaolin entering the filter based upon measurements of turbidity.

$$C_{\text{Inf}} = -0.0005\text{NTU}^2 + 1.5642\text{NTU} \quad \text{Equation 2.10}$$

Where C_{Inf} = Influent kaolin concentration (mg/l),

NTU = measured turbidity (NTU).

However, measurement of particle size (Section 2.8.8) entering and leaving the gravel filters showed a reduction in average particle size, thought to be due to the increased

removal of larger particles within the filters. Consequently, the particle suspension characteristics of the effluent differ from the influent. To test if this resulted in a different turbidity/concentration relationship for the effluent, 22 effluent samples were collected during filter runs and analysed with respect to turbidity and concentration as per standard method 2540D. Turbidity of the glass fibre filtrate was also measured and found to be within the range of pure tap water turbidities leading to the conclusion that the glass fibre filters (Whatman GF/F, nominal pore size 0.7 μ m) retained all of the kaolin. The results are plotted in Figure 2.11 as series *Effluent* and clearly show that the effluent turbidity/concentration relationship differs from that of the influent. The Effluent relationship can be characterised by a polynomial equation with an R² value of 0.939 (Equation 2.11).

$$C_{\text{Eff}} = -0.0013\text{NTU}^2 + 0.8593\text{NTU} \quad \text{Equation 2.11}$$

Where C_{Eff} = effluent kaolin concentration (mg/l),
 NTU = measured turbidity (NTU).

For calculations of mass balance and removal efficiency, Equation 2.10 was used to transform influent turbidities into concentrations whilst Equation 2.11 was used to transform effluent turbidities. In all previous studies identified (in which kaolin was used as a particulate for removal), a single relationship between turbidity and concentration was utilised for calculating both influent and effluent concentrations. The significance of this upon removal efficiencies and mass of kaolin retained by the filter is discussed in Section 2.9.2.

2.8.2 Filter Sediment Loading

The average sediment loading per column in the experiments was 9.5g per removal efficiency phase and 105.3g per clogging phase. Average cumulative sediment loadings over the entire seven phases of the filter run are presented in Table 2.3. Loadings have been non-dimensionalised by filter cross-sectional area so as to allow comparison with roughing filter and SuDS filter sediment loadings, hence a loading of 9.5g over a single column of diameter 100mm is equivalent to a loading of 1,212g/m².

Table 2.3. Sediment loading on filter runs S, FG, LG and RG.

Phase	1	2	3	4	5	6	7
Loading (g/m ²)	0	1,212	14,625	15,836	29,249	30,461	30,461

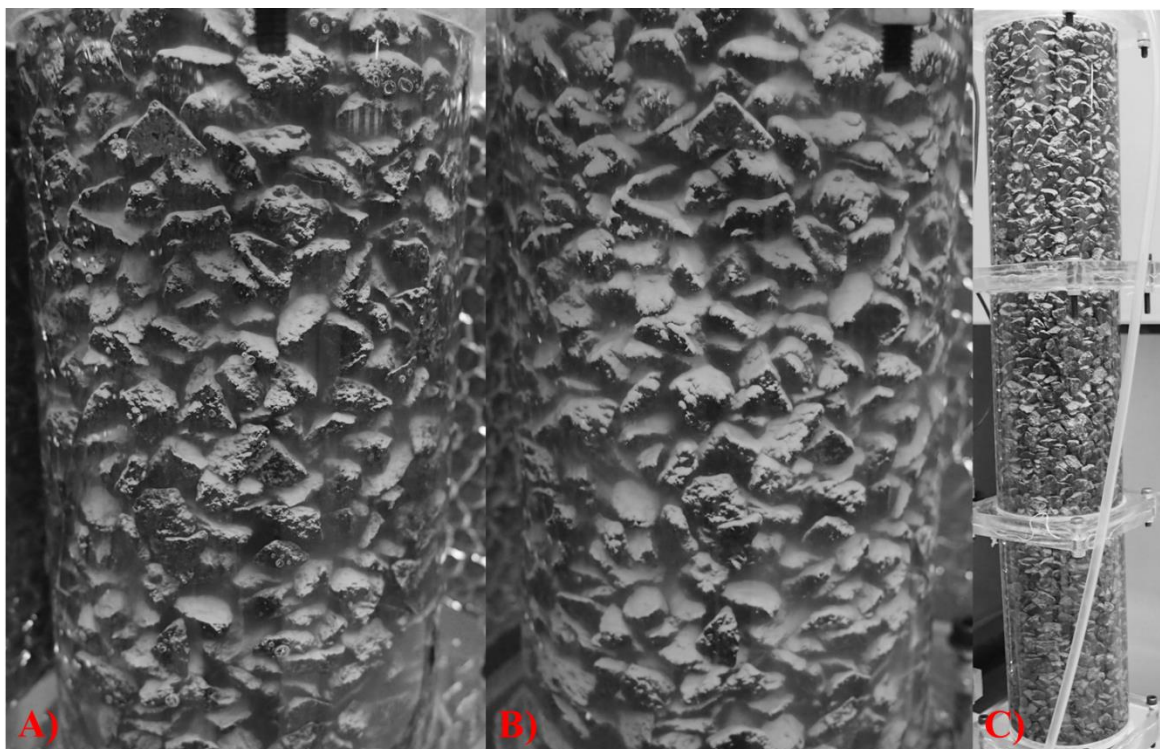


Figure 2.12. White kaolin accumulating on grey angular gravel during Run LF. Flow direction from top to bottom. A) inlet after first clogging phase, B) inlet after second clogging phase, and C) entire column after second clogging phase showing increased removal closer to the inlet.

As can be seen in Figure 2.12, greater removal occurred at the inlet of each filter. Figure 2.13 shows deposition within inlet of Run RG after the column has been drained and the inlet cap removed. Although draining the column has disturbed the sediment, it is apparent that a considerable proportion of the filter had been blocked leaving only a few flow channels open.

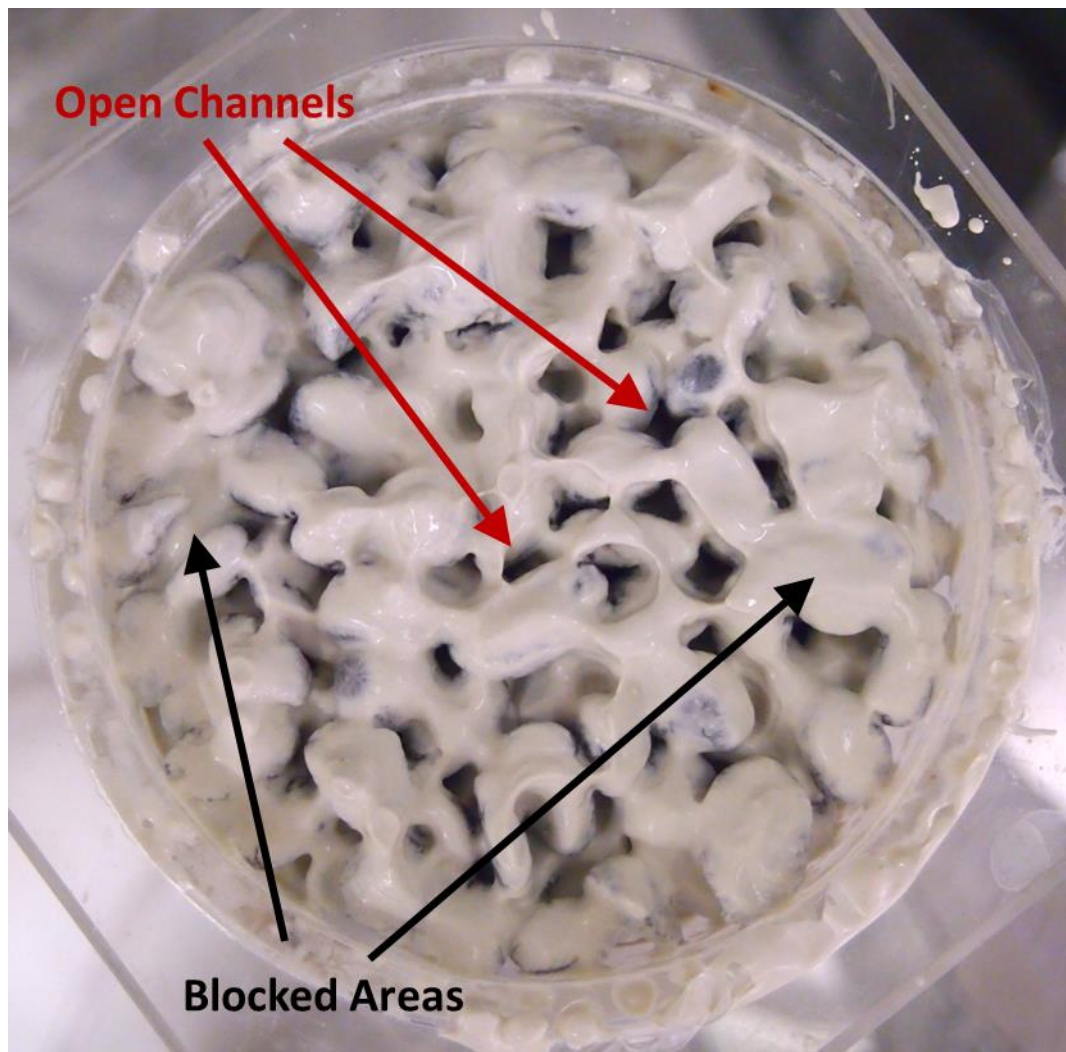


Figure 2.13. Filter RG drained and with inlet cap removed during Phase 7 (measurement of retained kaolin mass). A considerable amount of kaolin has been retained at the inlet with some areas of the filter completely blocked whilst, in other areas, narrow flow channels into the filter remain open.

Indicative sediment loads on roughing filters were calculated using Equation 2.7 with a range of probable total suspended solids and filtration rates. The time unit used was 24 hours hence sediment loads are per day. The filtration load factor was 1, hence the filters are assumed to operate 24 hours per day. The seven phases of kaolin removal and clogging simulated in the experiment would therefore be equivalent to 42.3 days of roughing filter operation at a flow rate of 0.3m/h and an average TSS of 100mg/l (100g/m³). Table 2.4 shows a range of equivalent operating durations for a roughing filter with different combinations of influent TSS and filtration rate.

Table 2.4. Roughing filter sediment load and equivalent duration simulated by runs S, FG, LG and RG.

TSS (g/m ³)	V _f (m/hr)	T (-)	LF (-)	Sediment Load (g/m ²)	Average Duration of Filter Operation Simulated (days)						
					1	2	3	4	5	6	7
10	0.3	24	1	72	0.0	16.8	203.1	219.9	406.2	423.1	423.1
10	0.7	24	1	168	0.0	7.2	87.1	94.3	174.1	181.3	181.3
10	1	24	1	240	0.0	5.0	60.9	66.0	121.9	126.9	126.9
10	1.5	24	1	360	0.0	3.4	40.6	44.0	81.2	84.6	84.6
100	0.3	24	1	720	0.0	1.7	20.3	22.0	40.6	42.3	42.3
100	0.7	24	1	1680	0.0	0.7	8.7	9.4	17.4	18.1	18.1
100	1	24	1	2400	0.0	0.5	6.1	6.6	12.2	12.7	12.7
100	1.5	24	1	3600	0.0	0.3	4.1	4.4	8.1	8.5	8.5
500	0.3	24	1	3600	0.0	0.3	4.1	4.4	8.1	8.5	8.5
500	0.7	24	1	8400	0.0	0.1	1.7	1.9	3.5	3.6	3.6
500	1	24	1	12000	0.0	0.1	1.2	1.3	2.4	2.5	2.5
500	1.5	24	1	18000	0.0	0.1	0.8	0.9	1.6	1.7	1.7

Indicative sediment loads on roadside SuDS filters were calculated using Equation 2.8 with a range of probable total suspended solids, road widths, filter widths and gully spacing of 1m (no gullies), 24m (dual carriageway, 0.5° slope) and 79m (dual carriageway, 6° slope). Only a single annual rainfall depth of runoff producing storms (total depth >1mm) derived from Glasgow rain gauge data was used because, as noted by Duncan (1999), TSS is linked to the availability of sediment on the road surface rather than the annual rainfall depth. Results are tabulated in Table 2.5 and show the huge variation in sediment loading on roadside SuDS filters depending on their design. The sediment loading in the experiment filter runs was equivalent to 10.3 years of operation of a 0.5m wide filter adjacent to a dual carriageway road in which the average TSS was 210g/l (210g/m³) and with over-the-edge drainage.

Table 2.5. Roadside SuDS filter sediment load and equivalent duration simulated by runs S, FG, LG and RG.

TSS (g/m ³)	D _{>1mm} (m/yr)	W _R (m)	Gully spacing (m)	A _F (m ² /m)	Sediment Load (g/m ² /yr)	Average Duration of Filter Operation Simulated (years)						
						1	2	3	4	5	6	7
60	0.965	3.65	1	1	211	0	5.7	69.2	74.9	138	144	144
720	0.965	10.6	1	0.2	36824	0	0.0	0.4	0.4	0.8	0.8	0.8
210	0.965	7.3	1	0.5	2959	0	0.4	4.9	5.4	9.9	10.3	10.3
210	0.965	7.3	24	0.5	71009	0	0.0	0.2	0.2	0.4	0.4	0.4
210	0.965	7.3	79	0.5	233737	0	0.0	0.1	0.1	0.1	0.1	0.1

The sediment load calculations show that a significant amount of clogging has taken place within the filter. This should be borne in mind when assessing the change in removal efficiency and tracer properties with clogging.

2.8.3 Kaolin Removal Efficiency

Kaolin removal efficiency was established at three points during the filter clogging process: the first flow of kaolin through a clean filter bed, after the first clogging phase and after the second clogging phase. Removal efficiency was measured at a further four stages during the low flow filter experiment to establish if and when an increase in removal efficiency due to “filter ripening” occurred. Samples from the kaolin suspension feed tank and the column effluent were collected at regular intervals, the turbidity measured and converted into kaolin concentrations, as shown in Figure 2.14.

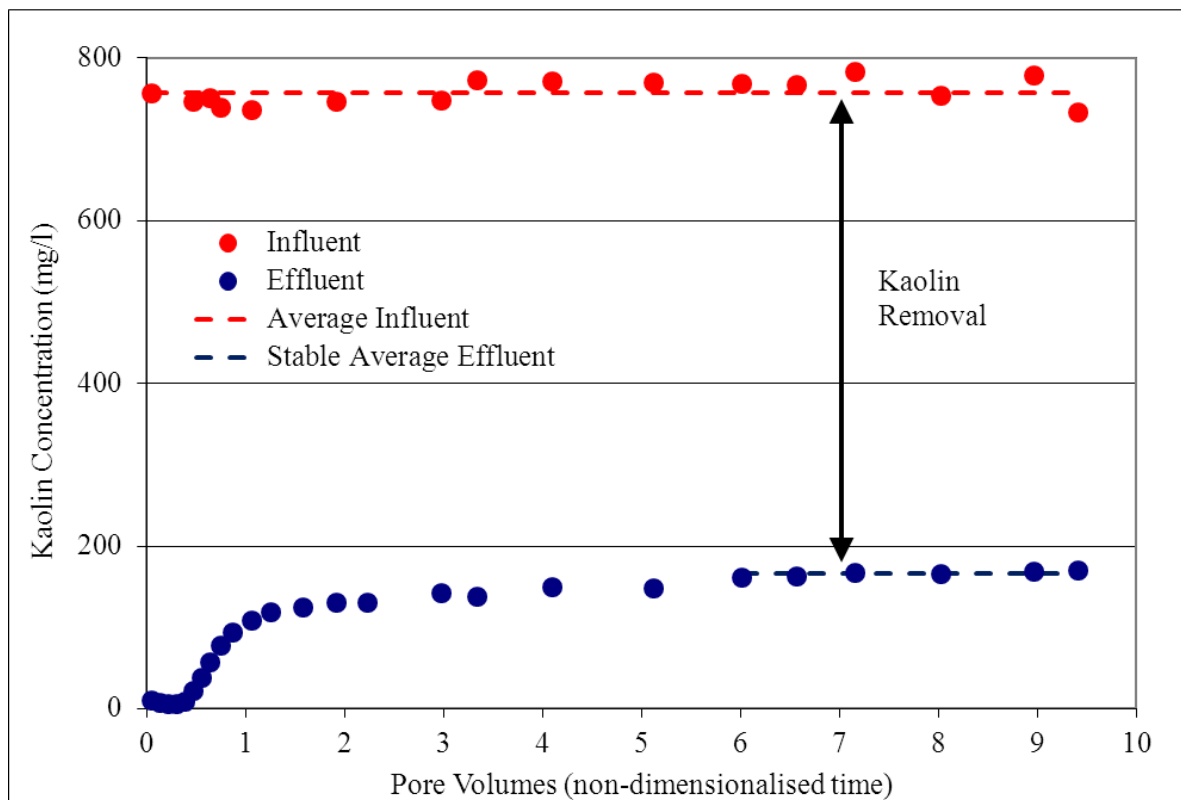


Figure 2.14. Representative influent and effluent kaolin profiles (from Run S, Column A, Phase 6). Average influent concentration and stable average effluent concentration used to establish removal efficiency.

Once a steady effluent concentration was reached, the average effluent concentration was divided by the average influent to obtain the removal efficiency. Kaolin breakthrough occurs before one pore volume, indicating short-circuiting and a deviation from perfect plug flow, and peaks after one pore volume indicating removal of kaolin within the filter (Figure 2.14). Kaolin effluent concentration rises by 33mg/l (19%) between four and 10 pore volumes in Figure 2.14 and similar trends were visible in all kaolin breakthrough profiles. This rise in effluent kaolin concentration was attributed to the reduction in mean particle size in the kaolin stock tank over time (Section 2.4.3): smaller particles require a longer time to settle hence removal efficiency is reduced and kaolin effluent concentration rises.

Table 2.6. Removal efficiency, porosity and average velocity of filter runs S, FG, LG and RG. The increase in average velocity with clogging is due to the decrease in porosity. Porosity calculated based on mass balance of kaolin passing through filter and estimated kaolin bulk density of 1455g/l.

		Removal Efficiency (%)			Mass of Kaolin Retained (g)			Porosity (%)			Average Velocity (m/hr)		
		Phase			Phase			Phase			Phase		
		2	4	6	2	4	6	2	4	6	2	4	6
S	A	82.8	79.4	78.1	8.7	98.0	193.3	49.2	45.4	41.3	0.72	0.79	0.88
	B	82.6	79.6	78.3	8.5	102.0	207.0	51.0	47.0	42.5	0.68	0.76	0.85
FG	A	76.5	79.0	80.8	8.5	111.9	217.3	49.9	45.4	40.9	0.70	0.77	0.86
	B	76.7	79.6	81.6	8.1	106.9	212.4	50.5	46.3	41.8	0.68	0.73	0.82
LG	A	79.7	78.2	78.2	5.5	77.2	143.5	39.1	35.2	31.7	0.72	0.74	0.76
	B	80.3	77.2	78.1	4.9	71.0	130.7	38.7	34.4	30.6	0.73	0.78	0.79
RG	A	76.0	78.1	76.2	7.5	97.0	179.9	39.1	35.2	31.7	0.86	0.92	1.08
	B	75.5	77.6	76.9	8.1	107.1	195.5	38.7	34.4	30.6	0.91	0.98	1.16

Table 2.7. Removal efficiency, porosity and average velocity of filter run LF. The increase in average velocity with clogging is due to the decrease in porosity. Porosity calculated based on mass balance of kaolin passing through filter and estimated kaolin bulk density of 1455g/l.

Run LF	Removal Efficiency (%)		Mass of Kaolin Retained (g)		Porosity (%)		Average Velocity (m/hr)	
Phase	A	B	A	B	A	B	A	B
1	-	-	-	-	50.2	50.3	0.23	0.22
2	84.0	82.8	10.1	9.2	49.9	50.0	0.24	0.23
3	85.0	83.4	18.3	16.6	49.7	49.8	0.24	0.22
4	84.8	83.9	26.4	24.1	49.5	49.6	0.24	0.22
5	83.5	82.0	35.0	31.9	49.2	49.4	0.24	0.23
6	84.3	83.6	43.6	39.8	49.0	49.1	0.24	0.23
7	-	-	87.2	83.0	47.7	47.9	0.24	0.24
8	88.0	89.0	96.1	91.3	47.5	47.7	0.24	0.23
9	-	-	138.4	130.5	46.3	46.5	0.25	0.24
10	90.4	90.5	148.3	139.2	46.0	46.3	0.26	0.24

Table 2.6 and Table 2.7 show removal efficiencies of a clean gravel bed (Phase 2) vary between 75.5% and 84.0% with an average of 79.7% for all runs. Removal efficiency is

highest in Run LF which was attributed to flow velocities that were half that of the other runs and a column that was 1/3 longer. There is no clear “best” or “worst” filter configuration based on removal efficiency. However, on average, the rounded gravel had the lowest removal efficiency across all measurement phases (RG: 76.7%, S: 80.1%, FG: 79.0%, LG: 78.6%). The rounded gravel had the lowest initial pore volume due to tighter packing of the individual gravel particles. This tighter packing may result in a higher total surface area of rounded gravel than angular gravel, however also results in pore velocities initially 25% higher than for angular gravel. Furthermore, the total gravel surface area may be increased but the surface area perpendicular to the flow direction on which deposition may take place is decreased (as shown in Figure 2.15) and, as this surface is rounded, deposition stability is reduced leading to a lower volume of kaolin that may be stored on each grain of gravel.

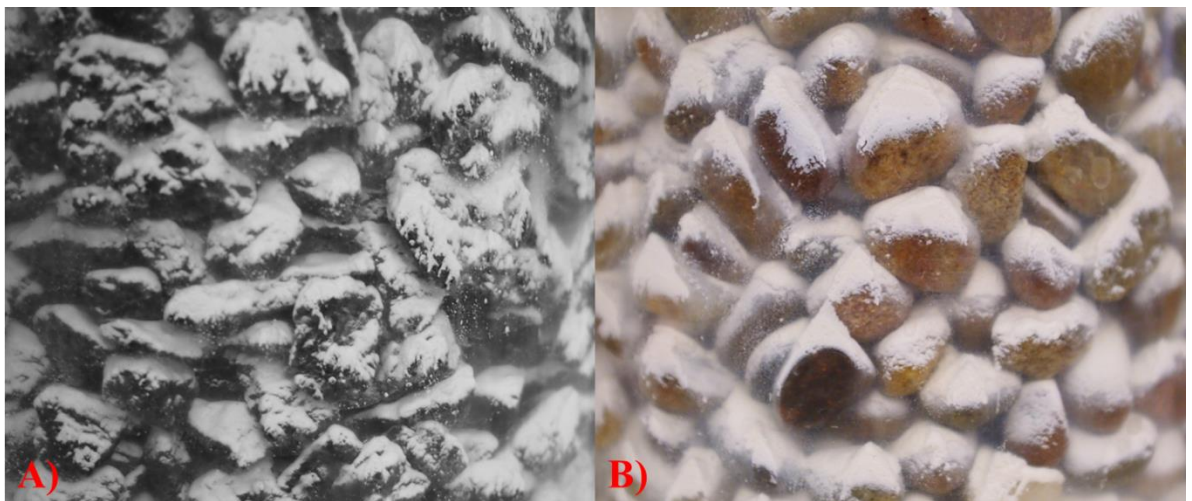


Figure 2.15. A) angular gravel with kaolin deposits after second clogging phase, and B) rounded gravel with kaolin deposits after second clogging phase. The angular gravel presents a larger, flatter surface area perpendicular to the flow on which kaolin may deposit as well as maintaining a greater porosity, and hence lower average pore velocities, than does the rounded gravel.

In runs S, FG, LG and RG there is no clear evidence for filter ripening (an increase in removal efficiency) or filter failure between the clean, intermediate (Phase 4) and clogged (Phase 6) stages: the maximum changes were a decrease in removal efficiency of 4.5%

(average of columns A & B) for Run S and in increase of 4.6% (average of columns A & B) for Run FG.

In Run LF there is an increase in average removal efficiency from 84.0% to 88.5% after the first clogging stage and to 90.4% after the second stage of clogging with corresponding porosities of 49.1%, 47.6% and 46.1%. In Run LF, these clogging phases were preceded by five removal efficiency measurement phases over which the average porosity decreased from 50.3% to 49.1% and in which there was no discernible change in removal efficiency.

Filter ripening therefore appears to occur only once there has been a substantial amount of deposited kaolin and only in the low flow run. A potential explanation for this is that in runs S, FG, LG and RG, kaolin deposition is coupled with a reduction in pore volume and an increase in pore velocity (due to the constant inflow rate) of, on average, 20.04%. This would act to reduce the removal efficiency at the same time as the increased surface area due to deposited kaolin would increase the surface area with the net effect of no discernible filter ripening. In the low flow velocity experiment, the increase in velocity was only 10.2%.

2.8.4 Tracer Characteristics & Repeatability

Effluent conductivity measurements taken at 10 second intervals were used to determine the breakthrough and residence time distribution (RTD) of a 10ml pulse of NaCl tracer. Curve-fitting software CXTFIT/Excel was used to fit a convection-dispersion model to the data and estimate model parameters. Figure 2.16 shows the RTDs for Run S, column B for the clean filter (T1B) and clogged filters (T2B & T3B) as it was representative of all tracer RTDs in this study.

The decrease in peak height and increasing skewedness of the RTDs with kaolin deposition is indicative of an increase in dispersion within the filter. This is borne out by the CXTFIT/Excel model parameters shown in Table 2.8 in which dispersivity increases from 1.126cm to 3.873cm for column B (shown in Figure 2.16) with a similar increase for column A.

Figure 2.16 also shows a decrease in time to tracer breakthrough and peak with kaolin deposition and a decrease in the slope of the rising limb of the RTDs. The decrease in time to peak indicates that the average pore velocity has increased, as was estimated based on the fixed inflow rate but decreasing filter volume due to kaolin deposition. The decreasing slope of the tracer rising limb indicates that flow path heterogeneity is increasing within the filter: some paths are becoming disproportionately faster than others leading to earlier breakthrough of the tracer carried in these paths. It is hypothesised that this indicates a shift from uniform transport through the filter to transport dominated by preferential flow paths.

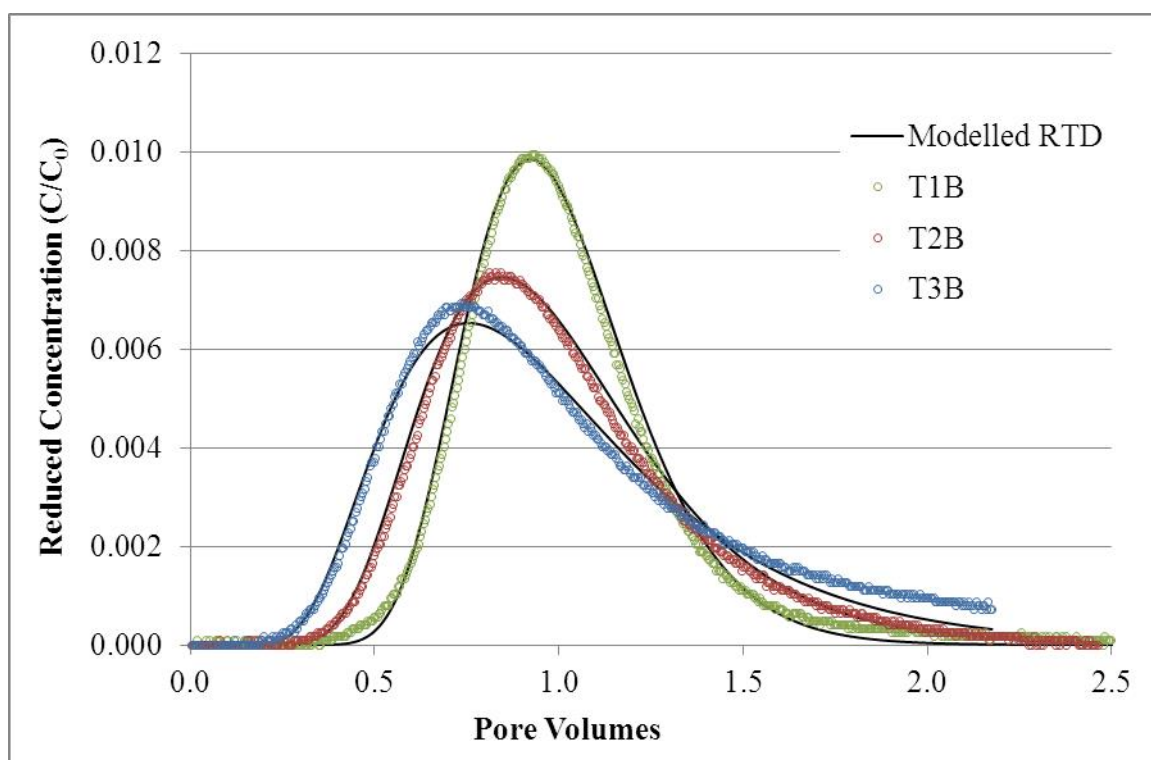


Figure 2.16. Residence time distributions for Run S, column B with CXTFIT/Excel fitted convection-dispersion models.

Table 2.8. CXTFIT/Excel parameters and estimated average pore velocity of tracers for Run S.

Run S	Pore Volume (ml)		Dispersivity (cm)		Estimated Average Pore Velocity (m/hr)	
	A	B	A	B	A	B
T1	1758	1825	1.287	1.126	0.72	0.71
T2	1770	1799	1.960	2.309	0.78	0.77
T3	1694	1728	3.869	3.873	0.86	0.88

To be a useful tool for characterising changes in filter hydrodynamics with clogging, tracer RTDs must be consistent and reproducible. Potential sources of error and steps taken to remove or mitigate them are listed below.

2.8.4.1 Tracer Volume

Tracer pulse duration is an important factor for CXTFIT/Excel and dependent upon the volume of tracer injected as well as the injection flow rate. Tracer volume was controlled using a 10ml graduated pipette filled with 10ml of tracer. The level was judged by eye and typically with an accuracy of ± 0.1 ml. With the injector setup described in Section 2.7.1, the entire volume of tracer was injected into the column.

2.8.4.2 Flow Rate

As a result of the use of a peristaltic pump to deliver the flow, slight variations in flow rate over the duration of tracer breakthrough are possible. Due to the injector setup (Section 2.7.1), the 10ml tracer is injected at exactly the same flow rate as the preceding and subsequent flows. The entire volume of effluent from the beginning of tracer injection to the end of the RTD was collected (between 3 and 5 litres) then weighed to determine the volume (with an allowance for temperature effects on density) and, with the known duration of the RTD, the average flow rate. This average flow rate was used for the CXTFIT/Excel model.

2.8.4.3 Density

If the tracer density were significantly different from the pore fluid then tracer transport would not be representative of the pore fluid flow. There are two sources of differing density: the concentration of NaCl in the tracer and the relative temperature difference between the tracer and the pore fluid.

Any solution containing NaCl will be denser than the kaolin/tap water suspension. To minimise the effect of density driven flow, the tracer stock was prepared at as low a concentration as could reliably be measured at the column outlet after mixing with the column pore volume had taken place. This was 1000mg/l resulting in a specific gravity of

1.00053 and a stock concentration of $\sim 1200\mu\text{S}/\text{cm}$. The tap water/kaolin (background) conductivity showed little variation within each experiment ($\pm 0.1\mu\text{S}/\text{cm}$) and the peak effluent concentration was between $\sim 15.0\mu\text{S}/\text{cm}$ greater than the background for the first tracer of each run (with minimum dispersion and mixing) and $\sim 7.0\mu\text{S}/\text{cm}$ for the last tracer of each run (with greater dispersion and mixing). With a probe measurement accuracy of $0.1\mu\text{S}/\text{cm}$, this tracer concentration gave at least 70 distinguishable data points with which the increase in conductivity from the background to peak could be defined. This was sufficient to define the shape of the RTD at a high resolution.

The effect of density difference due to temperature was minimised by keeping the tracer stock in a sealed container submerged within the temperature controlled kaolin suspension tank prior to injection into the column. By minimising the time between filling the injection pipette with tracer and injecting the tracer, the tracer was at the same temperature as the column pore fluid.

2.8.4.4 Conductivity Probe

Conductivity is temperature dependent. To prevent small variations in temperature from affecting the conductivity reading, the Hach HQ40D meter includes a range of temperature corrections methods. The NaCl specific non-linear method with reference temperature of 20°C was found to perform best over the temperature range observed in the experiments ($\sim 18\text{-}21^\circ\text{C}$ depending upon ambient room temperature). This was tested by heating a sample of column effluent containing tracer from 18 to 21°C over approximately 30 minutes and recording both temperature and conductivity change (Figure 2.17). As there is little change in average conductivity, the temperature correction method is adequate. Note that the variation in conductivity shown in Figure 2.17 is larger than was observed in the experiments where the temperature was either constant or varied by a maximum of 0.3°C over the tracer measurement period and at a much slower rate. Background concentration rates were constant to within $\pm 0.1\mu\text{S}/\text{cm}$.

A second potential source of error associated with the conductivity probe was the residence time of the measurement flow cell. Mixing within the flow cell would have an averaging effect on the conductivity reading that would smooth the RTD and reduce peaks. The

volume of the flow cell was approximately 2ml, hence at the tracer flow rate of 50ml/min, the residence time is 1.67 seconds. As readings are taken every 10 seconds, mixing within the flow cell is unlikely to have affected the RTDs.

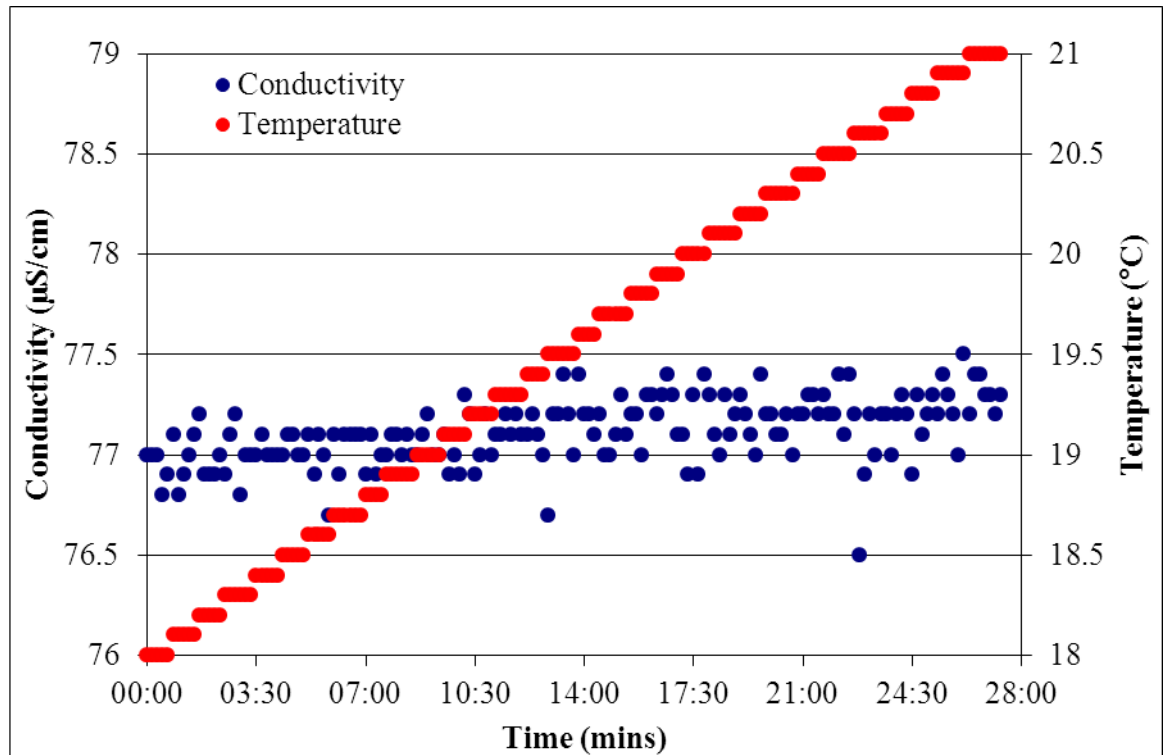


Figure 2.17. Relationship between tracer conductivity and temperature for NaCl non-linear temperature correction with reference temperature of 20°C. The tracer sample of constant NaCl concentration was heated from 18 to 21°C whilst conductivity was monitored.

2.8.4.5 Kaolin Concentration

The presence of kaolin was found to have no influence on conductivity readings hence the concentration of kaolin did not affect the RTDs. High concentrations of NaCl were found to reduce the zeta potential of a kaolin suspension thus reducing stability and encouraging kaolin particles to flocculate. This in turn would lead to greater settlement and removal of kaolin within the filter. However, at the low tracer concentration of 1000mg/l, NaCl had no effect on zeta potential which remained in the range -21.1 to -28.7mV (average -24.7mV) and indicates incipient suspension stability verging on moderate stability (American Society for Testing and Materials, 1985).

2.8.4.6 Tracer Repeatability

Taking into account the potential sources of error outlined in Sections 2.8.4.1 to 2.8.4.5, tracers were found to be highly repeatable, as can be seen from the tracer RTD shape in Figure 2.18 and the low standard deviation for each tracer RTD descriptive parameter in Table 2.9. The four tracers were performed on a single gravel column on four consecutive days prior to kaolin deposition. The slight differences between each tracer RTD are thought to be due to different flow rates from the peristaltic pump, tracer volumes and temperature.

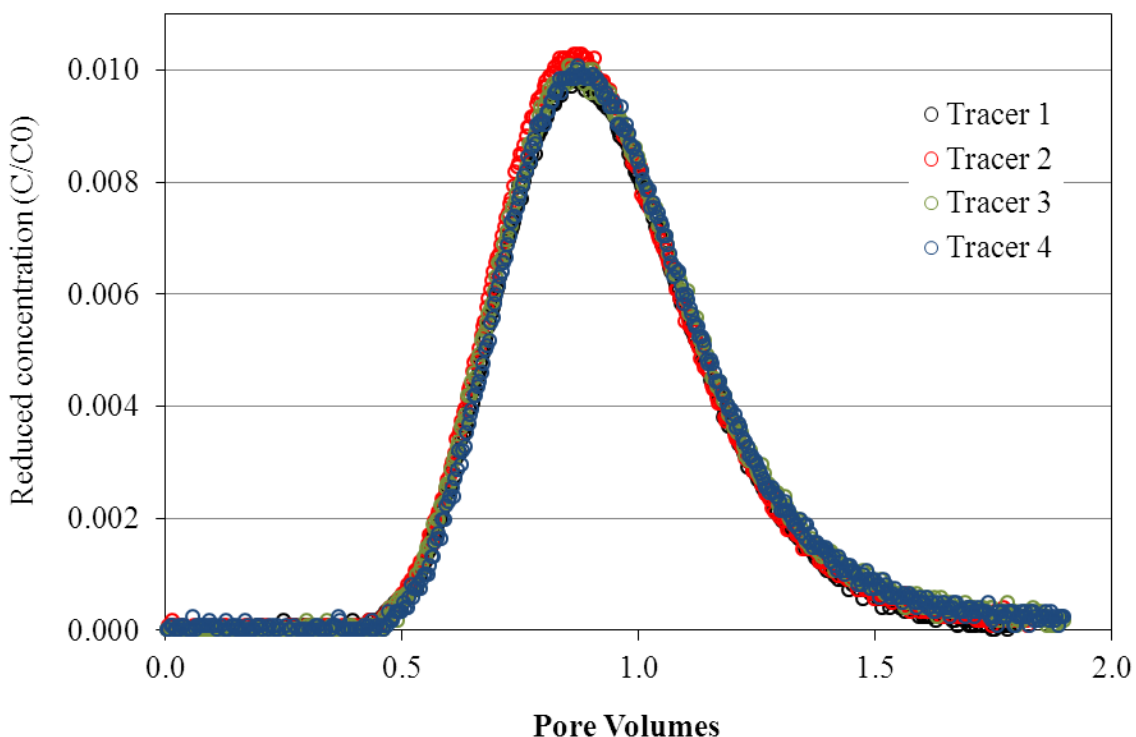


Figure 2.18. Tracer RTDs to evaluate repeatability of tracer procedure. All four RTDs overlap indicating consistent tracer transport through the clean filter and a consistent tracer delivery and breakthrough measurement procedure.

Table 2.9. Tracer RTD descriptive parameters and standard deviation.

Tracer	Filtration Rate (m/hr)	% Recovery	Residence Time (-)	Variance (-)	Minimum Travel Time (PV)	Time to Peak (PV)	Dispersivity (cm)
Tracer 1	0.3223	96.3%	0.95	0.0507	0.432	0.87	1.039
Tracer 2	0.3299	96.2%	0.95	0.0603	0.431	0.87	1.028
Tracer 3	0.3434	98.2%	0.96	0.0604	0.464	0.86	1.047
Tracer 4	0.3437	97.6%	0.96	0.0598	0.472	0.87	0.981
St. Dev.	0.0105	1.8%	0.01	0.0047	0.021	0.01	0.029

2.8.5 Clean Bed Pore Volume Estimation from Tracer RTD

The pore volume of the filter is a critical parameter when evaluating the lifetime removal efficiency of a gravel filter as it determines the capacity for sediment storage. The initial pore volume of each filter was measured as described in Section 2.7.1; however pore volume then decreases as sediment is deposited within the filter.

Initial pore volumes were also derived from fitting an equilibrium convection-dispersion model to each residence time distribution by using pore volume, in conjunction with dispersivity, as a parameter for fitting. The use of the equilibrium model assumes that the tracer does not adsorb onto the gravel media and that the entire pore volume is “mobile” i.e. there are no stagnant areas or disconnected pore regions. The first assumption can be verified as at least 95% of the tracer was recovered at the outlet. The second assumption cannot be verified. As the gravel is of a relatively uniform size (8-11mm, 4-8mm) and does not pack tightly, it is unlikely that there will be a significant volume of disconnected pore regions within the gravel body, however there may be small regions of stagnant, immobile pore regions, particularly close to the inlet and outlet.

Comparing the initial measured pore volume with that estimated from curve fitting determines how accurate the use of the convection-dispersion model with pore volume as a fitting parameter can be. As can be seen from Table 2.10, the tracer derived pore volume (hereafter referred to as tracer PV) are, on average, 4.96% lower than the measured value and are all within $\pm 10\%$.

Table 2.10. Comparison between measured pore volume and tracer PV estimated from fitting an equilibrium convection-dispersion model to tracer RTDs for the five experiments (S, FG, LG, RG & LF) and two columns (A & B). N.B. pore volumes include inlet and outlet mixing sections (approximately 350ml each) and tubing (approximately 40ml).

Run	Measured Pore Volume (ml)		Tracer PV (ml)		Difference (%)	
	A	B	A	B	A	B
S	1967.0	1933.4	1863.2	1825.1	-5.28	-5.61
FG	1894.0	1880.1	1915.0	1814.2	1.11	-3.50
LG	1928.5	1961.9	1778.9	1783.2	-5.05	-4.30
RG	1636.0	1560.9	1485.4	1458.0	-9.21	-6.59
LF	2692.3	2664.8	2882.1	2660.0	7.05	-0.18

2.8.6 Clogged Bed Pore Volume Estimation from Tracer RTD

At the end of each filter run, the mass of kaolin retained within each filter was measured as described in Section 2.7.4. Results are presented in Table 2.11.

Table 2.11. Comparison between tracer PV and mass balance PV. A settled kaolin bulk density of 1455g/l yielded the lowest total difference in pore volumes. Run RG was excluded from the analysis.

Run	Mass of Kaolin Retained (g)		Tracer PV (ml)		Mass Balance PV (ml)		Difference in Pore Volumes (%)	
	A	B	A	B	A	B	O	O
S	132.2	151.5	1694.1	1728.5	1788.3	1728.5	-5.27	0.00
FG	151.1	158.3	1689.4	1761.3	1689.7	1666.0	-0.02	5.72
LG	106.4	100.2	1801.1	1780.6	1784.6	1826.4	0.92	-2.51
RG	170.7	169.0	1097.4	1102.8	1405.2	1332.4	-21.90	-17.23
LF	62.8	49.5	2614.7	2682.1	2607.4	2597.8	0.28	3.68

The bulk density of kaolin deposited within the filter was not known, but could be determined based upon the volume that kaolin occupied, which in turn could be determined by the change in the pore volume within the filter. Similar to the estimation of initial pore volume, the final clogged pore volume can be estimated from equilibrium convection-dispersion model parameters fitted to the clogged RTD. Again it is assumed that the tracer

is conservative (a valid assumption as once again at least 95% of the tracer was recovered) and that there are no disconnected pore regions. This second assumption may no longer be valid as it was possible that kaolin deposition led to the formation of significant disconnected pore regions or stagnant regions of no flow.

The bulk density of settled kaolin was estimated by iteratively solving Equation 2.12 for each filter with an assumed bulk density until the sum of the residuals for all filter runs were minimised.

$$PV_F = PV_I - \frac{M_{KF}}{\rho_{KS}} \quad \text{Equation 2.12}$$

Where PV_F = final pore volume of clogged filter estimated from tracer RTD,

PV_I = initial pore volume of filter measured when filling column with water,

M_{KF} = final mass of kaolin retained in filter measured when column dismantled,

ρ_{KS} = assumed bulk density of kaolin settled within the filter.

Results are presented in Table 2.11. Run RG columns A and B were excluded from the analysis as the mass balance PV was substantially larger than the tracer PV. This is thought to be because the rounded surface of the gravel led to less stable kaolin deposits and increased cascading of settled kaolin within the filter. Cascading kaolin would then be capable of entirely blocking pore channels leading to the formation of disconnected pore regions.

Table 2.12. Bulk density of settled kaolin derived from central, upper and lower tracer RTD estimates of column pore volume.

		Bulk Density (g/l)
Tracer Pore Volume Estimate	Upper	1529
	Central	1455
	Lower	1434

Upper and lower 95% confidence intervals were calculated for pore volume in CXTFIT/Excel. Combining all lower estimates of pore volume and solving Equation 2.12 gives a lower estimate of the kaolin bulk density. Similarly, combining all upper estimates of pore volume and solving Equation 2.12 gives an upper estimate of the kaolin bulk density. Central, upper and lower estimates of settled kaolin bulk density are given in

Table 2.12. These fall within the expected range of 1178-2600g/l (Section 2.4.3), however are likely to be slightly lower than the true settled kaolin bulk density (hence overestimating the kaolin volume) as there was no way to distinguish immobile pore water from the volume of water displaced by settled kaolin.

2.8.7 Intermediate Clogged Bed Pore Volume Estimation from Tracer RTD

The mass of kaolin retained within the filters at the end of each phase was estimated from the removal efficiency mass balance in Section 2.8.3. The density of the settled kaolin was estimated within 95% confidence limits based on the mass of kaolin retained and the reduction in mobile pore volume in Section 2.8.6. It is therefore possible to calculate the pore volume within the filter after each phase based on the amount of kaolin retained. Table 2.13 shows a comparison between the intermediate tracer PVs (at the end of Phase 3, T2) and the removal efficiency mass balances. Unlike for the clogged filters (Phase 6, T3), the mass of kaolin retained within the filter was not known, hence the intermediate clogged RTDs could not be used to refine the estimate of settled kaolin bulk density. The central, upper and lower estimates of settled kaolin bulk density were used to reflect the uncertainty in this measurement.

Tracer PV was, on average, 3.30% lower than the central pore volume estimate, 3.65% lower than the upper estimate, 2.93% lower than the lower estimate and all pore volumes fell within a range of -5.6% to +6.10%. Accuracy of the tracer PV at intermediate stages of clogging is therefore similar to that of the initial and final stages of clogging.

Table 2.13. Tracer PVs compared with removal efficiency PVs (with upper, central and lower estimates of settled kaolin bulk density).

Run	Tracer PV (ml)		Removal Efficiency PV (ml)					
			Upper		Central		Lower	
	A	B	A	B	A	B	A	B
S	1770	1799	1853	1815	1835	1796	1828	1789
FG	1786	1834	1764	1756	1743	1735	1735	1728
LG	1841	1774	1839	1879	1824	1866	1819	1861
RG	1456	1395	1523	1436	1505	1416	1498	1409
LF	2671	2616	2591	2568	2574	2553	2569	2547

For the rounded gravel Run RG, the clogged tracer PV (Phase 6, T3) was far below that determined from the mass of kaolin retained within the filter (Section 2.8.6). This was attributed to the formation of disconnected pore regions reducing the volume of the filter accessible to the tracer. As shown in Table 2.14, the intermediate tracer (T2) was much more similar to the mass balance PV than the clogged tracer (T3). This suggests that the formation of disconnected pore regions only occurs during the second clogging phase.

Table 2.14. Comparison between tracer PVs and mass balance PVs for rounded gravel filter Run RG.

Run RG	Tracer PV(ml)		Mass Balance PV (ml)		Difference in Pore Volume (%)	
	A	B	A	B	A	B
T2	1456	1395	1514	1426	-3.86%	-2.19%
T3	1097	1100	1403	1308	-21.79%	-15.89%

2.8.8 Particle Size Breakthrough

The change in particle size during kaolin breakthrough was measured from samples collected for turbidity analysis during the first addition of kaolin (Phase 2) of runs S, FG, LG and RG. Figure 2.19 shows the kaolin breakthrough profile for Run S, Column A (Kaolin C/C_0) with tracer T1A breakthrough (Tracer C/C_0), the average background effluent particle size (Background Size) and range in median background size for all filter runs, and the average influent kaolin suspension particle size (Influent Average Size) with range in influent median size for all filter runs. Finally, the effluent mean particle size is shown (Effluent Size).

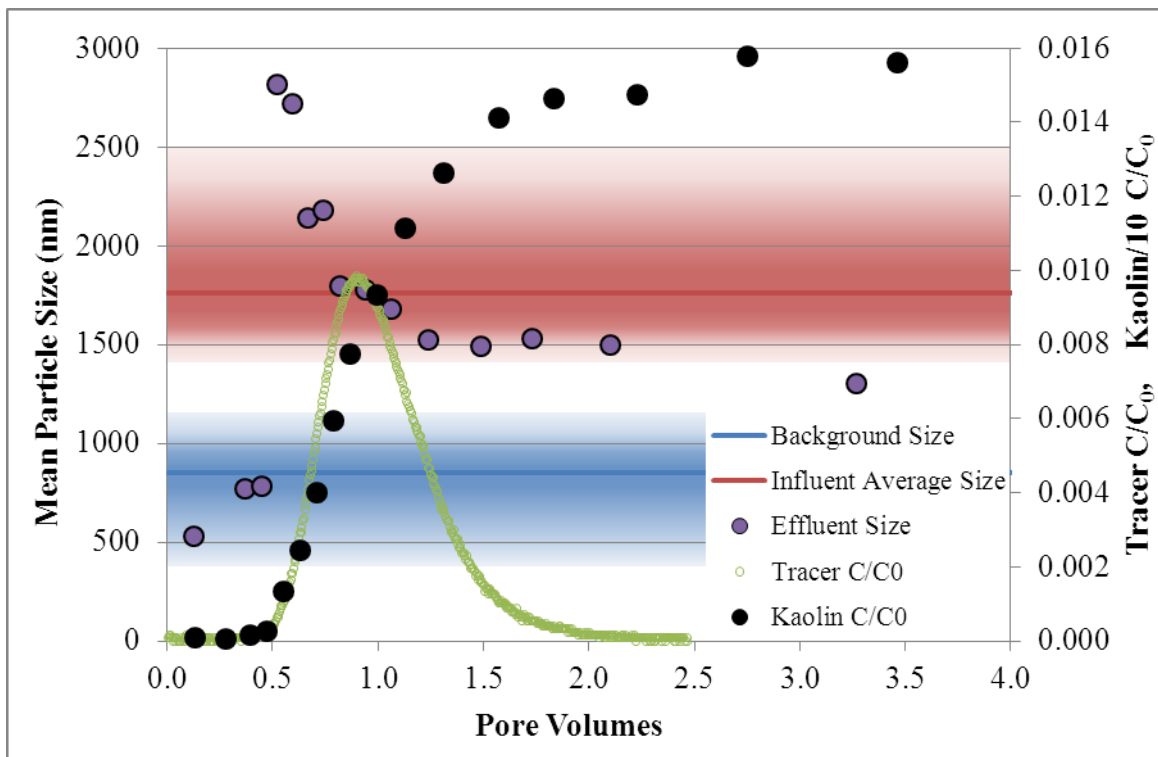


Figure 2.19. Run S, Column A evolution of effluent particle size during kaolin breakthrough. Tracer breakthrough RTD T1A shown for reference along with average background particle size (with blue shading indicating the range in median sizes observed) and average influent particle size (with red shading indicating the range in median sizes).

It is clear that immediately upon kaolin breakthrough (between 0.47 and 0.55 pore volumes), the median effluent particle size is higher than the median influent particle size (2815nm compared with 1762nm). By the time of the tracer peak, the median effluent particle size is equal to the median influent particle size and by full kaolin breakthrough (3.5 pore volumes and onwards) the median effluent particle size is lower than the median influent.

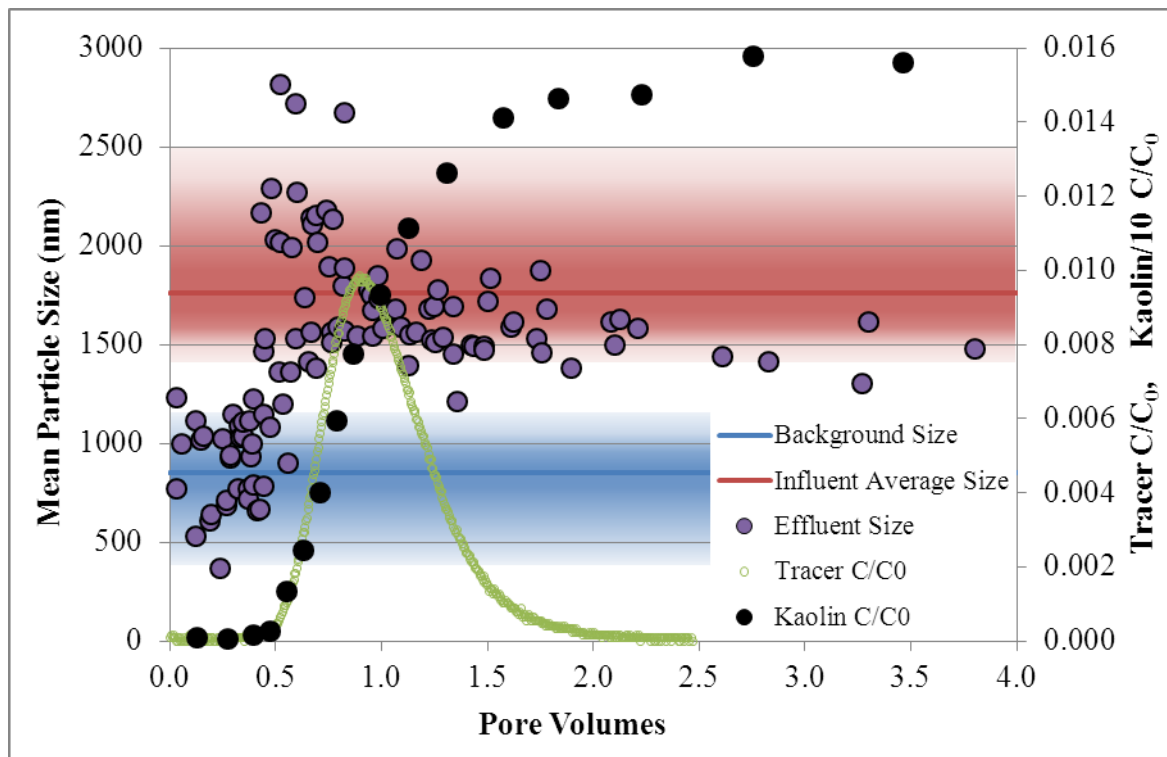


Figure 2.20. Run S, FG, LG & RG aggregated effluent median particle sizes. Run S, Column A kaolin breakthrough and tracer T1A breakthrough are shown for reference.

Similar, although less pronounced trends are visible when aggregating the results for runs S, FG, LG and RG, as shown in Figure 2.20. This result first appears somewhat counterintuitive. The two main particle removal mechanisms for gravel filters are gravitational settlement and straining (sieving), both of which should result in an increased removal efficiency of larger particles and hence an effluent median particle size lower than the influent, as is the case after approximately two to three pore volumes.

The initial peak in effluent median particle size can be explained by considering the transport properties of different particle classes through porous media. Carrigan et al. (1996) showed that of all the gas molecules released from an underground nuclear explosion, those with a higher atomic mass (larger molecules) and lower diffusivity were transported to the surface through faults and fractures more rapidly than those molecules with a lower atomic mass. Auset & Keller (2004) found that in artificial pore networks of varying pore size, larger colloids were confined to the centre streamlines of the pore

channels due to their size whilst smaller colloids occupy both the central and peripheral streamlines. Due to friction with the pore walls, the central streamlines tend to have a higher velocity than the peripheral streamlines.

Therefore, there are more opportunities for the smaller particles in a kaolin suspension to be transported in low velocity streamlines through the filter than large particles, leading to an enhanced transport and earlier breakthrough of large particles. Whilst many small particles will be transported in fast flow channels along with the large particles, this process affects the average particle size and skews the PSD towards larger particles in the initial breakthrough period.

The first effluent samples containing kaolin (around 0.5 pore volumes in Figure 2.20) are composed of a greater proportion of large particles transported in central streamlines. Despite the increased removal efficiency of large particles, overall this leads to a median effluent particle size that is larger than the influent median particle size and closer to the upper value of the influent particle size distribution.

At the point of full kaolin breakthrough (around three pore volumes), kaolin particles from the very first injection of kaolin that were transported through the filter in the lowest velocity streamlines, or which took a more tortuous path, exit the filter and both kaolin concentration and effluent particle size reach a steady state. Because of the increased removal of the larger particles, the median particle size at this point is lower than the influent median particle size.

2.9 Discussion

The aims of this chapter were to measure the efficiency of gravel filters at removing colloidal particles and determine how the removal efficiency varies with accumulation of deposited particles. Conservative tracers were used to determine change in filter hydraulics with clogging. Particle size measurement of the filter influent and effluent kaolin suspensions were made to determine how removal affects particle size distribution.

2.9.1 Kaolin as Surrogate for Road & River Particulate Pollution

Kaolin is commonly used as a surrogate for river particles and is appropriate for analysing the removal efficiency of roughing filters (Ahsan, 1995; Wegelin et al., 1987). Kaolin is somewhat less ideal for roadside SuDS filters where there is typically a large range in particle sizes entering the filter from colloidal particles up to several millimetres; kaolin is entirely within the colloidal particle range. Removal mechanisms for colloidal particles are predominantly settling under gravity and direct interception (Boller, 1993). Straining and wedging between gravel particles would also occur but are likely to be insignificant due to the high ratio of gravel size to kaolin size. Straining is likely to become significant once particle size exceeds $928\mu\text{m}$ for 4-8mm gravel and $1547\mu\text{m}$ for 8-11mm gravel based upon the particle diameter to media diameter of Barton & Buchberger (2007), both of which are at the upper end of the road runoff particle size distribution.

If particles larger than $928\mu\text{m}/1547\mu\text{m}$ were to enter the gravel filter, the system would be expected to switch from deep-bed filtration in which particles are able to penetrate deep into the filter media and utilise the entire volume for particle removal to straining dominated filtration. Particles removed by straining would alter flow paths through the filter as well as present additional surfaces for colloidal particles to attach. In straining-dominated filtration the top several layers of gravel quickly block with strained particles and the pressure head could become high enough to prevent road runoff entering the filter. The blocking of the upper surface is a common failure mechanism in roadside SuDS filters (Pittner & Allerton, 2010) without pre-treatment. However, it is recommended that all roadside SuDS filters constructed in the UK include pre-treatment (Pittner & Allerton, 2010) in the form of flow over a grass verge or through gully pots before entering the filter, both of which would be expected to remove the coarser particles.

The effect of larger road runoff particles on roadside SuDS filter clogging and pollutant removal efficiency was not investigated in this study for the following reasons:

1. The removal of colloidal particles was of more interest as these are both more difficult to remove and also contain other pollutants such as pollutant metals

adsorbed to their surface (Ellis & Revitt, 1982; Lau & Stenstrom, 2005; Stovin et al., 2010).

2. Particles that would cause significant straining are likely to be removed by pre-treatment hence deep-bed filtration would occur in SuDS and not surface straining.
3. For the practical reason that turbidity and size distribution measurement of a rapidly settling suspension was not possible with the available equipment.

2.9.2 Kaolin Turbidity/Concentration Relationship

In the field of water treatment it is common practice to use turbidity measurement in conjunction with a calibration curve as a surrogate for directly measuring total suspended sediment (TSS) concentration. This is because turbidity measurement is quicker, cheaper, can be carried out in the field and allows many more samples to be analysed than the alternative which is filtration through a glass fibre filter paper.

It is well known that, in addition to concentration, turbidity is dependent upon other particle suspension properties such as sediment colour, shape and size (Clifford et al., 1995). In this study and others (Lin et al., 2008; Rooklidge et al., 2002; Wegelin et al., 1987), a decrease in average particle size was measured between filter inlet and outlet which is entirely in line with filtration theory: larger particles are more likely to be removed by settlement and straining. Some studies measure both turbidity and TSS separately treating these parameters as unrelated and calculating the removal efficiency of each (Galvis, 1999; Ochieng et al., 2004; Rooklidge et al., 2002). Galvis, 1999 and Rooklidge et al. (2002) both found lower removal efficiency for turbidity than TSS whilst Ochieng et al. (2004) found both to be comparable. The approach taken by Wegelin et al. (1987) was to measure removal efficiency based on particle counts of each size class.

Without access to a particle counter and with a desire to adequately characterise the kaolin breakthrough curve (requiring more samples than could conveniently be analysed by membrane filtration), the approach taken in this thesis was to derive two relationships between turbidity and TSS: one for the influent kaolin suspension and one for the effluent kaolin suspension. Had a single relationship based on the influent kaolin suspension been

used in this study, the effluent concentration would have been over-estimated, resulting in a removal efficiency of 66.3% instead of 82.8% for Run S, column A for example.

Yet there are numerous studies in which removal efficiency is based upon the difference between influent and effluent turbidity (Ahn et al., 2007; Ingallinella et al., 1997; Losleben, 2008; Mahvi et al., 2004) or TSS derived from a single relationship between TSS and turbidity (Ahsan, 1995) and it is suspected that these studies and others like them underestimate removal efficiency.

Lin et al. (2008) state that they initially used turbidity to determine TSS, but found that increasing the influent concentration increased turbidity derived removal efficiency by 7%. A membrane filtration derived measure of concentration showed no change in removal efficiency over the same increase in influent concentration. They attributed the difference to the non-linear relationship between turbidity and TSS and based all further removal efficiencies upon membrane filtration derived concentrations.

Based upon the influent and effluent kaolin turbidity/TSS relationships of Equation 2.10 and Equation 2.11 (shown in Figure 2.11, Section 2.8.1), it is clear that the curves converge at low concentrations and diverge as concentration increases. Hence, as concentration increases, the error caused by using a single turbidity/TSS relationship that does not take into account the change in particle size distribution between influent and effluent increases, as observed by Lin et al. (2008).

Many studies may therefore have underestimated removal efficiency in filters and hence underestimated the mass of sediment retained, particularly at high suspended sediment concentrations. Often there will be situations in which removal efficiency based solely on turbidity is sufficient. For instance, if the purpose of monitoring removal is to determine if the roughing filter effluent is suitable for slow sand filtration, it is as useful for the operator to have empirical knowledge of how the sand filter behaves at a given turbidity as at a given TSS. In developing countries where roughing filters are most often used, the filtration equipment and operator skills necessary to measure TSS – vacuum pump, filter holder, drying oven, high precision (calibrated) balance and a large number of glass fibre filters – may not be available or would not be available for the long-term operation of the

treatment works. For this reason, there would be no benefit in developing a filter management strategy that relied on TSS measurement and turbidity is preferable.

However, if the purpose of the study is to compare the removal efficiency of different filter designs that may produce different effluent particle size distributions (e.g. media of different shape, size or roughness), or accurate knowledge of the mass and volume of sediment retained is required, removal efficiencies based on turbidity are not suitable.

The approach taken in this thesis in which an influent turbidity/TSS relationship and an effluent turbidity/TSS relationship were established is an improvement over a single turbidity/TSS relationship. It is also a compromise between accuracy of kaolin retained and high frequency of sampling necessary to define the kaolin breakthrough curve.

2.9.3 Tracers

A method for reliably delivering a known quantity of sodium chloride tracer and measuring the resulting tracer breakthrough profile in the effluent was devised. The method was found to be highly repeatable hence small changes in tracer residence time distribution (RTD) curves could be used to infer changes in filter hydraulics.

With curve-fitting software CXTFIT/Excel, pore volume was used as a fitting parameter in a convection-dispersion model of tracer transport. Pore volume derived from the tracer RTDs (referred to as tracer PV) were compared with known pore volumes measured during filling of the gravel filters. It was found that, with knowledge of the influent tracer volume, concentration, flow rate and effluent tracer breakthrough profile, it was possible to predict the clean bed pore volume within at least 10% of the measured value for all 10 filters. On average the tracer PVs were 4.96% lower than the measured value.

Transport of tracer through the filter, and hence the RTD curve, is only influenced by the mobile pore volume: the volume of the filter that is accessible to the tracer by either convection or dispersion. The tracer PV is therefore a measure of the mobile pore volume, hence why it is lower than the physical measure of pore volume which includes regions inaccessible to a tracer.

The bulk density of the kaolin deposits within the filters was determined from the mass of kaolin retained within each filters (measured when dismantling the filter at the end of the filter run) divided by the reduction in mobile pore volume after kaolin deposition determined from tracer PVs. There are several sources of error within this measure of bulk density: error from the measure of kaolin retained (by filtration, drying and weighing), error associated with the tracer measurement (volume, concentration and flow rate) but most significant is the error associated with the tracer measure of pore volume. This measure only includes mobile pore water. Any increase in immobile pore water with clogging was attributed to displacement by deposited kaolin, hence over-estimating the bulk density of the kaolin deposits.

Such an increase in immobile pore water could result from entire pore channels becoming disconnected from the main pore volume due to kaolin deposition, as shown in Figure 2.21, B. Feedback between increasing flow velocity and decreasing deposition is expected to reduce the number of channels that block completely (see Chapter 5), however the downward drift of large kaolin deposits that have exceeded the limit of stability would be less affected by velocity and could block pore channels, as shown in Figure 2.21, C.

Unstable deposits become more likely with increasing kaolin deposition and with rounded gravel (Ahn et al., 2007). The greatest error in clogged tracer PV was observed after the second stage of clogging of the rounded gravel filter. Here the pore volume was underestimated by, on average, -19.8% which was consistent with the increase in immobile pore volume described above.

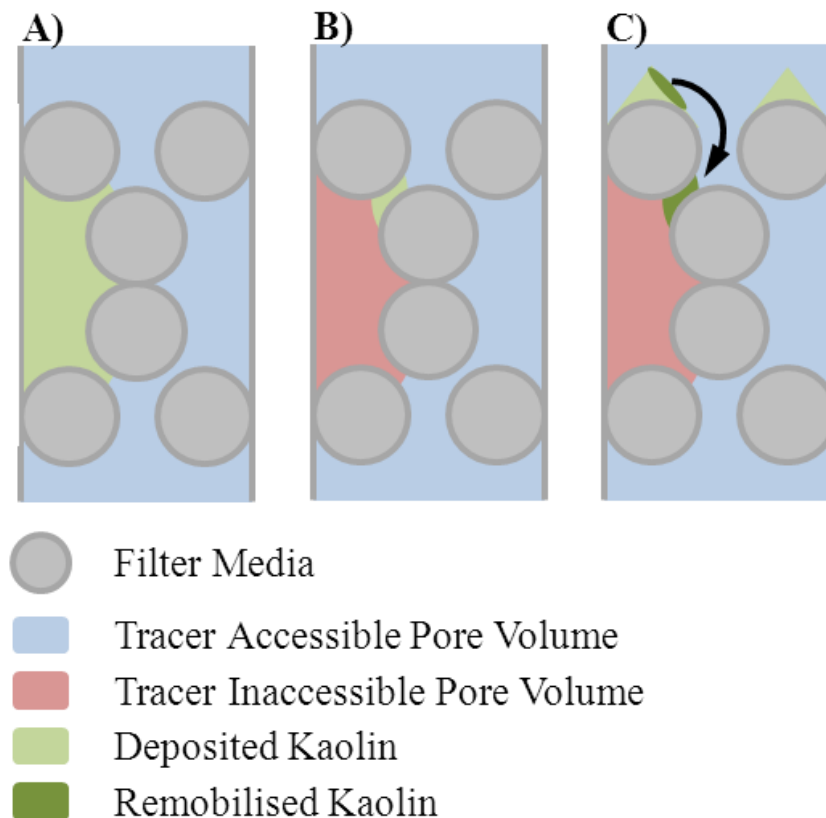


Figure 2.21. A and B show two kaolin deposition patterns that result in a similar tracer accessible pore volume but require very different amounts of kaolin to be retained. The tracer PV would under predict the total pore volume for case B hence kaolin bulk density would be under predicted. C shows how the downward drift of deposited kaolin that has exceeded the stability limit could cause the deposition pattern in B.

At intermediate stages of clogging neither pore volume nor mass of kaolin retained can be directly measured. The mass of kaolin retained can be inferred from the sediment loading and removal efficiency for each phase and then the settled kaolin bulk density used to estimate the decrease in pore volume due to kaolin deposition. Tracer PVs agreed with the removal efficiency mass balance PVs to within 6.1% and were 3.3% lower on average for all 10 filters, an improvement over the initial clean bed accuracy. A potential reason for this improved agreement is that the bulk density estimate of settled kaolin is too low as it incorporates immobile pore volume. This leads to an over prediction of settled kaolin volume and under prediction of total volume thus compensating for the tracer PVs inability to measure immobile pore volume.

In addition to measuring filter transport properties such as dispersivity, tracer residence time distributions have the ability to measure mobile pore volume within 10% of the true mobile pore volume. This allows the volume of sediment retained in a filter to be calculated over the period between two tracer injections and is an alternative to routine monitoring of influent and effluent concentrations to establish removal efficiencies on which retention can be based. The main setting in which this application of tracers may be useful is expected to be in laboratory or pilot-scale assessment of filter design parameters. In such a setting an understanding of how filter removal efficiency and head loss are related to the accumulation of sediment and reduction in mobile pore volume would be very useful, particularly if it would allow the frequency of these measurements to be reduced.

In roughing filters operated for drinking water pre-treatment head loss, influent and effluent concentrations are used to assess if a filter is performing satisfactorily. It is therefore likely that they would be routinely monitored and there would be no value in additionally measuring mobile pore volume from tracer RTDs. However, should a filter be behaving incorrectly, tracers to establish the mobile pore volume may be a useful diagnostic tool.

2.10 Conclusions

Key findings of this chapter were that the change between influent and effluent turbidity of a kaolin suspension cannot be used as a proxy for TSS removal efficiency based on a single relationship between turbidity and TSS. This is because the mean particle size is reduced by filtration. Instead, a turbidity/TSS relationship for the influent and effluent suspensions can be used, provided that the change in effluent particle size over time is not significant.

The mobile pore volume of a filter can be estimated to within 10% by using pore volume as a parameter for fitting a convection dispersion model to tracer breakthrough curves. Subsequent tracer derived pore volumes can be used to determine the change in mobile pore volume due to sediment accumulation within a filter and may be a useful tool for assessing filter status.

Enhanced transport of large particles through heterogeneous porous media has previously been observed by Carrigan et al. (1996) and Auset & Keller (2004). A similar phenomenon was detected in this study through monitoring filter influent and effluent PSD over time. This was attributed to the exclusion of large particles from the narrower, slower pore channels with the result that large particles were either removed or confined to larger, high velocity channels whilst small particles were transported in both fast and slow channels. The net result was a skewing of the effluent PSD towards large particles during the initial stage of filtration. The enhanced transport of larger particles is not thought to significantly affect filter removal efficiency or the longevity of the filter, but is worth considering when carrying out experiments and monitoring filter performance: the initial effluent suspension (and hence any measurement of concentration, turbidity or PSD made during this stage) is not representative of the general behaviour of the filter.

Whilst the removal efficiency and tracer transport measurements provide information for characterising bulk filter performance, the change in tracer RTD and enhanced transport of large particles indicate that pore channels and spatial heterogeneity may be significant. Bulk measurement of filter performance cannot capture such spatial heterogeneity and so the remainder of this thesis focuses on techniques for measuring spatial variation in particle removal, understanding the processes involved, and how filter performance might be impacted.

Chapter 3 – Magnetic Resonance Imaging: a non-invasive tool to characterise and quantify spatial variation in particle accumulation

3.1 Abstract

Magnetic Resonance Imaging (MRI) offers the opportunity for non-invasive measurement of particle accumulation within a filter. Although increasingly being used for non-biomedical applications, such studies on gravel filters have not been identified. In this study, MRI was used as a tool for characterising and quantifying fine particle accumulation within a gravel filter; the specific objective of which was to relate pore geometry and velocity to the spatial and temporal variation in clogging. To obtain this data at an appropriate scale and resolution for analysis, a high magnetic field strength MRI machine was used to image the filters. The filters consisted of 100mm diameter Perspex columns filled with 10mm dolomite gravel. MRI scans were performed sequentially on the filter before, during and after substantial clogging with kaolin clay at a high flow rate and a low flow rate. Scan resolution was 300 μ m with a maximum scan volume of 100mm wide, 130mm high and 180mm long.

An image processing methodology using the free and open source software ImageJ was developed. The method was able to segment the raw MRI intensity data into solid (gravel and kaolin) and fluid (water) regions and reproduce experimentally measured porosities to within 1.75%. Analysis of the segmented images allowed trends in clogging to be quantified, such as increased kaolin deposition at the inlet during low flows and more uniform deposition throughout the filter at high flow rates. The imaging and analysis procedures developed herein are shown to reliably differentiate between water, gravel and deposited kaolin. MRI thus provides a valuable tool for characterising the 3D spatial variation of particle deposition and is appropriate for answering an important aim of this thesis: to better understand the particle removal processes occurring during gravel filtration.

3.2 Introduction

Magnetic resonance imaging (MRI) has traditionally been used in medical and veterinary applications as a non-invasive method for imaging the internal organs of patients in two or three dimensions. MRI has also been used in flow-particle applications: for instance Sederman et al. (1998) used MRI to measure flow velocities in 5mm diameter glass ballotini; Amitay-Rosen et al. (2005) measured porosity change over time during colloid particle deposition; Baumann & Werth (2005) measured colloid breakthrough in silica gel; Kleinhans et al. (2008) used MRI to measure sorting patterns in gravel and Haynes et al. (2012) used MRI to measure flow-related restructuring of bed particles in gravel bed rivers.

The use of MRI to measure changes in porosity has been established (e.g. Amitay-Rosen et al., 2005) and the following advantages displayed: imaging is entirely non-invasive via the use of laboratory-based flow columns; spatial variation in sediment accumulation can be measured in any user-defined plane of orientation; and, there is the ability to measure propagation of a suitable tracer or direct measurement of flow velocities with suitably tailored MRI pulse sequences (Johns et al., 2000; Hingerl, 2013). Yet, this technique remains in its infancy in flow-sediment research and has not previously been applied to filters containing gravel-sized angular media, where fluid flow is likely more variable in velocity than that found in smaller grain filters.

The wealth of data on pore network connectivity offered by a fully 3D scan has more often been collected using x-ray tomography (Gruber et al., 2012; Blunt et al., 2013; Cooper et al., 2003) than by MRI. Whilst a valuable technique offering excellent spatial resolution, x-ray tomography is limited in the size of sample that can be scanned and hence is better suited for soil and rock samples than coarse grained gravel filters. Furthermore, MRI offers the potential for fluid velocity and tracer propagation measurement that x-ray tomography cannot match. It should be noted that the present investigation did not utilise velocity imaging, although it does serve as a precursor to such an experiment.

Given these characteristics, it appears beneficial to employ MRI to image inside a SuDS or water treatment filter system in order to provide unprecedented detail of the 3D/4D internal

processes of sediment transport and deposition within. Such enhanced understanding has the potential to lead to improved gravel filter and SuDS design.

This chapter explores the use of MRI as a tool for non-invasive characterisation and quantification of the spatial variation in sediment accumulation in a gravel filter during clogging. The experiment setup and method of image acquisition are described, followed by data processing techniques, then data analysis examining how measurements of porosity and pore connectivity vary spatially across the filter. Discussion focuses on the quality of the MRI derived pore volume, the fundamental sediment removal processes at work, the use of MRI as a tool for elucidating these processes and potential improvements to the methodology.

3.3 Data Collection Methodology

The aim of the experiments was to determine how pore geometry affects the spatial variation of sediment deposition, how this changes over time and how it is influenced by pore velocity. Two experiments were run, one at a low flow rate and the other at a higher flow rate. 3D MRI scans of the clean gravel, after one week clogging with kaolin and after two weeks clogging were taken.

3.3.1 Experiment Setup

Due to restrictions of the MRI bore size and requirement for non-magnetic components, a bespoke plastic column was developed to be compatible with the MRI. The column had an internal diameter of 100mm, length of 210mm with mixing sections at inlet and outlet (to distribute flows evenly over the entire width of the column), a perforated plastic mesh to hold the gravel media in place at either end and an inlet and outlet manifold (Figure 3.1). The column was designed to fit tightly within a 2m long, 132mm internal diameter tube that in turn fitted tightly within the 152mm bore of the largest radio frequency coil available at the MRI facility. Inserting the column within a the larger plastic tube made it possible to place the column ± 1 mm (Section 3.3.2) within the MRI for each scan and ensured that, if any leaks were to occur, water would not come in to contact with the electric components of the MRI machine.

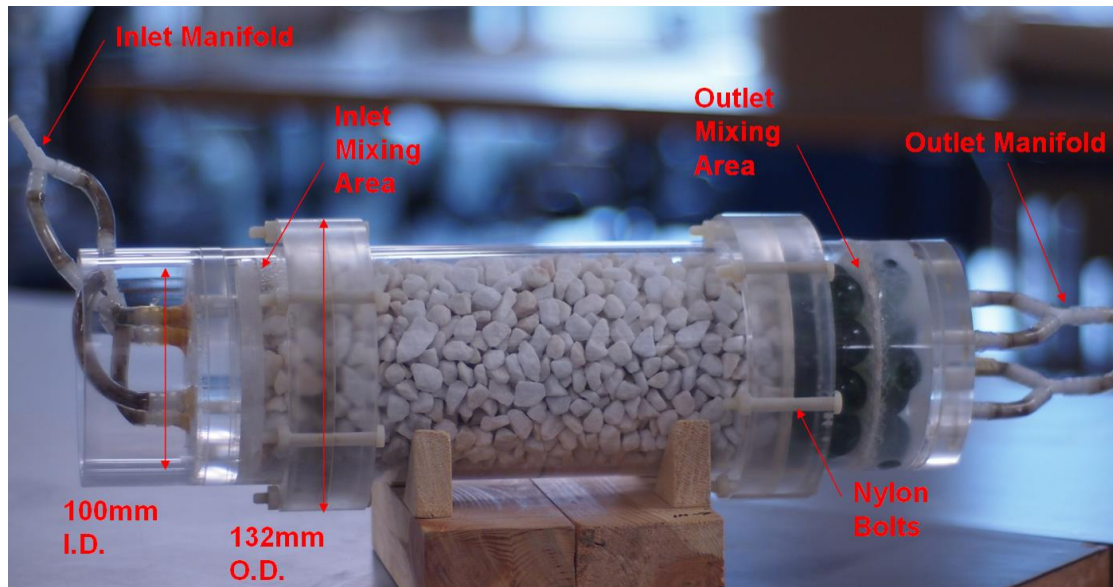


Figure 3.1. MRI column components.

The column was filled with a known mass of sub-angular dolomite gravel sieved at standard $\frac{1}{2}$ phi intervals to provide a range from 8mm to 11.2mm; this approximates to 10 gravel particles per cross-section of the diameter of the column. Dolomite was used because it has a very low metal content and therefore limits any distortion or artefacts in the resulting MR image. Based on published rates of dolomite dissolution (Zhang et al., 2007) at low temperatures (25°C), atmospheric pressure, neutral pH and a dolomite gravel surface area calculated from the MRI scans (Section 3.6.1), the mass loss within the filter due to dolomite dissolution was estimated to be 0.185g over the two week experiment. This is equivalent to 0.0072% of the initial filter mass hence dissolution of the dolomite media can be ignored.

The column was filled by hand with care taken to place the gravel from a consistent height of approximately 5cm above the gravel surface and the column was gently tapped after every layer of gravel was placed. This was to ensure that the gravel was not compacted (as per roughing filter and SuDS filter construction), but was also not prone to shifting when the column was moved in and out of the MRI machine (as substantial movement would make it difficult to determine where sediment deposition occurred).

Flow rates of 49.2 and 102ml/min were used equating to filtration rates of 0.376 and 0.779m/hr which were within the expected range of flow rates in roadside filter drains and

well within those of gravel roughing filters (Lin et al., 2008). This flow rate was supplied by a peristaltic pump with two heads, each consisting of three rollers and set up out of phase. Small bore peristaltic pump tubing was used in each pump head and joined by a Y-connector to a single larger bore tube connected to the column inlet. The combination of using two pump heads with the rollers out of phase and small bore tubing (requiring a greater number of revolutions per minute of the pump head) reduced the pulsation of the peristaltic pump, in comparison to a single pump head with large bore tubing.

Kaolin was used as a surrogate for the river sediment and fine road runoff particles that roughing filters and roadside SuDS filters are designed to remove. The properties of kaolin which make it a suitable surrogate together with justification for using a high concentration to result in substantial clogging in a short period of time are discussed in Chapter 2, Sections 2.4 and 2.5. The experiments were run at the MRI facility so as to reduce the chance of deposited kaolin being disturbed whilst transporting the column into the MRI machine. The feed stock of kaolin was kept in suspension via magnetic stirrer and recirculated through the column as per the clogging phase of the removal efficiency experiments (Chapter 2, Section 2.7). Each day a one litre sample of tank water was taken for analysis of turbidity and particle concentration by filtration (Chapter 2, Section 2.4.3) and one replacement litre of concentrated kaolin stock was added to the tank. This allowed the amount of kaolin retained in the filter to be measured.

The experiment programme is detailed in Table 3.1. A total of 130g of kaolin passed through each filter over a two week period with 74.24g and 89.70g calculated to have been retained in the low flow and high flow filters respectively. Scans took approximately 20 hours and were scheduled so as to take place over the weekend.

Table 3.1. Experiment programme. Each MRI scan has been assigned a label with L standing for low flow and H for high flow, a number corresponding to the phase of the experiment and either C or E to denote if the scan followed a clogging phase or an erosion phase. For example, L1C signifies the scan was for the low flow experiment during the first phase of clogging (the clean scan) whilst H4E signifies the high flow experiment in the 4th phase and after erosion.

Phase	Low Flow - 0.376m/hr	High Flow - 0.779m/hr
I	L1C - clean gravel filter	H1C - clean gravel filter
II	4.2 days of flow through filter 42.5g kaolin accumulated in filter L2C - partially clogged	4.19 days of flow through filter 54.24g kaolin accumulated in filter H2C - partially clogged
III	4.2 days of flow through filter 74.24g kaolin accumulated in filter L3C - clogged	4.02 days of flow through filter 89.70g kaolin accumulated in filter H3C - clogged
IV		1hour clean water flow at 3.44m/hr H4E - 1st stage of erosion
V		1hour clean water flow at 4.58m/hr H5E - 2nd stage of erosion

3.3.2 Image Acquisition

Scans were acquired using the Bruker 7T MRI machine at the Glasgow Experimental MRI Centre (GEMRIC) using the largest bore (152mm) radio frequency (RF) coil available. The scan type used was a 3D rapid acquisition relaxation enhanced (RARE) sequence. The RARE scan consisted of a train of RF pulses $90^\circ_x [-t_e - 180^\circ_y - t_e -]_n$ with an echo time (t_e) of 11 ms, a RARE factor of $n = 8$ and a repetition time of 4000 ms. The bandwidth was set at 200 kHz and anti-aliasing was set to 2 to reduce wraparound artefacts. The scan took 20 hours in total with an additional hour to post-process the data. The resulting data is a 3D array composed of 333x433x600 voxels with each 15-bit voxel representing one of 32768 possible signal intensities. The resolution was 300 μ m and so the field of view (total imageable area) was 100mm wide, 130mm high and 180mm long. This data is most often viewed as a series of 2D (X-Y) slices in which the slice number is equivalent to the third dimension (Z). Image resolution was an appropriate compromise between scan time, the

desired image extent and the volume that can be post-processed and viewed on a high-end desktop computer; scale dependency was not investigated in this study as it would have necessitated additional scans.

Alignment points on the MRI machine, on the plastic tube and on the column, were used to ensure the column was positioned in exactly the same location (within $\pm 1\text{mm}$) for each scan. The MRI was then tuned to give optimum signal and a trial scan was used to ensure the selected field of view aligned with the actual position of the column in the MRI.

3.4 MRI Scan Quality

Artefacts in the MR image can occur due to the presence of ferromagnetic or paramagnetic materials, non-uniformity in the RF field, steep changes in signal, intensity inhomogeneity and gradient non-linearity (Sederman & Gladden, 2001; Kleinhans et al., 2008; Vovk et al., 2007; Jelinkova et al., 2011). When medical MR imaging made the transition from 1.5T to 3T (and higher) field strength scanners, many of these artefacts were found to be more pronounced. However, Dietrich et al. (2008) have shown that with small modifications to the RF pulse sequences, parallel imaging and raw data post-processing of 3T MRI, it was possible to reduce the effect of artefacts to the level of 1.5T whilst retaining the higher signal to noise ratio for a given acquisition time.

As the RARE sequence employed has previously successfully been used to image water within the pores of dolomite gravel by Haynes et al. (2012), it was used without further modification. The resulting MR image (e.g. Figure 3.2) shows no signs of paramagnetic or ferromagnetic artefacts due to the use of low metal content dolomite. However, gradient non-linearity is present; this refers to differences in the magnetic field created by the gradient coils and is particularly pronounced at their extremities as visible where the image becomes rounded towards the edge of the scan volume in the along-bore direction (shown in Figure 3.2). As indicated in Figure 3.2, only the undistorted volume was used in data analysis; this comprises a region of interest (ROI) 63.3mm x 100mm x 100mm.

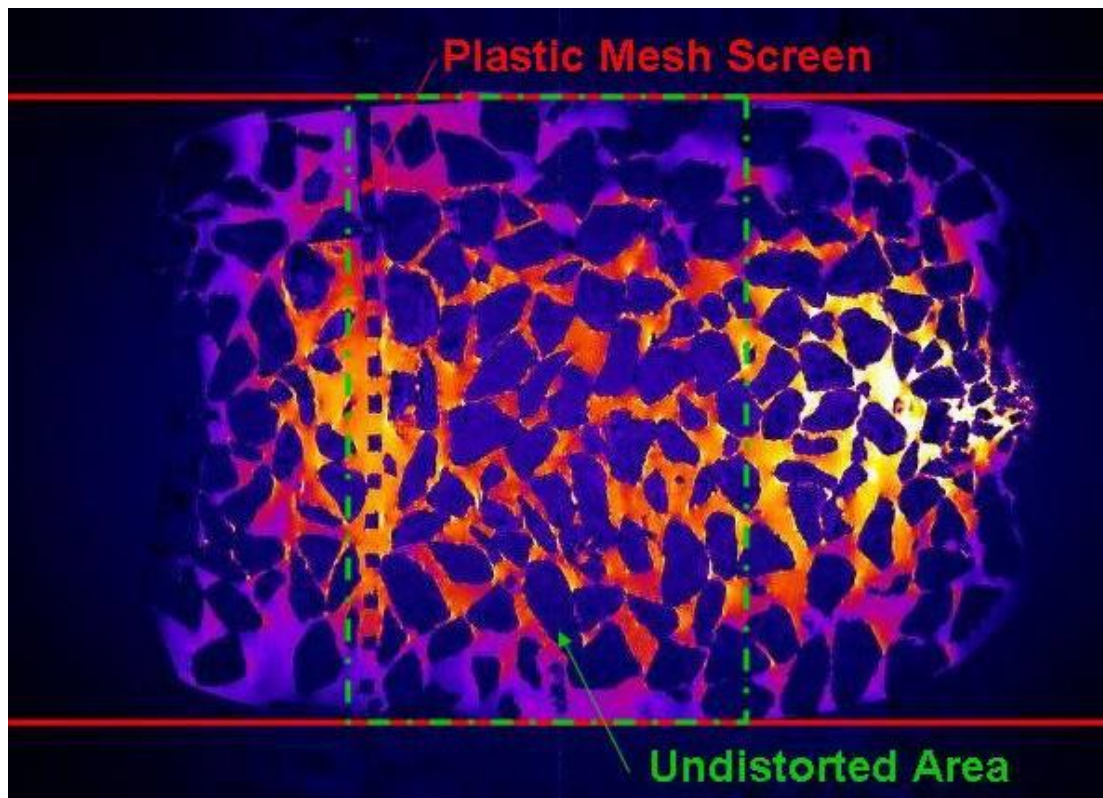


Figure 3.2. Slice through centre of full scan volume showing MRI signal intensity. Signal intensity is linked to water concentration: water filled pore volumes result in high intensity (hot colours) whilst gravel, column components and areas outside the column result in low intensity (cool colours/black). Image dimensions are 180mm long, 130mm high and 100mm deep. The volume within the green box is not distorted and is 63.3mm long.

Similarly, intensity inhomogeneity is also clearly visible in Figure 3.3. This occurs due to the imaged object itself or imperfections in the image acquisition process (Vovk et al., 2007) and is manifest as a variation in intensity across the image. This has minimal effect on the data of the present study as the signal intensity of water is distinct enough from that of gravel as to allow segmentation between water and gravel in all but the outermost edges of the scan (located within Region C of Figure 3.3). With image post-processing (Section 3.5), the unsegmentable area was reduced to just 25 voxels from the edge giving a good quality scan volume 282 voxels in diameter and 211 voxels deep (this translates as 84.9mm diameter by 63.3mm long).

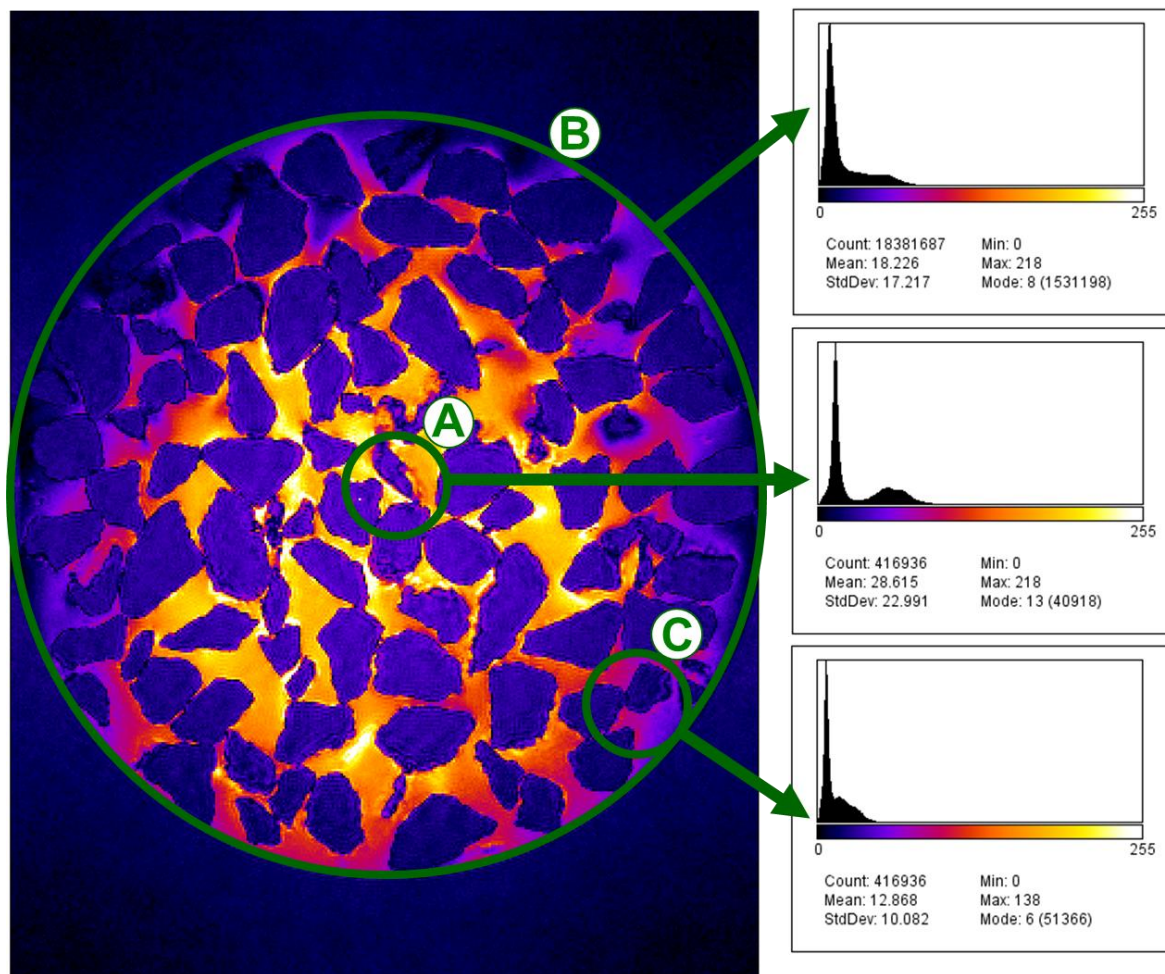


Figure 3.3. Histogram of intensity values. The central segment of the scan is bi-modal (as shown by Region A), yet the overall histogram (Region B) is not bi-modal due to the overlap in water and gravel intensity at the edges of the image (Region C). N.B. the contrast of the image has been increased to aid visualisation, whereas contrast in the histograms was unaltered.

Following pilot trials, all scanned data continued to be scrutinised after collection. Whilst the first scan (L1C) data was high quality, the second scan (L2C) suffered from poor quality (Figure 3.4); detailed review highlighted that this was due to the choice of Tx₀, Tx₁ and Gain set during scan acquisition. These are set automatically by the Bruker Paravision 4.0 controlling software after a short tri-pilot test scan with the aim of obtaining the best image quality possible; however, this automated procedure was unsuccessful for scan L2C. As a repeat of scan L2C with different settings would have necessitated re-running the experiment, with a notable cost implication, it was elected to continue the low-flow test focussing on scans L1C and L3C, with cautious and judicious interpretation of scan L2C

being used if required. To mitigate against similar problems, all subsequent scans cross-checked the automated setting selection to ensure they were similar to those for scan L1C; no further problems with image quality were encountered. The implications of the image quality, resolution and maximum ROI area are further discussed in Section 3.7.1.

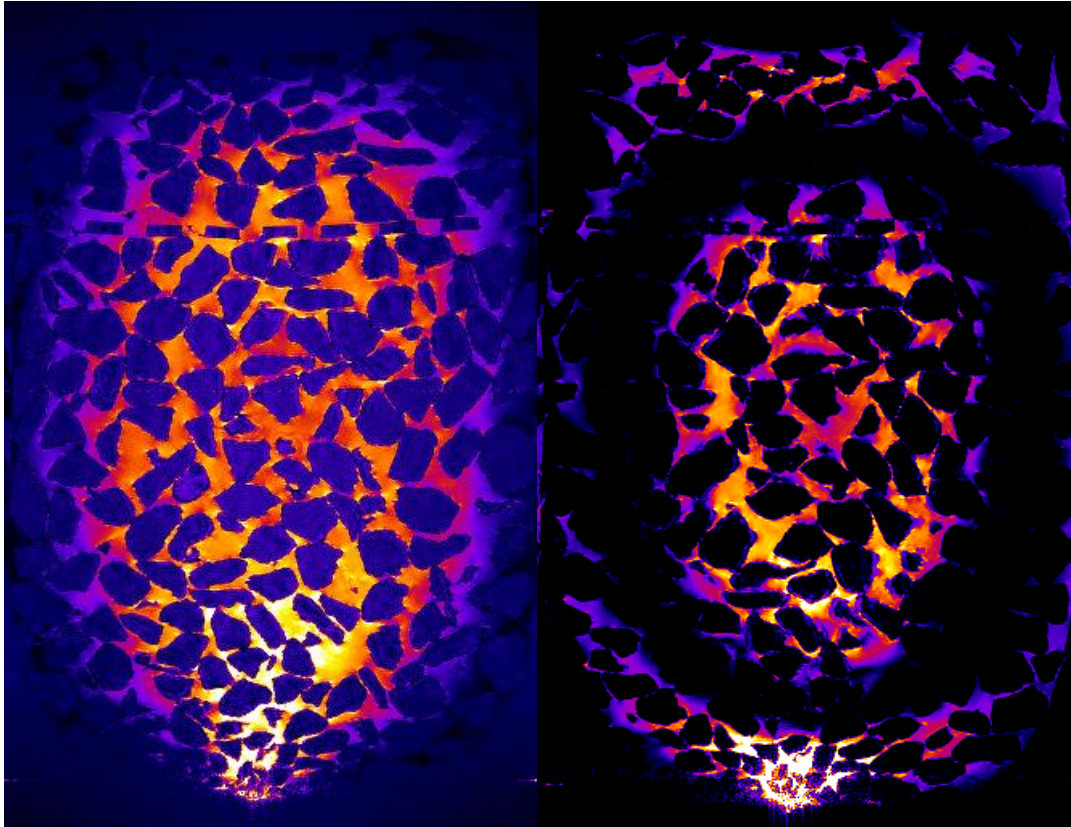


Figure 3.4. Scan L1C (left) showing good quality image. Scan L2C (right) showing poor quality image. In L2C the black regions present within the ROI represent locations of no MRI signal. In these regions it is impossible to distinguish solid from liquid and hence to determine the location of deposited kaolin.

3.5 Image Processing

For most types of further analysis (e.g. porosity and pore network structure) it is necessary to split the MRI image into water and non-water phases (known as segmentation). Image segmentation is inherently user subjective and image analysis experts can produce different results depending on the methods they use (Baveye et al., 2010). Automated algorithms exist, but they are used for different applications (counting number of cells, tracing

neurons, determining void space etc.) with data collected from different techniques (MRI, x-ray tomography, light microscopy) and even then, the data has often undergone very different pre- and post-processing. As such, there is not a standard image segmentation protocol and so a range of methods were investigated using the Java-based public domain software ImageJ developed by the National Institutes of Health; this software has been successfully applied to water-gravel MRI (Haynes et al., 2009; Haynes et al., 2012) and was selected for its open architecture approach to 3rd party plugins for image processing. It was not the goal of this project to develop new custom software or ImageJ plugins, but rather to evaluate existing software packages, plugins and their combinations so as to find the method most suitable for the data and for the end purpose: spatial measurement of porosity change within the ROI.

In this section we assess the quality of a range of common image processing methods (and combinations of methods), select an optimum image processing method and quantify the uncertainty in porosity measurement associated with the MRI scan resolution. A detailed review of the underlying image processing theory and its application to the MRI scan data can be found in Appendix A, divided into pre-segmentation processing, segmentation and post-segmentation processing.

3.5.1 Segmentation Quality

To establish which combination of pre-processing, segmentation and post-processing was optimal, the most promising pre-processing methods identified in Appendix A, Section A.1 were combined with the most promising segmentation and post-processing methods identified in Sections A.2 and A.3 and summarised in Figure 3.5 below. This resulted in 31 methods with a total of 166 different combinations of settings.

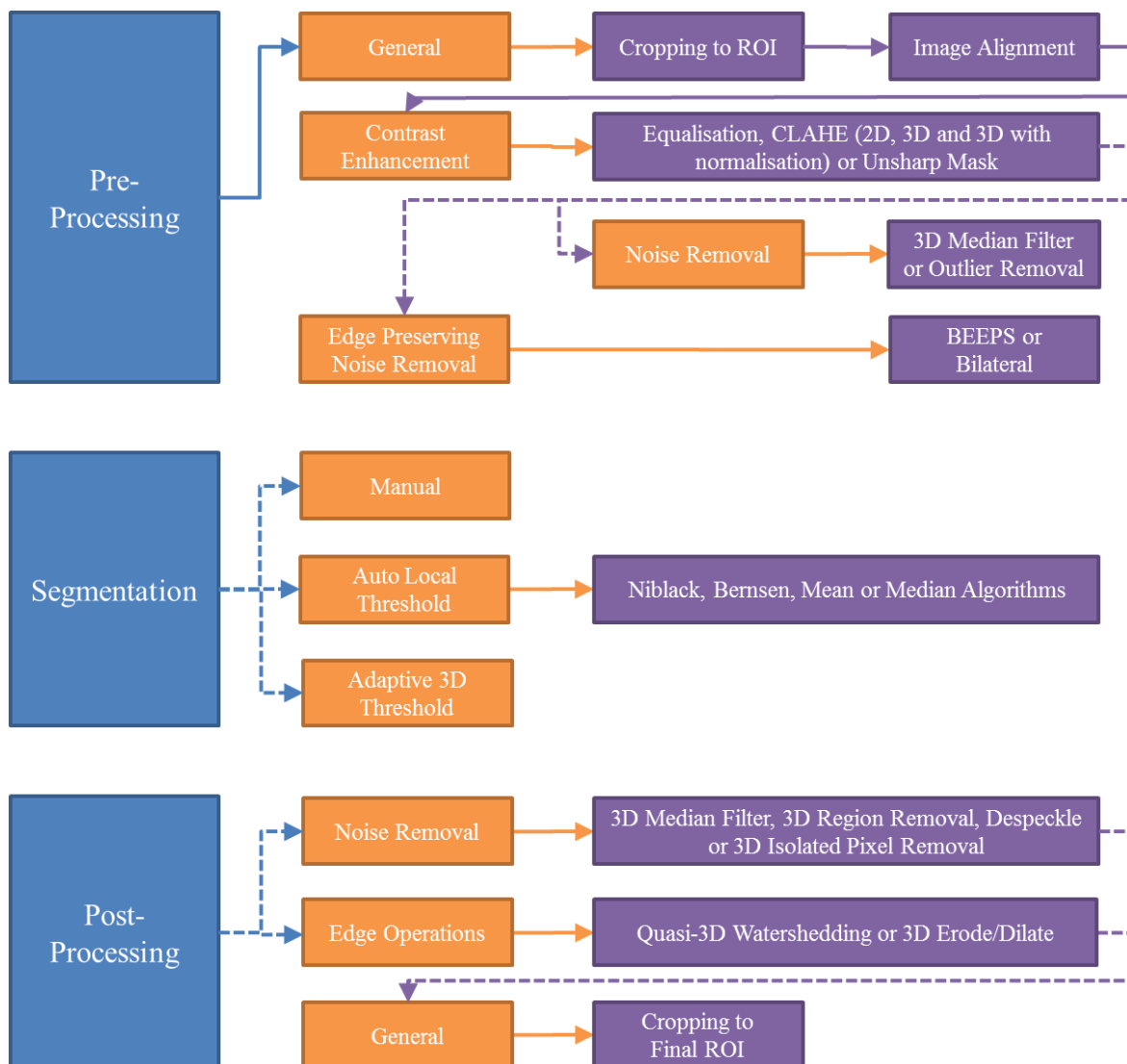


Figure 3.5. Summary of image pre-processing, segmentation and post-processing procedures culminating in 31 methods for processing the images.

To ascertain which was most suitable, the segmented image produced by each method was:

- subjected to a visual assessment and comparison with nine manually segmented slices,
- compared with a measured bulk porosity and
- compared with the known diameter of the inlet mesh screen.

Table 3.2 provides a summary of data for this evaluation process and is found at the end of this section. In order to better understand the data generated, and debate its fitness for purpose, additional detail is first provided on each measureable utilised.

3.5.1.1 Visual Assessment

To reduce the image processing combinations into a more manageable quantity for numerical evaluation, nine image slices from scan L1C were processed and compared, by eye, with nine corresponding slices manually segmented with the software ArcGIS (ESRI) (see Appendix A, Section A.2.1 for details of manual segmentation). Each method was given a score out of three (1 = good, 2 = adequate and 3 = inadequate) in the following categories: area successfully segmented, lack of salt and pepper noise in resulting image and successful splitting of particles in close contact. Examples of these are shown in Figure 3.6. The rationale behind performing this step first was that there is no value in further analysing a processing method that does not accurately represent the structure of the gravel and pore space, even if that method happens to produce an accurate bulk porosity. Methods that scored a 3 for any category were rejected whilst the remaining methods with the lowest combined scores were selected for further analysis resulting in the six methods tabulated in Table 3.2, Section 3.5.2.

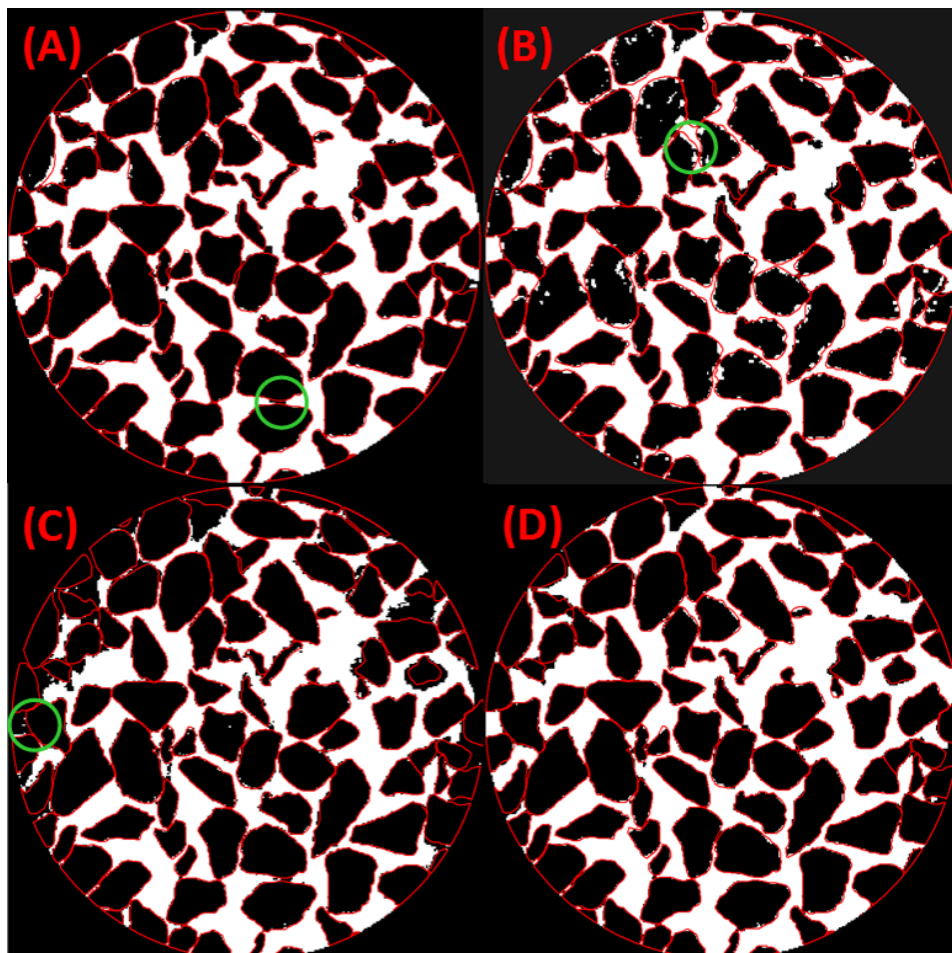


Figure 3.6. first stage of the quality analysis with processed images showing pore space (white) and gravel (black) overlaid by manually segmented gravel outlines (red): Examples of (A) poor separation of particles in close contact, (B) noisy image, (C) low extent of area segmented and (D) good quality for all three measures. Some areas of poor quality are circled in green.

3.5.1.2 Comparison with Measured Bulk Porosity

The bulk porosity of the two columns was measured as detailed in Chapter 2, Section 2.7.1 by filling with water from a tank of known mass and temperature and measuring the mass change. As the ROI of the MR image does not cover the entire column (see Figure 3.2), the porosity measured experimentally for the entire column may not be the same as the porosity of the ROI. However, as care was taken to fill each column uniformly, the porosities should be similar and this can be improved by averaging the results of the two bulk porosity measurements. The average bulk porosity measurement was 42.70%, but this includes the area close to the wall which would be expected to have a higher porosity than

the internal portions of the column due to “wall effects” (i.e. where gravel particles rest against the curved column wall rather than against another gravel particle, the packing density is lower hence porosity is higher). This was problematic as the MRI ROI did not include the area close to the wall and so was unaffected by wall effects. The bulk porosity measurement was corrected for these wall effects using the findings of Dudgeon and Aust (1968) where, for spherical particles, there is a 25% increase in porosity within a zone $\frac{1}{2}$ a particle diameter thick against the wall (see Equation 1 & Equation 2). Once corrected for wall effects, the bulk porosity of the internal section of the column (within the MRI ROI) was determined to be 40.76%.

$$V_v = L \frac{\pi}{4} D_I^2 P + L \frac{\pi}{4} (D^2 - D_I^2) \frac{5}{4} P \quad \text{Equation 1}$$

$$P_{bulk} = \frac{1}{L \frac{\pi}{4} D^2} V_v \quad \text{Equation 2}$$

Where L = column length

P = porosity in region unaffected by walls

P_{bulk} = experimentally measured bulk porosity

V_v = volume of voids (pore space)

D = diameter of column

D_I = diameter of internal region of column unaffected by walls

However, it should be borne in mind that the correction employed is for spherical particles. Irregular particles could, potentially, have tighter or looser packing at the wall depending on the ‘fit’ of the more angular shapes. Review of the MR images clearly show such local variability and, given the relatively small ROI, the corrected porosity will reflect this such that values are likely plus or minus a few percent of the theoretical value of 40.76%. Whilst this comparison between the corrected bulk porosity and the segmented image porosity is an important measure of the quality of the segmentation method, as the wall effects cannot be measured directly from the available data the corrected bulk porosity must not be the sole measure defining quality; thus, the other measures of quality must also be satisfied.

3.5.1.3 Comparison with Plastic Mesh Opening Diameter

The plastic mesh at the inlet of the ROI consists of spherical openings 4.8mm diameter to a tolerance of $\pm 0.05\text{mm}$. Due to their regular shape and size and because they could be measured both physically and in the processed image, these openings are useful for assessing the quality of the processed image. The six image processing methods that met the initial quality requirements were evaluated based on the area and circularity of 10 openings. Only openings that were not obscured by a piece of gravel in a neighbouring slice were selected and, so as to reduce user bias, these 10 unobscured openings were selected based on a geometric pattern as shown in Figure 3.7.

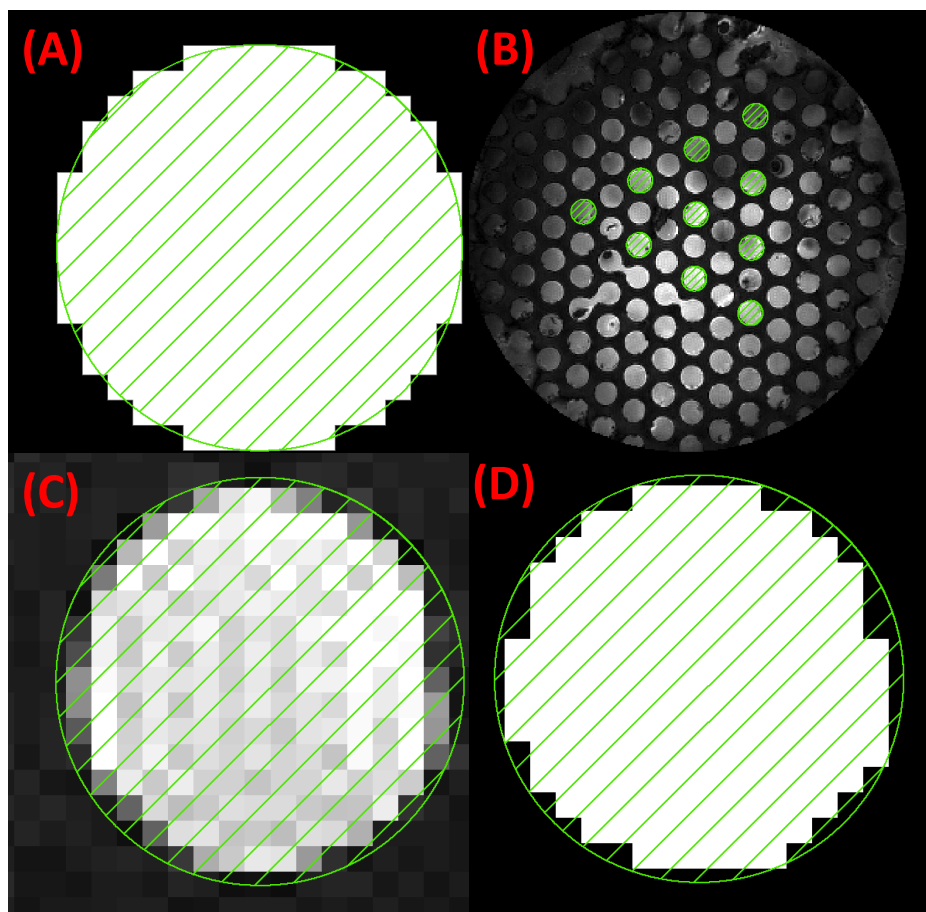


Figure 3.7. (A) pixelated representation of a perfectly circular 4.8mm opening at resolution of $300\mu\text{m}$, (B) geometrical arrangement of the 10 openings selected for analysis, (C) unprocessed MR image of an opening with ideal circular opening superimposed and (D) opening shown in C after a good quality segmentation method was applied. The area of the opening in D is underestimated by approximately 10%.

As the MR image is composed of pixels, the area and circularity of the segmented image openings are compared to a pixelated representation of a perfectly circular opening with a diameter of 4.8mm. If the processed image mesh openings (D in Figure 3.7) are equal to the known mesh opening characteristics (A in Figure 3.7) in terms of circularity and area, then the gravel particles are likely to have been segmented to a similar degree of accuracy.

Such an additional measure of segmentation accuracy complements the visual assessment and use of bulk porosity for evaluating segmentation quality; whilst also allowing potential error in porosity measurement based on image resolution to be measured (Section 3.5.5).

3.5.2 Selection of Image Processing Method

After applying each measure of image quality in sequence to the 31 methods (and 166 variants) identified in Section 3.5.1, the six methods that best met all criteria were selected and summarised in Table 3.2. The optimal image processing method was determined to be Method 2. Method 2 satisfies the quality criteria of segmenting a large area with low resulting noise and good separation of particles in close proximity. It also provided reasonably good replication of the measured bulk porosity (corrected for wall effects) and the area and shape of the openings in the plastic mesh.

It was clear that contrast limited adaptive histogram equalisation (CLAHE) was the best contrast enhancement procedure as five of the top six methods use it whilst post-processing resulted in no improvement in quality for most methods. Method 1 best reproduced the bulk porosity as well as the area of the plastic mesh openings; yet did not perform as well with respect to area segmented, noise or circularity of the plastic mesh. The discrepancy between poor circularity and good area of the plastic mesh demonstrated that the geometry of the plastic mesh openings was poorly represented; a feature of the processing method that will likely apply to the representation of the gravel particles, hence making Method 1 unsuitable. This highlights the need for multiple measures of quality that take into account geometry rather than relying purely on bulk porosity.

Table 3.2. Image processing quality evaluation procedure that, for the six selected methods 1) lists the steps in the processing and segmentation procedure, 2) details results of the visual assessment of segmentation quality, 3) states difference in porosity compared with experimentally measured bulk porosity, and 4) compares circularity and area of the plastic mesh openings with their measured values. Overall, Method 2 was deemed to be the optimum method.

		Method 1	Method 2	Method 3	Method 4	Method 5	Method 6	
		Contrast enhancement	CLAHE	CLAHE	CLAHE	CLAHE	CLAHE	Equalised
Processing & segmentation procedure		Noise removal	3D median	Bilateral filter	Bilateral filter	3D median	Outlier removal	Bilateral filter
		Segmentation	3D adaptive	ALT-Niblack	ALT-Bernson	ALT-MidGrey	ALT-Niblack	ALT-Mean
		Post-processing	None	3D median	None	None	None	None
		Segmentation quality (1= good, 2= adequate, 3= unsatisfactory)	Area	2	1	1	1	2
	Noise	2	1	1	2	2	2	
	Edge segmentation	2	2	2	2	2	1	
		Reference value	Difference between method value and reference value					
Bulk porosity (%)		40.76	-1.25	-1.36	-2.99	-3.69	-4.82	-5.02
Plastic mesh openings	Circularity	1	12.50%	-5.10%	-4.06%	-4.38%	-6.88%	-1.56%
	Area	208	1.59%	-9.66%	-9.68%	-8.49%	-13.56%	-11.47%

Of the remaining methods, Method 2 provided the best segmentation quality with respect to area and noise, the best bulk porosity quality and plastic mesh openings quality broadly comparable to the remaining methods. Method 2 was therefore the best method overall.

3.5.3 Sensitivity to Image Stack Processing Direction

With an optimum image processing method chosen, the 3D quality of the data can be assessed. As the data was collected in 3D, it should be processed in 3D so as to preserve the intra-slice structure of the data (Elliot & Heck, 2007). Yet some of the 3D steps for processing the data resulted in poorer quality segmentation than their 2D counterparts, and for some 2D processing steps a 3D equivalent was not available. To test the hypothesis that 2D processing does not faithfully segment 3D data and may introduce errors, the raw MRI data was re-sliced into three orthogonal planes (i.e. X-Y, X-Z and Y-Z) and 2D processed images and 3D processed images were created for each plane. The methods used for each stage of the processing are summarised in Table 3.3.

Table 3.3. Processing methods for each stage of 2D and 3D processing comparison.

Stage	2D	3D
Contrast enhancement	CLAHE	3D CLAHE
Noise removal	Bilateral filter	3D median filter
Segmentation	Auto local threshold - Niblack	Adaptive 3D threshold
Post-processing	Despeckle	3D median filter

The bulk porosity of each orthogonal plane was measured leading to a set of three porosities for the 2D processed images and three for the 3D processed images. Porosity varied by a maximum of 2.20% (equivalent to a standard deviation of 1.21) for the 2D processed images, depending in which orthogonal plane was the Z-axis in which the 2D analysis was carried out, whilst the variation was a maximum of 0.04% (0.02 standard deviations) for the 3D processed images. Clearly this shows that 3D processing is far superior to 2D processing, yet the 3D processing was unable to accurately replicate the measured bulk porosity and manually segmented slice porosities, as shown in Table 3.4.

To determine the relative degree to which each processing stage contributed to these errors, 16 image sets consisting of every possible combination of 2D and 3D processing stages were created for each of the three orthogonal planes, as shown in Table 3.4. The resulting range in porosities for each image was calculated and shows that contrast enhancement is the most significant factor determining processing direction dependent error followed by segmentation method. Noise removal had a much smaller effect and post-processing noise removal an insignificant effect.

Table 3.4. 16 combinations of 2D and 3D processing (Methods A-P) ranked from low to high standard deviation of the bulk porosities of images processed in the x, y and z orthogonal planes. Range refers to the difference between the maximum and minimum porosities in the three orthogonal planes. See Table 3.3 for details of each processing stage.

Method	Processing stage				Standard deviation	Range (%)	Bulk porosity
	Contrast enhance	Noise removal	Segmentation	Post-processing			
A	3D	2D	3D	2D	0.006	0.01	-9.86%
B	3D	2D	3D	3D	0.011	0.02	-9.74%
C	3D	3D	3D	2D	0.013	0.03	-9.25%
D	3D	3D	3D	3D	0.020	0.04	-9.13%
E	3D	2D	2D	3D	0.168	0.33	-6.37%
F	3D	2D	2D	2D	0.173	0.33	-6.51%
G	3D	3D	2D	3D	0.189	0.34	-6.94%
H	3D	3D	2D	2D	0.201	0.35	-7.05%
I	2D	2D	3D	3D	0.916	1.82	-8.31%
J	2D	2D	3D	2D	0.933	1.86	-8.43%
K	2D	3D	2D	3D	1.068	1.92	-4.79%
L	2D	3D	2D	2D	1.111	2.00	-4.86%
M	2D	3D	3D	3D	1.120	2.22	-7.49%
N	2D	3D	3D	2D	1.143	2.27	-7.59%
O	2D	2D	2D	3D	1.144	2.08	-4.32%
P	2D	2D	2D	2D	1.206	2.20	-4.38%

Given the hierarchy of factor significance, it was surprising that the combination of 3D contrast enhancement and 3D segmentation with 2D noise removal and post-processing produced the highest bulk porosity error (despite having the lowest processing direction dependent error) (Method A in Table 3.4). The use of 3D contrast enhancement is thought to reduce the processing direction dependent error for the following reason: if two adjacent pixels in neighbouring slices have identical intensities, but one is surrounded by lower intensity pixels within its slice whilst the other is surrounded by higher intensity pixels, those two pixels will be treated very differently by a 2D contrast enhancement (that only considers surrounding pixels in one slice) than by a 3D contrast enhancement that will consider neighbouring pixels in both slices.

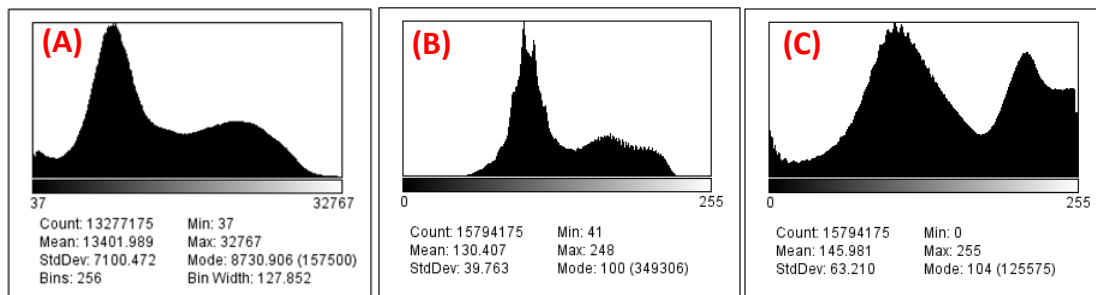


Figure 3.8: (A) 2D implementation of CLAHE, (B) 3D implementation of CLAHE and (C) histogram normalisation followed by 3D implementation of CLAHE.

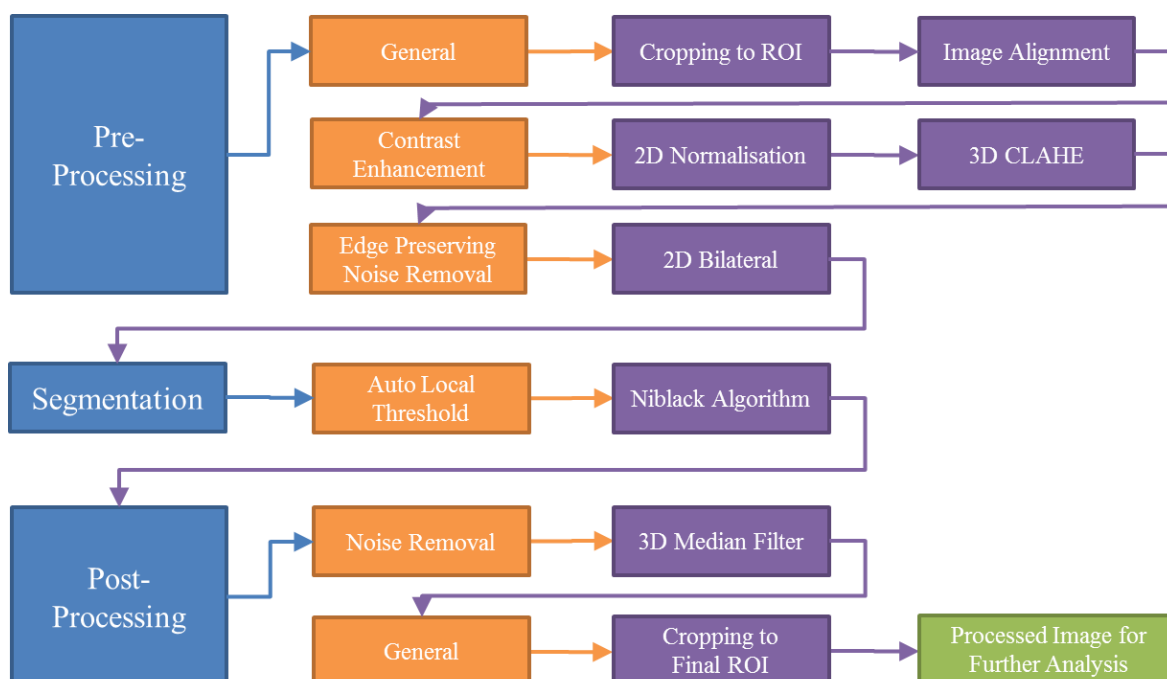
Upon further examination of the 3D CLAHE implementation, it was found that the histogram was not stretched to the same extent as with 2D CLAHE (see Figure 3.8) and that this accounted for the poor segmentation and large difference in porosity compared to the bulk porosity. By utilising histogram normalisation prior to 3D CLAHE, this deficiency was overcome and led to a refinement of Method 2, selected as the optimum image processing method in Section 3.5.2.

3.5.4 Optimum Image Processing Method

Taking into account the processing direction dependent error identified in Section 3.5.3, the selected image processing method (Method 2) can be refined by substituting CLAHE contrast enhancement with normalisation followed by a 3D implementation of CLAHE. This brings the advantage of lowering the processing direction dependent error to an acceptable value (a range of 0.76%) without the poor representation of bulk porosity associated with the all 3D processing method (-9.86%). Inherent in this compromise is a slight deterioration in segmented image quality; however, this is more than compensated for by the improvement in processing direction dependent error, as summarised in Table 3.5. The refined Method 2 procedure, as summarised in Figure 3.9, was then applied to all MRI scans.

Table 3.5. Method 2 segmented image quality with refinement.

Measure of Quality		Reference value	Difference between method value and reference value	
			Method 2	Refined Method 2
Bulk porosity (%)		40.76	-1.36	-1.75
Processing direction dependent range in bulk porosity (%)		-	2.08	0.76
Plastic mesh openings	Circularity	1	-5.10%	-5.94%
	Area (pixels ²)	208	-9.66%	-10.92%

**Figure 3.9. Summary of the image processing steps that constitute Refined Method 2, deemed to be the optimum method.**

3.5.5 Quantification of Error & Uncertainty

Despite the care taken to develop an image processing methodology that most faithfully reproduced the structure and porosity of the data in 3D, some uncertainty and errors are likely to remain. As visible analysis showed no signs of paramagnetic distortion or artefacts within the region of interest and the porosity of the segmented image matches the experimentally determined bulk porosity to within 1.75% (when compared with the average bulk porosity of the two columns corrected for wall effects and assuming spherical

particles), the principle sources of error are due to the resolution of the image and the resulting delineation of the gravel particle edges.

To elucidate, when collecting the MR signal, the MRI uses the gradient coils to manipulate the magnetic field so that, with Fourier analysis of the data, the measurement volume can be discretised into voxels (in this case 300 μ m cubes) and the signal from individual voxels can be measured. The signal is proportional to the volume of water occupying each voxel and so if a voxel contains 50% water and 50% gravel, the signal from that voxel will be lower than one containing 100% water and higher than one containing 0% water. When segmenting an image, each pixel must be classified as either gravel or water and so a pixel containing 51% water would ideally be classified as water, depending on the segmentation algorithm. The edges between gravel and water are very sensitive to the choice of segmentation method and to the resolution of the image, as shown in Figure 3.10.

Comparison between the actual gravel size and that calculated from the segmented image was not possible as each piece of gravel is unique and its shape is not known *a priori*. However, the mesh opening size was known and was also measured for the segmented image (Section 3.5.1.3) allowing an estimate of the edge uncertainty to be made which subsequently may be applied to the gravel slices. For the chosen image processing method, the area of each 4.8mm diameter mesh opening is 10.92% greater than the physical measurement. As this error only occurs where there is an abrupt interface between solid and water, it can be non-dimensionalised by the perimeter of the solid/water interface yielding a value of 0.3648 pixels. In other words, for every pixel of interface between solid and water, the area could be out by up to ± 0.3648 pixels².

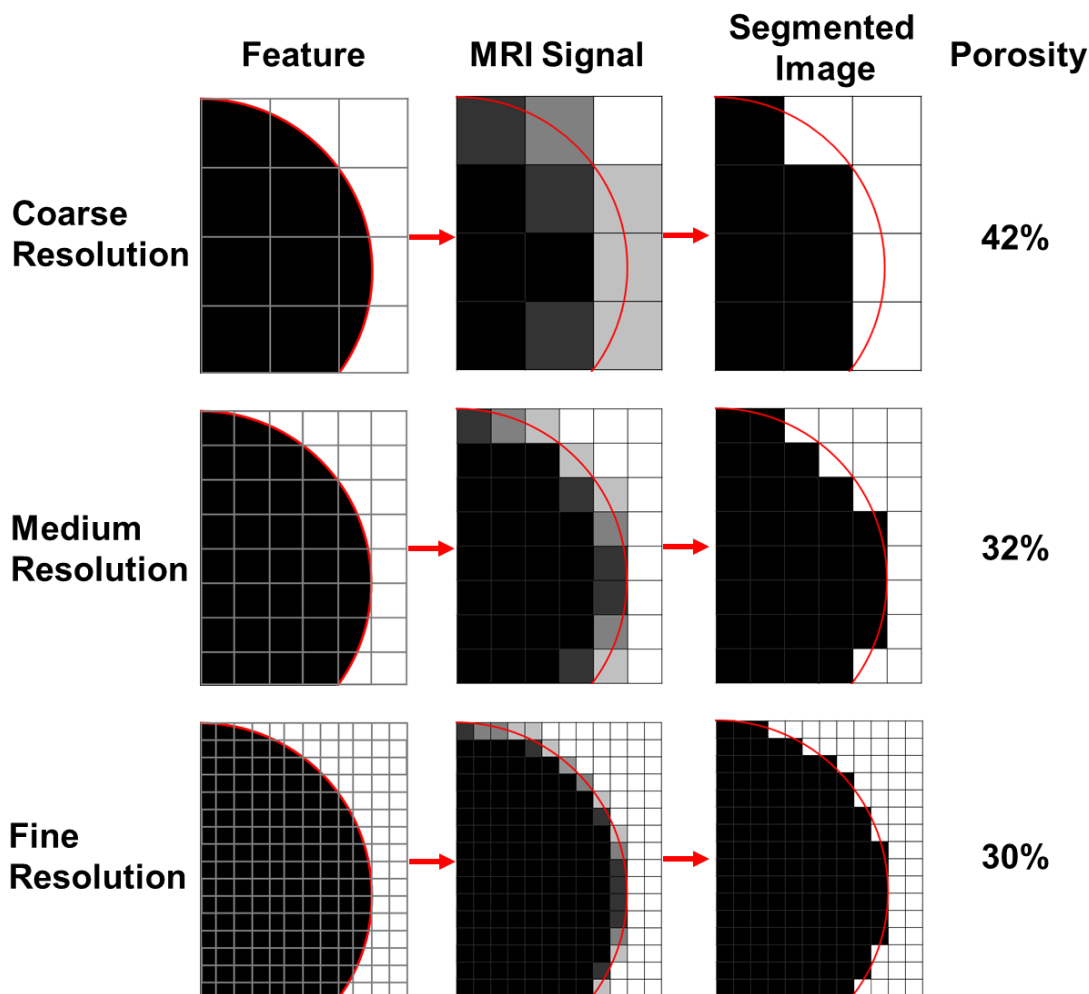


Figure 3.10. Example of how resolution can affect the resulting porosity of an image after segmentation. A mock MRI signal is created for each pixel depending on the proportion of gravel (black) or water (white) in each pixel and a simple segmentation method applied whereby a signal $>50\%$ is taken to be water. Porosities shown are for the segmented image and are somewhat higher than the actual porosity of 29.84% although the finer the resolution, the closer the segmented image porosity approaches the actual porosity.

The interface between gravel and water was measured for the nine manually segmented slices and, after the error was applied, it was predicted that the porosity of the segmented slices could vary up to a maximum of $\pm 3.81\%$ due to the effect of image resolution on the segmentation of interfaces. This error could explain why no segmentation method could perfectly replicate bulk porosity whilst satisfying the other measures of quality.

3.6 Image Analysis Results

Two gravel filters were scanned in the MRI machine: one to investigate kaolin deposition at low flow rates and the other at higher flow rates. In total, there were eight MRI scans as part of this project (detailed in Table 3.1, Section 3.3.1), however Scan L2C was of poor quality and was removed from the analysis (Section 3.4). Columns were, firstly, scanned prior to any flow with kaolin, after one week of kaolin deposition and after two weeks of kaolin deposition; this was in order to analyse the temporal change in porosity with kaolin deposition. Secondly, additional scans were performed after two weeks of kaolin deposition for the high flow rate column only; these scans were subjected to two short duration, high velocity flows intended to erode some of the deposited kaolin. The aim of these second-stage erosion tests was to determine to what degree fine deposits are only temporarily stored (or vice versa, to what degree they are permanently captured) in gravel-based SuDS and roughing filters.

With the scans segmented and aligned as per the methodology of Section 3.5.4, it was possible to determine where the kaolin was deposited or eroded by subtracting the pore space of the initial clean scan from subsequent scans. Figure 3.11 shows such an operation for a representative slice through the high flow rate filter for each stage of deposition and erosion. The full 3D ROI for both filters were subjected to similar treatment and the data evaluated with respect to 1) bulk parameters of porosity, number of regions and surface area (Section 3.6.1); 2) slice-by-slice evaluation of porosity in the three orthogonal planes; and 3) analysis of change in porosity in 3D regions regularly spaced throughout the filter.

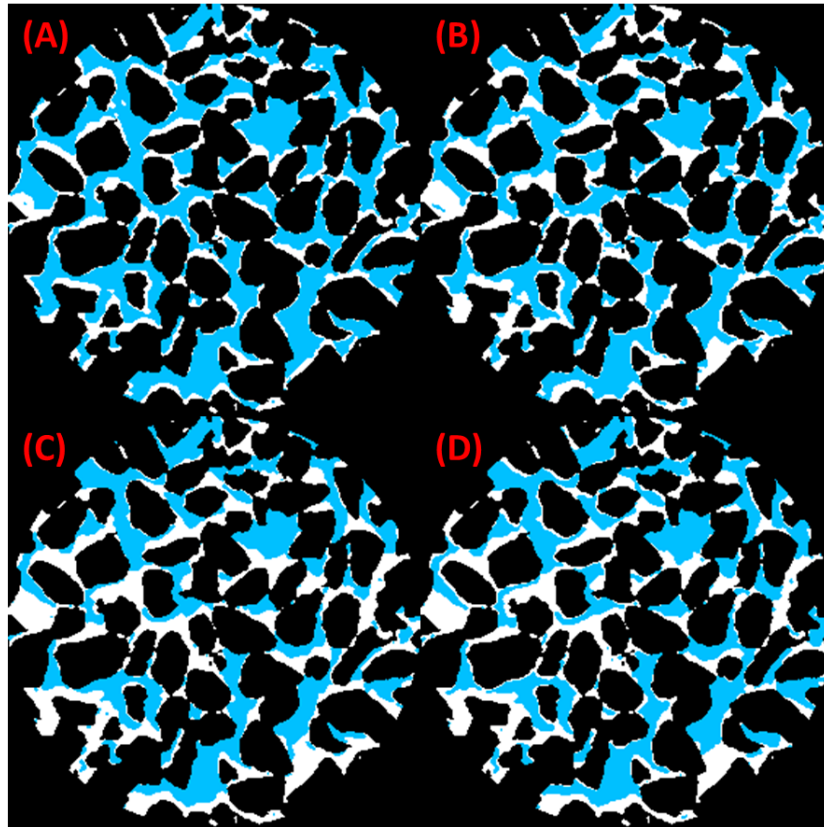


Figure 3.11. Change in pore space during the high flow experiment. The location of gravel (black), pore water (blue) and deposited kaolin (white) is shown after (A) one week deposition, (B) two weeks deposition, (C) first stage of erosion and (D) second stage of erosion.

3.6.1 Bulk Porosity, Number of Regions and Surface Area Analysis

Method of Analysis: The change in porosity over time is the simplest way of characterising the clogging of each filter. There are two methods available for this with results from each presented in Table 3.6: 1) using the porosity derived from the MRI scan and 2) using the experimentally measured bulk porosity for scans L1C and H1C together with estimated porosities for the remaining scans. The reason bulk porosities could not be measured for scans L3C, H2C, H3C, H4E and H5E was this would require draining of the column and disturbance of the settled kaolin. Instead, a mass balance approach was used to measure the mass of kaolin retained in the filter between each scan and, using a bulk density of 1455g/l for the deposited kaolin (determined in Chapter 2, Section 2.8.6), the decrease in porosity of the column as a result of kaolin deposition was estimated. As the MRI derived porosities

do not include the areas in proximity with the column walls, the measured bulk porosities in Table 3.6 have been corrected to remove the increased porosity at the walls (as per the methodology of Section 3.5.1) and allow comparison with the MRI derived porosities. The value in comparing the MRI derived porosity with the experimentally measured and estimated porosities is discussed in Section 3.7.3.

Here we define a pore space region as a volume of the pore space that is connected such that it is possible for a particle of kaolin to travel from one point in the region to all other points. A pore space region is defined as active if it is connected to both the inlet and outlet of the ROI. The number of distinct pore space regions was measured for each scan using the *Find Connected Regions* plugin of ImageJ. This provides a measure of the change in active pore space available and is distinct from the total porosity measurements because kaolin deposition can cause some pores to become disconnected from the main pore body.

In addition, gravel and gravel/kaolin surface area was measured with the *IsoSurface* plugin to ImageJ developed by Doube et al. (2010) and implementing the marching cubes algorithm of Lorensen and Cline (1987). In the active surface area measurement (Table 3.6), pore space regions not connected to the main pore region were not included and so this surface area represents the area that would be available for the attachment of pollutants such as suspended particles, pollutant metals and dissolved substances.

Table 3.6. Experimentally measured (subscript _M) and estimated (subscript _E) bulk porosities for entire column compared with MRI derived parameters for the region of interest (ROI). Active porosity and active surface area refer to measurements for the single largest connected pore region.

	Low flow		High flow				
	L1C	L3C	H1C	H2C	H3C	H4E	H5E
Bulk porosity (entire cColumn)	40.43 _M	34.58 _E	41.17 _M	36.90 _E	34.11 _E	34.35 _E	34.72 _E
MRI derived porosity (%)	40.29	16.71	41.1	29.71	24.88	25.39	25.71
Number of regions	388	3441	492	585	933	1192	998
Active porosity (%)	40.27	16.18	41.07	29.65	24.76	25.11	25.52
Surface area (mm²)	179,049	123,847	172,194	150,013	141,619	136,332	138,649
Active surface area (mm²)	178,610	115,284	171,534	148,865	139,303	132,021	135,095

Results: The results show close agreement between the bulk porosity of the entire column and the MRI derived porosity of the ROI for the clean gravel scans L1C and H1C. This is to be expected as agreement between these porosity measurements and MRI scans was used as one of the criteria for selecting the optimum image processing method. With clogging, the bulk porosity and MRI porosity diverge. Table 3.6 shows the MRI porosity was consistently lower than the bulk porosity and the difference was more pronounced for the low flow scan L3C (17.87%) than the high flow scan H3C (9.23%).

In the column experiments of Chapter 2, greater accumulation of kaolin at the inlet was clearly visible through the column side walls. A similar trend was observed through the walls of the MRI column and is in line with filtration theory in which particle removal is considered to be a first order process (Iwasaki et al., 1937). It is proposed that, as the MRI ROI is located closer to the column inlet, the lower MRI porosity than bulk porosity is the result of greater kaolin deposition at the inlet and within the ROI than the average deposition within the filter as a whole. This is supported by the greater difference for scan L3C than H3C: the higher velocity of scan H3C led to somewhat more uniformly distributed kaolin throughout the filter.

As pore channels fill with kaolin they become disconnected from the main pore volume, the number of distinct pore space regions increase and the active porosity decreases. These disconnected regions are typically small and amount to a difference between total porosity and active porosity of 0.53% for the low flow experiment and 0.13% for the high flow experiment. A similar trend is observed for the active surface area in which active surface area is 6.91% lower than the total surface area after low flow clogging (scan L1C to L3C) and only 1.64% lower after high flow clogging (scan H1C to H3C). The implications of this for gravel filters are a reduced potential for the removal of particles and pollutants such as pollutant metals due to the inaccessible pore volumes, discussed further in Section 3.7.3.1.

From visual analysis of the column outflow during the erosion stages prior to scan H4E and H5E, it was ascertained that erosion of settled kaolin only occurred immediately following an increase in flow rate and with no further erosion thereafter. The MRI data shows a 0.35% and 0.41% increase in porosity after H4E and H5E respectively, translating to a removal of 2.15% and 2.57% of the deposited kaolin. This is important as it indicates that the water quality of the outflow from a gravel filter SuDS will decrease during a high runoff event, potentially affecting the downstream SuDS components and watercourse.

However, during the experiment it was observed that the particle dynamics associated with the re-entrainment of deposited kaolin was very different from the discrete particle and small floc process by which it originally settled. Instead, large aggregations of settled kaolin became dislodged and cascaded like an avalanche into the neighbouring pore with a predominant shift in kaolin from top to bottom, rather than from inlet to outlet. Thus it is important to note that the bulk measures of porosity presented here would show no change to porosity values in this case, as they do not account for the local spatial shifts of deposited kaolin within the filter. The degree of sediment movement within the filter under erosion can only be ascertained by 3D analysis of the MRI data.

A further caveat is required for the MRI derived change in porosity during erosion; this method cannot account for material that has been eroded from near the column wall above the ROI and comes to settle within the ROI, or material that erodes within the ROI and settles below it. In the unlikely event that, upon erosion, all the deposited kaolin in the area

above the ROI becomes deposited within the ROI with no erosion within the ROI itself, or vice-versa, then this could lead to a change in porosity of $\pm 6.28\%$. Whilst this makes analysis of the erosion scans difficult, the difference between deposition and erosion processes is in itself an interesting finding with implications further discussed in Section 3.7.3.1. These limitations apply only to the analysis of the erosion scans and do not affect the clogging scans as, during clogging, kaolin deposition is much more uniform within and outwith the ROI.

3.6.2 Slice-by-slice Porosity Analysis

Analysing the change in average porosity on a slice-by-slice basis allows trends in clogging to be observed. The processed images were re-sliced in the three orthogonal planes as shown in Figure 3.12; this yielded three data sets: (i) longitudinal (Z plane), which showed trends from the inlet to the outlet; (ii) vertical (Y plane), which showed trends from top to bottom; and (iii) lateral (X plane), which shows any variability across the column.

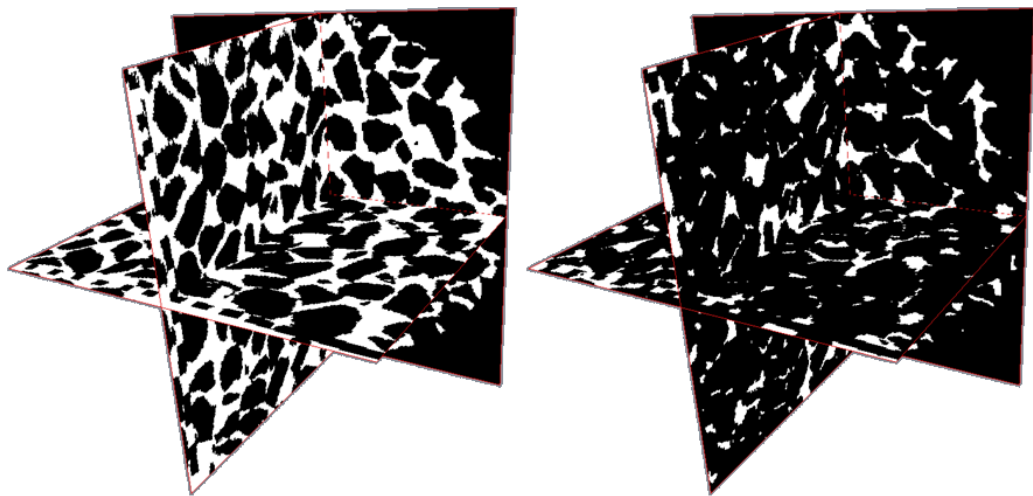


Figure 3.12. Scan L1C (left) and scan L3C (right) showing slices in each of the three orthogonal planes.

Note that when analysing the data, the ROI was reduced so as to omit the first 31 slices in the Z plane where porosity is influenced by the plastic mesh. When measuring in the X and Y planes, the first and last 20 slices were omitted because, as the ROI is circular, the first and last slices are very small and so their porosities are very sensitive to small changes in

volume and are not truly representative. By the 21st slice, the area is 50% that of the ROI at its widest point and measurements were considered to be reliable. Figure 3.13 illustrates the reduced ROI for X and Y plane measurement.

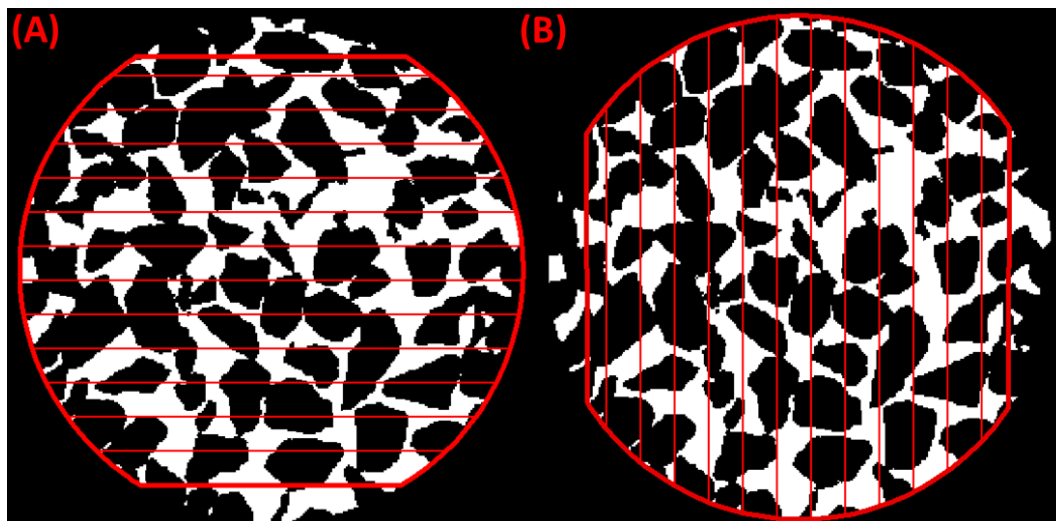


Figure 3.13. Reduced ROIs for slice-by-slice analysis: A) X plane slices and B) Y plane slices.

3.6.2.1 Trends in Porosity and Porosity Change

For each phase of clogging and for each orthogonal plane, the average porosity of every slice was measured together with the change in average porosity, as presented in Figure 3.14. Comparison between each scan can be made by fitting linear trend lines to the slice average porosities and measuring the gradient, then measuring the change in the gradient (hereafter referred to as the slope) between each scan (Table 3.7).

Table 3.7. Change in gradient (slope) between each scan. A negative value denotes a decreasing slope with increasing slice number. The steeper the slope, the larger the trend.

Scans	Z plane	Y plane	X plane
L1C-L3C	-3.7×10^{-5}	5.0×10^{-5}	2.7×10^{-4}
H1C-H2C	-1.4×10^{-4}	4.0×10^{-5}	-6.0×10^{-5}
H1C-H3C	-1.5×10^{-4}	9.0×10^{-5}	2.0×10^{-5}
H2C-H3C	-2.0×10^{-6}	5.0×10^{-4}	8.0×10^{-5}
H3C-H4E	-1.2×10^{-4}	-6.0×10^{-5}	2.0×10^{-4}
H3C-H5E	2.0×10^{-5}	1.6×10^{-4}	2.2×10^{-4}
H4E-H5E	1.4×10^{-4}	2.3×10^{-4}	1.0×10^{-5}

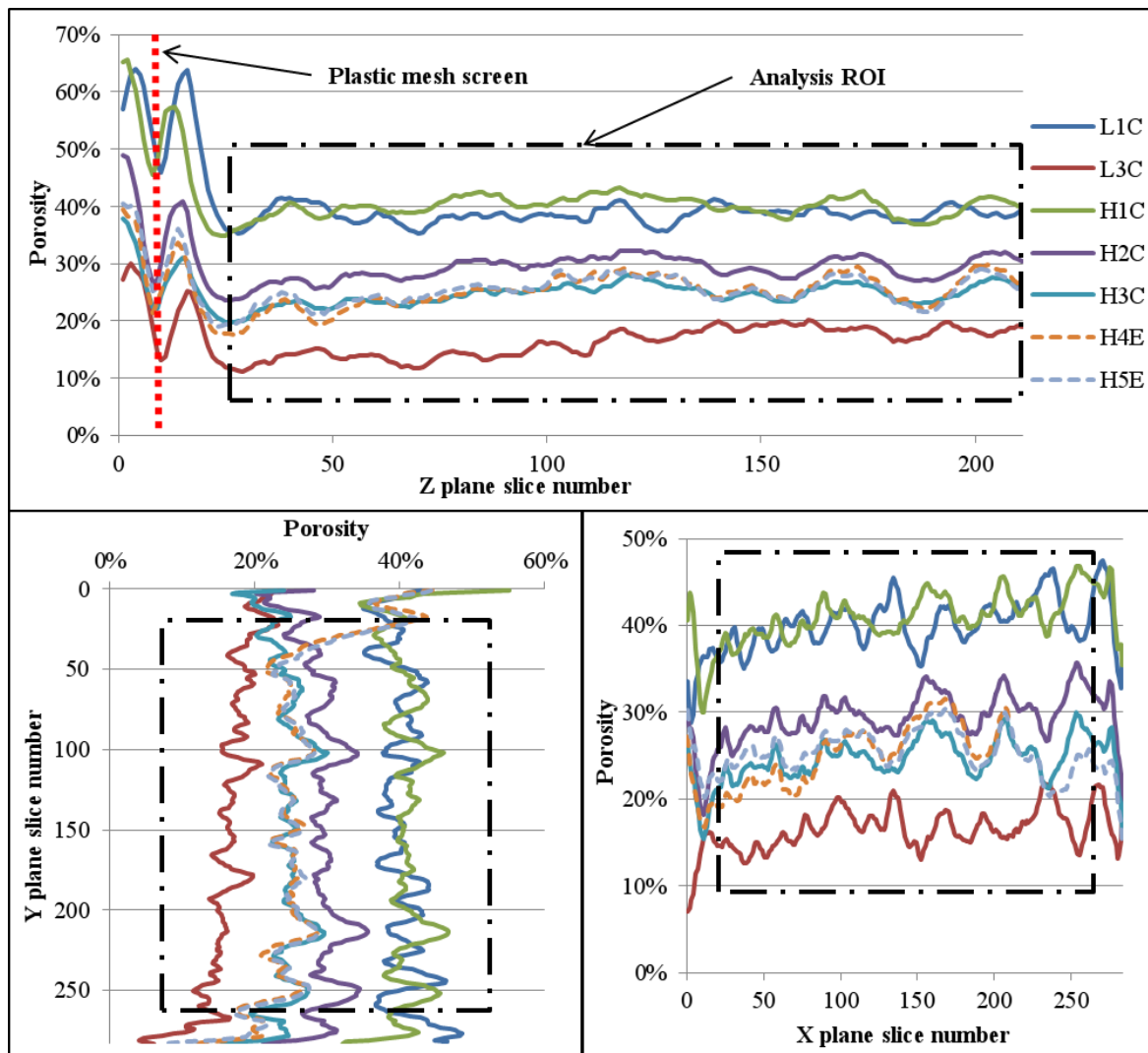


Figure 3.14. Slice average porosities for each of the seven scans in three orthogonal planes: Z plane from inlet (slice 32) to outlet (slice 211); Y plane from top (21) to bottom (263); and X plane from right (21) to left (263).

Z Plane Trends:

Looking at Figure 3.14 it is clear that the clean scans L1C and H1C have higher porosities than the clogged and partially clogged scans in each and every slice. Variability in clean scan slice porosity was low with a range of 6.28% and standard deviation of 1.33% for L1C and 6.42% and 1.53% for H1C.

It is evident that the greatest change in porosity with clogging occurs in the low flow experiment (shown by greater y-offset of the data between L1C and L3C compared with

H1C and H3C). In addition, variability increased for scan L3C with a range of 8.42% and standard deviation of 11.30% whilst the variability remained approximately constant for scan H3C with a range of 6.09% and standard deviation of 1.49%.

It is clear that the erosion (scans H4E and H5E) results in very little change to the Z plane trend or porosity value compared to scan H3C. This is because most of the movement is from top to bottom as shown by vertical analysis.

Using Table 3.7, the negative gradient from inlet to outlet shows that the porosity change is greatest at the inlet and hence there is more kaolin deposition at the inlet. This increased clogging at the inlet is more than twice as pronounced in the low flow experiment where the slope is -3.7×10^{-4} (scan L1C-L3C) than in the high flow experiment where the slope is -1.5×10^{-4} (scan H1C-H3C). In the first stage of clogging in the high flow experiment (scan H1C-H2C), there is significantly greater change in clogging at the inlet than in the second stage of clogging (scan H2C-H3C) as shown by the slopes of -1.4×10^{-4} and -2.0×10^{-6} respectively.

In addition to linear trend lines, a logarithmic trend was also fitted to the inlet to outlet change in porosity data to determine if removal is a first-order process determined by distance into the filter. The regression coefficient of the trend lines are compared to determine which provides the better fit. Whilst neither produces a particularly strong fit, the linear trend was superior for all scans (Table 3.8).

Table 3.8. Regression coefficients indicating “goodness of fit” for linear and logarithmic trend lines fitted to the change in porosity for each clogged scan.

Scan	R ² value	
	Linear trend	Logarithmic trend
L1C-L3C	0.73	0.73
H1C-H2C	0.68	0.58
H1C-H3C	0.55	0.35

X and Y Plane Trends:

Trends are visible in Figure 3.14 from top to bottom with more deposition at the bottom during low flows. At high flows there is no discernible top to bottom trend during deposition but during erosion there is clear removal of deposited kaolin from the top of the column and deposition at the bottom.

There are no discernible X plane trends in deposition for both low and high flow experiments; however, during erosion, there is more change in the right side of the column. This is thought to be due to the formation of preferential flow paths, evidence for which can be found in the analysis of the data in Section 3.6.3.

3.6.2.2 Correlation of Initial Porosity with Change in Porosity

To test the hypothesis that the slice initial porosity will influence the degree of clogging, the correlation between initial porosity and percentage change in porosity was determined. Percentage change in porosity was used instead of absolute change in porosity because slices with a high initial porosity would be expected to have a higher change in absolute porosity simply because there is a larger volume available for kaolin deposition.

The correlations are summarised in Table 3.9 and Figure 3.15. The gradient describes the trend, whilst the P value gives an indication of the significance of the correlation. As the null hypothesis was for no correlation, a low P value indicates correlation between initial porosity and change in porosity.

Table 3.9. Correlation between initial porosity and percentage change in porosity for each scan. A steep gradient (either positive or negative) equals a strong trend whilst the smaller the P value, the more significant the correlation.

Scans	Z Plane		Y Plane		X Plane	
	Gradient	P Value	Gradient	P Value	Gradient	P Value
L1C-L3C	-0.726	2.36×10^{-2}	-0.734	9.02×10^{-21}	0.533	3.88×10^{-4}
H1C-H2C	-0.615	1.27×10^{-7}	-0.542	5.72×10^{-34}	-0.446	1.37×10^{-8}
H1C-H3C	-0.343	3.44×10^{-3}	-0.507	3.48×10^{-16}	-0.332	1.46×10^{-5}
H2C-H3C	0.091	1.38×10^{-1}	-0.120	4.44×10^{-2}	0.207	9.65×10^{-3}
H3C-H5E	-0.787	2.40×10^{-5}	1.027	1.33×10^{-6}	3.791	3.35×10^{-14}

The predominantly negative gradients of the Z plane and Y plane correlations denote a negative correlation between initial slice porosity and percentage change in slice porosity with clogging: slices with a high initial porosity had a low change in porosity and vice versa. However, as can be seen from the P values in Table 3.9 and the spread of the data points around the trend lines in Figure 3.15, the Z plane correlation is weak.

The X plane correlation shows no clear trend during deposition. During erosion there is considerable scattering of data points which skew the trend lines in Figure 3.15. This suggests that change in porosity due to erosion is not determined by slice initial porosity, but by another factor such as pore geometry or connectivity.

As a result, the data of Table 3.9 and Figure 3.15 show that there is a correlation between initial porosity and change in porosity, but this correlation is weak. The spatial trends in clogged filter porosity therefore cannot be predicted based on slice averaged initial porosities and a more sophisticated method for analysing the change in porosity is required.

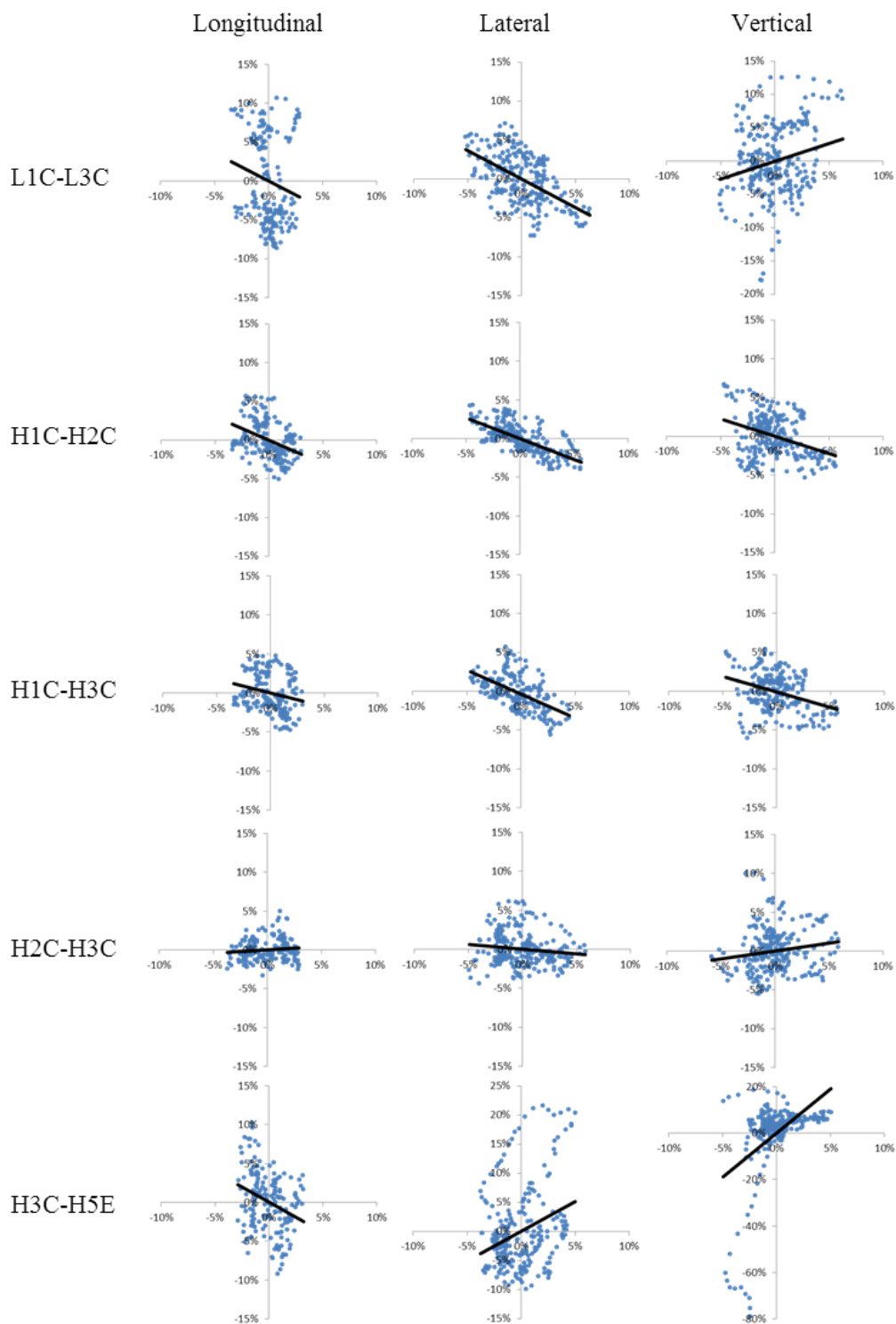


Figure 3.15. Relationship between initial porosity (x-axis) and percentage change in porosity (y-axis), both normalised by average initial porosity and average percentage change respectively. Positive gradient denotes correlation between large initial porosities and large percentage changes in porosity, as well as between small initial porosities with small percentage changes in porosity. For a negative gradient, the inverse is true whilst zero gradient or a large P number denotes no statistically significant correlation. Associated gradients and P values shown in Table 3.9.

3.6.3 3D Region Analysis

3.6.3.1 Spatial Variation in Volume Change

Some spatial trends are masked by the slice-by-slice approach because it is the average of an entire slice. To overcome this, an ImageJ script was written (making use of the 3D spherical crop function in the “3D Tools” plugin written by Thomas Boudier) that divided the ROI into an array of 1170 spherical regions, as shown in Figure 3.16. The volume change of each region before and after clogging was measured as well as the percentage change with respect to the initial volume. For the measurement method used in ImageJ, it was necessary for each spherical region to contain a minimum of one voxel of pore space. It was found that the minimum region diameter that satisfied this criterion was 20 voxels. As such, each region was 20 voxels in diameter with a 20 voxel centre-to-centre spacing so as to ensure the maximum number of valid regions for data analysis.

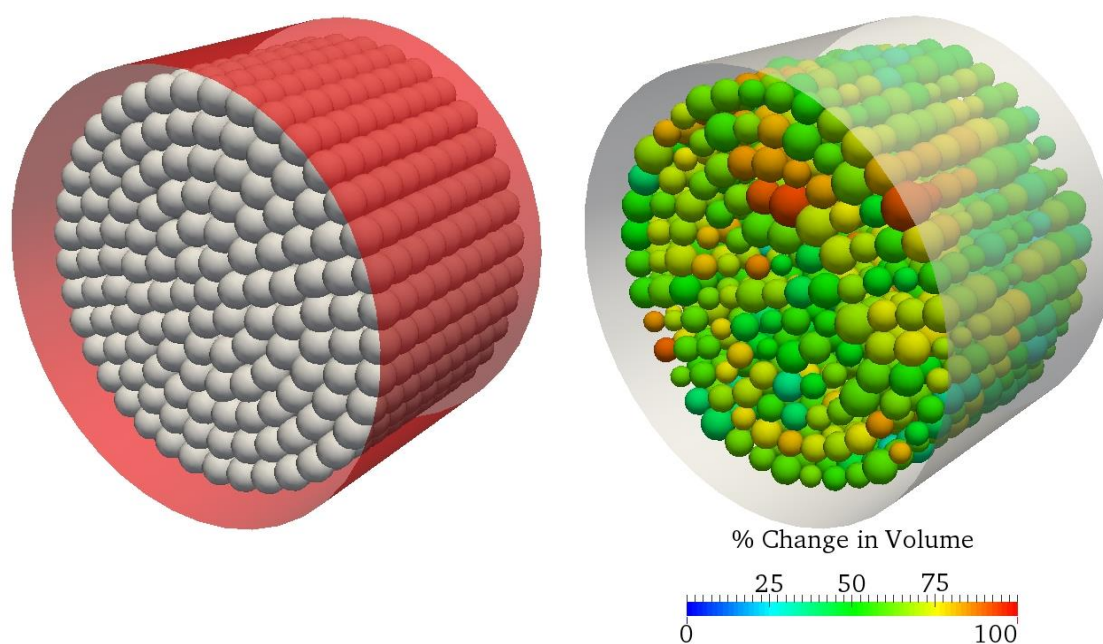


Figure 3.16. Left: location of 3D circular regions (white spheres) within the ROI (red cylinder). Right: region volume represents initial pore volume within each region whilst colour represents percentage change in region volume between scan L1C and L3C.

Linear regression of the volume change of each region (using the X, Y and Z coordinate of the centre of each region for plotting purposes) shows if volume change is linked to its spatial location within the filter. Results of this correlation are presented in Table 3.10 showing trends in volume change for each orthogonal plane.

Table 3.10. Correlation between initial porosity and percentage change in porosity for each scan. A steep gradient (either positive or negative) equals a strong trend whilst the smaller the P value, the more statistically significant the correlation.

Scans	Z Plane		Y Plane		X Plane	
	Gradient	P Value	Gradient	P Value	Gradient	P Value
L1C-L3C	-10.42	4.81×10^{-26}	0.17	8.19×10^{-1}	2.54	4.46×10^{-4}
H1C-H2C	-3.52	1.24×10^{-12}	-0.51	1.54×10^{-1}	-1.75	1.02×10^{-6}
H1C-H3C	-3.47	9.77×10^{-6}	-1.34	1.81×10^{-2}	0.08	8.82×10^{-1}
H2C-H3C	0.04	9.25×10^{-1}	-0.83	1.18×10^{-2}	1.83	1.97×10^{-8}
H3C-H5E	1.51	7.86×10^{-2}	-5.40	5.52×10^{-19}	4.47	2.27×10^{-13}

In the low flow experiment (scans L1C-L3C) there is a strong Z plane trend with negative gradient indicating that as depth into the filter increases, change in porosity decreases i.e. there is more clogging at the inlet. A similar trend is visible in the first stage of clogging in high flow experiment (scans H1C-H2C); however both the gradient and the strength of the correlation are weaker than in the low flow experiment and are not apparent in the second stage of clogging (scans H2C-H3C). This suggests more uniform deposition of kaolin with distance through the filter in the high flow experiment than in the low flow experiment and that uniformity of deposition increases with time. A possible mechanism for this is an increase in flow velocities at the inlet due to deposition of kaolin and a reduction in pore volume, resulting in less subsequent deposition at the inlet.

Y plane trends in the data are virtually non-existent. X plane trends show greater deposition at the bottom of the low flow filter (Table 3.10, scans L1C-L3C vertical). In the high flow experiment, there is initially greater deposition at the top of the filter (scans H1C-H2C) followed by greater deposition at the bottom (scans H2C-H3C) with a net effect of no vertical trend over the clogging period (scans H1C-H3C). This can be explained by preferential flow paths that change in response to the deposition of kaolin within the filter and the resulting modification to the morphology.

Linear regression of the percentage change in volume with respect to the initial volume for all regions shows if the degree of clogging is linked to the initial pore volume. Results of this correlation are presented in Table 3.11 and Figure 3.17.

Table 3.11. Correlation between initial volume of each region and percentage change in volume for each scan. A steep gradient (either positive or negative) equals a strong trend whilst the smaller the P value, the more significant the correlation.

Scans	All regions	
	Gradient	P Value
L1C-L3C	-1.7×10^{-5}	3.98E-18
H1C-H2C	-1.6×10^{-5}	6.94E-64
H1C-H3C	-1.5×10^{-5}	1.81E-27
H2C-H3C	-7.0×10^{-6}	5.45E-10
H3C-H4E	-1.2×10^{-3}	5.07E-05
H4E-H5E	1.2×10^{-5}	2.24E-22

Note that P values are not directly comparable with the slice-by-slice approach because there were 1170 regions compared with 179 slices and, with this type of statistical test, a greater number of data points always results in lower P value. The 3D region method was considered more successful than the slice-by-slice approach as measurements were not averaged over an entire slice, but were instead averaged over a far smaller volume.

Table 3.11 and Figure 3.17 show negative correlation between initial pore volume and percentage change in pore volume for each region indicating greater relative clogging of small pores. The correlation is most statistically significant in the first stage of clogging at high flows (H1C-H2C). This may be evidence that preferential flow paths exist in the larger pores and are more pronounced at higher flows. During the second stage of clogging the trend is weaker and less statistically significant suggesting that, as kaolin is deposited within the filter, the preferential flow paths are altered.

During erosion, the negative correlation between initial pore volume and change in pore volume weakens (H3C-H4E) and finally reverses (H4E-H5E). This is further evidence that the erosion process is not simply the reverse of deposition.

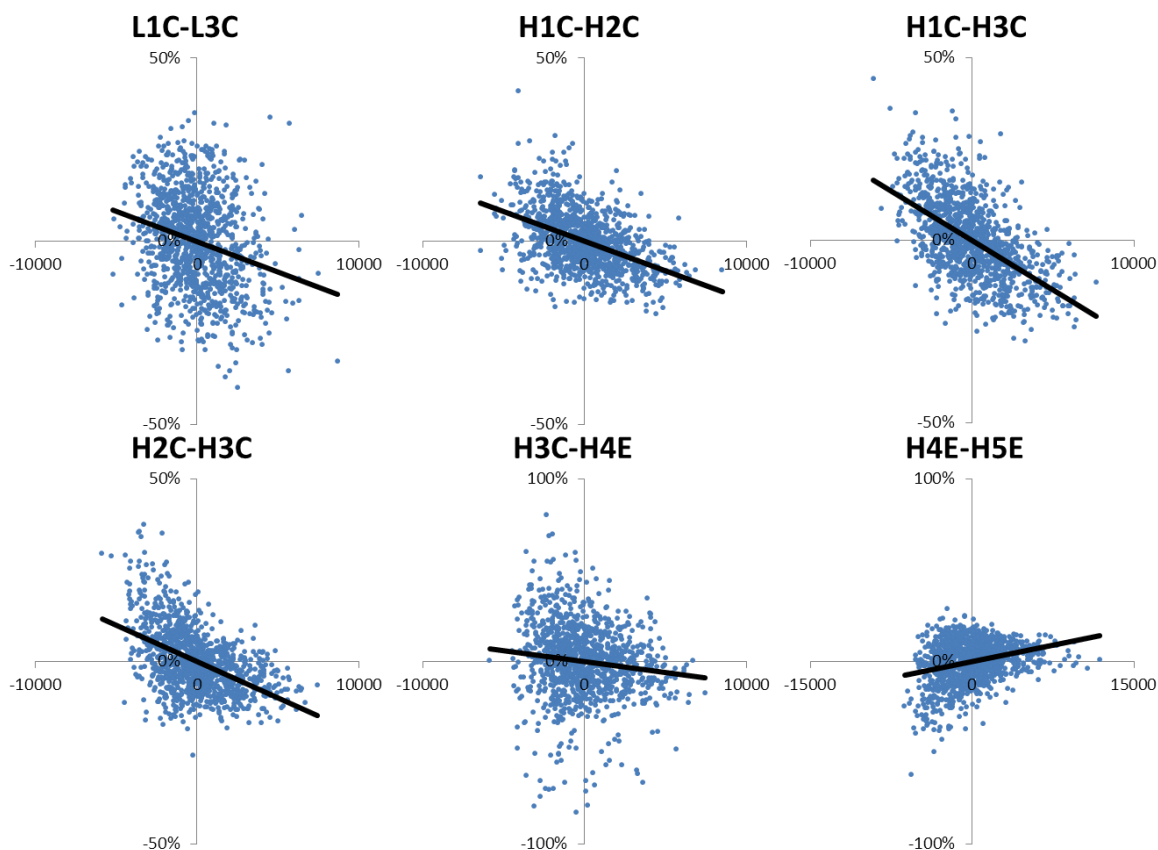


Figure 3.17. Relationship between initial region volume (x-axis) and percentage change in region volume (y-axis) for all 1170 regions, both normalised by average initial volume and average percentage change respectively. Positive gradient denotes correlation between large initial volumes and large percentage changes in volume, as well as between small initial volumes with small percentage changes in volume. For a negative gradient, the inverse is true whilst zero gradient or a large P number denotes no statistically significant correlation. Associated gradients and P values shown in Table 3.11.

3.6.4 Summary of Experimental Data

In summary, the above data set can be distilled into the following findings which warrant detailed discussion in Section 3.7 (or Chapter 4 and Chapter 5, where highlighted); these include:

- MRI data is appropriate to porosity analysis. Clean gravel filters indicate variability in porosity of $\sim 2.0\%$ due to irregular packing arrangements of the sediment. Pixilation of grain boundaries was calculated to contribute up to a maximum of $\pm 3.81\%$ error in porosity.
- Porosity reduced by 58.5% and 39.5% within the ROI of the low flow and high flow experiments respectively. Active surface area reduced by 35.45% and 18.79% for low flow and high flow whilst number of pore regions increased by 786% and 90% respectively.
- Longitudinal (Z plane) deposition patterns during clogging indicate: (i) greater deposition in near-inlet locations under low flow conditions; and, (ii) more evenly distributed deposition along the filter length under high flow conditions.
- Vertical (Y plane) deposition patterns relate to flow conditions, in that higher flow rates distribute kaolin at all depths within the filter, whilst lower flow rates result in greater deposition at the base.
- Lateral (X plane) trends show slight preference towards preferential flow on the right of the columns; this is thought to be experiment-specific to the gravel packing used in the present thesis and is discussed in the flow modelling section of Chapter 5. It is important to note that this was not considered to be indicative of upscaling to roughing filter or SuDS filter processes.
- Change in porosity was correlated with initial porosity: greater percentage change in smaller pores.
- Flushing flows only reinstate $\sim 2\%$ of porosity in the filter.
- Under flushing flows, the erosion process of re-entraining and redistributing kaolin deposits is not the inverse of the sedimentation process. Instead, it indicates a

notable change to the vertical distribution of sediment, via the avalanching of sediment to lower regions of the filter. No longitudinal (Z plane) changes are observed. This process is not a function of initial porosity, rather related to the pore geometry and connectivity at the onset of flushing and is further investigated in Chapter 4.

3.7 Discussion

Key points that will be covered in this discussion are: use of MRI as a tool for characterising deposition within a gravel SuDS or water treatment filter; a critical review of the image processing methodology; and implications of the trends in filter clogging based on bulk analysis of porosity, slice-by-slice analysis and 3D region analysis.

3.7.1 Suitability of MRI

One aim of this chapter was to determine if MRI is a suitable technique for analysing the change in porosity of a gravel filter as it clogs with fine material such as kaolin. This chapter has clearly shown the technique viable and of merit in 2D and 3D analysis, but requires the user to be aware of certain limitations when conducting analysis. A brief description of each limitation and the implications for the experiment design are given:

1. The sample must contain free protons to generate a signal. As such, only the fluid in the columns generated a signal and it was not possible to differentiate between the dolomite gravel, the settled kaolin and any air pockets within the column. Care was taken when filling the column to ensure air pockets were not introduced and markers were cut in to the plastic mesh within the scan ROI so that each scan could be aligned in 3D with the previous scan. By subtracting the volume of the filter from which there was no signal in the clean gravel scan from the volume of no signal in the clogged scan, it was possible to determine the volume of settled kaolin. This procedure is only valid provided the gravel does not alter position during or between scans. Great care was taken to very gently insert and remove the column from the MRI machine. The success of this method can be verified from analysis of the resulting scans: there were no regions that imaged as gravel/kaolin

in the first scan and water in the 1st or 2nd stage clogging scan showing that there was no discernible movement of gravel.

2. Only samples with low metal content can be imaged at high field strengths. Samples that contain magnetic or paramagnetic elements disrupt the MR signal making some natural geological materials unsuitable (Chen et al., 2006). As a result, dolomite gravel with a very low metal content was used as the filter media and the column was constructed entirely of plastic with nylon securing bolts. The resulting MR image was free from magnetic and paramagnetic distortions.
3. Duration of the scan acquisition is directly related to scan resolution and scan volume (Haynes et al., 2009). The RARE scan sequence employed in this study took 20 hours at a resolution of 300 μ m. Often a compromise will need to be made between scan resolution and scan volume to suit the length of time the MRI machine is available. Scans documented herein were initiated on a Friday afternoon and allowed to run over the weekend when the MRI facility is not normally fully utilised.
4. High field strength MRI machines are rare and more typically used for biomedical research. The RF coil used in this study is termed the “rabbit coil” as it was designed and tuned for scanning rabbits. With the initial setup, it was found that the signal arising from the water was greater than the maximum the rabbit coil could be tuned to. Rather than construct a new, smaller column or send the RF coil to the manufacturer for modification, we chose to fill the inlet and outlet mixing areas of the existing column with large round glass beads so as to reduce the volume of water and allow the existing RF coil to be tuned. Not only must suitable hardware be available but also the expertise to create custom MRI sequences applicable to porous media research is required. Fortunately this was available at the GEMRIC facility.
5. MR signal intensity and image quality varies across the scan volume, particularly when working close to the maximum scan volume. This resulted in a maximum good quality scan volume 282 voxels in diameter and 211 voxels deep out of an original scan volume of 333 x 433 x 600 voxels. Much of this reduction was due to gradient non-linearity and the rounded distortion at the extremities of the image in the along-bore direction. Similar distortion has been corrected for by Jovicich et al.

(2006) for work on human imaging, allowing the good quality scan volume to be extended, but requires the use of a special MRI phantom to characterise the degree of distortion which is specific to each MRI machine. The reduced scan volume used in this study was still sufficient to analyse the spatial variation in clogging within the filter.

Taking into account these limitations imposed by the nature of magnetic resonance imaging, it was possible to obtain a 3D image of sufficient size and resolution to define the pore space within a gravel filter and, with successive scans, measure the spatial variation in particle accumulation within that filter. Furthermore, although it was not implemented in this study, it is technically feasible to couple this pore volume measurement with tracer studies that allow the imaging of flow paths and flow velocities.

Whilst the image resolution of $300\mu\text{m}$ is coarse compared with x-ray microtomography which can resolve features as small as $5\mu\text{m}$ (with synchrotron radiation), x-ray microtomography is limited by the size of sample that can be scanned (e.g. a core 6.35mm in diameter and 5.67mm long in the case of Iassonov et al. (2009)). In porous media research this limits the use of x-ray microtomography to soils and sands. Medical x-ray CT scanners do allow larger sample sizes and could be of use to gravel filters, but do not offer the ability to measure tracer propagation (Werth et al., 2010). PET (positron emission tomography) and SPECT (single photon emission computed tomography) scanners can measure both volumes large enough to be relevant to gravel filter research and the propagation of a radioactive tracer, but current state-of-the-art systems are limited to resolutions in the order of millimetres (Boutchko et al., 2012).

As such, we can conclude that MRI is a very valuable tool for measuring the change in hydraulics of gravel filters (and indeed many other types of porous media) as they clog with particles.

3.7.2 Image Processing

Whilst the raw data output from the MRI acquisition was suitable for visualising the change in pore volume with clogging, substantial image processing was then required to

transform the raw data into a state suitable for quantitative analysis. Much of this processing was concerned with removing “noise” from the raw data and counteracting the variation in water signal intensity across the ROI so as to allow binary segmentation into water phase and solid phase. The present thesis developed a robust methodology for assessing the output of processed data using four measures of quality: visual, bulk porosity comparison of MRI and experimental data, mesh representation, and direction dependent errors. By ensuring good results for each measure of quality, we can be reasonably confident that the image processing and segmentation produces a pore volume that accurately represented both the structure of the sample and the porosity to within 1.75% (based on the corrected average bulk porosity measurement).

The method developed in this chapter was considered an improvement over the methods commonly reported in the literature for analysing porous media MRI data such as Baldwin et al. (1996), Amitay-Rosen et al. (2005), Kleinhans et al. (2008), Haynes et al. (2009), and Haynes et al. (2012) to name a few, as these studies have several deficiencies:

1. They use global segmentation methods that cannot account for variations in water signal intensity and which, based on the data collected in this thesis, would have limited the volume that could be segmented as well as introducing errors in the pore regions (e.g. over-segmentation in some regions and under-segmentation in others).
2. They generally do not compare the MRI derived porosity to an independently measured porosity and, where they do, our bulk porosity error of 1.75% is very similar or better. Kleinhans et al. (2008) do make a comparison with estimated porosity based on geometrical models of spherical bead packing with errors ranging from -1.7% to +1%, depending upon bead size(s). Haynes et al. (2012) used a laser scanner to measure the surface of a gravel bed and found 1.3% difference in porosity of 2D slices compared to the MRI derived porosity for the same region, although if the error is due to pixels on the interface between gravel and water, then this error is likely to be larger when considered in 3D and fully within the gravel bed rather than on the surface.
3. They all process the data entirely in 2D and do not consider 3D processing direction dependent errors which, in this study, were found to be significant: a

range in porosity of 2.20% was found when processing entirely in 2D which was reduced to 0.75% with the addition of 3D processing steps.

4. Whilst they all recognise the importance of edge errors, none quantify them with the exception of Haynes et al. (2012) in which the influence of edge errors was determined by varying the thresholding value by ± 5 bins (out of 255) resulting in a porosity change of up to 1.9%. In this thesis, the uncertainty due to the edge errors was quantified based on the plastic mesh and estimated to be $\pm 0.3648 \text{ pixels}^2$ for each pixel of interface between gravel and water. This translates into a maximum error in the segmented image porosity of $\pm 3.81\%$ in the clean gravel scans. Clogged scans were expected to have a lower uncertainty due to the reduced interface between gravel and water (measured as a reduced pore surface area, Table 3.6, Section 3.6.1) resulting in an uncertainty of $\pm 2.64\%$ for the low flow experiment and $\pm 3.13\%$ for the high flow experiment.

In this regards, the method adopted in this chapter has more in common with those used in the field of x-ray and micro-CT data acquisition where the importance of 3D and locally adaptive processing techniques are recognised (Elliot & Heck, 2007; Iassonov et al., 2009), although edge effects are reduced in micro-CT due to the higher resolution of features and more homogenous signal intensity.

Scan resolution could have been increased slightly by extending the scan time or by utilising a smaller RF coil and the processing method could be adapted to include a step to offset the edge error (such as 3D morphological erosion). However, using a smaller RF coil would require a new, smaller column and subsequently, a greatly decreased scan volume whilst increasing the resolution with the current coil may allow the resolution to be increased from $300\mu\text{m}$ to $200\mu\text{m}$, but this would require increasing the scan acquisition time from 20 hours to a predicted 70 hours to scan the same volume and would greatly increase the time to perform each subsequent image processing step.

3.7.3 Results Discussion

The change in porosity as the filters clog and erode were measured by MRI on three levels: bulk properties of the entire ROI, a slice-by-slice analysis of the ROI in three planes and

by dividing the ROI into regularly spaced regions and measuring the change in porosity in each region. Each method has its advantages and limitations.

3.7.3.1 Bulk Properties

Bulk properties are quick and straightforward to measure and allow comparison with the experimentally measured bulk porosity. This can be useful for measuring the overall change in the filter and essential for validating the image processing, but it does not provide any information on the spatial variation of the change in porosity.

The image processing method was chosen to ensure that the MRI derived bulk porosity for Scan L1C (low flow clean) closely matched the experimentally derived porosity (Table 3.6), yet the Scan H1C (high flow, clean) porosities were also extremely close, showing that this method is generically applicable for similar clean gravels. MRI derived porosities for clogged scans were substantially different from the estimated bulk porosity (based on a mass balance approach). This was attributed to greater clogging within the MRI ROI (which is closer to the inlet) than at the outlet.

Other bulk parameters that were measured were the number of regions and the surface area. Whilst pores in disconnected regions are still filled with water, they are not available for further kaolin deposition or the attachment and removal of other pollutants. It should be noted that some regions that appear disconnected may in fact be connected by paths smaller than the image resolution of 300 μm or be linked by areas that may have been incorrectly segmented such as those between grains in close proximity. Nevertheless, the number of regions allows an estimate of the active porosity which is important for filter hydraulics and particle removal efficiency.

In the low flow experiment, the total amount of kaolin removed was 1.5 times greater than in the high flow experiment whereas the change in pore volume associated with disconnected regions was 5.4 times greater. This suggests that, at lower flows, there is a disproportionate increase in disconnected regions and a decrease in active porosity. As such, clogging at higher flow velocities may make more efficient use of the pore volume available for kaolin storage. However, as the disconnected pore volumes are only 0.53%

and 0.13% of the total pore volume in the low and high flow experiments respectively, this increased storage volume is likely offset by other factors such as a reduced removal efficiency resulting in the net decrease in removal efficiency observed in experiments.

In low flow clogging experiments, surface area decreases by 30.8% and active surface area (the surface area of the active porosity) by 35.5%. After two weeks clogging at high flow, the decrease in surface area and active surface area is only 17.8% and 18.8% respectively. For the removal of pollutants such as pollutant metals, there must be an available surface site for adsorption. It has been shown that sand filters often go through a period of filter ripening in which the removal of particles either increases the surface area of the filter or creates conditions under which the removal of subsequent pollutants becomes more favourable in a process known as “filter ripening” (Bradford et al., 2003). If a ripening period occurred in this study, it had passed by the time of the clogged scans. The implication of this reduction in surface area is a reduction in the removal efficiency of dissolved pollutants. This is due to a reduction in the surface area available for adsorption and would be expected to be more pronounced in the low flow experiment. Removal of dissolved pollutants is also linked to removal of particulates, especially clays, as these provide a surface for adsorption. Coupling a decrease in surface area, a decrease in particle removal efficiency and a decrease in filter residence time leads to a further reduction in the removal efficiency of dissolved pollutants with clogging of the filter.

3.7.3.2 Slice-by-slice Analysis

Slice-by-slice analysis is also straightforward but allows some spatial variation in deposition to be observed as well as correlation between initial porosity and change in porosity. MRI was able to confirm there was greater deposition at the column inlet and at the base of the column. This shows direct evidence for what could only be inferred from the difference in bulk porosity between the estimated porosity and the MRI derived porosity (Section 3.6.1). The right sides of the columns showed increased clogging which was unexpected. Possibly this is due to the formation of high velocity preferential flow paths in the left side of the columns.

Iwasaki et al. (1937) and many subsequent studies considered particle removal within slow sand filters as a first-order process with depth into the filter. It therefore follows that the reduction in porosity of a filter due to kaolin accumulation should also be a first-order process with depth. To test if this was apparent in the MRI dataset, both linear and logarithmic trends were fitted to the Z-direction slice averaged porosity. The regression coefficients appear to show that a linear trend better fits the data. The kaolin mass balance (summarised in Table 3.12) shows that in the entire 200mm filter, 1.53 times more kaolin was deposited between scans H1C-H2C than between H2C-H3C, yet the porosity change within the MRI ROI was 2.36 times as great and the slope (change in gradient between scans) was 70 times as steep. Between scans H1C-H2C, more of the kaolin deposition occurred at the inlet resulting in the steeper gradient. Between scans H2C-H3C, a substantial amount of kaolin was retained within the filter, but the low porosity change signifies it was not retained within the ROI and the low slope signifies that what kaolin was retained within the ROI was retained closer to the outlet.

Table 3.12. Summary of clogging in high flow experiment. Accumulated kaolin was calculated by mass balance and is for entire 200mm column (see Table 3.1). Change in porosity was derived from the MRI scan for the 63.3mm deep ROI (see Table 3.6). Slope is the change in gradient of average porosity of each slice from inlet to outlet (see Figure 3.14). Ratio is the ratio of the H1C-H2C value to the H2C-H3C value.

Scans	Accumulated Kaolin (g)	Change in Porosity (%)	Slope
H1C-H2C	54.24	11.39	-1.4×10^{-4}
H2C-H3C	35.46	4.83	-2.0×10^{-6}
Ratio	1.53	2.36	70

These MRI scans would appear to suggest that kaolin removal within these filters was not a first-order process, as was proposed by Iwasaki et al. (1937), adopted by later researchers such as Yao et al. (1971) and observed by Close et al. (2006) when monitoring the removal efficiency of colloidal microsphere at low concentrations in a clean gravel media. Criticism of the first-order removal of particles with depth have been made before (Amirtharajah, 1988; Wegelin et al., 1987) and it has long been recognised that removal efficiency must also be a function of the specific deposit (the volume of sediment accumulated per unit of

pore volume): increasing initially in a process known as filter ripening, presumably due to the increase in surface area for attachment or reduction in pore throats promoting straining (Herzig et al., 1970); then decreasing, presumably as flow velocities increase or suitable attachment sites are saturated until particle breakthrough and the end of the filter run.

As the first-order process view does not take into account changes in removal efficiency over time associated with filter ripening and increased velocities due to clogging, perhaps it can best be thought of as a first-order process zone that diminishes as the degree of clogging exceeds a threshold resulting in a clogging front that moves from inlet to outlet. Ahsan (1995) inferred a similar clogging front from headloss measurements along a filter's length. As shown in Table 3.12, if a clogging front exists, then by the time of scan H3C it has progressed beyond the extent of the ROI.

By correlating the initial porosity with the percentage change (i.e. normalized to the initial porosity) it was shown that slices with a low initial porosity clogged more (in percentage terms) than slices with a high initial porosity. In other words, the low porosity slices were filling quicker. This suggests that areas in slices with a high initial porosity were becoming preferential pathways for kaolin transport, in which less deposition takes place due to the higher velocities. A limitation of the slice-by-slice approach is that it is not possible to identify the preferential pathways and their existence is muted, or indeed entirely masked, by the averaging effect of considering an entire slice that must contain a number of pores of differing initial diameter.

3.7.3.3 3D Region Analysis

The strength of the 3D region analysis is that regions of any size and spacing can be specified so as to capture the spatial variability in porosity and change in porosity. As with the slice-by-slice approach, it is possible to measure trends in the change in porosity both spatially and with respect to the initial porosity with similar results. However, the 3D regions approach is superior as measurements are averaged over a much smaller volume than with the slice-by-slice approach.

With the 3D region approach, spatial variations in kaolin deposition trends were identified for both the low flow and high flow experiment. Correlating region initial porosity with change in region porosity identified that preferential flow paths must play a role in kaolin deposition within the filter. Such preferential flow paths require further analysis with respect to pore network connectivity (Chapter 4) and pore network flow velocities (Chapter 5) in order to characterise their relative importance to particle removal within gravel filters.

3.7.3.4 Comparison of Analysis Methods

Of the three analysis methods investigated in this chapter, the slice-by-slice approach is by far the most common method of analysing MRI data. This appears to be for several reasons:

1. Conventionally MRI is used in a medical setting where 2D slices in each orthogonal plane are sufficient for medical diagnosis; hence MRI software is designed to provide these slices.
2. The acquisition of multiple 2D slices at discrete locations along a sample are sufficient to describe, for instance, the average porosity of a column packed with polystyrene beads as shown by Amitay-Rosen et al. (2005) or a sandstone core (Sham et al., 2013).
3. 2D slices are much quicker to acquire than full 3D volume. This often means that image resolution does not have to be sacrificed to complete a scan within the available time and that multiple scans can be taken in quick succession. This allowed Baumann & Werth (2005) to image the concentration of super-paramagnetic colloids in a single longitudinal slice through a 10mm diameter, 75mm long column filled with silica gel media at three minute intervals, and for Phoenix et al. (2008) to track copper diffusion through a biofilm.
4. Finally, although a 3D image of the entire volume is collected, many authors, such as Sederman et al. (1998), Kleinhans et al. (2008) and Jelinkova et al. (2011) only use the 3D data to visualise the sample. For quantitative analysis they instead reduce the sample to a series of 2D slices, as was done in the slice-by-slice approach of Section 3.6.2.

Bulk porosity and pore volume measurements are rarer for MRI data because, as detailed above, 2D slice data is often collected in place on the full volume 3D scan. Kleinhans et al. (2008) used a 100% water reference sample and the strength of the MR signal to measure the bulk porosity of coarse sediments. In certain situations this method would be preferable to the method of determining bulk porosity used in this thesis as it does not rely on segmenting the data (which is a potential source of error). However, the authors noted that, each time a scan was initialised, the MRI software selects different initialisation settings depending upon the properties of the sample being measured (e.g. liquid volume). In order to get a consistent MR signal from a given volume of water, they had to “trick” the scanner into using the same initialisation settings by initialising a scan on the 100% water reference sample, then scanning all samples in succession without re-initialising. Such an approach was not feasible for this thesis as a week between scans was required to clog the gravel media and other researchers would need to use the MRI machine in the meantime.

Bulk porosity and pore volume measurements were made from x-ray microtomography data of soils and porous asphalt by Munkholm et al. (2012) and Gruber et al. (2012) respectively. Munkholm et al. (2012) also measured surface area but did not distinguish it from active surface area, possibly because with their resolution of 20 μm , it was not possible to identify small pores that would connect regions of the soil. Gruber et al. (2012) did make the distinction between porosity and active porosity and found the latter to be 30% smaller. This is far greater than the 0.53% and 0.15% difference between porosity and active porosity of low flow and high flow experiments of this thesis, but this discrepancy is likely due to the graded gravel and bitumen disconnecting pore regions in the asphalt and highlights the importance of measuring active porosity as opposed to simply measuring porosity.

Pore networks are sometime derived and used to describe 3D trends in the data (see Chapter 4), but no method as simple and straightforward to implement as the 3D regions method was identified in the literature. The “best” data analysis method will depend on the purpose of the study and the equipment available. For many studies, 2D slice data is sufficient and is often the easiest to acquire. However, for this study a combination of bulk properties of the entire 3D volume and 3D region analysis yielded the most beneficial data as it allowed the change in active porosity and surface area to be determined as well as the

3D spatial variation in clogging (without averaging across an entire slice which masks the importance of preferential flow paths) and the correlation between degree of clogging of a region with that regions location and initial porosity.

3.8 Conclusions

In this chapter we have shown that MRI is a suitable tool for monitoring porosity change within a gravel filter. With the image processing methodology developed, it was possible to reproduce experimentally measured porosities to within 1.75% over a region of interest 84.9mm diameter and 63.3mm length.

Analysis of the bulk change in pore volume showed flow rate affected clogging progression: more kaolin was removed at a lower flow rate but the reduction in active porosity per unit of kaolin was greater due to the formation of disconnected regions of pore volume. Surface area decreased with clogging from which we can infer reduced dissolved pollutant removal efficiency.

Slice-by-slice analysis of the 3D volume showed that whilst there was increased kaolin deposition closer to the inlet of both high and low flow rate filters, a linear trend better fitted the data than the first-order trend proposed by Iwasaki et al. (1937). Between the first and second stages of clogging at high flows there was no trend in the change in deposition within the MRI region of interest. From this it was concluded that if removal is a first-order process, this can only be during clean bed filtration supporting the definition of a mobile first-order process zone proposed by (Ahsan, 1995). By the first stage of clogging at high flows the front of the first-order process zone had passed outwith the MRI region of interest.

The correlation between initial pore volume and percentage change in pore volume showed that small pores are more likely to clog with kaolin whilst large pores are more likely to form preferential flow paths with reduced clogging. This important finding of the role of preferential flow paths is investigated further in Chapter 4 and Chapter 5.

Chapter 4 – Pore Network Analysis

4.1 Abstract

In this chapter pore networks are derived from 3D topological data using the ImageJ plugin BoneJ to perform medial axis thinning, as appropriate to quantitative analysis. The topological data was collected by MRI scanning of a gravel media filter at progressive stages of clogging with kaolin clay, as detailed in Chapter 3. Network statistics such as connectivity density were calculated at each stage of kaolin deposition. A method by which the change in pore diameter between scans could be mapped onto the pore network was devised by defining common reference points between clean and clogged filter networks. This allowed spatial variation in pore diameter change along the pore network to be assessed. This methodology also allowed other data sources such as the change in velocity derived from numerical models (Chapter 5) to be mapped onto the pore network.

4.2 Introduction

Slice-by-slice and 3D region analysis of the kaolin deposition patterns within the gravel filter highlights spatial trends and variations in the data (Chapter 3), but information on the pore connectivity is lost with these methods. Pore connectivity is critical for determining the hydrodynamics of the filter (Lindquist & Venkatarangan, 2000; Peth, 2010) and hence for the spatial variation in kaolin deposition. To obtain data in a form conducive to analysis retaining connectivity, it is common to reduce the pore network to a skeleton; this has precedent from studies in soils (Vogel & Roth, 2001; Peth et al., 2008; Luo et al., 2010), in permeable rocks (Lindquist & Venkatarangan, 2000; Blunt et al., 2013) and even for medical applications such as quantifying the effects of osteoporosis in bones (Cooper et al., 2003).

The aims of this chapter were to identify and apply an appropriate pore network skeletonisation algorithm, compare pore network connectivity for each MRI scan of the clogging filters and develop a method by which the change in pore diameter – and hence clogging – at each point in the network could be measured.

4.3 Pore Network Analysis

A pore network skeleton consists of the two elements: a series of connected points which form the *backbone* of the pore between nodes; and the *nodes* where three or more pores meet. Two main methods for determining the pore network skeleton are medial axis trimming and maximal balls; the merit of each is discussed below with the intention of appropriate selection for analysis in the present thesis.

4.3.1 Medial Axis Trimming

Medial axis trimming consists of iteratively eroding the pore space in three dimensions until a single voxel remains. This voxel is the medial axis of the pore space and, if the number of erosive steps is recorded, also contains information on pore diameter. Performing this erosion for all regions in the pore space results in the series of connected medial axes that constitutes the pore backbone, as shown in Figure 4.1. After generating the pore network, ‘pruning’ can be applied to remove dead-end pore paths and short sections of pore network that are often the result of irregularities in the pore geometry (Lindquist & Venkatarangan, 2000).

4.3.2 Maximal Balls

In the maximal balls approach, a sphere centred on each pore space voxel of the image is expanded until it comes into contact with a solid (gravel) region or the image edge. The radius of each sphere is recorded and spheres that are entirely contained within larger spheres are removed. The largest balls represent pore nodes, whilst the smallest balls represent pore throats. This method has been shown to produce a more realistic representation of pore morphology (Silin et al., 2003). Al-Kharusi and Blunt (2007) extended the work of Silin et al. (2003) by including clusters to account for adjacent maximal balls of identical size and extracted pore networks from which absolute permeability could be calculated.

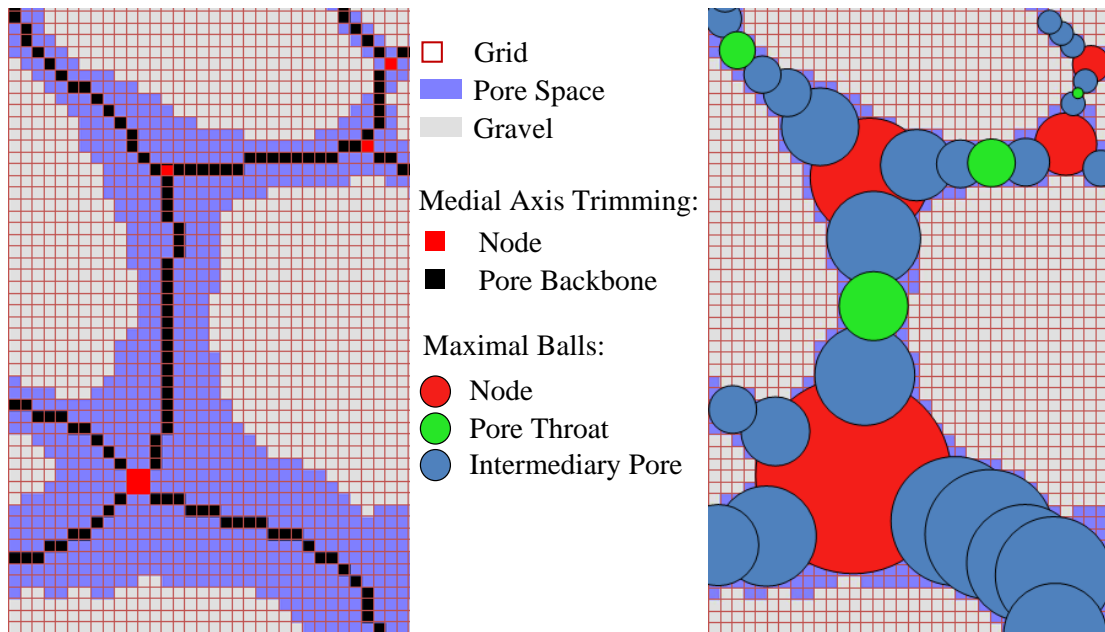


Figure 4.1. 2D example of skeletisation by medial axis trimming (left) and maximal balls (without removal of clusters of identical size, right) for a representative sample of pore geometry derived from the MRI data. Nodal points where three or more pores meet are highlighted in both methods; pore throats are identified in the maximal balls method. N.B. skeletisation is considerably more complicated in 3D than in this 2D representation.

4.3.3 Selection and Implementation of Skeletisation Method

The maximal balls approach is more suited to identifying pore morphology such as pore throat diameters and pore aspect ratio than medial axis trimming, yet the volume that can be processed is limited by the large amount of processing power and computer memory required. For example, the 300 by 300 by 300 voxels of Al-Kharusi & Blunt (2007) could not be analysed as a single section and had to be reduced to a volume 200 by 200 by 200 voxels, despite powerful computing availability. Thus, as the present MRI data set is larger than this (283 by 283 by 211 voxel ROI), the maximal balls methodology would be unsuitable for this thesis. In comparison to maximal balls, the alternative medial axis trimming method, when applied to the MRI data, took a trivial amount of time (25 seconds) to perform on a modern desktop computer. Whilst it may not offer as much information on pore throat sizes as the maximal balls approach, medial axis trimming was used in this study as it has been shown to perform adequately (Keller et al., 2011; Peth et

al., 2008) and, due to ease of implementation, it has become the standard skeletisation procedure in image processing software such as ImageJ.

Medial axis trimming has been implemented in ImageJ in 2D and 3D in the BoneJ plugin (Doube et al., 2010). Originally designed for the analysis of trabecular and cortical changes in bone due to osteoporosis, this implementation of 3D medial axis trimming has since been used by Munkholm et al. (2012) to analyse soil pore networks and, in theory, is applicable to any porous media. The medial axis trimming algorithm used in BoneJ is based on the work of Lee et al. (1994) and a plugin to post-process and analyse the skeleton is also included, developed by Arganda-Carreras et al. (2010). Yet, this skeletisation method does not record the pore diameter along with the medial axis. To overcome this, a Euclidean distance transform with the Local Thickness ImageJ plugin (Dougherty & Kunzelmann, 2007) was used to calculate the thickness of the pore space which was then mapped on to the pore skeleton.

Many studies use the pore skeleton, and morphological characteristics derived from the pore skeleton (such as number of skeleton sections, total skeleton length, number of nodes and connectivity), to compare different samples: for instance different types of rock (Lindquist & Venkatarangan, 2000; Blunt et al., 2013; Al-Kharusi & Blunt, 2007) or different soil samples (Luo et al., 2010; Munkholm et al., 2012). Often the morphological characteristics are then related to physical measurements such as strength or permeability or to inform numerical models of permeability, hydrodynamics and even the spread of microorganisms (Otten et al., 2010). Some papers then go on to use the numerical models to predict how pore network morphological characteristics may change over time (Boever et al., 2012). However, no papers have been identified in which the change in morphological characteristics of a pore skeleton have been measured over time. This is thought to be because analysis of dynamic processes within porous media remain rare due to material properties and associated limitations of equipment/techniques appropriate to taking multiple internal scans of a single sample over time. In this study, multiple scans of two samples at various stages of clogging were obtained by MRI making it possible to measure the change in pore skeletons with clogging, but also necessitating the development of a methodology for analysing this experimental data.

4.4 Methodology

4.4.1 Quality of Pore Network Medial Axis

First, the quality of the medial axis thinning algorithm was assessed for this specific application: determining the skeleton of a 3D MRI scan of 10mm gravel before and after kaolin deposition. The 3D pore space data was re-sliced and the skeleton calculated for each orthogonal plane so as to assess if image stack processing direction affected the resulting skeleton, skeleton properties were analysed and a visual comparison was made with the medial axis thinning algorithm employed in the proprietary software Avizo Fire 7.0 (Visualization Sciences Group, France).

4.4.2 Bulk Properties of Pore Network

Measurements such as connectivity density, number of three connected and four connected nodes (points where three and four branches of the pore network meet), average branch length, average tortuosity and total pore length were made for the entire network. The same measurements were then made for the next scan and it is relatively straightforward to draw comparisons between each scan. Whilst the majority of these measurement terms are self-explanatory, it is worth highlighting that connectivity density is a measure of the number of pore network branch connections per unit volume and is based on the Euler characteristic of the network. As noted by Cooper et al. (2003), connectivity density is preferable to purely topological descriptions of the network, such as number of branches or number of junctions, as it accounts for the number of connections in a given volume. Thus, analysis in the following sections places emphasis on this descriptor.

In this thesis, each “skeleton section” is defined as the medial axis of a distinct pore region (see Chapter 3, Section 3.6.1 for a definition of pore regions). All the pore network branches of a single skeleton section are connected with each other, but are not connected with any other skeleton sections.

4.4.3 Change in Pore Network Properties with Clogging

Measuring the change in pore diameter of the pore network and correlating this with the initial diameter and with the local topography was more complicated than measuring bulk properties of the entire network at a single point in time. This was because, by necessity, the medial axis of a clogged pore network will occupy a different spatial location to the clean pore network. As shown in Figure 4.2, in some areas (A) the only change is in the diameter of the pore network, in others (B & C) the clean and clogged pore networks run in tandem whilst in others (D) the pore space clogs completely hence there is no clogged scan medial axis at this point.

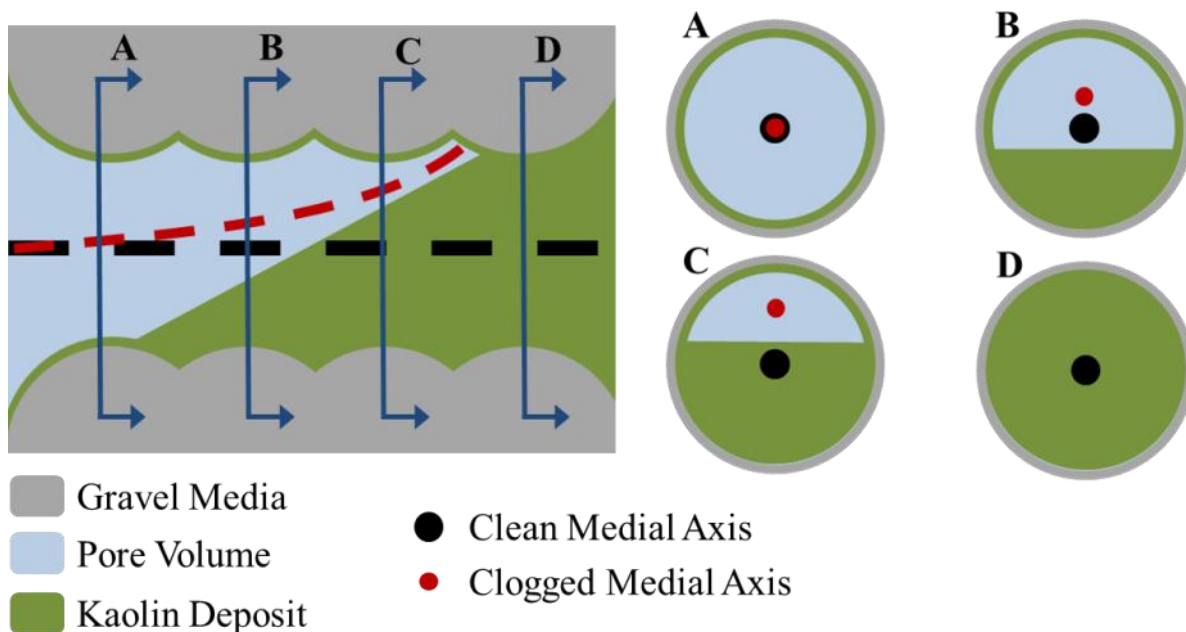


Figure 4.2. Four possible configurations of the medial axes during clogging: A) kaolin deposition is equally distributed around the pore gravel surface resulting in a decreased pore diameter but the medial axis location does not change with clogging; B) kaolin deposition predominantly occurs at the channel base and the medial axis shifts with clogging; C) further deposition at the base means the clean pore medial axis is no longer within the pore region of the clogged MRI scan; and D) the pore is completely clogged with kaolin and so there is no pore space and no clogged medial axis.

To allow comparison between clean and clogged pore networks, the following methodology was developed, tested and validated on a simple representation of the four medial axis configurations (see Figure 4.2), and finally applied to the MRI pore space data:

- A Euclidean distance transform was used to determine the local pore thickness of the clean scan (hereafter referred to as *Clean Scan Thickness*) and clogged scan (*Clogged Scan Thickness*).
- *Clogged Scan Thickness* subtracted from *Clean Scan Thickness* to give *Change in Thickness*. N.B Sometimes negative values arise from this subtraction at the extreme edges of the pores. As they are at the pore edges, they do not affect the pore skeleton and can be removed in ImageJ with the macro code: `if(v < 0) v=0`.
- The skeleton of the clogged scan is calculated using the BoneJ plugin and the skeleton value set to 1. Multiplying the skeleton by *Change in Thickness*, the change in pore thickness was mapped on to each voxel of the skeleton. This correctly identified the change in thickness of regions A, B and C, but not D as there was no region D in the clogged scan (see Figure 4.2 for description of regions A, B, C and D).
- Subtracting the clogged scan pore space from the clean scan pore space gave the volume of kaolin deposition. Calculating the thickness gave the *Kaolin Deposition Thickness*.
- The skeleton of the clean scan was calculated with the skeleton value set to 1, then multiplied by the *Kaolin Deposition Thickness*. This resulted in no value for any voxel in regions A and B, and a value of the kaolin thickness for regions C and D.
- Region C was not required as it already existed on the clogged scan skeleton and should not be duplicated. Dividing the skeleton by the *Clean Scan Thickness* resulted in values less than 1 for region C (as the *Kaolin Deposition Thickness* must be less than the *Clean Scan Thickness* for region C) and values of 1 for region D (as in region D the pore has become completely clogged and so *Kaolin Deposition Thickness* is equal to the *Clean Scan Thickness*). Region C can be removed with the macro script: `if (v < 1) v=0`.

- The change in thickness of region D on the clean scan skeleton can now be reinstated by multiplying by *Change in Thickness*, *Kaolin Deposition Thickness* or *Clean Scan Thickness* as all will give the same result for region D.
- Region D on the clean scan skeleton is added to regions A, B and C from the clogged scan skeleton resulting in the change in thickness for all regions of the pore network.
- Change in thickness was expressed as a percentage change by dividing by the *Clean Scan Thickness*. The change in thickness for region D equals 100% whilst it is between zero and 100% for regions A, B and C.

4.5 Results

4.5.1 Quality of Pore Network Medial Axis

To assess the quality of the medial axis thinning algorithm, visual inspection of the pore space and medial axis was made for a representative subsection (50x50x50 pixels) of MRI scan L1C (Figure 4.3 & Figure 4.4) and a quantitative assessment of the pore network properties of the entire ROI was made (Table 4.1).

As discovered in the MRI image processing of Chapter 3, Section 3.5.3, processing a 3D dataset as a sequence of 2D images can introduce processing direction dependent errors. To determine if the medial axis trimming algorithm of BoneJ is affected by processing direction, the pore space was re-sliced and processed in each of the three orthogonal plains.

The skeletisation algorithm of proprietary software Avizo Fire (VSG, www.vsg3d.com) is also shown for comparison (created during a free trial of the software). The reason for this comparison was that Avizo Fire has been used in numerous studies (Gruber et al., 2012; Luo et al., 2010; Boever et al., 2012; Keller et al., 2011) and appears to be an industry standard for creating a medial axis skeleton of a pore network. Shortcomings of Avizo Fire are that it is not open source and it is designed for visualisation of a pore network rather than for assessing the change in characteristics of a pore network with clogging. As such, the network statistics that Avizo Fire produces are limited to total network length, average skeleton section length and average skeleton section thickness. BoneJ provides more

network statistics, outputs the data in a format more conducive for further analysis and, if it could be shown to be as robust as Avizo Fire, would therefore be the preferred option.

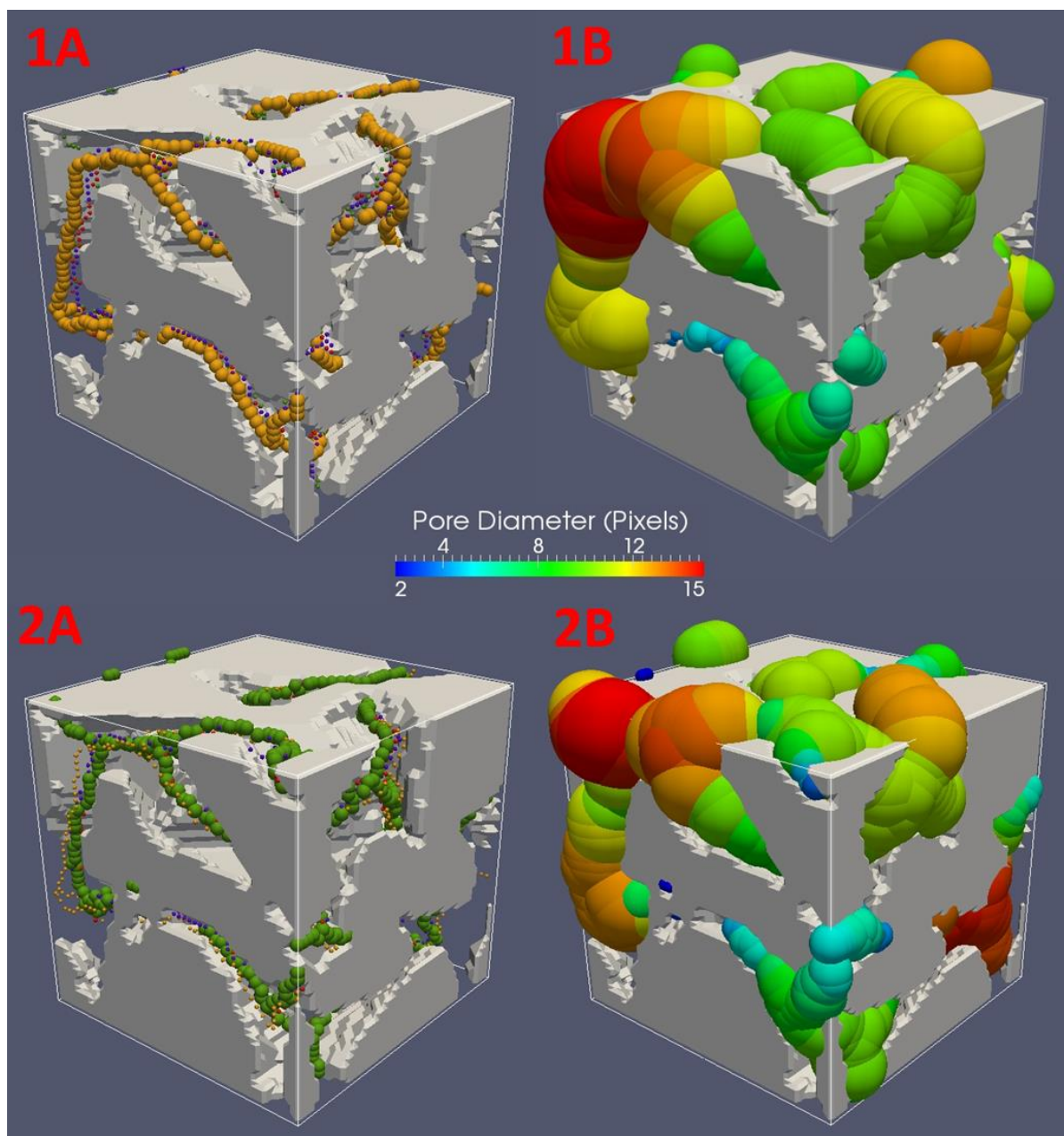


Figure 4.3. Medial axis thinning algorithm applied to a subsection of MRI scan L1C. Grey solid regions represent gravel, pore space is transparent. 1A is the medial axis from the Avizo algorithm whilst 1B is the same medial axis, this time showing pore diameters. 2A is the medial axis from the BoneJ algorithm whilst 2B is the pore diameters with all processing carried out in the Z plane.

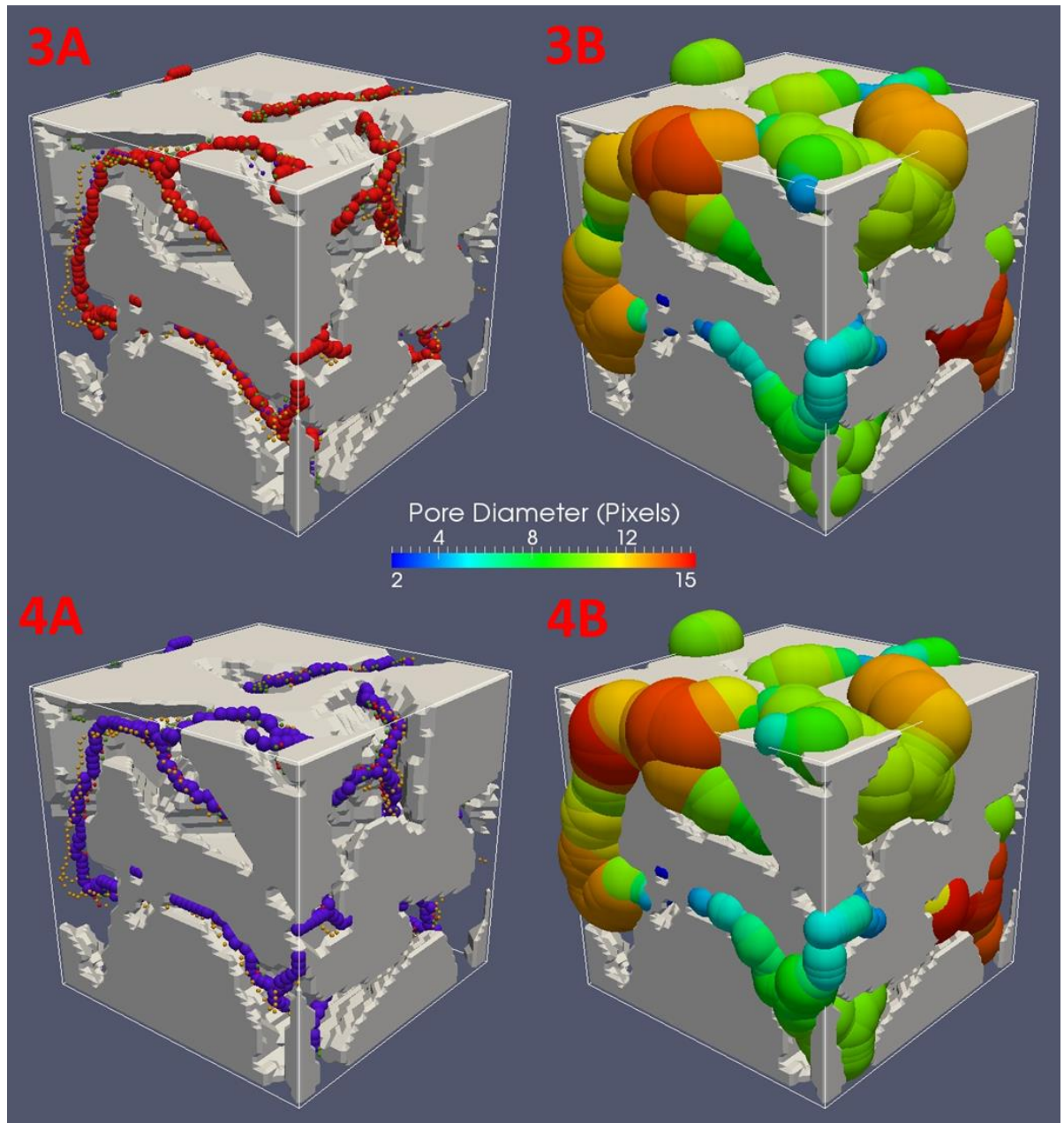


Figure 4.4. Medial axis thinning algorithm applied to a subsection of MRI scan L1C. Grey solid regions represent gravel; pore space is transparent. 3A is the medial axis from the BoneJ algorithm and 3B is the pore diameters processed in the X plane. 4A is the medial axis from the BoneJ algorithm and 4B is the pore diameters processed in the Y plane.

Processing the data in all three orthogonal planes with BoneJ and in the Z plane with Avizo Fire shows that the exact position of the medial axis within the pore is somewhat

influenced by processing direction but the general structure of the network is consistent (Figure 4.3 & Figure 4.4).

Table 4.1 shows that the standard deviation of each pore network parameter between the three orthogonal planes is low. The number of skeleton sections was higher in the Z plane than X and Y planes (14% relative standard deviation) because of the cylindrical shape of the ROI leading to short (mostly two pixel) sections of pore network around the circular edge. The maximum tortuosity also exhibited a high relative standard deviation (6.3%) but, as shown by the much lower relative standard deviation of the average tortuosity (1.2%), this was likely to be due to a small number of outliers.

Table 4.1. Network properties for pore network derived from the entire MRI scan L1C processed in X, Y and Z planes. Medial axis and network properties calculated by BoneJ skeletonize3D and Analyse Skeleton plugins respectively.

		Z Plane	X Plane	Y Plane	Relative st. dev.
Skeleton properties	Number of skeleton sections	201	151	149	14%
	Number of branches	9,733	9,412	9,488	1.44%
	Number of junctions	5,229	5,136	5,196	0.74%
	Number of triple points	3,979	3,910	4,040	1.34%
	Number of quadruple points	882	913	826	4.12%
Branch properties	Average branch length (pixels)	12.24	12.36	12.31	0.38%
	Maximum branch length (pixels)	79.08	72.29	77.26	3.76%
	Total branch length (pixels)	119,140	116,288	116,799	1.06%
	Average tortuosity	1.23	1.26	1.23	1.19%
	Maximum tortuosity	7.86	8.45	7.23	6.34%
Connectivity	Connectivity density	1.46×10^{-4}	1.48×10^{-4}	1.48×10^{-4}	0.75%

The BoneJ medial axis trimming algorithm produced a structurally similar pore network to the industry standard Avizo Fire, output more useful network parameters and produced a network with a low processing direction dependent variation in network parameters. The BoneJ implementation of medial axis trimming was therefore suitable for the task of defining the change in pore network diameter and connectivity as the gravel media clogs with kaolin.

4.5.2 Bulk Properties of Pore Network

Visualising the network (as in Figure 4.5 and Figure 4.6) and describing the bulk network properties (as in Table 4.3, Table 4.4, Table 4.5 and Table 4.5) as they change with clogging is useful for assessing the overall change in the pore network connectivity. Figure 4.5 and Figure 4.6 show the change in pore geometry with clogging. Despite a substantial reduction in porosity from 40.29% to 16.71%, the medial axis remains recognisable although there is a general reduction in the length of the pore network and number of connections with an increase in skeleton sections due to fragmentation of the network.

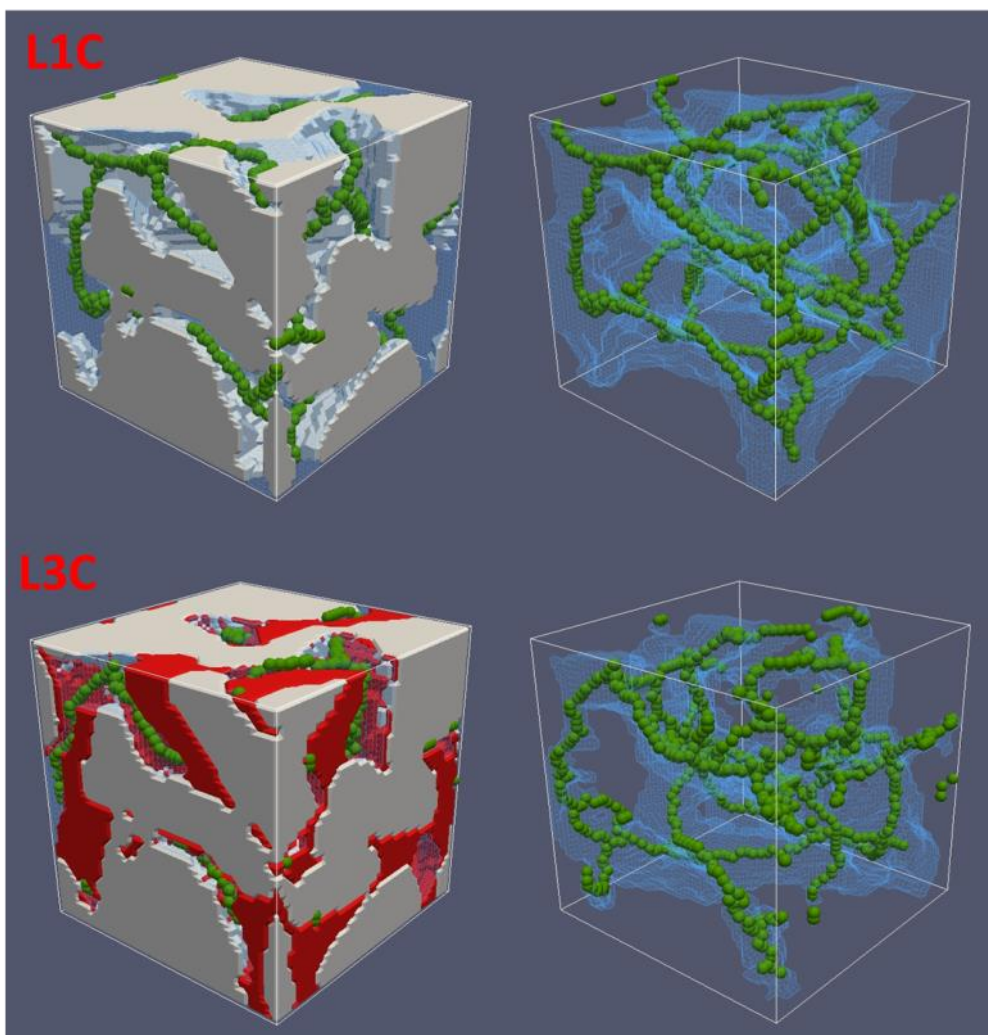


Figure 4.5. Medial axis overlaid on pore space for representative subsection of MRI scan L1C and L3C. Pore networks are shown (green) together with gravel (white), pore space (blue) and kaolin deposition (red).

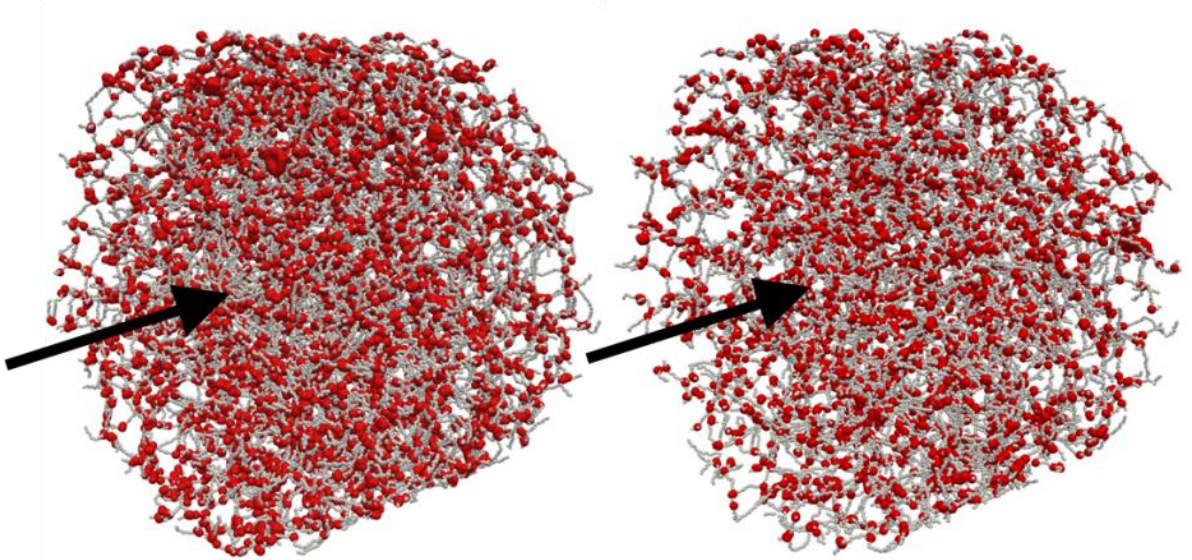


Figure 4.6. Comparison between pore network of scan L1C (left, clean) and L3C (right, clogged). The network medial axis is represented by grey spheres and branch junctions (nodes) by red spheres. Flow direction through the cylindrical MRI ROI is indicated by the black arrows. General trends visible are a reduction in the extent of the pore network and number of junctions with clogging, particularly at the inlet.

Table 4.2 shows pore network descriptors for the clean scans L1C and H1C and the percentage difference between the two. As the two columns were prepared with a standard procedure, the pore network characteristics were similar. Greatest differences are for the measure of maximum branch length and maximum tortuosity, both of which were most likely affected by outliers: a single large or tortuous branch could increase the maximum length or tortuosity without affecting the average. In terms of the main findings of Table 4.2, analysis of the number of skeleton sections and number of branches data showed that the majority of the pore space (98% of the branches) were connected to a single section of the pore network. Additional skeleton sections tended to be small (often a single branch) and, in the clean scans, were the result of an ROI smaller than the entire gravel volume leading to branches cut off from the network outside the ROI. For the clogged scans the increase in skeleton sections represented fragmentation of the pore network due to kaolin deposition. Characteristics such as number of branches and junction connectivity density were based on the single largest section of the pore network. Some parameters were also normalised by the ratio of the pore volume to that of the largest scan pore volume. This allowed, for instance, the number of junctions in scan H1C (which had the largest pore

volume) to be compared with scan L1C (with 98% of the largest pore volume) by prorating the data of L1C against the benchmark volume of H1C.

Table 4.2. Comparison between initial clean scan pore networks for MRI scans L1C and H1C with percentage difference. Columns were prepared with a standard procedure hence the difference in pore network properties was due to the configuration of the gravel particles.

			L1C	H1C	Percentage Difference
Skeleton properties	All sections	Number of skeleton sections	190	226	18.95%
		Number of branches	8,137	7,468	-8.22%
	Largest section	Number of branches	8,015	7,314	-8.75%
		Number of junctions	4,301	3,951	-8.14%
		Number of triple points	3,273	3,056	-6.63%
		Number of quadruple points	720	665	-7.64%
		Connectivity density	1.46×10^{-4}	1.30×10^{-4}	-10.85%
Branch properties	Largest Section	Average branch length (pixels)	12.11	12.19	0.65%
		Maximum branch length (pixels)	79.08	62.93	-20.43%
		Total branch length (pixels)	97,035	89,122	-8.15%
		Average tortuosity	1.24	1.24	-0.11%
		Maximum tortuosity	7.86	11.72	49.10%
Properties normalised by pore volume	Number of skeleton sections		194	226	16.62%
	Number of branches		8175	7314	-10.53%
	Number of junctions		4387	3951	-9.93%
	Total branch length (pixels)		98,970	89,122	-9.95%

In general, similar data provided in Table 4.3 to Table 4.5 indicate that the number of branches, junctions, total branch length and connectivity density associated with the single largest skeleton section decrease with clogging. These values also decrease during erosion. This, together with visual inspection of the pore networks suggests that kaolin deposition was disconnecting pore branches and, as proposed in Chapter 2, section 2.9.3, the high flows of the erosive stages H4E and H5E re-mobilised deposited kaolin in large sections that then drift downwards and were able to clog pores; hence the large decrease in connectivity density during erosion despite there being no more kaolin entering the filter.

Table 4.3. Pore network properties derived from scans L1C and L3C (low flow, clogging) for entire ROI.

			L1C	L3C
Skeleton properties	All sections	Number of skeleton sections	190	1,588
		Number of branches	8,137	8,306
	Largest section	Number of branches	8,015	7,234
		Number of junctions	4,301	3,637
		Number of triple points	3,273	2,724
		Number of quadruple points	720	658
		Connectivity density	1.46×10^{-4}	9.35×10^{-5}
Branch properties	Largest Section	Average branch length (pixels)	12.11	10.63
		Maximum branch length (pixels)	79.08	60.00
		Total branch length (pixels)	97,035	76,910
		Average tortuosity	1.24	1.26
		Maximum tortuosity	7.86	9.09
Properties normalised by pore volume	Number of skeleton sections		194	4031
	Number of branches		8175	18,364
	Number of junctions		4387	9233
	Total branch length (pixels)		98,970	195,246

Table 4.4. Pore network properties derived from scans H1C, H2C and H3C (high flow, clogging) for entire ROI.

			H1C	H2C	H3C
Skeleton properties	All sections	Number of skeleton sections	226	291	517
		Number of branches	7,468	6,238	6,971
	Largest section	Number of branches	7,314	6,021	6,574
		Number of junctions	3,951	3,230	3,389
		Number of triple points	3,056	2,525	2,547
		Number of quadruple points	665	541	593
		Connectivity density	1.30×10^{-4}	9.96×10^{-5}	1.00×10^{-4}
Branch properties	Largest Section	Average branch length (pixels)	12.19	12.46	11.69
		Maximum branch length (pixels)	62.93	56.80	61.92
		Total branch length (pixels)	89,122	75,011	76,844
		Average tortuosity	1.24	1.23	1.26
		Maximum tortuosity	11.72	10.80	13.16
Properties normalised by pore volume	Number of skeleton sections		226	403	858
	Number of branches		7314	8339	10,906
	Number of junctions		3951	4474	5622
	Total branch length (pixels)		89,122	103,894	127,481

Table 4.5. Pore network properties derived from scans H3C, H4E and H5E (high flow, erosion) for entire ROI.

			H3C	H4E	H5E
Skeleton properties	All sections	Number of skeleton sections	517	708	634
		Number of branches	6,971	6,378	6,401
	Largest section	Number of branches	6,574	5,819	5,918
		Number of junctions	3,389	3,003	3,080
		Number of triple points	2,547	2,385	2,441
		Number of quadruple points	593	458	498
		Connectivity density	1.00×10^{-4}	7.59×10^{-5}	8.01×10^{-5}
Branch properties	Largest Section	Average branch length (pixels)	11.69	11.88	12.02
		Maximum branch length (pixels)	61.92	59.61	62.02
		Total branch length (pixels)	76,844	69,110	71,110
		Average tortuosity	1.26	1.24	1.23
		Maximum tortuosity	13.16	18.85	9.41
Properties normalised by pore volume	Number of skeleton sections		858	1158	1021
	Number of branches		10,906	9516	9526
	Number of junctions		5622	4911	4958
	Total branch length (pixels)		127,481	113,022	114,468

4.5.3 Change in Pore Network Properties with Clogging

To view the relationships between the change in pore diameter with the initial pore diameter and X, Y and Z location, the methodology outlined in Section 4.4.3 was employed. When calculating the degree of clogging, it is helpful to convert the pore diameter to a pore volume; this is because a small change in diameter of a large sphere can lead to a larger change in volume than an equivalent change in diameter of a small sphere. Thus, this section focusses upon volume changes as presented by total volume change and percentage volume change.

Figure 4.7 shows that, during the clogging process, there is 1) clearly spatial heterogeneity in particle deposition, even between neighbouring pores, and 2) overall trends in the data with more deposition at the inlet of both the high and low flow filters and substantially more deposition at the base of the low flow filter.

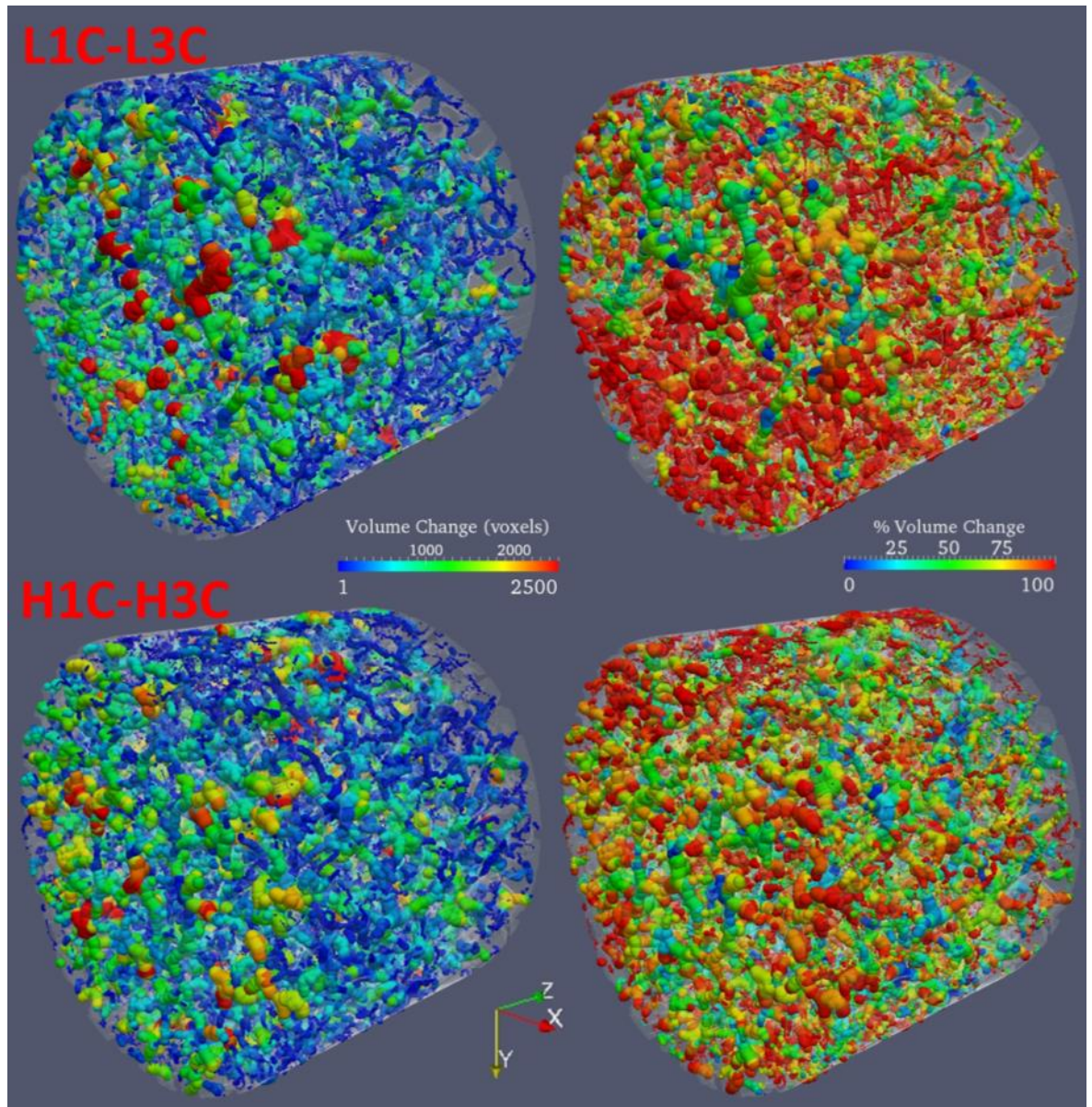


Figure 4.7. Spatial variation in absolute volume change (left) and percentage volume change (right) for the low flow experiment L1C-L3C (top) and high flow H1C-H3C experiment (bottom) for each point in the pore skeleton after two weeks clogging. The diameter of each sphere denotes the initial unclogged pore diameter (at a scale of 0.5 to aid visualisation). N.B. each voxel is $0.3\text{mm} \times 0.3\text{mm} \times 0.3\text{mm}$ hence the volume of one voxel is 0.027mm^3 .

Similar analysis of the erosion scans (Figure 4.8) shows a redistribution of deposited particles within the filter: the degree of clogging increases in some pores, decreases in others and there is a general movement of particles from top to bottom.

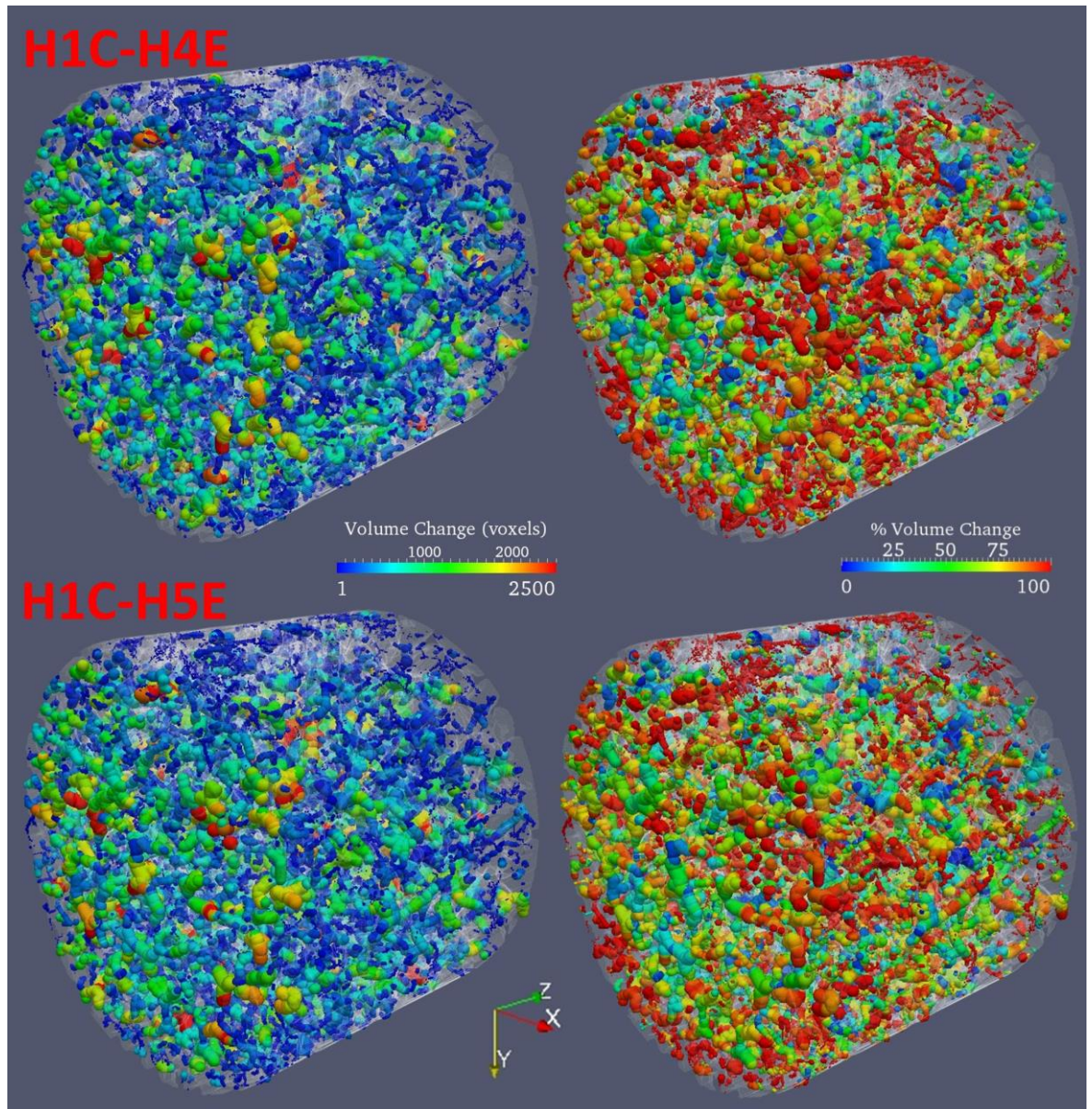


Figure 4.8. Spatial variation in absolute volume change (left) and percentage volume change (right) for the high flow experiment first stage of erosion (H1C-H4E, top) and second stage of erosion (H1C-H5E, bottom) for each point in the pore skeleton. The diameter of each sphere denotes the initial unclogged pore diameter (at a scale of 0.5 to aid visualisation). N.B. each voxel is 0.3mm x 0.3mm x 0.3mm hence the volume of one voxel is 0.027mm³.

General trends in how the pore network was altered by clogging were evident from such visual analysis of the networks; however, a quantitative measure of particle deposition within the network was required. As with the slice-by-slice approach (Chapter 3, Section

3.6.2) and the 3D region porosity (Chapter 3, Section 3.6.3), correlation between the degree of clogging with initial pore volume and spatial location was measured with linear regression. The degree of clogging was measured as a change in volume for each point in the pore skeleton (determined from the pore diameters before and after clogging) and as a percentage change in volume.

Table 4.6. Correlation between volume change of pore network with initial pore volume and spatial location. A steep gradient (either positive or negative) equals a strong trend whilst the smaller the P value, the more significant the correlation.

Correlation of volume change with:		Scans				
		L1C-L3C	H1C-H2C	H1C-H3C	H1C-H4E	H1C-H5E
Initial volume	Gradient	0.641	0.344	0.507	0.480	0.487
	P Value	0.00	0.00	0.00	0.00	0.00
X	Gradient	-0.189	-0.256	-0.356	-0.201	-0.314
	P Value	1.56×10^{-11}	7.68×10^{-29}	1.41×10^{-33}	3.58×10^{-10}	6.43×10^{-22}
Y	Gradient	0.235	-0.125	0.101	0.368	0.405
	P Value	1.35×10^{-17}	3.42×10^{-8}	6.06×10^{-4}	1.18×10^{-28}	7.83×10^{-33}
Z	Gradient	-0.462	-0.908	-0.711	-0.432	-0.424
	P Value	3.96×10^{-48}	1.35×10^{-279}	7.21×10^{-102}	1.30×10^{-32}	1.89×10^{-30}

The positive gradients for the linear regression between volume change and initial volume showed that larger pores have a larger volume change for all scans (Table 4.6). The strongest correlation between volume change and spatial location was in the Z axis (inlet to outlet) for all scans. These gradients were negative, showing that more deposition occurred at the inlet. For scans L1C-L3C, H1C-H4E and H1C-H5E, there was a stronger correlation between the Y axis (top to bottom) than the X axis (left to right) showing more deposition at the bottom than at the top. Scans H1C-H2C and H1C-H3C showed a stronger correlation between the X axis than the Y axis.

Table 4.7. Correlation between percentage volume change of pore network with initial pore volume and spatial location. A steep gradient (either positive or negative) equals a strong trend whilst the smaller the P value, the more significant the correlation.

Correlation of % Volume Change with:		Scans				
		L1C-L3C	H1C-H2C	H1C-H3C	H1C-H4E	H1C-H5E
Initial Volume	Gradient	-0.00007	-0.00012	-0.00008	-0.00011	-0.00011
	P Value	0.00	0.00	0.00	0.00	0.00
X	Gradient	0.00013	0.00016	0.00008	0.00031	0.00010
	P Value	2.01×10^{-31}	4.31×10^{-27}	2.55×10^{-8}	1.88×10^{-78}	1.62×10^{-9}
Y	Gradient	0.00028	-0.00052	-0.00028	-0.00022	-0.00019
	P Value	3.41×10^{-144}	3.20×10^{-280}	2.48×10^{-90}	1.99×10^{-37}	4.32×10^{-28}
Z	Gradient	-0.00041	-0.00055	-0.00049	-0.00049	-0.00036
	P Value	4.23×10^{-228}	2.54×10^{-242}	2.75×10^{-212}	3.84×10^{-150}	9.96×10^{-83}

The negative gradients for the linear regression between percentage volume change and initial volume showed that smaller pores had a larger percentage volume change for all scans (Table 4.7). As with the volume change analysis, percentage volume change had a strong negative correlation with the Z axis showing increased deposition at the inlet. Visually the increased deposition at the inlet was much more apparent for the low than the high flow filter (Figure 4.7); however the linear regression denotes significant correlation at both flow rates.

4.6 Discussion

4.6.1 Quality of Pore Network Medial Axis

Medial axis trimming, implemented in ImageJ by the plugin BoneJ (Doube et al., 2010), is a method for extracting pore network skeletons from 3D topological data. Maximal balls is an alternative method that provides more useful information on the pore network such as the location of pore throats, pore diameter and connections between pores. However, maximal balls is more difficult to implement and more computationally intensive. Al-Kharusi & Blunt (2007) were limited to studying a volume $200 \times 200 \times 200$ pixels and note that their algorithm was not suitable for extracting large networks with standard computer

resources. With advances in computing power since 2007 it is reasonable to assume that the maximal balls approach could have been used in this thesis for the ROI volume 283x283x180 pixels, however medial axis trimming was chosen due to ease of implementation and the ability to extract networks from much larger volumes, should it be required in the future.

One limitation of medial axis trimming – the inability to measure pore size – was overcome by calculating local pore thickness independently using a Euclidean distance transform. The resulting thickness was then mapped onto the medial axis allowing visualisation of the pore space with free visualisation software ParaView (Kitware, www.paraview.org). The accuracy of the resulting pore network was assessed by visual comparison of a 50x50x50 pixel subvolume with proprietary software Avizo Fire which uses a different skeletisation algorithm. Both skeletons were similar, particularly with regards to the main section of the pore network. The primary difference was in the exact placement of pore branch junctions within large and irregular pores (Figure 4.3 and Figure 4.4).

Further analysis of the pore network involved re-slicing the entire MRI data ROI in the three orthogonal planes then calculating the medial axis in each plane. The resulting network characteristics were very similar with respect to connectivity density (0.75% relative standard deviation), total and average branch lengths (1.06%, 0.38%), number of junctions (0.74%) and average tortuosity of each branch (1.19%). Differences were in the number of skeleton sections (14%), maximum branch length and maximum tortuosity (both of which may be the result of a single outlier) and number of quadruple points (4.12%). The range in number of skeleton sections was due to very short sections (often just two voxels) at the circular edge of the scan ROI. These skeleton sections made up a negligible proportion of the total pore network length and did not affect the measure of connectivity density as this was only measured for the single largest skeleton section.

4.6.2 Change in Pore Network Diameter

No studies have been identified which investigate the change in pore network diameter and characteristics over time due to particle deposition. This is thought to be because few

studies take multiple 3D tomographic scans of a single sample over time in which there is a structural change in the pore geometry. Most studies instead compare multiple samples of different soil types (Munkholm et al., 2012), rock cores of different origins (Blunt et al., 2013) or investigate the transport of fluids through a porous network in which the porous media remains unaltered (Pini & Benson, 2013). One exception is the work of Chen et al. (2009) in which the accumulation of zirconia colloids within a spherical glass bead media was characterised over a 1.79mm^3 region ($299 \times 299 \times 299$ voxels) by x-ray microtomography with four successive scans. Lattice Boltzmann modelling of the resulting scan geometry was performed but no network analysis was undertaken. Another notable exception is the work of Amitay-Rosen et al. (2005) in which multiple MRI scans of a clogging filter were taken over time; however analysis of the results was limited to nine 2D sections throughout the volume and hence no pore skeleton or network properties were extracted.

With no precedent found in the literature, it was necessary to develop a methodology for analysing and comparing the change in the pore network with clogging. Different pore networks were compared based on several bulk network characteristics such as connectivity density. These measures were useful for describing change in the networks with clogging. However, as they are a property of the entire network, they do not quantify spatial variability in kaolin deposition and network change, nor do they shed any light on how pollutants are transported through the network.

Establishing the change in pore network diameter at each point in the network can allow quantification of the spatial variability in kaolin deposition throughout the network. This approach required a common reference point between the clean and clogged scan pore networks. As shown in Figure 4.2, the pore network shifts with clogging hence there was no common reference point but each point in the clogged pore network must be in one of four states relative to the original clean pore network. A method for assigning each point of the clogged network into one of the four states was devised (Section 4.4.3). Pore diameter for each point in the clean and clogged pore networks were calculated from a Euclidean distance transform and were mapped onto the assigned pore network allowing the change in diameter to be calculated.

Spatial trends in the absolute and percentage volume changes of each point in the network were analysed as well as correlation between change in volume and initial volume. Results showed that sections of the pore network with a small initial diameter were more likely to experience a high percentage volume change due to kaolin deposition or to clog completely than pores with a high initial porosity.

4.7 Conclusions

The main finding of this chapter was that medial axis pore skeletons derived from sequential 3D tomographic scans of a clogging filter provide useful information on changes in pore structure that can be used to define network connectivity. The medial axis skeleton can also be used as a reference point onto which changes in pore diameter, and hence amount of kaolin deposition can be mapped as well as for comparing changes in velocity derived from numerical modelling (Chapter 5). The assessment of clogging based on the change in pore network characteristics presented in this chapter is preferable to the assessment based purely on change in porosity presented in Chapter 3. This is because the aim of this thesis was to understand the mechanisms resulting in spatial heterogeneity in particle deposition and, from the data presented here, it is apparent that pore network connectivity was an important influence on particle deposition.

Chapter 5 – Numerical Modelling of Flow in MRI Derived Pore Geometry

5.1 Abstract

In this chapter we explore the relationship between flow velocities derived from a numerical model and the spatial variation in kaolin deposition identified in the MRI scans of Chapter 3. A numerical model was directly applied to the pore geometry derived from MRI scans at various stages of clogging. The chosen numerical modelling software was OpenFOAM (OpenFOAM Foundation, www.openfoam.org) which proved to be a suitable tool for generating the computational mesh, solving for Eulerian flow fields and Lagrangian particle tracking.

By evaluating the model output sensitivity to the choice of model configuration and input parameters with a parametric study, the optimum model setup was identified. Results of the model show a close relationship between local velocity and local kaolin deposition with greater deposition in areas of low velocity. Initially pore diameter determines pore velocity and this correlation strengthens with moderate clogging due to positive feedback. At high degrees of clogging the majority of the flow is confined to a few preferential flow paths and at this point pore connectivity appears to be the dominant factor determining velocity rather than pore diameter. This has important implications for particle transport and retention within the filter.

Lagrangian particle tracking of tracer-like particles highlighted a predicted reduction in removal efficiency of both suspended particles and dissolved pollutants as the filter clogs and preferential flow paths form.

5.2 Introduction

Spatial variation in kaolin particle deposition was observed within a clogging gravel filter (Chapter 3). It appeared probable that this spatial variation resulted from spatial variation in flow velocities, which in turn are dependent upon the local pore geometry. As such, flow velocities will vary temporally and feedback between clogging and further deposition must

exist. Understanding flow velocity and how it changes over time is therefore crucial to understanding the pattern of particle deposition within the filter.

Unlike alternative methods for capturing the pore geometry (such as x-ray tomography), MRI offers the capability of measuring fluid flow rates by tracking the progress of a tracer that alters the magnetic susceptibility of the fluid (Baumann & Werth, 2005; Ramanan et al., 2010) or with tailored pulse sequences (Johns et al., 2000; Hingerl, 2013). Suitable tailored pulse sequences have not currently been implemented at the Glasgow Experimental MRI Centre (GEMRIC) and the development of such a sequence was outwith the scope of this PhD. Paramagnetic tracers have been used at GEMRIC but, due to the high demand for time on the MRI machine, logistically it was not possible to incorporate an additional tracer scan prior to each of the 20 hour scans from which the pore geometry was obtained. Thus, this thesis focuses on developing a novel approach towards obtaining indicative flow velocities from numerical modelling of the detailed pore geometry obtained from the snapshot MRI scans reported in Chapter 3. The intention was that this reduces the time and cost outlay compared to that of undertaking further MRI-based examination of fluid flow (by tracer or pulse sequences).

Modelling of pore fluid flow is becoming more common (Blunt et al., 2013), particularly by the oil and gas industry and in the field of carbon capture and storage. Modelling approaches often applied are based on permeability (Hingerl, 2013), pore network models (Kress et al., 2012), lattice Boltzman simulations (Ahrenholz, 2008; Papafotiou et al., 2008; Chen et al., 2009) and finite element/volume methods (also known as direct modelling) with software such as COMSOL Multiphysics (Narsilio et al., 2010), ANSYS-CFX (Gruber et al., 2012) and similar packages. Yet studies modelling the temporal change in flow velocities resulting from particle deposition are rare: only the work of Chen et al. (2009) in which the deposition of colloidal zirconia particles on 210-300 μm glass beads was monitored by X-ray difference microtomography and flow velocities obtained from a lattice Boltzmann simulation has been identified by the author.

With this in mind, the aim of this chapter was to 1) determine if direct modelling of gravel filter flow velocities during clogging was possible and feasible; 2) establish correlations between flow velocities, kaolin deposition and the spatial variation of each; and 3) interpret

model results with respect to the transport and removal of pollutants within a gravel filter. Lagrangian particle tracking was incorporated into the model. The aim was not to model kaolin deposition and clogging over a filter lifetime, but to determine if phenomenologically similar breakthrough profiles could be obtained for simulated tracers as for the physical column breakthrough experiments of Chapter 2.

This chapter covers the justification for the choice of modelling approach and numerical modelling software together with a description of the parameters used in the chosen software. A parametric study based on a representative sub-volume of pore geometry is presented; the purpose of which was to justify the modelling approach used for the full volume and identify potential sources of error in the results. Flow velocity and Lagrangian tracer particle transport results are presented for the full volume and interpreted with respect to pollutant transport through a clogging gravel filter.

5.3 Methods and Method Development

5.3.1 OpenFOAM Software

The Open-source Field Operation And Manipulation (OpenFOAM) software released by OpenCFD Ltd. (www.openfoam.com) was used to simulate the physics involved in this study. OpenFOAM is a free and open source computational fluid dynamics (CFD) package comprising a flexible set of applications written in C++. These applications include utilities to perform pre-processing of the data, mesh generation and post-processing of results; solvers to solve for compressible, incompressible and multiphase flows, particle tracking flows, combustion and chemical reactions, heat transfer, electromagnetics and stress analysis of solids; and libraries that are accessible to both the package and user developed solvers and utilities (OpenFOAM Foundation, 2013).

OpenFOAM was considered to be an appropriate package for the following reasons:

- it is powerful, flexible and efficient,
- it can solve for both flow velocities and particle transport,

- parallelization is built in at a low level allowing most applications to be run in parallel on multiple processors and for user developed applications to be run without parallel-specific coding (Ambrosino, 2011),
- as it is open source, the user has full access to the underlying code,
- there is an active community and forum for discussing model development,
- the mesh generation utilities are capable of producing high quality meshes of very complex domains such as pore networks within a gravel filter.

Disadvantages are that it is not commercial software and mistakes sometimes make it into the release version (although these are often picked up and reported as bugs by the OpenFOAM community), there is no graphical user interface and there is limited documentation on most solvers and utilities requiring the user to search the community forum and read the source code to understand the capabilities and limitations of each application.

Despite these disadvantages, OpenFOAM (version 2.1.1) was chosen over the commercial software COMSOL Multiphysics (www.comsol.com) because of the strength of OpenFOAM's mesh generation utility *snappyHexMesh* which allowed the generation of a high quality mesh of the filter pore network.

5.3.2 Geometry

3D depictions of the gravel filter pore volume were obtained by MRI scanning filters at three stages of clogging with kaolin clay particles: clean, partially clogged and clogged (as described in Chapter 3). With processing of the MRI images, it was possible to segment them into solid (gravel and kaolin) and pore volume (water) phases. This pore volume was the domain within which all numerical modelling was applied. Two domains were defined: the first covered the full MRI scan region of interest (84.9mm diameter and 63.3mm length), the second was a sub-volume extracted from this larger volume (15mm wide, 15mm tall and 63.3mm long). The sub-volume was created so as to allow quicker testing of the parameters in the parametric study of Section 5.3.6.

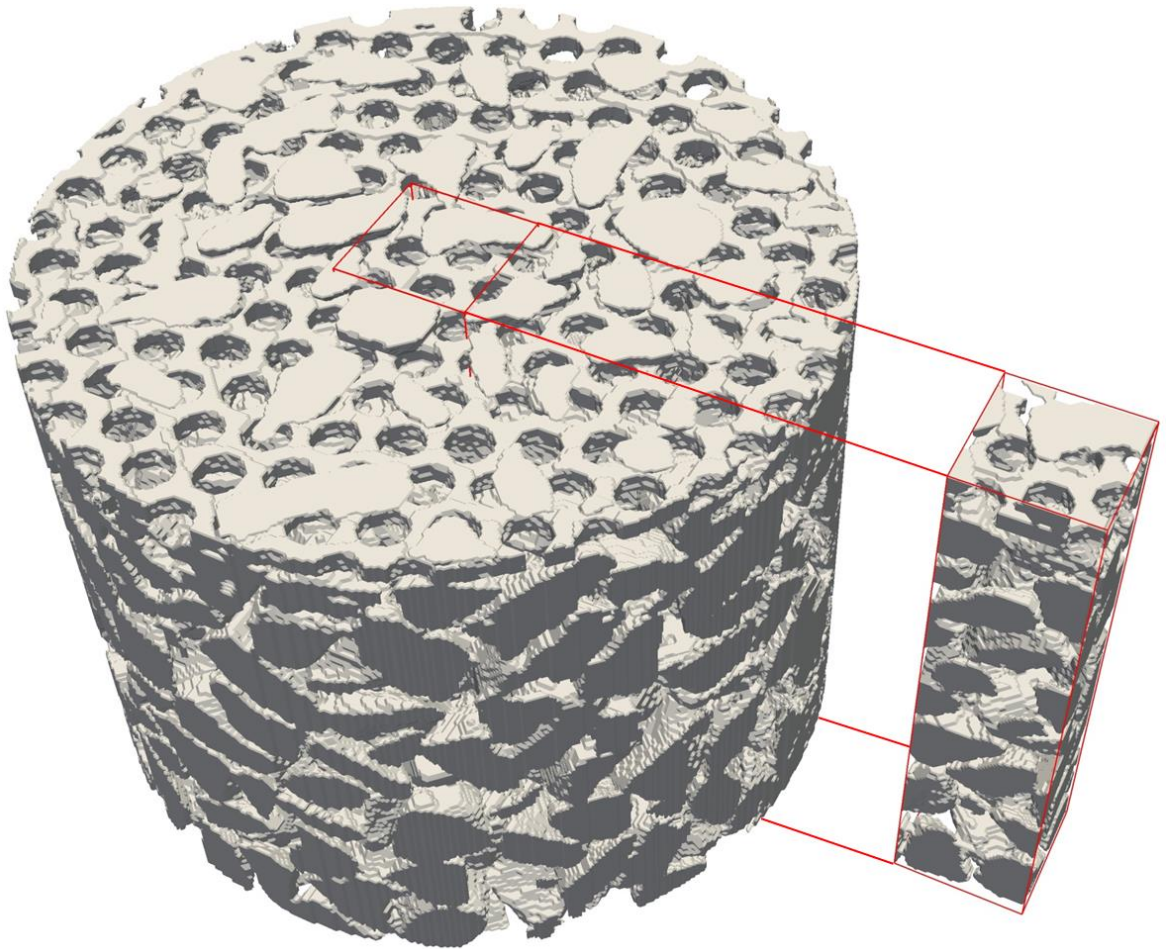


Figure 5.1. Full and sub-volume gravel STLs derived from MRI scan H1C. The regularly spaced circular openings of the plastic mesh are visible on the top surface.

A surface representing the solid phase of the MRI scan was created from a 3D stack of TIFF images and then exported as an ASCII STL (stereolithography) format using the graphics software Blender (Blender Foundation, www.blender.org) (shown in Figure 5.1). STL is a common 3D graphics format that describes a raw unstructured triangulated surface and was the input to the OpenFOAM mesh generation and refinement utility *snappyHexMesh*.

The *snappyHexMesh* utility effectively cuts out the gravel surface from a specified computational domain and refines the cells adjacent to the surface (as shown in Figure 5.2).

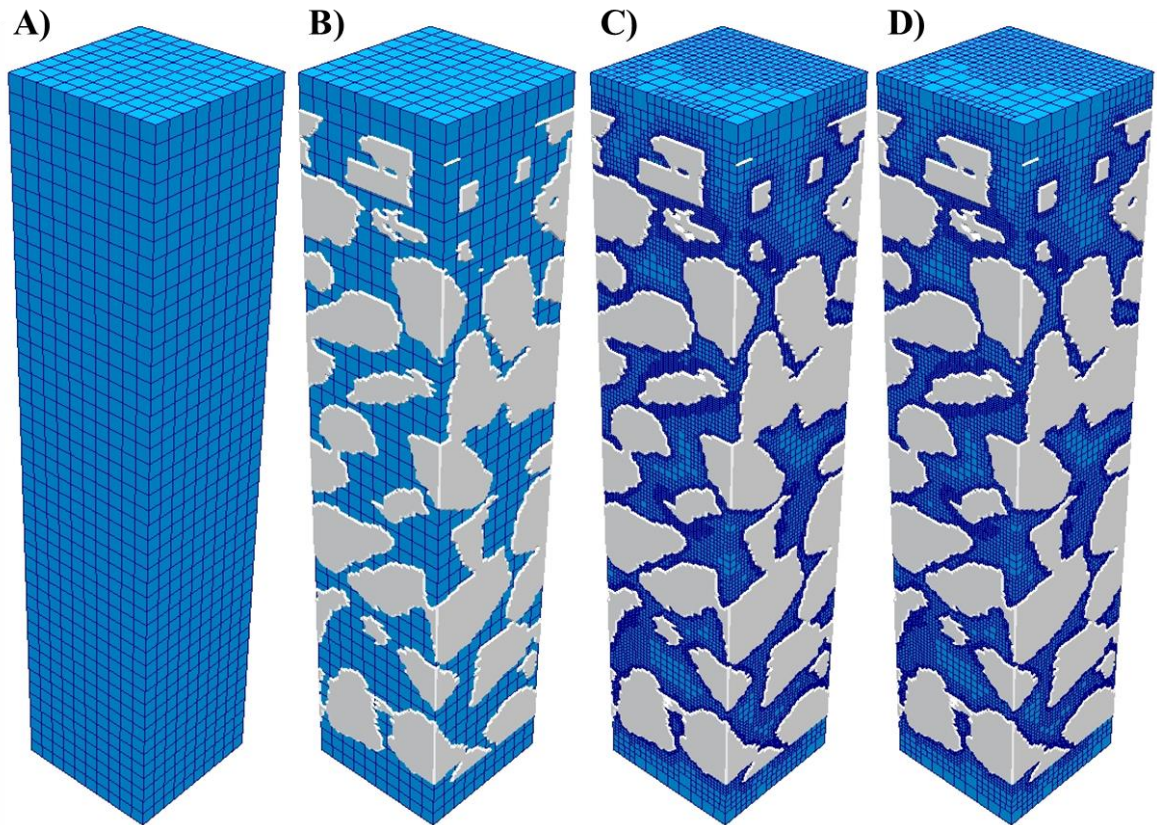


Figure 5.2. *snappyHexMesh* process from A) background hexahedral mesh definition, B) generation of STL gravel surface edge mesh, C) splitting background mesh cells at surface intersections, and D) removal of cells within gravel regions and refinement of surface vertices.

The *snappyHexMesh* process is as follows:

1. Define a background hexahedral mesh consisting of regularly spaced cells.
2. Generate an edge mesh file of the STL surface.
3. Split background mesh cells at surface edges and insert additional levels of refinement.
4. Remove cells in which more than 50% of their volume lies within the STL surface i.e. cells that lie within gravel regions.
5. Snapping of cells adjacent to the STL surface by moving individual cell vertex points onto the surface. This is an iterative procedure that is repeated until the minimum user-specified mesh quality control requirements are met.

For the cuboid sub-volume, the background hexahedral mesh was created using the OpenFOAM utility *blockMesh* to define the extent of the computational domain along with base level mesh density. For the cylindrical full volume, *blockMesh* could be used, but it produced an uneven mesh over the cylinder diameter and some cells with a high aspect ratio, which was undesirable. Instead, 3rd party mesh generation software Cubit (Sandia National Laboratories, cubit.sandia.gov) was used for the full volume as this produced a much more even distribution of cells. Typical background meshes for each domain are shown in Figure 5.3. For both domains, the meshed volume extends above and below the gravel STL surface so that boundary conditions would not affect the solution within the gravel volume.

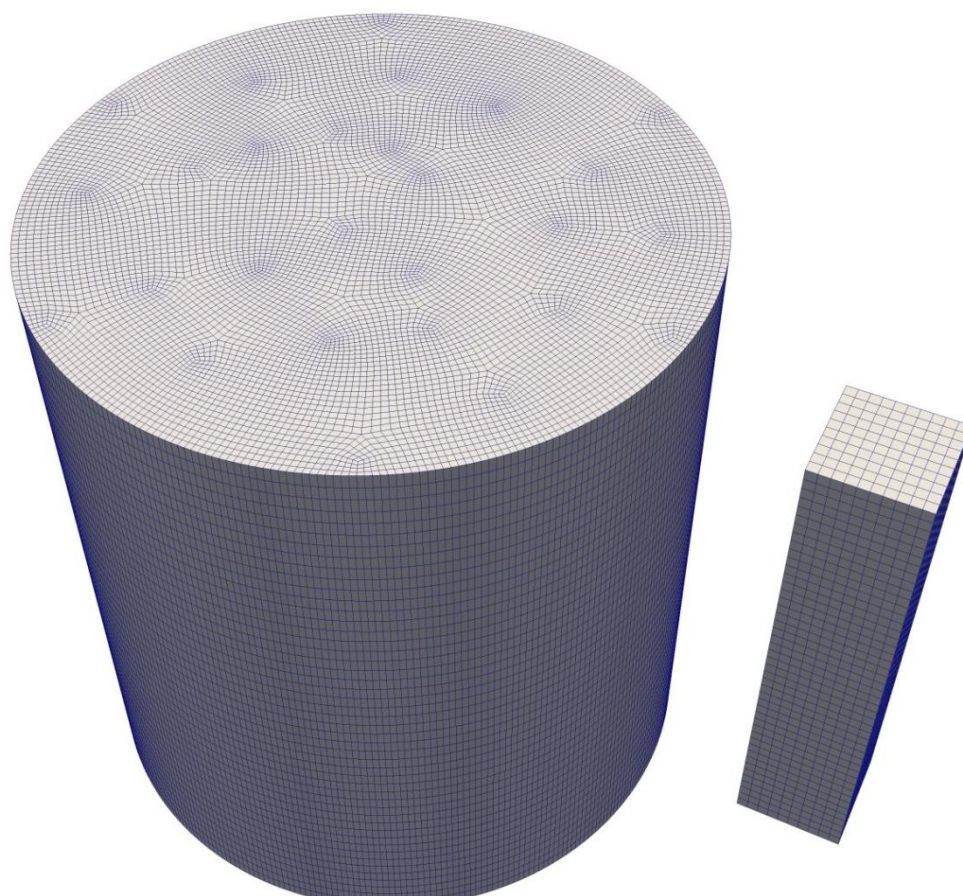


Figure 5.3. Cylindrical full volume background mesh generated with Cubit and cuboid sub-volume background mesh generated with the *blockMesh* utility.

Details of the *snappyHexMesh* dictionary file specifying the meshing parameters can be found in Appendix C.1. Parameters such as the base level mesh density and number of

refinement levels were investigated in the parametric study (Appendix B). Both parameters determine the resolution of the refined mesh. A greater resolution results in more accurate depiction of the pore network but requires more computing power to generate the mesh and to run the subsequent solvers. A high base level mesh density with low refinement levels produces a similar number of cells to a low base level mesh density with high refinement levels; the difference being the former has more cells within the centre of each pore whilst the later has more cells on the STL surface. The relative significance of each is evaluated in Appendix B, and summarised in Section 5.3.6. Figure 5.4 shows the effect of refinement levels.

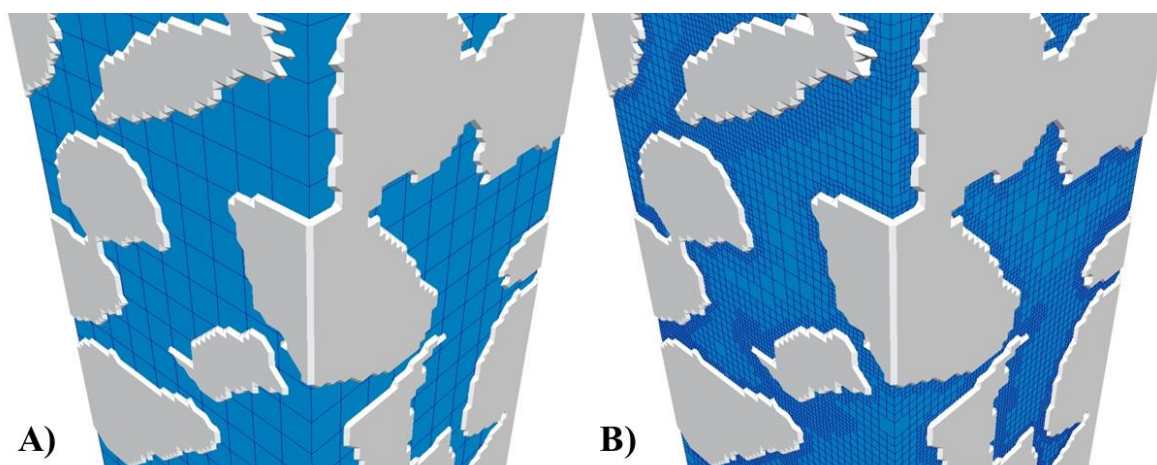


Figure 5.4. A) coarse base level mesh density with no surface refinement and B) the same coarse sub-volume mesh with three levels of surface refinement.

The *checkMesh* utility checks the validity for the mesh and reports on the quality with measures such as aspect ratio, mesh non-orthogonality or skewness. Generally, *snappyHexMesh* produced a good quality mesh but if this is not the case then either the quality parameters of *snappyHexMesh* can be made more stringent or the finite volume solution and discretisation schemes (*fvSolution* and *fvScheme*, Section 5.3.3.1) may need to be modified to ensure convergence with a sub-optimum quality mesh.

5.3.3 Eulerian Finite Volume Method

To understand the difference between Eulerian and Lagrangian frames of reference, an analogy is often made with observing a flowing river from a fixed point on the bank of the

river (Eulerian) and from a boat floating down the river (Lagrangian). The difference is in the Eulerian approach the flow is measured as it passes through the point(s) of reference whereas with the Lagrangian approach each individual fluid parcel is tracked as it moves through space and time. As such, the Lagrangian frame of reference is very cumbersome to apply to fluid dynamics and is more suited to solid mechanics (Belytschko et al., 2000), hence a Eulerian frame of reference was adopted in this study to solve for fluid dynamics.

In a finite volume method (FVM), the computational domain is divided into a finite number of control volumes over which the governing equations of the chosen solver are discretised and solved. Here, each control volume is equal to a mesh cell as defined in Section 5.3.2.

5.3.3.1 Solver

Numerous solvers exist within OpenFOAM. The gravel filter is fully submerged in water, potentially with turbulent flows, and the desired output was a steady state flow distribution. *simpleFoam* is a steady state, incompressible, single phase solver capable of accounting for turbulence and, as such, should be the most computationally efficient solver for our purpose.

The SIMPLE in *simpleFoam* stands for Semi-Implicit Method for Pressure Linked Equations. This method allows the coupling of the Navier-Stokes equations with an iterative procedure that is summarised as follows (Various Contributors, 2013):

1. Boundary conditions set.
2. Discretised momentum equation is solved allowing computation of the intermediate velocity field.
3. Mass fluxes at cell faces are computed.
4. Pressure equation solved and under-relaxation applied.
5. Correct the mass fluxes at cell faces.
6. Velocities corrected on the basis of the new pressure field.
7. Boundary conditions updated.

8. Process repeated from step 2 until convergence criteria are satisfied.

The solver finite volume discretisation schemes are given in the *fvSchemes* file of Appendix C.2. Solution and algorithm control was specified in the *fvSolution* file of Appendix C.3. The pressure field was solved with a preconditioned conjugate gradient (PCG) solver with diagonal incomplete-Cholesky (DIC) preconditioner. The velocity field was solved with a smooth solver with Gauss-Seidel smoothing. Relaxation factors to control the amount of under-relaxation were specified but were not tailored so as to find the optimum compromise between highly stable computation and short run time. As all simulations were stable, the factors used were assumed to err on the safe side.

5.3.3.2 Turbulence

There are three types of turbulence model that may be implemented with the *simpleFoam* solver: laminar (no turbulence), Reynolds-averaged stress (RAS) modelling and large-eddy simulation. Large-eddy simulation was not investigated in this project for the reason that, at the low levels and scale range of turbulence expected in the model, there is little advantage of large-eddy simulation over RAS modelling.

$$\text{Re}' = \frac{V_0 D_g \rho}{\mu(1-\phi)} \quad \text{Equation 5.1}$$

Where V_0 = superficial approach velocity (m/s),

D_g = Effective gravel particle diameter (m),

ρ = fluid density (kg/m³),

μ = dynamic viscosity (Pa.S),

ϕ = porosity.

Modified Reynolds numbers, Re' , have been used to predict the flow regime in porous beds such as soils (Hellström & Lundström, 2006), glass beads (Rodier et al., 1997) and quartz sand (Kemblowski & Mertl, 1974) assuming spherical particles and a Newtonian fluid. This approach was used to acquire indicative flow regimes in the gravel filter with Equation 5.1 whereby if $\text{Re}' < 10$, the flow is considered to be laminar or turbulent if $\text{Re}' > 2000$. For the MRI scan H1C (unclogged) porosity of 41.1% and the scan H3C

(clogged) porosity of 24.9%, the Re' numbers were estimated to be 3.66 and 3.09 respectively hence well within the laminar regime.

However, there may be local regions of turbulent or transition flow, particularly in the clogged experiment where preferential pathways through the filter have formed leading to increased velocities.

The main classes of RAS models available – also commonly known as Reynolds Averaged Navier-Stokes (RANS) models – were $k-\varepsilon$, $k-\omega$ and *Spalart-Allmaras*. An additional 13 models were available in OpenFOAM v2.1.1, but as they were mostly variations of the $k-\varepsilon$ model they were not investigated further.

The $k-\varepsilon$ model solves two differential equations: one for kinetic energy k and one for turbulent dissipation ε . Limitations of this model are that coefficients must be empirically derived and it is only truly valid for fully turbulent flows. Strengths are it is robust, easy to implement, computationally cheap and widely used (Nallasamy, 1987).

$k-\omega$ models solve for kinetic energy k and turbulent frequency ω and appear to perform better at low Reynolds numbers and transitional flows; however, they require high mesh resolution near to the wall (Menter, 1994). The *Spalart-Allmaras* model is a one-equation model that was developed for aerodynamic flows (Spalart & Allmaras, 1994).

Thus, the $k-\varepsilon$ model was chosen to investigate the effects of turbulence on the *simpleFoam* solver as it is the most widely used and validated model. Reasonable estimates of the coefficients k and ε were made and used as boundary conditions for the case. The effect of the estimated coefficients was evaluated in the parametric study (Appendix B.2).

5.3.3.3 Surface Roughness

In OpenFOAM, it is possible to specify surface roughness as wall functions which are applied as boundary conditions to specific patches of the computational domain. This allows different wall function models to be applied to different surfaces and hence for each surface to have its own roughness.

The choice of wall function depends on the solver (compressible or incompressible) and on the turbulence model (LES or RAS) and is specified through the turbulent viscosity field *nut*. To test if the model was sensitive to the choice of wall function and surface roughness, the *nutkWallFunction* and *nutkRoughWallFunction* were run for both laminar flows and flows with a RAS model of turbulence in Appendix B.2. In addition, the *nutkRoughWallFunction* parameters C_s and K_s were varied. C_s is the roughness constant (generally set between 0.5 and 1) whilst K_s is the roughness height in metres, also known as the equivalent sand-grain height (Tapia, 2009).

5.3.3.4 Boundary & Initial Conditions

Boundary conditions in this study consisted of a fixed value velocity inlet and a fixed value pressure outlet. The inlet velocity was either $1.044 \times 10^{-4} \text{m/s}$ or $2.165 \times 10^{-4} \text{m/s}$ corresponding to the filtration rate of 0.376m/hr or 0.779m/hr in the low and high flow MRI experiments respectively. The outlet pressure was 0 which, for OpenFOAM incompressible solvers, corresponds to atmospheric pressure.

In OpenFOAM, each field requires a file that specifies dimensions (units), the internal field initial condition and the boundary condition for each patch. Patches are groups of mesh cell faces that share a common characteristic. The patches in our case were: *inlet*, *outlet*, *fixedWalls* and *surfaceGravel* whilst the fields for a laminar model were pressure (p), velocity (U) and turbulent viscosity field (*nut*). Additional fields for a turbulent model were kinetic energy (k), turbulent dissipation (ϵ) and Reynolds stress tensor (R). *surfaceGravel* defines the boundary between the gravel surface and the computational domain whilst *fixedWalls* defines the outer edge of the computational domain that is neither *inlet*, *outlet* nor *surfaceGravel*. The boundary conditions are specified in Table 5.1 and Table 5.2. To include surface roughness, *nutkWallFunction* is replaced with *nutkRoughWallFunction*.

Table 5.1. List of boundary conditions/initial values for each patch and fields required for both laminar and turbulent models.

Patch		Fields required for laminar & turbulent models		
		p	U	ν_{t}
<i>internalField</i>	value	uniform 0	uniform (0 0 0.0002165)	uniform 0
<i>inlet</i>	type	<i>zeroGradient</i>	<i>fixedValue</i>	<i>calculated</i>
	value	-	uniform (0 0 0.0002165)	uniform 0
<i>outlet</i>	type	<i>fixedValue</i>	<i>zeroGradient</i>	<i>calculated</i>
	value	uniform 0	-	uniform 0
<i>fixedWalls</i>	type	<i>zeroGradient</i>	<i>fixedValue</i>	<i>nutkWallFunction</i>
	value	-	uniform (0 0 0)	uniform 0
<i>surfaceGravel</i>	type	<i>zeroGradient</i>	<i>fixedValue</i>	<i>nutkWallFunction</i>
	value	-	uniform (0 0 0)	uniform 0

Table 5.2. List of boundary conditions/initial values for each patch and additional fields required for turbulent models only.

Patch		Additional fields required for turbulent models		
		k	ε	R
<i>internalField</i>	value	uniform 0.001	uniform 0.1	uniform (0 0 0 0 0)
<i>inlet</i>	type	<i>fixedValue</i>	<i>fixedValue</i>	<i>fixedValue</i>
	value	uniform 0.001	uniform 0.1	uniform (0 0 0 0 0)
<i>outlet</i>	type	<i>zeroGradient</i>	<i>zeroGradient</i>	<i>zeroGradient</i>
	value	-	-	-
<i>fixedWalls</i>	type	<i>kqRWallFunction</i>	<i>epsilonWallFunction</i>	<i>kqRWallFunction</i>
	value	uniform 0.001	uniform 0.1	uniform (0 0 0 0 0)
<i>surfaceGravel</i>	type	<i>kqRWallFunction</i>	<i>epsilonWallFunction</i>	<i>kqRWallFunction</i>
	value	uniform 0.001	uniform 0.1	uniform (0 0 0 0 0)

These boundary conditions specify a constant inlet velocity of $2.165 \times 10^{-4} \text{ m/s}$ (corresponding to the filtration rate of 0.779 m/hr in the high flow experiment) which drives flow through the computational domain. The *fixedValue* velocity set to a uniform value of (0 0 0) imposes a no-slip boundary on the *fixedWalls* and *surfaceGravel* boundaries.

5.3.3.5 Constant Properties

Some properties that remain constant throughout the simulation must be specified. For the *simpleFoam* solver these are the gravity vector of the computational domain and the kinematic viscosity of the fluid. The density of the fluid is implicit within the use of

kinematic viscosity (instead of dynamic viscosity) and so does not need to be specified, but as a consequence, all pressure output values are normalised by the density.

5.3.4 Lagrangian Particle Tracking

With Lagrangian particle tracking (LPT), each individual particle or parcel of fluid is tracked as it moves through space and time, either with respect to its point of origin or to its coordinates in the previous timestep. The particles are tracked within the computational domain defined by the mesh, yet as the Lagrangian equations are ordinary differential equations, they do not have to be discretised across the mesh and it is possible to track particles at below mesh resolution.

The approach used in this study was linked Euler-Lagrangian modelling in which the flow field was derived from the steady state *simpleFoam* solution and particle positions, velocities and interactions from the Lagrangian model. Two types of particles were tracked: the first was intended to simulate tracer propagation through the filter, similar to the NaCl tracer used in the column experiments of Chapter 2, Section 2.3. These particles had negligible mass (and hence momentum) and were of the same density as the transporting fluid (water). The second type of particles were intended to represent kaolin transport through a filter. These particles had a density and size distribution equal to the kaolin used in the column experiments. How each class of particles interacted with surfaces is detailed in Section 5.3.4.2.

5.3.4.1 Particle Properties

Particles were modelled as rigid spheres. For the particles simulating a tracer, a negligible size of 1×10^{-30} m and a density equal to that of the water was used. These particles therefore had negligible mass resulting in a very short particle response time: effectively they have no momentum and follow the flow streamlines like NaCl ions in solution.

Particles simulating kaolin transport had a size distribution equal to that measured for the kaolin used in the column experiments (Chapter 2, Section 2.4.3) and a density of

2650kg/m³. These particles therefore can settle under gravity and have momentum allowing them to cross flow streamlines and come into contact with the gravel surface

Details of particle properties, forces, interactions, injection and dispersion model can be found in the *kinematicParticleProperties* files of Appendix C.4.

5.3.4.2 Solver and Model Definitions

The *icoUncoupledKinematicParcelFoam* is a transient solver for the passive transport of a single kinematic particle cloud (OpenFOAM Foundation, 2013). This solver allows one-way coupling in which the particles obtained their velocity from the internal flow, in this case already calculated by the *simpleFoam* solver, yet there is no interaction between particles and the internal field. This assumption of one-way coupling is valid when the particles are considered to be dispersed.

The LPT algorithm implemented by OpenFOAM is the *TrackToFace* method (Macpherson et al, 2009):

1. The fluid velocity, calculated for each cell face, is interpolated for the current particle position within a cell.
2. The forces acting on the particle are computed and the equations of motion solved to determine its trajectory.
3. The particle follows this trajectory until it crosses a new cell face.
4. At the point of crossing, new fluid velocities are interpolated and forces are calculated based on the new particle position.
5. The particle is once again moved until it crosses a new cell face.

At every face crossing, the algorithm checks if the face forms part of a surface patch or if it is part of the internal field. If the face is part of a wall surface patch, the specified wall patch interaction is invoked. If the face is part of the outlet surface patch, the particle is removed from the computational domain.

Forces

Forces acting on each particle are gravity and sphere drag (assuming spherical particles). These forces, together with the particle properties of mass, density, size and velocity obtained from the internal field are used to solve a set of ordinary differential equations known as the Basset, Boussinesq and Oseen (BBO) equations.

Interactions

In the *icoUncoupledKinematicParcelFoam* solver particles do not interact with the fluid phase, but can interact with patches and with each other. Patch interactions can be *escape*, *stick* or *rebound*. Patch interactions are invoked during the *TrackToFace* algorithm when the particle radius crosses a patch face. With the *escape* interaction, the particle is removed from the computational domain. This interaction was used for the *outlet* patch. With *stick*, the particle sticks to the patch face. With *rebound*, the particle rebounds from the patch face with a restitution coefficient, e , specifying energy loss from a rebound (where $e=1$ describes a perfectly elastic rebound) and an energy loss due to friction with the wall specified by μ (where $\mu=0$ describes zero energy loss due to friction).

A relatively inelastic rebound from *fixedWalls* and *SurfaceGravel* patches was considered to be the most realistic interaction for particles simulating kaolin. By definition, a conservative tracer should not stick to surfaces and, given enough time, each particle of the tracer would be recovered at the outlet. Of the available surface interactions, *rebound* with no loss of energy would appear the most appropriate. However, due to the very low mass of the tracer particles, it was found that particles rebounding from a surface were unable to cross the flow streamlines that brought them into contact with the surface in the first place and either became impinged upon that surface or confined to the low velocity area adjacent to the surface. Effectively, rebounding tracer particles would stick to the gravel surface and hence were simulated as *stick* as it was computationally more efficient. Due to this limitation of the software, only that proportion of particles that passed through the *outlet* patch were analysed as conservative tracer particles.

Whilst particle-particle collision is an option, it is extremely computationally expensive for numerous particles in a complex geometry. As the kaolin particles, at their maximum concentration, make up 0.75% of the volume of the suspension, they may be considered dispersed. The probability of particle-particle interaction is therefore low and was not included in the simulations.

Particle Injection

Particle injection controls the number (or mass) of particles that enter the computational domain per time step, their initial location and their initial velocity and trajectory. Location can be either a specified patch or manually with a specified Cartesian coordinate for each particle. Manual injection was used so that initial conditions were identical for each case of the parametric study, even when mesh resolution was varied (Appendix B). A single injection inserted 2362 particles into the computational domain with an initial velocity equal to the superficial flow velocity.

5.3.4.3 Dispersion Model

To ascertain the effects of dispersion on the transport of tracer particles through the filter, some cases were run with the stochastic dispersion model *stochasticDispersionRAS*. This model only applies when a RAS turbulence model is included in the Lagrangian particle tracking model.

5.3.4.4 Particle Tracks

Particle tracks can be recorded using the *particleTracks* utility which records particle location at each timestep and exports the data for visualisation in ParaView. The tool was extended to record particle origin ID, time, velocity, diameter and particle fate along with location at each time step in a tool named *myExtendedParticleTracks*. Particle fate was defined as “escape” if the particle escaped the computational domain through the outlet patch, “stick” if the particle becomes inactive within the computational domain and “in-transit” if the particle was still travelling through the computational domain by the end of the simulation. The additional data recorded by *myExtendedParticleTracks* allowed correlation between particle diameter with velocity, tortuosity and the fate of the particle to

be determined. This information could not be derived from the existing *particleTracks* utility.

5.3.5 Case Execution

Each OpenFOAM simulation requires a case directory. Within each case directory are initial conditions and boundary conditions contained within the *0* directory, mesh and constant properties contained within the *constant* directory and run control parameters contained within the *system* directory.

With the mesh generated by *snappyHexMesh*, the simulation was executed as follows:

1. Decompose mesh for parallel computation.
2. Execute *simpleFoam* in parallel.
3. Reconstruct converged *simpleFoam* solution.
4. Calculate wall shear stress for converged case with *wallShearStress* utility.
5. Export internal field to VTK format and visualise with ParaView.
6. Run *foamLog* to generate details of solver convergence from the log file.
7. Run *sample* to sample internal field values across specified lines and planes.
8. Compare convergence details and sample values in spread sheet software.
9. Use converged *simpleFoam* solution as initial conditions for Lagrangian particle tracking with *mapFields* utility.
10. Decompose converged *simpleFoam* solution and execute (in parallel) *icoUncoupledKinematicParcelFoam*.
11. Reconstruct velocity fields and Lagrangian fields for each timestep.
12. Export Lagrangian fields to VTK and visualise with ParaView.
13. Run *myExtendedParticleTracks* to generate particle tracks in VTK format for visualisation and in CSV data format for analysis with spread sheet software.
14. Clean up unnecessary files from case such as decomposed folders and Lagrangian time directories to free hard disk space.

All cases were run on a desktop PC with AMD Phenom II x4 965 3.4GHz processor, 16GB DDR3 RAM (with an additional 32GB virtual RAM on SSD) and ATI Radeon HD 5700 graphics card. The operating system was Ubuntu 12.10 and all figures were created in ParaView unless otherwise stated.

Parallel runs were performed across four processors for *snappyHexMesh*, *simpleFoam* and *icoUncoupledKinematicParcelFoam* commands using the native message passing interface (MPI) of Ubuntu 12.10. Bash scripts were used to execute all the commands on multiple cases. Example bash scripts are contained in Appendix C.5 and C.6.

Cases were split across each processor using *decomposePar* and were reconstructed using *reconstructPar*, or *reconstructParMesh* in the case of the *snappyHexMesh* generated mesh. Wall shear stress was calculated using *wallShearStress* and *sample* was used to extract field values across a specified line or plane through the computational domain.

foamLog generated details on run time and convergence of the simulation from the *simpleFoam* log file whilst *grep* was used to extract details of particle fate at each timestep from the *icoUncoupledKinematicParcelFoam* log file.

Finally *foamToVTK* was used to convert the simulation results to VTK format, a widely used data format supported by the free scientific visualisation software ParaView. As OpenFOAM has no graphical user interface, ParaView is used for visualising and analysing the results. VTK file size can be limited by only converting the internal field of the *simpleFoam* results at the converged timestep and by only converting the required Lagrangian fields of the *icoUncoupledKinematicParcelFoam* results. Otherwise the results take up excessive hard disk space and can be unwieldy to analyse.

5.3.6 Parametric Study & Optimum Parameters

The aim of the parametric study was to evaluate the sensitivity of the model to 1) physical parameters of the gravel filter that could not be measured, and 2) elements of the modelling approach that needed to be tested. The Eulerian *simpleFoam* parameters were:

- Solution scheme: linear or corrected
- Turbulence and turbulent coefficients
- Surface roughness and roughness coefficients
- Interlinked turbulence with surface roughness
- Mesh resolution and mesh surface refinement levels
- Interlinked turbulence with surface refinement
- Surface STL generation procedure
- Viscosity

The Lagrangian *icoUncoupledKinematicParcelFoam* parameters were:

- Lagrangian dispersion, with and without Lagrangian turbulence
- Turbulence
- Surface Roughness
- Interlinked Lagrangian turbulence with surface roughness
- Mesh resolution and mesh surface refinement levels
- Surface STL generation procedure
- Viscosity

From the results of the parametric study (which can be found in Appendix B), it is apparent that the solution scheme does not affect flow velocities, wall shear stress or particle transport and so the limited scheme is preferable as it is generally more stable.

Turbulence, surface roughness, Lagrangian turbulence and the choice of their coefficients do not significantly affect flow velocities, wall shear stress or particle transport when considered individually. When considered together, turbulence and surface roughness have the capacity to significantly affect flow velocities (7.3% change in maximum velocity) and wall shear stress (1755% change in maximum wall shear stress), yet the surface roughness coefficients are not accurately known in this study. Hand calculations suggest that the flow

regime is laminar and so the need to accurately specify surface roughness coefficients can be avoided without compromising flow velocity computation by utilising a laminar model.

Mesh resolution and the levels of surface refinement do affect flow velocities and wall shear stress. An initial size of 0.6mm with a maximum surface refinement of 2 levels appears to accurately capture all of the pore space and produces similar (0.72% difference) maximum velocities to a mesh with an initial size of 1.5mm and maximum surface refinement of 4 levels, yet run times were 3.4 times shorter. Such a mesh was therefore preferable.

Smoothing the surface during STL generation produced a surface that looked more like a gravel surface. The resulting maximum velocities were 6.00% lower than an unsmoothed surface. The resolution of the MRI derived geometry and the pixelated representation of the gravel surface could therefore be affecting the model accuracy. However, as the smoothed surface had a different pore volume and pore network connectivity compared with the unsmoothed surface, an MRI scan at much higher resolution would be required to quantify the effect of geometry resolution on flow velocities. In this study, the unsmoothed surface should be used as this provides equivalent pore volume and pore network connectivity to those assessed in Chapter 3 and Chapter 4 respectively.

Kinematic viscosity was shown to affect the flow velocities (3.4% difference in maximum velocity) and wall shear stress (93.3% difference in maximum wall shear stress) but had very little effect on Lagrangian particle transport. The kinematic viscosity of a water/kaolin suspension is thought to vary spatially and in time throughout the filter as the concentration of kaolin changes. It is not possible to incorporate a varying kinematic viscosity value without extensively re-writing the *simpleFoam* solver or utilising a two-phase solver such as *twoPhaseEulerFoam* and so a constant viscosity equal to $1.0 \times 10^{-6} \text{ m}^2/\text{s}$ (water at 20°C) should be used.

Lagrangian dispersion increases the sticking rate of particles. When simulating a conservative tracer, particle sticking is undesirable and so a Lagrangian dispersion model should not be included; whereas, when simulating kaolin particles for removal, the ability

for particles to cross flow stream-lines due to dispersion may be desirable and so, in this case, a Lagrangian dispersion model should be included.

5.3.7 Full Volume Cases

The full volume computational domains were derived from the MRI scans of two gravel filters (low flow rate and high flow rate) at various stages of clogging with kaolin clay. The pertinent details of each scan are given in Table 5.3, whilst full details are contained in Chapter 3, Section 3.3.1. After deposition of kaolin, the high flow filter was subjected to a high flow rate for approximately one hour before scan H4E and an additional higher flow rate for another hour prior to scan H5E. Scans H4E and H5E were modelled with an inlet flow velocity equivalent to the velocity under which the kaolin was deposited to allow comparison with scans H1C, H2C and H3C.

Models of the full volume of each MRI scan were run with the optimum parameters identified in Section 5.3.6: limited solution scheme, laminar flow model, no surface roughness model, unsmoothed surface, kinematic viscosity of $1.0 \times 10^{-6} \text{ m}^2/\text{s}$ and a mesh generated from an initial cell size of $600 \times 600 \times 600 \mu\text{m}$ and maximum of two levels of surface refinement ($150 \times 150 \times 150 \mu\text{m}$).

Table 5.3. Full volume MRI scan and numerical model details. Note that the computational domain pore volume is equivalent to the ‘active’ pore volume, defined in Chapter 3 as pore space connected to the main pore network.

Case	Experiment and stage	Experiment flow rate (ml/min)	Computational domain pore volume (litres)	Modelled inlet flow velocity (m/s)
L1C	Low flow - clean	49.2	0.141	1.044×10^{-4}
L3C	Low flow -clogged	49.2	0.055	1.044×10^{-4}
H1C	High flow - clean	102	0.144	2.165×10^{-4}
H2C	High flow – partial clogging	102	0.103	2.165×10^{-4}
H3C	High flow - clogged	102	0.085	2.165×10^{-4}
H4E	High flow - 1st Erosion	102/450	0.087	2.165×10^{-4}
H5E	High flow - 2nd Erosion	102/600	0.088	2.165×10^{-4}

Lagrangian particle tracking was run with 2362 particles (so chosen to ensure an even radial distribution of particles at the inlet) to simulate the propagation of a tracer through the filter. As such, a model of Lagrangian dispersion was not included.

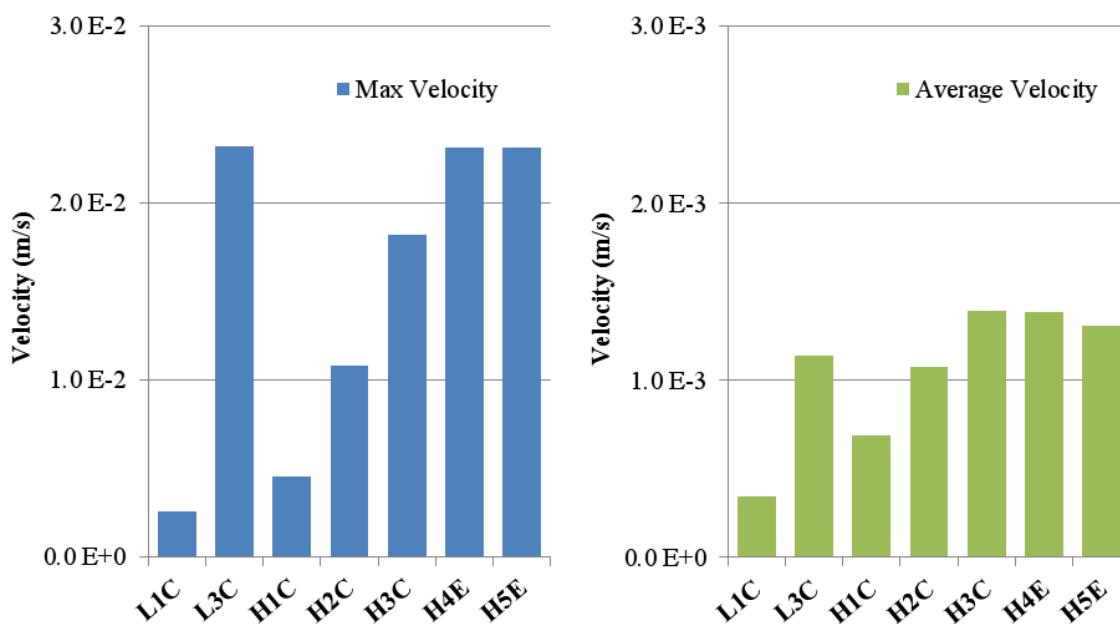
Results were analysed with respect to flow velocities and flow paths within the entire computational domain (Section 5.3.7.1), flow velocities mapped onto the medial axis, as defined in Chapter 4 (Section 5.3.7.2) and the Lagrangian transport of tracer particles (Section 5.3.7.3).

5.3.7.1 Eulerian Flow Characteristics

By comparing velocities for each MRI scan, we can see how inflow rate affects maximum and average velocities within the gravel filter and how these change over time as the filter clogs. Table 5.4 and Figure 5.5 illustrate these effects: increasing the flow velocity from 1.044×10^{-4} m/s to 2.165×10^{-4} m/s doubles the average pore velocity (102% increase) in the clean gravel scans (case L1C compared with case H1C) whilst maximum velocities only increase by 78%. With clogging, the low flow filter average velocity increases by 232% whilst maximum velocity increases by 803% (case L1C compared with case L3C).

Table 5.4. *simpleFoam* results for full volume cases.

Case	Steps to convergence	Convergence time (mins)	Max Velocity (m/s)	Average velocity (m/s)
L1C	31	136.4	0.00257	0.00034
L3C	27	134.3	0.02320	0.00114
H1C	31	128.0	0.00459	0.00069
H2C	31	142.8	0.01080	0.00108
H3C	31	151.5	0.01820	0.00139
H4E	31	150.3	0.02310	0.00138
H5E	31	141.7	0.02310	0.00131

**Figure 5.5.** *simpleFoam* maximum and average velocity results for full volume cases.

The high flow filter average velocity increases by 102% whilst the maximum velocity increases by 297%. The greater increase in velocities during the low flow filter compared with the high flow filter is partially due to greater deposition of kaolin in the low flow filter. This results in a greater reduction in computational domain for the low flow filter and hence, with a constant inflow rate, a greater increase in flow velocities. Interestingly, the average flow velocities decrease during erosion (cases H4E and H5E compared with H3C, Table 5.4 and Figure 5.5) in line with the increase in pore volume caused by erosion, yet at the same time the maximum velocity increases. This has been attributed to the nature of the erosion process (which was witnessed through the clear side walls of the filter): the

high erosion flow rates washed some deposited kaolin out of the filter but also triggered “avalanches” of large clumps of kaolin that quickly became deposited elsewhere in the filter (Chapter 2, Section 2.9.3). This re-ordering of deposited kaolin appeared to block (or partially block) flow channels that could not be blocked under the lower deposition flow rates whilst unblocking other channels. The net result appeared to be a change in the flow paths, a decrease in network connectivity (Chapter 4, Section 4.5.2) and an increase in maximum flow velocities in the remaining open channels without significant change in pore volume.

The spatial variation in flow velocity is illustrated for a single, representative slice of the low flow filter cases (Figure 5.6) and the high flow filter cases (Figure 5.7). The formation of preferential flow paths leads to an increase in velocity along the flow paths. In some regions (see Figure 5.6) flow velocity decreased as that path becomes partially blocked and flow was re-routed through alternative paths.

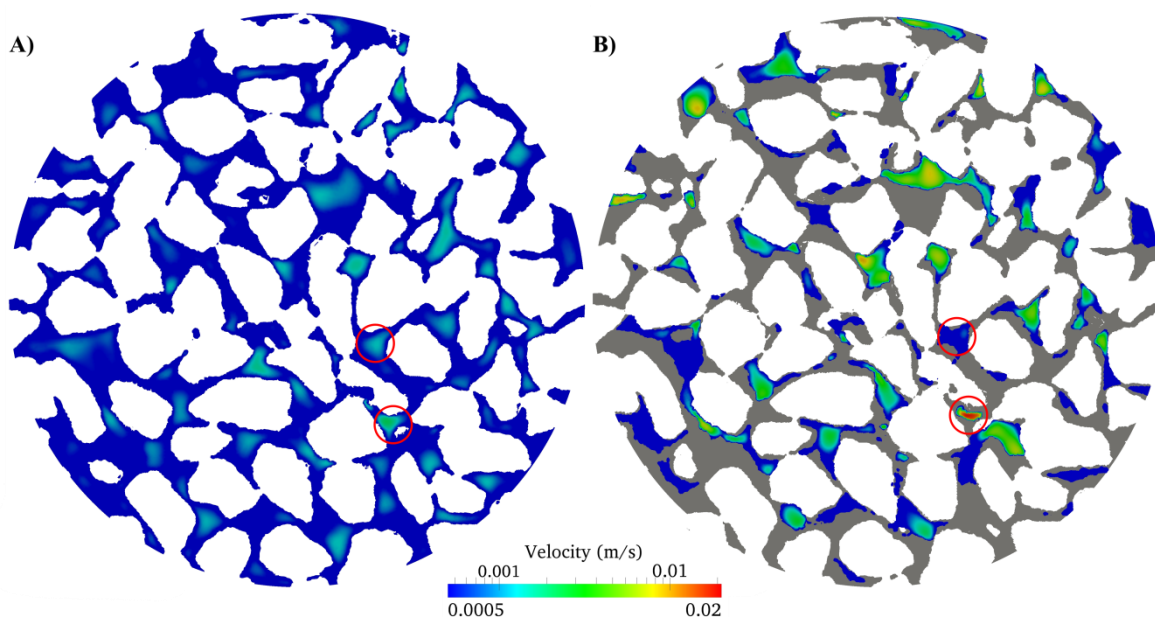


Figure 5.6. Flow velocities in a slice perpendicular to the flow direction through the centre of A) case L1C and B) case L3C. The slices are representative of the velocity distribution throughout the filters. Colour (blue to red) denotes flow velocity within the pore space whilst grey denotes location of deposited kaolin. A logarithmic scale was necessary to display the range in pore velocities encountered. The red circles indicate an area in which velocity had increased with clogging and an area in which velocity had decreased with clogging. Changes in velocity were a function of initial pore diameter and flow velocity, relative change in diameter with clogging as well as changes in pore connectivity.

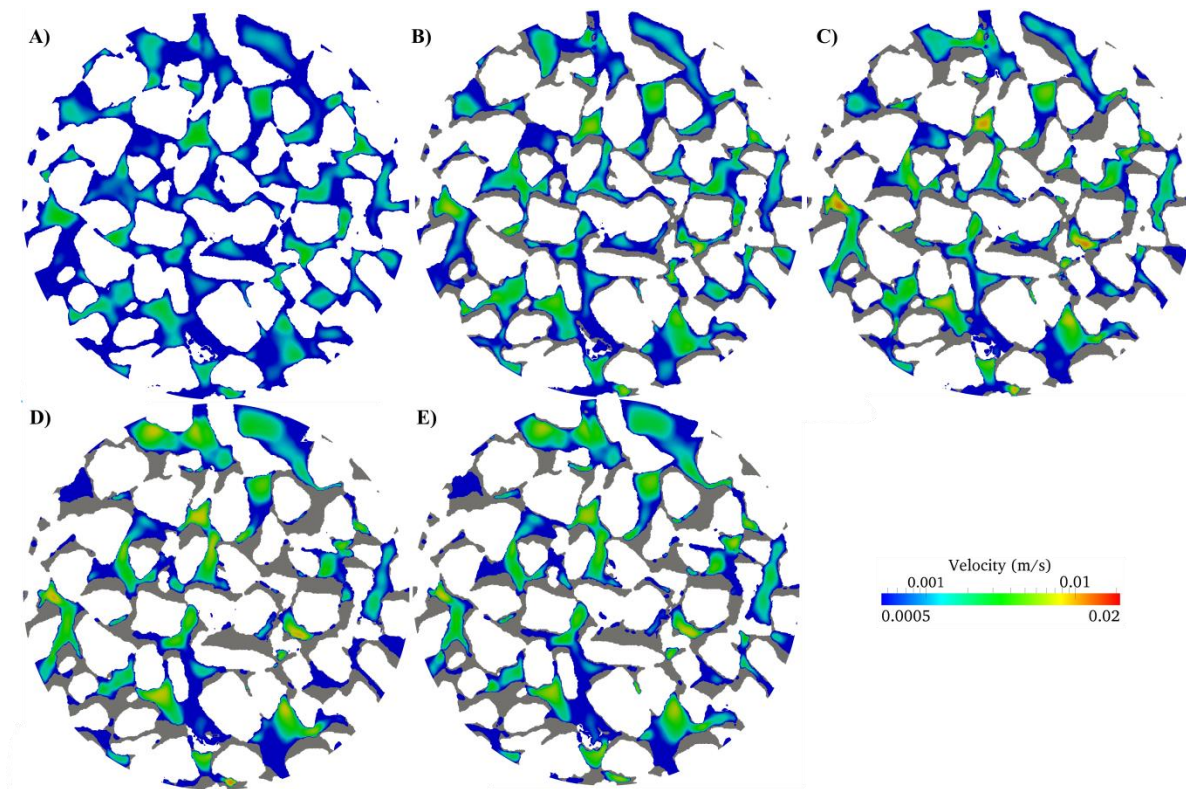


Figure 5.7. Flow velocities in a slice perpendicular to the flow direction through the centre of A) case H1C, B) case H2C, C) case H3C, D) case H4E and E) case H5E. The slices are representative of the velocity distribution throughout the filters. Colour (blue to red) denotes flow velocity within the pore space whilst grey denotes location of deposited kaolin. A logarithmic scale was necessary to display the range in pore velocities encountered. On average the velocity increases during clogging phases with relatively little change during erosive phases.

5.3.7.2 Medial Axis Flow Velocities

By mapping the calculated flow velocities onto the pore network medial axis, as defined in Chapter 4, Section 4.3, it was possible to establish correlation between the velocity and the degree of kaolin deposition at each point in the pore network (Figure 5.8). The hypotheses tested in this way were:

- A. In the clean scans, pore velocity will be positively correlated with pore diameter as the larger pores will be preferential pathways. The strength of the correlation between pore velocity and pore diameter will increase with increased clogging as smaller pores block with deposited kaolin.

- B. There will be positive correlation between the initial velocity and final velocity. High velocity channels will be subject to less kaolin deposition whilst low velocity channels will clog.
- C. Percentage reduction in pore diameter will be negatively correlated with clean scan velocity, with clogged velocity and with percentage increase in velocity. Kaolin will be less likely to deposit in pores with a high initial velocity or in which velocity increases with clogging.

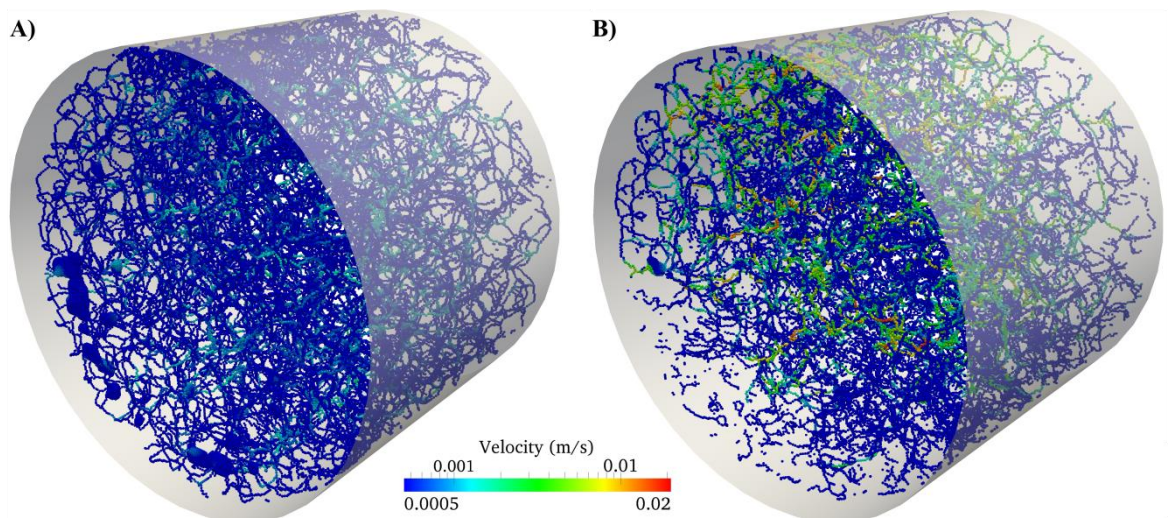


Figure 5.8. Medial axis pore velocity for A) case L1C and B) case L3C. A logarithmic scale was necessary to display the range in pore velocities encountered.

Table 5.5 summarises the correlations tested for hypothesis A, B and C. The p-value denotes the statistical significance of the correlation (with a number approaching 0 indicating higher significance) whilst the gradient denotes the strength of the correlation. For hypothesis A it is apparent that pore velocity and pore diameter are positively correlated (due to a P-value of 0 and a positive gradient) and, with the exception of case H3C, the strength of the correlation increases with clogging. From this we infer that more kaolin is deposited in the initially small and slow flowing pore channels and less in the larger, faster channels with positive feedback between pore velocity and pore diameter as clogging progresses. The close-to-zero gradient of case H3C may suggest that as clogging progresses and velocities in the remaining open pores increase, pore velocity may have passed a tipping point at which it is no longer correlated with pore diameter. Instead, pore connectivity may be more important: a narrow pore channel aligned with the flow direction

may be able to transmit a higher flow than a collection of larger, but poorly connected pores and hence becomes the preferential pathway in place of the larger pores.

Table 5.5. Correlations between pore flow velocities and pore diameters.

Hypothesis	Scan	X Variable	Y Variable	Gradient	P Value
A	L1C	Pore velocity	Pore diameter	0.000033	0.00
	L3C			0.000127	0.00
	H1C			0.000076	0.00
	H2C			0.000109	0.00
	H3C			-0.000005	1.63×10^{-1}
B	L1C-L3C	Clean scan velocity	Clogged scan velocity	3.438033	0.00
	H1C-H2C			1.618183	0.00
	H1C-H3C			1.970457	0.00
C	L1C-L3C	Clean scan velocity	% Reduction in pore diameter	-3368.36	5.68×10^{-34}
		Clogged scan velocity		-1365.91	1.00×10^{-246}
		Change in Velocity		-1482.23	2.26×10^{-253}
	H1C-H2C	Clean scan velocity	% Reduction in pore diameter	-4519.22	0.00
		Clogged scan velocity		-2629.08	0.00
		Change in Velocity		-3481.59	0.00
	H1C-H3C	Clean scan velocity	% Reduction in pore diameter	-3882.99	2.13×10^{-230}
		Clogged scan velocity		-1455.01	2.03×10^{-299}
		Change in Velocity		-1517.80	4.41×10^{-222}

For hypothesis B, the data of Table 5.5 clearly shows that the velocity of the initial clean scan is positively correlated with the velocity of the clogged scan. The strength of this correlation increases with clogging (see H1C-H2C compared with H1C-H3C) and is stronger for the low flow scan than the high flow scan (see L1C-L3C compared with H1C-H3C). The most probable mechanisms for this are the positive feedback between initial velocity and change in diameter, and hence clogged velocity, coupled with the greater change in velocity in the low flow scans (see Figure 5.5).

For hypothesis C there is a negative correlation between velocity and the percentage reduction in pore diameter. For both the high and low flow experiment, this correlation is stronger for the clean scan velocity than for the clogged scan velocity. This suggests that the influence of the initial pore geometry and flow paths on kaolin deposition are greater than the positive feedback between deposition and velocity change.

5.3.7.3 Lagrangian Tracer Analysis

Analysis of the paths of 2362 tracer particles shows how the transport of tracer particles varies as clogging progresses. The change in tracer particle paths and velocities with clogging are shown in Figure 5.9, whilst the change in particle fate, average time of travel, average distance travelled and average tortuosity (split by fate) along with model simulation time are given in Table 5.6.

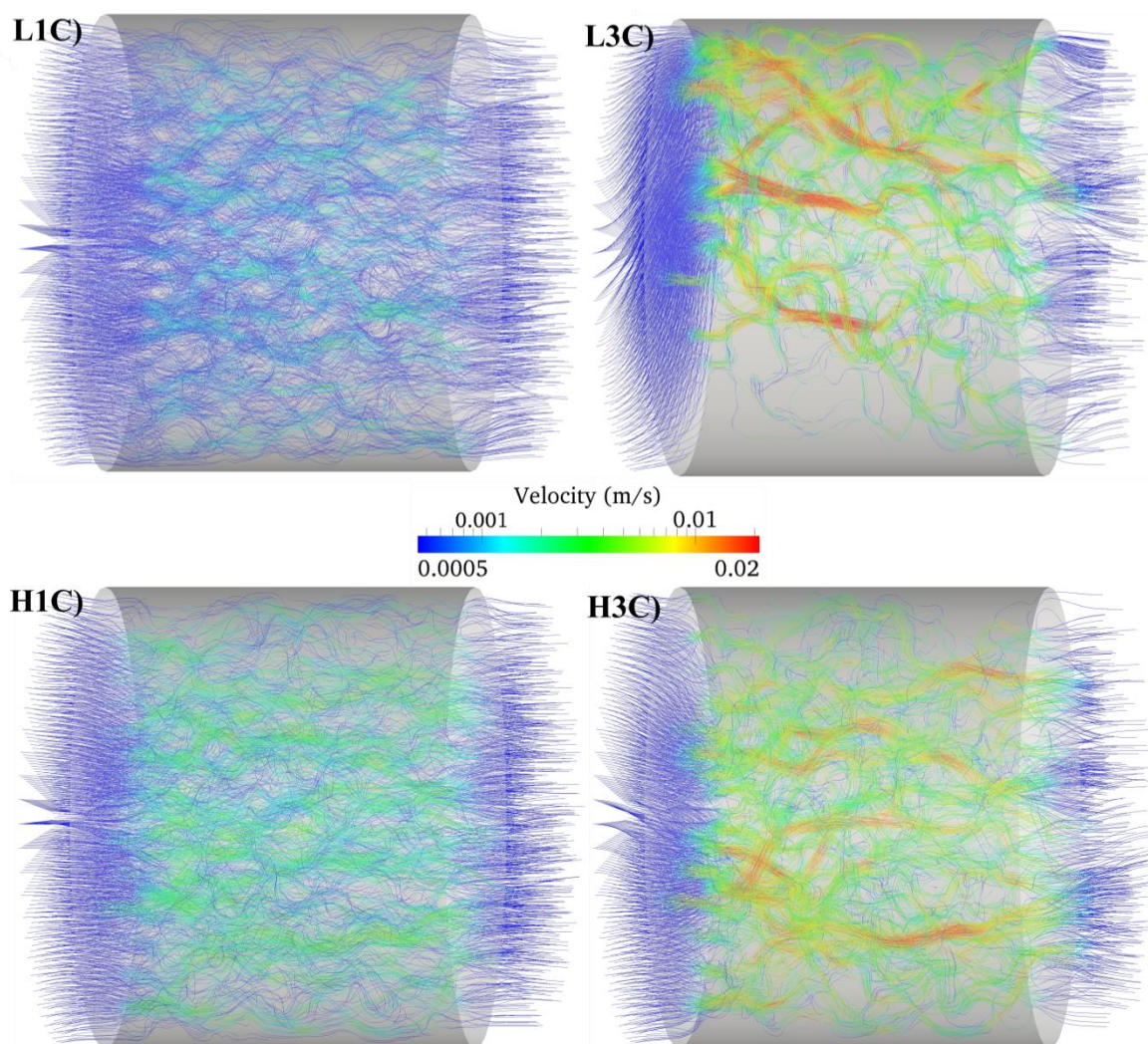


Figure 5.9. Change in tracer paths and velocity with clogging for 2362 tracer particles. Clogging increases particle velocity to a greater degree in the low flow experiment due to the greater reduction in pore volume. Average particle velocity is greater in the H3C simulation but the maximum velocity of a small number of particles was greatest in the L3C simulation.

Table 5.6. Lagrangian particle tracking transport characteristics for tracer particles. Fate refers to whether particles stick to surfaces, escape through the outlet boundary or remain in transit at the end of the simulation. Residence time is measured in pore volumes so that clean, clogged, low flow and high flow experiments are comparable, and in seconds for interpretation of the results.

		L1C	L3C	H1C	H2C	H3C	H4E	H5E
Fate	Number of particles	2362	2362	2362	2362	2362	2362	2362
	Number stick	286	1152	470	836	1109	821	760
	Number escape	728	891	1490	1242	1016	1296	1332
	Number in-transit	1348	319	402	284	237	245	270
Residence time (pore volumes)	Average escape	1.37	2.25	1.68	1.94	1.86	2.00	1.97
	Minimum escape	0.89	0.99	0.82	0.91	0.87	0.64	0.79
	Maximum escape	3.34	4.27	3.37	4.72	5.31	5.16	5.33
	Average all	1.50	2.18	1.87	2.03	2.02	2.14	2.17
Residence time (seconds)	Average escape	328.5	210.3	197.8	164.0	130.9	142.7	142.6
	Minimum escape	214.0	93.0	97.0	77.0	61.0	46.0	57.0
	Maximum escape	799.0	799.0	398.0	399.0	373.0	368.0	386.0
	Average all	358.7	203.7	220.1	172.1	141.7	152.8	157.1
Distance (mm)	Average escape	104.4	130.1	105.6	113.6	117.2	120.4	117.0
	Minimum escape	94.8	107.9	95.1	95.5	99.5	97.9	97.4
	Maximum escape	121.9	178.8	126.6	146.6	162.0	184.2	163.2
	Average all	62.7	59.4	70.5	65.1	58.8	66.8	67.1
Tortuosity	Average escape	1.17	1.44	1.19	1.27	1.31	1.34	1.30
	Minimum escape	1.07	1.14	1.07	1.08	1.12	1.10	1.10
	Maximum escape	1.35	2.00	1.42	1.64	1.81	2.00	1.82
	Average all	1.19	1.44	1.18	1.26	1.28	1.31	1.29
Run time/ Clock time (mins)		192.5	94.7	98.4	67.5	62.4	60.4	61.7

From Figure 5.9 it is apparent that, with clogging and a reduction in the pore volume, the velocity of the pore water and of the suspended tracer particles increased. This increase was greatest in the low flow experiment where the clogged porosity (case L3C) was 16.71% compared with 24.88% for the high flow experiment (case H3C) (Chapter 3, Table 3.6). A change in particle path was also notable with the relatively even distribution of particles in cases L1C and H1C reduced to a few fast channels. This illustrates the

importance of preferential flow paths on particle transport with implications upon particle removal discussed in Section 5.4.3.

Table 5.6 shows the particle transport characteristics. Considering only those particles that escape through the outlet boundary, the average residence time (measured in pore volumes), distance travelled and tortuosity all increase with clogging. The increase in velocity with clogging was negated by the more tortuous and hence longer route the particles take through the filter together with the decrease in pore volume due to clogging. This resulted in an increase in average residence time. However, when escape time is measured in seconds as opposed to pore volumes, there was a decrease in the average residence time and a large decrease in the minimum residence time with clogging. This corresponds with the shift in behaviour of NaCl tracers observed in the column tracer experiments of Chapter 2, discussed further in Section 5.4.3.

5.4 Discussion

The aim of this chapter was to apply CFD modelling to the MRI scan data of clogging gravel filters and determine if meaningful relationships between the spatial variation in gravel structure, flow velocity and kaolin deposition existed.

5.4.1 Model Accuracy

Establishing the accuracy of any numerical model is crucial before conclusions can be drawn from the output. Ideally, experimentally measured calibration data would be available to compare with the model output. Running the model with an alternative CFD package and comparing the output for discrepancies can identify shortcomings in one of the packages. In addition, a parametric study to determine the sensitivity of the model to input parameters and assumptions can be carried out.

With a paramagnetic tracer (Ramanan et al., 2010) or special pulse sequence (Hingerl, 2013) it is possible to directly measure tracer propagation and flow velocity with MRI. Such a tracer was not carried out as it would necessitate an additional MRI scan whilst the development of a pulse sequence tailored to the GEMRIC facility and sample would be

challenging and outwith the scope of this PhD. As such, experimentally measured calibration data was not available.

Two of the main commercial CFD packages comparable to OpenFOAM are ANSYS and COMSOL. OpenFOAM has been shown to be as accurate as ANSYS Fluent and ANSYS CFX (ANSYS Inc.) for both laminar and turbulent fluid flow (Nilsson, 2006; Kosík, 2013; Bayraktar et al., 2012; Andersen & Nielsen, 2008). COMSOL Multiphysics was trialed as an alternative to OpenFOAM, however the mesh generated by the OpenFOAM utility *snappyHexMesh* could not be converted into a form that could be imported into COMSOL and neither could the MRI scan data to allow use of the COMSOL native mesh generation utility. As such, COMSOL was not a viable alternative to OpenFOAM in this instance.

A parametric study was carried out on a subvolume of the MRI scan. Due to the low flow rates of both the low flow and high flow experiment, flow through the filter was likely to be laminar. This was verified in the parametric study by the minimal difference between the flow velocities of a laminar model and a $k-\varepsilon$ turbulence model (Appendix B, Section B.2). Flows were therefore modelled as laminar as this avoided the uncertainty associated with turbulence and surface roughness coefficients. However, a limitation of the laminar model was that accurate computation of wall shear stress requires a turbulent model and, as shown in Appendix B, Section B.2, was heavily dependent on the choice of wall roughness coefficients. For this reason wall shear stress was not reported in the results analysis and no conclusions regarding wall shear stress and kaolin deposition patterns could be made.

A further finding of the parametric study was that a fine mesh (0.6mm) with 2 levels of surface refinement was preferable to a coarser mesh (1.5mm) with 4 levels of surface refinement. Both produced similar velocity profiles across a representative pore, yet the fine mesh consisted of far fewer cells and hence was quicker to solve. The reason for this was that high levels of surface refinement produced many more surface cells not necessary for calculating flow velocities in a laminar model. However, had a surface roughness model been included, then a high number of surface cells could well have been advantageous.

Whilst there is insufficient data to prove that the model accurately reproduces all of the flow features that occurred in the column experiments, its reproduction of bulk flow and sedimentation results, along with the CFD software's proven track record, suggest that the model results on modification of flow pathways and clogging are qualitatively correct. Thus we can have confidence that the simulated correlations between pore geometry, modelled flow velocity and kaolin deposition are representative of what occurs in real gravel filters.

5.4.2 Eulerian Flow Velocities

The flow fields obtained from the Eulerian model illustrate the spatial variation in velocity and how this changes with clogging. As expected, velocities increase with a reduction in pore volume resulting from kaolin deposition. The percentage velocity increase is greatest in the low flow experiment, in line with the greater amount of kaolin deposited in this experiment.

Somewhat unexpectedly, the maximum velocity was recorded in the low flow experiment (0.02320m/s, scan L3C compared with 0.01820m/s, scan H3C) despite an inflow rate half that of the high flow experiment. This is thought to be due to the deposition pattern at low flows in which more kaolin was retained close to the inlet which allowed for the creation of constrictions and regions of localised high velocity. At high flows there was a more uniform distribution of kaolin throughout the filter creating fewer constrictions. This observation is consistent with deep-bed filtration theory for clean gravel beds where the ratio of the suspended particle diameter to media diameter is small. In such a system, the removal of particles by straining is negligible (Barton & Buchberger, 2007; Close et al., 2006) and sedimentation is the dominant process. At higher flow velocities, a greater transport distance through the filter is required for a particle to settle onto the media surface (Jegatheesan & Vigneswaran, 2005) hence the more even distribution of kaolin within the high flow experiment filter.

In Chapter 4, a method for comparing the change in pore volume with clogging at each point in the pore network was developed utilising the medial axis of the pore network. Mapping the flow velocity onto the same pore network medial axis is a useful tool for

comparing the relationship between maximum pore velocity, pore volume and change due to kaolin deposition at each point in the pore network.

Some care should be taken with the analysis of the medial axis velocities for three reasons:

1. Due to the no-slip surface boundary, the maximum velocity is most often located at the medial axis. However, depending upon pore geometry and particularly in large or irregularly shaped pores, this may not always be the case.
2. The velocity at the medial axis of a pore may not be representative of the velocity in the region of that pore in which the kaolin is deposited. Again, this is particularly true of large or irregularly shaped pores.
3. Medial axis points are uniformly spaced (at 300 μm intervals) and hence there are more medial axis points located within large pores than small pores. The effect of large pores is therefore slightly over-represented in any statistical analysis.

Taking these limitations into consideration, there is clearly a positive correlation between pore diameter and maximum pore velocity for scans L1C, L3C, H1C and H2C and the strength of the correlation increases with clogging. Significantly, this may allow pore diameter to be used to predict where kaolin deposition is most likely to take place, which in turn may allow clogging characteristics to be inferred based on pore size distributions that can be obtained for some porous media samples by techniques such as mercury intrusion porosimetry.

However, the correlation is not apparent in scan H3C. It is thought that by this point clogging within the filter has progressed to such an extent that flow velocities at a particular point are no longer defined by the pore diameter at that point; instead they are defined by the connectivity of the entire pore in which that point resides. For instance, a small diameter pore that is well connected and aligned with the principle flow direction would be expected to transmit a greater proportion of the flow than a collection of larger but isolated pores. The change from a system in which flow velocities are defined by pore diameter to one in which velocities are defined by pore connectivity is inextricably linked with the formation of preferential flow paths, discussed in Section 5.4.3. The significance

of this is that a prediction of clogging characteristics based on pore size distribution may only be valid up to a threshold, beyond which pore connectivity is important and there is no substitute for 3D data on pore geometry (e.g. from MRI or x-ray tomography) coupled with velocity measurements or flow velocity modelling.

5.4.3 Lagrangian Particle Tracking of Tracer

With Lagrangian particle tracking (LPT), it is apparent that flow paths through the relatively open and homogenous gravel filter prior to clogging are uniform. As the filter clogs, particle paths change dramatically with most particles confined to preferential flow paths through which they travel at an increased velocity. As a result of this, particles spend less time in the filter and there is a reduced surface area with which they can come into contact.

It is expected that the removal efficiency of pollutants such as pollutant metals would greatly reduce with the formation of the observed preferential flow paths. This is because the metal ions must adsorb onto a surface, yet the only available surfaces are in the preferential flow paths in which the adsorption capacity is likely to be reached. In contrast, the entire surface area of the clean filter is available for adsorption and so it would take longer for the adsorption capacity to be reached.

Likewise, it is expected that the removal efficiency of suspended particles would greatly reduce with the formation of preferential flow paths. An increase in velocity reduces the length of time a particle resides in the filter equating to a reduced chance that this particle will settle onto a collector surface (either gravel or deposited kaolin) under the influence of gravity. With the constant flow rate and kaolin (size and density) characteristics of the experiments, as the low flow areas of the filter continue to clog, velocities in the preferential flow paths will continue to increase.

A logical conclusion from the preferential flow paths observed in the MRI data is that, in a system with constant flow rate and constant influent particle characteristics, eventually the velocity within the remaining open channels must exceed the kaolin deposition threshold.

At this point a dynamic equilibrium will be reached between deposition and erosion of already deposited kaolin and the removal efficiency of the filter will effectively be zero.

Finally, LPT is a useful tool for understanding the change in behaviour of the conservative NaCl tracers observed in Chapter 2, Section 2.8.4 (reproduced in Figure 5.10 below). As the filter clogged, there was a progressive decrease in peak concentration of the NaCl tracer and an extension of the tail coupled with a shift in the centroid to the right. This was interpreted as showing more dispersion of the system and a decrease in hydraulic efficiency.

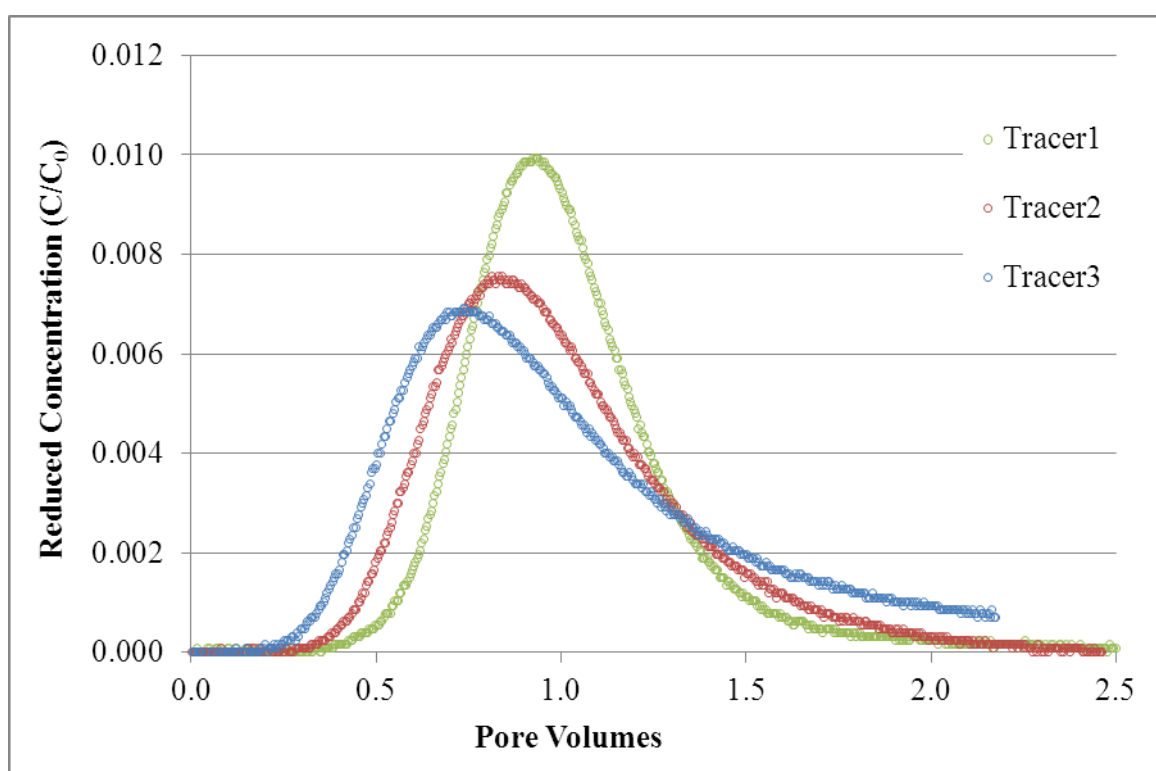


Figure 5.10. Residence time distributions (RTDs) for three NaCl tracers at successive stages of gravel filter clogging: Tracer 1 is for a clean gravel bed, Tracer 2 after first stage of clogging and Tracer 3 after second stage of clogging. See Chapter 2, Section 2.8.4 for experiment details.

From the LPT data we can see the reason for this increase in dispersion is the increase in average tortuosity of the particles which, when the pore volume has been corrected for the reduction in volume due to deposited kaolin (as discussed in Chapter 2), results in a greater

residence time within the filter. Similarly, the early breakthrough of Tracers 2 & 3 with respect to Tracer 1 can be explained from LPT: the increase in residence time due to a slight increase in minimum tortuosity of some particle paths together with the decrease in residence time resulting from an increase in velocity (due to the constant flow rate and decreasing pore volume) had the net result of decreased residence time for a small proportion of the particles.

5.5 Limitations and Further Work

Whilst the MRI scan data and modelling approach were suitable for the aims of this study, there is scope for improvement:

1. More frequent MRI scans would provide data on how rapidly the “clogging front” progresses through a filter whilst also better identifying the point at which pore velocity switches from being determined by pore diameter to being determined by pore connectivity in the high flow experiment.
2. Further scans extending the duration and degree of clogging reached in the low flow experiment would be necessary to determine if/when the switch from pore diameter determined velocity to pore connectivity determined velocity takes place at low velocities.
3. Including at least one tracer propagation scan would be very helpful in determining model accuracy and allow for calibration of model parameters.
4. Reducing filter diameter and length so that the entire filter volume fits within the good quality scan area (Chapter 3, Section 3.4) would allow flow velocities in the entire volume to be modelled. This would remove the hazard of potentially erroneous velocities at the boundaries of the pore geometry.
5. If surface roughness were adequately quantified then a surface roughness model could be applied. This would allow more meaningful calculation of wall shear stress which could in turn be used to predict where kaolin deposition might occur.

5.6 Conclusions

In this chapter we have shown that direct numerical modelling at the pore scale is feasible on a desktop computer and is a valuable tool for understanding the relationship between the spatial variation in velocity and the resulting spatial variation in particle deposition within a gravel filter.

OpenFOAM was suitable software for this task and a laminar flow model without surface roughness was appropriate. A parametric study revealed that the model was not sensitive to parameters such as viscosity, solution scheme, Lagrangian dispersion, mesh resolution and mesh refinement levels; however inappropriate turbulence and surface roughness coefficients did affect results, particularly in the zone close to surfaces.

Correlating flow velocity with change in pore volume highlighted the positive feedback mechanism between initial pore diameter and velocity and hence negative feedback with particle deposition. Maximum flow velocities of 0.0232m/s were observed in the low flow experiment, compared with 0.0182m/s in the high flow experiment. This was attributed to greater deposition at the inlet at the lower flow rate which forced higher localised velocities.

Lagrangian particle tracking helped establish the significance of preferential flow path formation on the removal of both suspended and dissolved pollutants. Preferential flow paths were particularly visible in the low flow experiment where flow was restricted to a few channels and the average tortuosity of the paths that the particles took increased from 1.19 to 1.44 at low flow. The formation of preferential flow paths was also visible in the high flow experiment, although to a lesser extent and average tortuosity only increased from 1.18 to 1.28.

With increasing particle retention, flow velocities increased and the active surface area decreased. Particles spent less time within the filter and, due to channelling into preferential flow paths, they would be expected to come into contact with a reduced surface area for removal. Numerical modelling of the filter pore volume therefore revealed this mechanism by which deposition affects particle removal.

Chapter 6 – Conclusions

The aim of this thesis was to improve understanding of how sediment accumulation within gravel media filters affects filter performance. Key findings of each chapter are summarised below.

6.1 Chapter 2

The pore volume of a gravel filter is an important parameter determining how much sediment, and hence how much pollutant, can be retained within the filter. By using pore volume as a fitting parameter when fitting a convection-dispersion model to tracer breakthrough curves, it has been shown that the tracer accessible pore volume of a gravel filter can be estimated to within at least 10%. Subsequent tracer breakthrough curves can be used to measure the change in mobile pore volume due to sediment accumulation. Such a measurement could be a useful diagnostic tool for assessing the status of a filter and determining when maintenance or remedial works are likely to be necessary.

Turbidity measurement are a quick alternative to measuring total suspended solids (TSS) gravimetrically and are far more practical when numerous measurements are required, or when measurements must be made in the field. However, a relationship between the concentration and turbidity of the suspended particles of interest (e.g. kaolin) are required to convert turbidity into TSS. It was found that a single relationship between kaolin concentration and turbidity was insufficient to calculate the mass of kaolin retained within the filter. This was because the mean particle size of the suspension decreases due to greater removal efficiency of larger particles within the filter hence influent and effluent suspensions had different light scattering properties and hence different turbidities. Deriving separate turbidity/TSS relationships for the influent and effluent particle suspensions was adequate for this thesis as effluent suspension characteristics were similar throughout and between filter runs; however this approach may not work when influent or effluent suspension characteristics vary considerably and gravimetric measurements of TSS should be used instead.

6.2 Chapter 3

With the use of MRI, the 3D structure and porosity of a filter was measured throughout a region of interest (ROI) 84.9mm diameter and 63.3mm long at a resolution of 300 μ m. The resulting 3D volume was free from image artefacts and distortion and the bulk porosity of the entire ROI was within 1.75% of the experimentally measured clean bed filter porosity.

With 2D processing of slices of raw MRI data it was possible to reproduce the experimentally measured bulk porosity giving the impression of accurate image segmentation into water and gravel phases. However, changing the orientation in which the 2D slices were processed resulted in a change in bulk porosity of 2.08%. By using mostly 3D processing steps, and most importantly performing the initial contrast enhancement in 3D, it was possible to reduce this slice processing direction dependent variation in porosity down to 0.76%. This echoes the recommendation of Elliot & Heck (2007) who state that, when 3D data is available, the data should be processed in 3D.

Changes in bulk properties of the filter indicated greater kaolin retention in the lower of the two flow rates investigated, in line with filtration theory. However, the data also indicated different kaolin accumulation characteristics. Even when taking account of the greater total amount of kaolin retained in the low flow rate filter, there was a greater reduction in active porosity and a similar decrease in active surface area. This was attributed to the formation of regions of pore volume disconnected from the main pore volume due to kaolin deposition. The implications of this for pollutant removal are reduced surfaces onto which particles can settle and dissolved pollutants can adsorb.

Removal, and hence porosity change, did not exhibit a strong first-order trend with distance into the filter as was proposed by Iwasaki et al. (1937). Between the first and second kaolin clogging phase, there was very little change in porosity within the MRI ROI (which was located towards the inlet of the gravel filter), but a mass balance measure of kaolin retention confirmed continued kaolin removal elsewhere within the filter. This evidence supports the mobile first-order process zone concept of removal proposed by Ahsan (1995) in which first-order removal occurs during the initial clean bed filtration

stage, but as particles accumulate and the inlet porosity reduces, the first-order zone shifts into an ever diminishing volume approaching the filter outlet.

Analysis of the change in porosity of discrete regions within the filter showed correlation between initial pore volume and percentage change in pore volume: small pores are more likely to clog whilst large pores are more likely to form preferential pathways in which velocities increase and subsequent particle removal becomes less likely.

When 3D volume data is available, as in this study, it was found to be of more benefit to analyse changes in bulk properties of the entire volume (such as average porosity, pore volume and surface area) and in discrete 3D regions evenly distributed throughout the volume than to reduce the data to a series of 2D slices. This was primarily because averaging porosity across an entire slice masked the presence (or absence) of preferential flow paths making quantitative analysis of their effects and importance impossible.

6.3 Chapter 4

Creating a pore network medial axis from the 3D segmented MRI data allowed the change in network characteristics with clogging to be measured. Networks became smaller and less well connected with clogging, particularly in the low flow experiment, whilst average branch tortuosity increased.

Analyses based upon the pore networks were better able to capture the presence of preferential flow paths. Without information on the volume of flow (and hence velocity) in each section of the network, it was not possible to identify preferential flow paths in the clean media scan, but by observing which sections of the pore network did not clog it was possible to infer sections with a higher velocity.

No evidence of previous studies of porous media in which the pore network medial axis was used for measuring the change in pore diameter with clogging was found. This was thought to be because firstly the successive 3D volume scans of clogging media necessary to create the pore networks are rare; and secondly the spatial location of the pore network shifts with accumulation of sediment within that network resulting in no common reference

point with which to compare the change in pore diameter. A method of defining a common reference point between successive scans and assigning the correct pore diameter at each stage of clogging for each point in the pore network was developed. Visualisation of the change in pore diameter clearly showed preferential flow paths develop and become more pronounced with clogging.

6.4 Chapter 5

Using the open source CFD modelling software OpenFOAM, flow velocities within the MRI derived pore geometry were simulated for each stage of clogging. Mapping the flow velocity onto the same pore network medial axis used in Chapter 4 allowed correlation between the flow velocity and the degree of clogging. Initial diameter was positively correlated with velocity and resulted in negative feedback with particle deposition. In the high flow rate experiment the strength of this correlation decreased with clogging and I hypothesise that, with considerable clogging and a high flow velocity, pore geometry and connectivity becomes more important than initial pore diameter in determining where particle deposition occurs.

Tracking of Lagrangian particles representing a conservative tracer allowed the transport of pollutants through a clogging filter to be assessed. The simulated pollutant breakthrough profiles and particle tracks showed that, with clogging, pollutant particles spend less time in the filter, are concentrated within preferential flow paths and encounter a reduced surface area during their journey through the filter, all of which is expected to result in a reduced removal efficiency of pollutants with clogging.

6.5 Reflection on Gravel Filter Design and Further Research

Gravel media SuDS must operate under very variable conditions: influent flow rates and suspended sediment characteristics vary from location to location depending on the road geometry and topography, local land use, amount of road traffic, climate, and pre-treatment. In roughing filters for drinking water treatment, inflow rate can be strictly regulated and hence the flow velocity within the filter can be controlled; this leaves

suspended sediment size, concentration and characteristics as the main variable, together with the change in flow paths as sediment is deposited.

Due to the variability in flow and sediment characteristics experienced by SuDS and roughing filters, it is neither possible nor of value to specify an “optimal” filter design that is appropriate for every situation. Instead, the approach taken in this thesis was to investigate the processes affecting fine sediment accumulation; in particular the link between local pore velocity, particle deposition and the formation of preferential flow paths. The understanding of filter operation gained from this approach has not led to a fundamental physical re-design of gravel filters (for practical reasons such as road slope and size, type and shape of gravel locally available, the physical design of SuDS filters are largely fixed) but has led to a better understanding of how filters clog: filter lifetime is not simply a function of the amount of sediment entering, the removal efficiency and the pore volume available for storage. Assuming a filter design life based on these parameters alone is incorrect and may explain why SuDS filters are predicted to operate for 10 years but many are considered to have failed after only a few years operation and why roughing filter effluent quality can be unpredictable from one filter run to the next. Filter design life and effluent quality are instead very much dependent on the formation of preferential flow paths, disconnected pore volumes and the subsequent increase in local pore velocity. A more realistic expectation of filter design life and effluent quality that takes these processes into account would allow better planning of maintenance activities.

According to Wegelin (1996), roughing filters can be operated until either an unacceptably high inlet pressure head is reached (leading to overflow of the inlet structure), or effluent quality deteriorates to an unacceptable level (termed pollutant breakthrough). The filter must then be cleaned by excavating the gravel media, washing it and replacing it. The same should be true for gravel media SuDS although, as it is not a regulatory requirement for effluent quality to be measured, it is unlikely that pollutant breakthrough would be detected.

Downward hydraulic flushing at a filtration rate of 10-30m/hr has been mentioned by Ahsan (1995) as an alternative method of removing retained sediment in direct horizontal roughing filtration. The erosion stages carried out in the current thesis (flow velocity of

3.44m/hr followed by 4.58m/hr) removed only ~2% of the deposited kaolin (Chapter 3, Section 3.6.1) suggesting that hydraulic flushing at lower flow rates is insufficient to meaningfully restore porosity. To flush at a filtration rate of 10-30m/hr would require a large volume of stored water, additional structures such as pipes and control valves connected to the filter and frequent maintenance of these structures. This would negate one of the major strengths of roughing filters which is their simplicity of design and operation and would be extremely costly to implement for SuDS filters.

Ahsan (1995) also noted that surface washing was more effective at restoring porosity than downward hydraulic flushing. In effect, SuDS filters are subjected to surface washing every rainfall event when they fill and empty. For this reason, particle erosion in SuDS filters may differ from the constant erosional flow rates investigated in this thesis. Further experiments with a variable water level would be required to determine the impact of surface washing on the erosion of retained particles and on subsequent particle retention.

The experiments in this thesis were carried out with kaolin as a surrogate for both suspended river sediment and road runoff particles. As noted in Chapter 2, Section 2.4, kaolin has a relatively narrow particle size distribution. Pre-treatment of road runoff (such as flowing over a grass verge or through a gully pot) is recommended in the design guidance. Pre-treatment would remove the larger particles but, despite this, kaolin may not be representative of road runoff particles entering a SuDS filter. Further experiments with different sized particle suspensions would be necessary to reveal how an operational SuDS filter might clog.

The method of identifying the pore skeleton and correlating initial porosity with change in porosity proposed in this thesis gave valuable information on the spatial heterogeneity in particle deposition. However, more advanced skeletonisation and network analysis techniques that can identify pore bodies, pore throats and take into account their coordination number and aspect ratio may help arrive at a more mechanistic understanding of the particle removal and remobilisation processes.

References

- Ahn, H.W., Park, N.S., Kim, S., Park, S.Y. & Wang, C.K., 2007. Modeling of Particle Removal in the First Coarse Media of Direct Horizontal-Flow Roughing Filtration. *Environmental Technology*, 28(3), pp.339–353.
- Ahrenholz, B., 2008. Prediction of capillary hysteresis in a porous material using lattice-Boltzmann methods and comparison to experimental data and a morphological pore network model. *Advances in Water Resources*, 31(9), pp.1151–1173.
- Ahsan, T., 1995. *Process Analysis and Optimization of Direct Horizontal-Flow Roughing Filtration*. Delft University of Technology.
- Al-Kharusi, A.S. & Blunt, M.J., 2007. Network extraction from sandstone and carbonate pore space images. *Journal of Petroleum Science and Engineering*, 56(4), pp.219–231.
- Ambrosino, F., 2011. *Wall Effects in Particle-Laden Flows*. Università Degli Studi Di Napoli “FedericoII.”
- American Public Health Association, 1999. *Standard Methods for the Examination of Water and Wastewater* 20th Editi. A. D. Eaton, L. S. Clesceri, & A. E. Greenberg, eds., Washington D.C.
- American Society for Testing and Materials, 1985. *Zeta Potential of Colloids in Water and Waste Water. ASTM Standard D 4187-82*,
- Amirtharajah, A., 1988. Some theoretical and conceptual views of filtration. *American Water Works Association*, 80(12), pp.36 – 46.
- Amitay-Rosen, T., Cortis, A. & Berkowitz, B., 2005. Magnetic resonance imaging and quantitative analysis of particle deposition in porous media. *Environmental science & technology*, 39(18), pp.7208–16.
- Andersen, C. & Nielsen, N.E.L., 2008. *Numerical investigation of a BFR using OpenFOAM*. Aalborg University.
- Arganda-Carreras, I., Fernández-González, R., Muñoz-Barrutia, A. & Ortiz-De-Solorzano, C., 2010. 3D reconstruction of histological sections: Application to mammary gland tissue. *Microscopy Research and Technique*, 73(11), pp.1019–1029.
- Arnold, C.L. & Gibbons, C.J., 1996. Impervious surface coverage: The emergence of a key environmental indicator. *Journal of the American Planning Association*, 62(2), pp.243–258.
- Auset, M. & Keller, A. a., 2004. Pore-scale processes that control dispersion of colloids in saturated porous media. *Water Resources Research*, 40(3).

-
- Baldwin, C., Sederman, A.J., Mantle, M., Alexander, P. & Gladden, L.F., 1996. Determination and Characterization of the Structure of a Pore Space from 3D Volume Images. *Journal of Colloid and Interface Science*, 181(1), pp.79–92.
- Barton, J.M. & Buchberger, S.G., 2007. Effect of Media Grain Shape on Particle Straining during Filtration. *Journal of Environmental Engineering*, 133(2), p.211.
- Baumann, T. & Werth, C.J., 2005. Visualization of colloid transport through heterogeneous porous media using magnetic resonance imaging. *Colloids and Surfaces A: Physicochemical and Engineering Aspects*, 265(1-3), pp.2–10.
- Baveye, P.C., Laba, M., Otten, W., Bouckaert, L., Dello Sterpaio, P., Goswami, R.R., Grinev, D., Houston, A., Hu, Y., Liu, J., Mooney, S., Pajor, R., Sleutel, S., Tarquis, A., Wang, W., Wei, Q. & Sezgin, M., 2010. Observer-dependent variability of the thresholding step in the quantitative analysis of soil images and X-ray microtomography data. *Geoderma*, 157(1-2), pp.51–63.
- Bayraktar, E., Mierka, O. & Turek, S., 2012. Benchmark Computations of 3D Laminar Flow Around a Cylinder with CFX, OpenFOAM and FeatFlow. *Int. J. of Computational Science and Engineering*, 7(3), pp.253–266.
- Beazley, K.M., 1972. Viscosity-Concentration Relations in Deflocculated Kaolin Suspensions. *Journal of colloid and interface science*, 41(1).
- Belytschko, T., Kam Liu, W. & Moran, B., 2000. *Nonlinear Finite Elements for Continua and Structures*, Chichester, UK: John Wiley & Sons, Ltd.
- Bentzen, T.R. & Larsen, T., 2009. Heavy Metal and PAH Concentrations in Highway Runoff Deposits Fractionated on Settling Velocities. *Journal of Environmental Engineering*, 135(11), p.1244.
- Bera, B., Mitra, S.K. & Vick, D., 2011. Understanding the micro structure of Berea Sandstone by the simultaneous use of micro-computed tomography (micro-CT) and focused ion beam-scanning electron microscopy (FIB-SEM). *Micron*, 42(5), pp.412–8.
- Blunt, M.J., Bijeljic, B., Dong, H., Gharbi, O., Iglauer, S., Mostaghimi, P., Paluszny, A. & Pentland, C., 2013. Pore-scale imaging and modelling. *Advances in Water Resources*, 51, pp.197–216.
- Boever, E. De, Varloteaux, C., Nader, F.H., Foubert, A., Békri, S., Youssef, S. & Rosenberg, E., 2012. Quantification and Prediction of the 3D Pore Network Evolution in Carbonate Reservoir Rocks. *Oil & Gas Science and Technology - Rev*, 67(1), pp.161–178.
- Boller, M., 1993. Filter mechanisms in roughing filters. *Aqua*, 42(3), pp.174–185.
-

-
- Boller, M. & Kavanaugh, M.C., 1995. Particle characteristics and headloss increase in granular media filtration. *Water Research*, 29(4), pp.1139–1149.
- Boutchko, R., Rayz, V.L., Vandehey, N.T., O’Neil, J.P., Budinger, T.F., Nico, P.S., Druhan, J.L., Saloner, D. a., Gullberg, G.T. & Moses, W.W., 2012. Imaging and modeling of flow in porous media using clinical nuclear emission tomography systems and computational fluid dynamics. *Journal of Applied Geophysics*, 76, pp.74–81.
- Bradford, S.A., Šimůnek, J., Bettahar, M., van Genuchten, M.T. & Yates, S.R., 2003. Modeling colloid attachment, straining, and exclusion in saturated porous media. *Environmental science & technology*, 37(10), pp.2242–50.
- Campbell, N., D’Arcy, B.J., Frost, A., Novotny, V. & Sansom, A., 2004. *Diffuse Pollution. An introduction to the problems and solutions*, London: IWA Publishing.
- Carrigan, C.R., Heinle, R.A., Hudson, G.B., Nitao, J.J. & Zucca, J.J., 1996. Trace gas emissions on geological faults as indicators of underground nuclear testing. *Nature*, 382(8 August).
- Chaudhury, K.N., Sage, D. & Unser, M., 2011. Fast O(1) Bilateral Filtering Using Trigonometric Range Kernels. *IEEE transactions on image processing*, 20(12), pp.3376–82.
- Chen, C., Lau, B.L.T., Gaillard, J.-F. & Packman, A.I., 2009. Temporal evolution of pore geometry, fluid flow, and solute transport resulting from colloid deposition. *Water Resources Research*, 45(6), pp.1–12.
- Chen, Q., Rack, F.R. & Balcom, B.J., 2006. Quantitative magnetic resonance imaging methods for core analysis. In R. G. Rothwell, ed. *New Techniques in Sediment Core Analysis*. London: The Geological Society of London, pp. 193–207.
- Chin, D.A., 2000. *Water Resources Engineering*, Englewood-Cliffs, NJ: Prentice-Hall.
- Christensen, B., 2006. *Using X-ray Tomography and Lattice Boltzmann Modeling to Evaluate Pore-scale Processes in Porous Media*. Technical University of Denmark.
- Claytor, R.A. & Schueler, T.R., 1996. *Design of Storm water Filtering Systems*, Ellicott City: Center for Watershed Protection.
- Clifford, N.J., Richards, K.S., Brown, R.A. & Lane, S.N., 1995. Laboratory and field assessment of an infrared turbidity probe and its response to particle size and variation in suspended sediment concentration. *Hydrological Sciences*, 40(June), pp.771–791.
- Close, M.E., Pang, L., Flintoft, M.J. & Sinton, L.W., 2006. Distance and flow effects on microsphere transport in a large gravel column. *Journal of environmental quality*, 35(4), pp.1204–12.
-

-
- Cooper, D.M.L., Turinsky, A.L., Sensen, C.W. & Hallgrímsson, B., 2003. Quantitative 3D analysis of the canal network in cortical bone by micro-computed tomography. *The Anatomical Record. Part B, New anatomist*, 274(1), pp.169–79.
- Crabtree, B. & Whitehead, M.R.A., 2006. Monitoring pollutants in highway runoff. *Water and Environment Journal*, 20(4), pp.287–294.
- D’Arcy, B.J., Ellis, J.B., Ferrier, R.C., Jenkins, A. & Dils, R., 2000. *Diffuse Pollution Impacts: The Environmental and Economic Effects of Diffuse Pollution in the UK*, Terrence Dalton Publishing Ltd., CIWEM.
- Dankers, P. & Winterwerp, J., 2007. Hindered settling of mud flocs: Theory and validation. *Continental Shelf Research*, 27(14), pp.1893–1907.
- Deletic, A. & Orr, D.W., 2005. Pollution buildup on road surfaces. *Journal of Environmental Engineering*, 131(January), p.49.
- Dierberg, F.E. & DeBusk, T.A., 2005. An evaluation of two tracers in surface-flow wetlands: rhodamine-WT and lithium. *Wetlands*, 25(1), pp.8–25.
- Dietrich, O., Reiser, M.F. & Schoenberg, S.O., 2008. Artifacts in 3-T MRI: physical background and reduction strategies. *European Journal of Radiology*, 65(1), pp.29–35.
- Dórea, C.C., 2005. *Chemically-Enhanced Gravel Pre-Filtration for Slow Sand Filtration*. University of Surrey.
- Doube, M., Kłosowski, M.M., Arganda-carreras, I., Cordelières, F.P., Dougherty, R.P., Jackson, J.S., Schmid, B., Hutchinson, J.R. & Shefelbine, S.J., 2010. BoneJ: Free and extensible bone image analysis in ImageJ. *Bone*, 47(6), pp.1076–1079.
- Dougherty, R.P. & Kunzelmann, K.-H., 2007. Computing Local Thickness of 3D Structures with ImageJ. *Microscopy and Microanalysis*, 13(S02).
- Dudgeon, C.R. & Aust, M.I.E., 1968. Relationship between porosity and permeability of coarse granular materials. In *Conference on Hydraulics and Fluid Mechanics*. The Institution of Engineers, Australia, pp. 76–80.
- Duncan, H.P., 1999. *Urban stormwater quality: a statistical overview*,
- Elliot, T.R. & Heck, R.J., 2007. A comparison of 2D vs. 3D thresholding of X-ray CT imagery. *Canadian Journal of Soil Science*, 1(October), pp.405–412.
- Elliot, T.R., Reynolds, W.D. & Heck, R.J., 2010. Use of existing pore models and X-ray computed tomography to predict saturated soil hydraulic conductivity. *Geoderma*, 156(3-4), pp.133–142.
-

-
- Ellis, J.B., Harrop, D. & Revitt, D., 1986. Hydrological controls of pollutant removal from highway surfaces. *Water Research*, 20(5), pp.589–595.
- Ellis, J.B. & Revitt, D.M., 1982. Incidence of heavy metals in street surface sediments: Solubility and grain size studies. *Water, Air & Soil Pollution*, 17(1), pp.87–100.
- Emerson, C.H. & Traver, R.G., 2008. Multiyear and Seasonal Variation of Infiltration from Storm-Water Best Management Practices. *Journal of Irrigation and Drainage Engineering*, 134(5), p.598.
- Faulkner, D., 1999. *Flood Estimation Handbook, Volume 2: Rainfall Frequency Estimation*, Wallingord: Institute of Hydrology.
- Fernández-Barrera, A.H., Rodríguez-Hernández, J., Castro-Fresno, D. & Vega-Zamanillo, A., 2010. Laboratory analysis of a system for catchment, pre-treatment and treatment (SCPT) of runoff from impervious pavements. *Water Science & Technology*, 61(7), pp.1845–52.
- Ferreira, T. & Rasband, W., 2012. *ImageJ User Guide, IJ 1.46r Revised Edition*,
- Galvis, G., 1999. *Development and Evaluation of Multistage Filtration Plants: An Innovative, Robust and Efficient Water Treatment Technology*. University of Surrey, Guildford, UK.
- German, J. & Svensson, G., 2002. Metal content and particle size distribution of street sediments and street sweeping waste. *Water Science & Technology*, 46(6-7), pp.191–198.
- Gonzalez, R.C. & Woods, R.E., 2008. *Digital Image Processing Third Edit.*, Prentice Hall.
- Grant, S.B., Rekhi, N.V., Pise, N.R. & Reeves, R.L., 2003. *A review of the contaminants and toxicity associated with particles in stormwater runoff*, Sacramento, CA.
- Gruber, I., Zinovik, I., Holzer, L., Flisch, A. & Poulikakos, L.D., 2012. A computational study of the effect of structural anisotropy of porous asphalt on hydraulic conductivity. *Construction and Building Materials*, 36, pp.66–77.
- Haynes, H., Ockelford, A.-M., Vignaga, E. & Holmes, W.M., 2012. A new approach to define surface/sub-surface transition in gravel beds. *Acta Geophysica*, 60(6), pp.1589–1606.
- Haynes, H., Vignaga, E. & Holmes, W.M., 2009. Using magnetic resonance imaging for experimental analysis of fine-sediment infiltration into gravel beds. *Sedimentology*, 56(7), pp.1961–1975.
- Hellström, J.G.I. & Lundström, T.S., 2006. Flow through Porous Media at Moderate Reynolds Number. In *Modelling For Processing*. Riga: International Scientific Colloquium, pp. 129–134.
-

-
- Herngren, L., Goonetilleke, A. & Ayoko, G.A., 2006. Analysis of heavy metals in road-deposited sediments. *Analytica Chimica Acta*, 571, pp.270–278.
- Herzig, J.P., Leclerc, D.M. & Le Goff, P., 1970. Suspensions through Porous Media—New differential equation for clogged beds is derived. *Industrial and Engineering Chemistry*, 62(5), pp.8–35.
- Hingerl, F., 2013. Comparative Experimental and Modeling Study of Fluid Velocities in Heterogeneous Rocks. In *AGU 2013 Fall Meeting*. San Francisco.
- HMSO, 2006. *Design Manual for Roads and Bridges, Volume 4, Section 2, Part 1, HA 103/06 Vegetated Drainage Systems for Highway Runoff*,
- HMSO, 1998. *Design Manual for Roads and Bridges, Volume 4, Section 2, Part 1, HA 39/98 Edge of Pavement Details*, HMSO.
- HMSO, 2000. *Design Manual for Roads and Bridges, Volume 4, Section 2, Part 3, HA 102/00 Spacing of Road Gullies*,
- HMSO, 2005a. *Design Manual for Roads and Bridges, Volume 6, Section 1, Part 2, TD 27/05 Cross-sections and Head Rooms*,
- HMSO, 2005b. *The Water Environment (Controlled Activities) (Scotland) Regulations 2005*, Scotland.
- Holland, J., Martin, J., Granata, T., Bouchard, V., Quigley, M. & Brown, L., 2004. Effects of wetland depth and flow rate on residence time distribution characteristics. *Ecological Engineering*, 23(3), pp.189–203.
- Iassonov, P., Gebrenegus, T. & Tuller, M., 2009. Segmentation of X-ray computed tomography images of porous materials: A crucial step for characterization and quantitative analysis of pore structures. *Water Resources Research*, 45(9), pp.1–12.
- Iassonov, P. & Tuller, M., 2010. Application of Segmentation for Correction of Intensity Bias in X-Ray Computed Tomography Images. *Vadose Zone Journal*, 9(1), p.187.
- Ingallinella, A.M., Stecca, L.M. & Wegelin, M., 1997. Up-flow roughing filtration: rehabilitation of a water treatment plant in Tarata, Bolivia. *Water Science & Technology*, 37(9), pp.105–112.
- Iwasaki, T., Slade, J.J. & Stanley, W.E., 1937. Some notes on sand filtration (with discussion). *American Water Works Association*, 29(10), pp.1591–1602.
- Janoo, V.C., 1998. *Quantification of shape, angularity, and surface texture of base course materials*,
-

-
- Jegatheesan, V. & Vigneswaran, S., 2005. Deep Bed Filtration: Mathematical Models and Observations. *Critical Reviews in Environmental Science and Technology*, 35(6), pp.515–569.
- Jelinkova, V., Snehota, M., Pohlmeier, A., van Dusschoten, D. & Cislerova, M., 2011. Effects of entrapped residual air bubbles on tracer transport in heterogeneous soil: Magnetic resonance imaging study. *Organic Geochemistry*, 42(8), pp.991–998.
- Johns, M.L., Sederman, A.J., Bramley, A.S., Gladden, L.F. & Alexander, P., 2000. Local transitions in flow phenomena through packed beds identified by MRI. *AIChE Journal*, 46(11), pp.2151–2161.
- Jovicich, J., Czanner, S., Greve, D., Haley, E., van der Kouwe, A., Gollub, R., Kennedy, D., Schmitt, F., Brown, G., Macfall, J., Fischl, B. & Dale, A., 2006. Reliability in multi-site structural MRI studies: effects of gradient non-linearity correction on phantom and human data. *NeuroImage*, 30(2), pp.436–43.
- Kadlec, R.H., 1994. Detention and mixing in free water wetlands. *Ecological Engineering*, 3(4), pp.345–380.
- Kayhanian, M., Suverkropp, C., Ruby, A. & Tsay, K., 2007. Characterization and prediction of highway runoff constituent event mean concentration. *Journal of Environmental Management*, 85(2), pp.279–295.
- Keller, L.M., Holzer, L., Wepf, R. & Gasser, P., 2011. 3D geometry and topology of pore pathways in Opalinus clay: Implications for mass transport. *Applied Clay Science*, 52(1-2), pp.85–95.
- Kemblowski, Z. & Mertl, J., 1974. Pressure drop during the flow of Stokesian fluids through granular beds. *Chemical Engineering Science*, 29(1), pp.213–223.
- Kleinhans, M., Jeukens, C., Bakker, C. & Frings, R., 2008. Magnetic Resonance Imaging of coarse sediment. *Sedimentary Geology*, 208(3-4), pp.69–78.
- Kosík, A., 2013. The CFD simulation of the flow around the aircraft using OpenFOAM and ANSA. In *Proceedings of the 5th ANSA & μ ETA International Conference*. Thessaloniki.
- Kress, J., Yun, T.S., Narsilio, G. a., Matthew Evans, T. & Lee, D.-S., 2012. Evaluation of hydraulic conductivity in 3D random and heterogeneous particulate materials using network model. *Computers and Geotechnics*, 40, pp.45–52.
- Lau, S.L., Han, Y., Kang, J.H., Kayhanian, M. & Stenstrom, M.K., 2009. Characteristics of Highway Stormwater Runoff in Los Angeles: Metals and Polycyclic Aromatic Hydrocarbons. *Water Environment Research*, 81(3), pp.308–318.
- Lau, S.L. & Stenstrom, M.K., 2005. Metals and PAHs adsorbed to street particles. *Water Research*, 39(17), pp.4083–4092.
-

-
- Lee, T.-C., Kashyap, R.L. & Chu, C.-N., 1994. Building skeleton models via 3D medial surface axis thinning algorithms. *CVGIP: Graphical Models and Image Processing*, 56(6), pp.462–478.
- Li, Y., Lau, S.L., Kayhanian, M. & Stenstrom, M.K., 2006. Dynamic characteristics of particle size distribution in highway runoff: Implications for settling tank design. *Journal of Environmental Engineering*, 132(8), p.852.
- Lin, E., Page, D. & Pavelic, P., 2008. A new method to evaluate polydisperse kaolinite clay particle removal in roughing filtration using colloid filtration theory. *Water Research*, 42(3), pp.669–76.
- Lindquist, W.B. & Venkatarangan, A., 2000. Pore and throat size distributions measured from synchrotron X-ray tomographic images of Fontainebleau sandstones. *Journal of Geophysical Research*, 105(B9), pp.21509–21527.
- Lindsey, G., Roberts, L. & Page, W., 1992. Inspection and maintenance of infiltration facilities. *Journal of Soil and Water Conservation*, 47(6), pp.481–486.
- Lorensen, W.E. & Cline, H.E., 1987. Marching cubes: A high resolution 3D surface construction algorithm. In *Proceedings of the 14th annual conference on Computer graphics and interactive techniques - SIGGRAPH '87*. New York: ACM Press, pp. 163–169.
- Losleben, T.R., 2008. *Pilot Study of Horizontal Roughing Filtration in Northern Ghana as Pretreatment for Highly Turbid Dugout Water*. Massachusetts Institute of Technology.
- Luo, L., Lin, H. & Li, S., 2010. Quantification of 3-D soil macropore networks in different soil types and land uses using computed tomography. *Journal of Hydrology*, 393(1-2), pp.53–64.
- Mahvi, A.H., Moghaddam, M.A., Nasser, S. & Naddafi, K., 2004. Performance of a Direct Horizontal Roughing Filtration (DHRF) System in Treatment of Highly Turbid Water. *Iranian Journal of Environmental Health Science and Engineering*, 1(1), pp.1–4.
- McKenzie, E.R., Wong, C.M., Green, P.G., Kayhanian, M. & Young, T.M., 2008. Size dependent elemental composition of road-associated particles. *The Science of the total environment*, 398(1-3), pp.145–153.
- Menter, F.R., 1994. Two-Equation Eddy-Viscosity Turbulence Models for Engineering Applications. *AIAA Journal*, 32(8), pp.1598–1605.
- Munkholm, L.J., Heck, R.J. & Deen, B., 2012. Soil pore characteristics assessed from X-ray micro-CT derived images and correlations to soil friability. *Geoderma*, 181-182, pp.22–29.
-

-
- Nallasamy, M., 1987. Turbulence Models and Their Applications to the Prediction of Internal Flows: A Review. *Computers & Fluids*, 15(2), pp.151–194.
- Napier, F., D'Arcy, B.J. & Jefferies, C., 2008. A review of vehicle related metals and polycyclic aromatic hydrocarbons in the UK environment. *Desalination*, 226(1-3), pp.143–150.
- Narsilio, G. a., Kress, J. & Yun, T.S., 2010. Characterisation of conduction phenomena in soils at the particle-scale: Finite element analyses in conjunction with synthetic 3D imaging. *Computers and Geotechnics*, 37(7-8), pp.828–836.
- National Statistics, 2008. *Scottish Transport Statistics*,
- Niblack, W., 1986. *An Introduction to Digital Image Processing*, Englewood-Cliffs, NJ: Prentice-Hall International.
- Nicholson, J. & O'Connor, B. a., 1986. Cohesive Sediment Transport Model. *Journal of Hydraulic Engineering*, 112(7), pp.621–640.
- Nilsson, H., 2006. Some Experiences on the Accuracy and Parallel Performance of OpenFOAM for CFD in Water Turbines. In B. Kågström, E. Elmroth, & J. Dongarra, eds. *Proceedings of the PARA '06 Workshop*. Springer-Verlag, pp. 168–176.
- Nkwonta, O. & Ochieng, G., 2009. Roughing filter for water pre-treatment technology in developing countries : A review. *International Journal of Physical Sciences*, 4(9), pp.455–463.
- Norris, M.J., Pulford, I.D., Haynes, H., Dorea, C.C. & Phoenix, V.R., 2013. Treatment of heavy metals by iron oxide coated and natural gravel media in Sustainable urban Drainage Systems. *Water Science & Technology*, 68(3), pp.674–80.
- O'Melia, C.R. & Stumm, W., 1967. Theory of Water Filtration. *American Water Works Association*, 59(11), pp.1393–1412.
- Ochieng, G.M.M., Otieno, F.A.O., Ogada, T.P.M., Shitote, S.M. & Menzwa, D.M., 2004. Performance of multistage filtration using different filter media. *Water S. A.*, 30(3), pp.361–368.
- OpenFOAM Foundation, 2013. *Open ∇ FOAM. The Opens Source CFD Toolbox User Guide 2.2.1 ed.*, OpenFOAM Foundation.
- Ostendorf, D.W., Peeling, D.C., Mitchell, T.J. & Pollock, S.J., 2001. Chloride persistence in a deiced access road drainage system. *Journal of environmental quality*, 30(5), pp.1756–70.
- Otten, W., Grinev, D., Perez-reche, F., Neri, F., da Costa, L., Biana, M., Gilligan, C. & Taraskin, S., 2010. Resilience of soil to biological invasion: analysis of spread on networks. In *19th World Congress of Soil Science*. Brisbane, Australia, pp. 68–71.
-

-
- Pal, S.K., Wallis, S.G. & Arthur, S., 2010. Assessment of Heavy Metals Emission on Road Surfaces. In *Proceedings of the 15th International Conference on Heavy Metals in the Environment*. Gdansk.
- Papafotiou, A., Helmig, R., Schaap, J., Lehmann, P., Kaestner, A., Fluhler, H., Neuweiler, I., Hassanein, R., Ahrenholz, B., Tolke, J., Peters, A. & Durner, W., 2008. From the pore scale to the lab scale: 3-D lab experiment and numerical simulation of drainage in heterogeneous porous media. *Advances in Water Resources*, 31(9), pp.1253–1268.
- Pattanaik, B.R., Gupta, A. & Shankar, H.S., 2004. Residence time distribution model for soil filters. *Water Environment Research*, 76(2), pp.168–174.
- Pendse, H., Tien, C., Rajagopalan, R. & Turian, R.M., 1978. Dispersion measurement in clogged filter beds: A diagnostic study on the morphology of particle deposits. *AIChE Journal*, 24(3), pp.473–485.
- Peth, S., 2010. Applications of Microtomography in Soils and Sediments. In B. Singh & M. Grafe, eds. *Developments in Soil Science, Volume 34, Synchrotron-Based Techniques in Soils and Sediments*.
- Peth, S., Horn, R., Beckmann, F., Donath, T., Fischer, J. & Smucker, a. J.M., 2008. Three-Dimensional Quantification of Intra-Aggregate Pore-Space Features using Synchrotron-Radiation-Based Microtomography. *Soil Science Society of America Journal*, 72(4), p.897.
- Phoenix, V.R., Holmes, W.M. & Ramanan, B., 2008. Magnetic resonance imaging (MRI) of heavy-metal transport and fate in an artificial biofilm. *Mineralogical Magazine*, 72(1), pp.483–486.
- Pini, R. & Benson, S.M., 2013. Characterization and scaling of mesoscale heterogeneities in sandstones. *Geophysical Research Letters*, 40(15), pp.3903–3908.
- Pittner, C. & Allerton, G., 2010. *SUDS For Roads*,
- Poleto, C., Bortoluzzi, E.C., Charlesworth, S.M. & Merten, G.H., 2009. Urban sediment particle size and pollutants in Southern Brazil. *Journal of Soils and Sediments*, 9(4), p.317327.
- Rajapakse, J.P. & Ives, K.J., 1990. Pre-Filtration of Very Highly Turbid Waters Using Pebble Matrix Filtration. *Water and Environment Journal*, 4(2), pp.140–147.
- Ramanan, B., Holmes, W.M., Sloan, W.T. & Phoenix, V.R., 2010. Application of paramagnetically tagged molecules for magnetic resonance imaging of biofilm mass transport processes. *Applied and environmental microbiology*, 76(12), pp.4027–36.
- Reingruber, H., Zankel, a., Mayrhofer, C. & Poelt, P., 2011. Quantitative characterization of microfiltration membranes by 3D reconstruction. *Journal of Membrane Science*, 372(1-2), pp.66–74.
-

-
- Richardson, C.P. & Tripp, G.A., 2006. Investigation of Boundary Shear Stress and Pollutant Detachment from Impervious Surface During Simulated Urban Storm Runoff. *Journal of Environmental Engineering*, 132(1), p.85.
- Ridler, T.W. & Calvard, S., 1978. Picture Thresholding Using an Iterative Selection Method. *IEEE Transactions on Systems, Man and Cybernetics*, 8(8), pp.630–632.
- Rodier, E., Dodds, A., Leclerc, D. & Clément, G., 1997. Changes in fluid residence time distribution during deep-bed filtration. *Chemical Engineering Journal*, 68, pp.131–138.
- Rooklidge, S.J., Ketchum, L.H. & Burns, P.C., 2002. Clay removal in basaltic and limestone horizontal roughing filters. *Advances in Environmental Research*, 7(1), pp.231–237.
- Rowlands, E.G. & Ellis, J.B., 2007. Highway Filter Drain Maintenance and Re-Instatement: A Waste Management Issue. In *Novatech*. Lyon, France, pp. 1173–1180.
- Sánchez, L.D., Sánchez, A., Galvis, G., Latorre, J. & Visscher, J.T., 2006. *Multi-Stage Filtration; Thematic Overview Paper 15*,
- Sansalone, J.J., Koran, J.M., Smithson, J.A. & Buchberger, S.G., 1998. Physical characteristics of urban roadway solids transported during rain events. *Journal of Environmental Engineering*, 124, pp.427–440.
- Schluter, W., 2005. *Bahaviour and Effectiveness of In-ground Sustainable Urban Drainage Systems in Scotland*. University of Abertay Dundee.
- Scholes, L., Revitt, D.M. & Ellis, J.B., 2008. A systematic approach for the comparative assessment of stormwater pollutant removal potentials. *Journal of Environmental Management*, 88(3), pp.467–478.
- Sederman, A.J. & Gladden, L.F., 2001. Magnetic resonance imaging as a quantitative probe of gas-liquid distribution and wetting efficiency in trickle-bed reactors. *Chemical Engineering Science*, 56, pp.2615–2628.
- Sederman, A.J., Johns, M.L., Alexander, P. & Gladden, L.F., 1998. Structure-flow correlations in packed beds. *Chemical Engineering Science*, 53(12), pp.2117–2128.
- Sezgin, M. & Sankur, B., 2004. Survey over image thresholding techniques and quantitative performance evaluation. *Journal of Electronic Imaging*, 13(1), pp.146–165.
- Sham, E., Mantle, M.D., Mitchell, J.K., Tobler, D.J., Phoenix, V.R. & Johns, M.L., 2013. Monitoring bacterially induced calcite precipitation in porous media using magnetic resonance imaging and flow measurements. *Journal of contaminant hydrology*, 152, pp.35–43.
-

-
- Shuster, W.D., Pappas, E. & Zhang, Y., 2008. Laboratory-Scale Simulation of Runoff Response from Pervious-Impervious Systems. *Journal of Hydrologic Engineering*, 13(9), p.886.
- Silin, D.B., Jin, G. & Patzek, T.W., 2003. Robust Determination of the Pore Space Morphology in Sedimentary Rocks. In *Proceedings of SPE Annual Technical Conference and Exhibition*. Denver, USA: Society of Petroleum Engineers, Inc., pp. 1–15.
- Siriwardene, N.R., Deletic, A. & Fletcher, T.D., 2007. Modeling of Sediment Transport through Stormwater Gravel Filters over Their Lifespan. *Environmental Science & Technology*, 41(23), p.80998103.
- Spalart, P.R. & Allmaras, S.R., 1994. A one-equation turbulence model for aerodynamic flows. *La Recherche Aerospace*, pp.5–21.
- Sternberg, S.R., 1983. Biomedical Image Processing. *IEEE*, pp.22–34.
- Stovin, V.R., Guymer, I., Gaskell, P. & Maltby, L., 2010. Evaluation of a highway runoff TSS model against new UK data. In *Proceedings of the 17th IAHR APD*. Auckland.
- Syring, S.M., Krishnamurthy, R. & MacKay, A.A., 2009. Attenuation of Roadway-Derived Heavy Metals by Wood Chips. *Journal of Environmental Engineering*, 135(9), p.747.
- Tang, G., Mayes, M. a., Parker, J.C. & Jardine, P.M., 2010. CXTFIT/Excel—A modular adaptable code for parameter estimation, sensitivity analysis and uncertainty analysis for laboratory or field tracer experiments. *Computers & Geosciences*, 36(9), pp.1200–1209.
- Tapia, X.P., 2009. *Modelling of wind flow over complex terrain using OpenFoam*. University of Gavle.
- Tarquis, A.M., Heck, R.J., Andina, D., Alvarez, A. & Antón, J.M., 2009. Pore network complexity and thresholding of 3D soil images. *Ecological Complexity*, 6(3), pp.230–239.
- Thévenaz, P., Sage, D. & Unser, M., 2012. Bi-exponential edge-preserving smoother. *IEEE transactions on image processing*, 21(9), pp.3924–36.
- Thorpe, A. & Harrison, R.M., 2008. Sources and properties of non-exhaust particulate matter from road traffic: a review. *The Science of the total environment*, 400(1-3), pp.270–282.
- Tsukahara, M., Mitrovic, S., Gajdosik, V., Margaritondo, G., Pournin, L., Ramaioli, M., Sage, D., Hwu, Y., Unser, M. & Liebling, T.M., 2008. Coupled tomography and distinct-element-method approach to exploring the granular media microstructure in a jamming hourglass. *Physical Review E*, 77(6), p.061306.
-

-
- United Nations High Commissioner for Refugees, 1992. *Water Manual for Refugee Situations*,
- Various Contributors, 2013. Unofficial OpenFOAM Wiki. Available at: openfoamwiki.net [Accessed September 14, 2013].
- Vogel, H.J. & Roth, K., 2001. Quantitative morphology and network representation of soil pore structure. *Advances in Water Resources*, 24(3-4), pp.233–242.
- Vovk, U., Pernus, F. & Likar, B., 2007. A Review of Methods for Correction of Intensity Inhomogeneity in MRI. *IEEE transactions on medical imaging*, 26(3), pp.405–421.
- Wang, Y., Li, Y., Fortner, J.D., Hughes, J.B., Abriola, L.M. & Pennell, K.D., 2008. Transport and retention of nanoscale C60 aggregates in water-saturated porous media. *Environmental Science & Technology*, 42(10), pp.3588–3594.
- Weber-Shirk, M.L. & Dick, R.I., 1997. Physical-chemical mechanisms in slow sand filters. *American Water Works Association*.
- Wegelin, M., 1996. *Surface Water Treatment by Roughing Filters. A design, construction and operation manual*, Duebendorf, Switzerland.
- Wegelin, M., Boller, M. & Schertenleib, R., 1987. Particle Removal by Horizontal-Flow Roughing Filtration. *Aqua*, 2(36), pp.80–90.
- Werner, T.M. & Kadlec, R.H., 2000. Wetland residence time distribution modeling. *Ecological Engineering*, 15(1-2), pp.77–90.
- Werth, C.J., Zhang, C., Brusseau, M.L., Oostrom, M. & Baumann, T., 2010. A review of non-invasive imaging methods and applications in contaminant hydrogeology research. *Journal of contaminant hydrology*, 113(1-4), pp.1–24.
- Woods-ballard, B., Kellagher, P., Martin, P., Jefferies, C., Bray, R. & Shaffer, P., 2007. *The SUDS manual*, CIRIA.
- Wu, P. & Zhou, Y., 2009. Simultaneous removal of coexistent heavy metals from simulated urban stormwater using four sorbents: a porous iron sorbent and its mixtures with zeolite and crystal gravel. *Journal of hazardous materials*, 168(2-3), pp.674–80.
- Yao, K.-M., Habibian, M.T. & O'Melia, C.R., 1971. Water and Waste Water Filtration: Concepts and Applications. *Environmental Science & Technology*, 5(11), p.1105.
- Zhang, R., Hu, S., Zhang, X. & Yu, W., 2007. Dissolution Kinetics of Dolomite in Water at Elevated Temperatures. *Aquatic Geochemistry*, 13(4), pp.309–338.
- Zhang, W., Morales, V.L., Cakmak, M.E., Salvucci, A.E., Geohring, L.D., Hay, A.G., Parlange, J.-Y. & Steenhuis, T.S., 2010. Colloid transport and retention in unsaturated
-

porous media: effect of colloid input concentration. *Environmental Science & Technology*, 44(13), pp.4965–72.

Zuiderveld, K., 1994. *Graphics Gems IV* P. S. Heckbert, ed., Pittsburgh: Academic Press.

Appendix A – Glossary of Image Processing

The theory and methodology underlying the pre-processing, segmentation and post-processing that resulted in the selection of an optimum MRI scan image processing method (Section 3.5.2) is documented in this appendix.

A.1 Pre-segmentation Processing

Pre-segmentation processing is an important step for improving the suitability of the data for the chosen segmentation method. Five methods were investigated as part of this research:

- General: cropping to ROI and image alignment.
- Contrast enhancement: histogram normalising, histogram equalising, local contrast enhancement and unsharp mask.
- Noise removal: mean filter, median filter, bandpass filter, Gaussian blur, outlier removal and background subtraction.
- Edge modification: sharpen and greyscale morphological erode/dilate sequence.
- Edge preserving noise removal: Bi-exponential edge preserving smoother and bilateral filter.

A.1.1 General

Cropping the MRI data was necessary as the region of interest (ROI) was smaller than the total volume scanned in the MRI. The total scan area also included areas outside the column which, despite the lack of water there, produced “noise”. Cropping the image to the ROI before locally adaptive thresholding produced a poorer segmentation as the area outside the ROI still contains information (noisy pixels) used in the search radius with the effect of producing errors at the edge of the ROI. Some image cropping before segmentation is permissible so as to reduce the volume and hence processing time. However, cropping to the ROI should therefore only be carried out in post-processing (after segmentation) as this way the segmentation errors occur outside the ROI.

Accurate image alignment between the clean gravel scan and subsequent clogged scans was crucial for determining kaolin deposition. Using markers inside the column as control points, images were aligned in the X and Y planes by translation and rotation and in the Z plane by adding or deleting slices. By using the bicubic interpolation option in ImageJ, translating the image by a fraction of a pixel and rotation by any angle was possible. Alignment in the z axis was possible in multiples of 0.3mm (the depth of each slice). Due to the use of interpolation, image alignment must be one of the very first pre-processing steps performed on the full grey-scale image; it is important to note that this step must come before binary processing as interpolating a black/white sediment/pore binary image would result in the creation of false grey pixels.

A.1.2 Contrast Enhancement

The MRI data was a 15-bit grey scale intensity histogram which was imported into ImageJ as 16-bit. As can be seen in Figure A.1 (left), the raw data does not cover the full range of possible intensities. As any automatic segmentation method relies on changes in intensity to determine the separate phases, increasing the contrast of the image is desirable.

Normalising the histogram involves stretching the data linearly over the entire range of possible intensities. As the raw data was 16-bit, but the data used for the segmentation is 8-bit, this stretching can be done without losing data and distorting the shape of the histogram, provided it was done before the conversion from 16-bit to 8-bit (see Figure A.1).

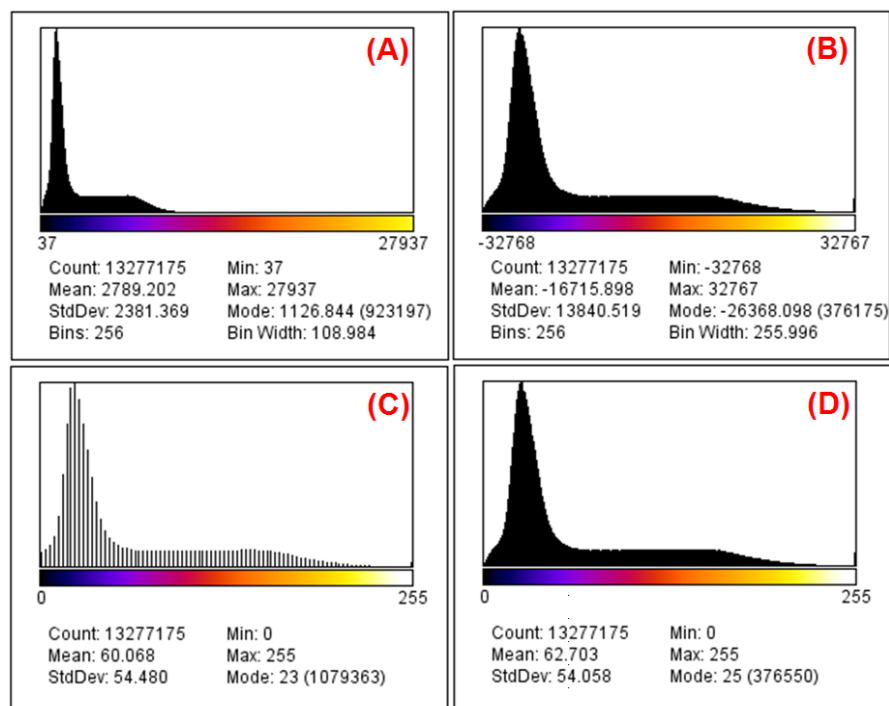


Figure A.1. (A) 16-bit unprocessed histogram of raw data. (B) normalised (i.e. contrast enhanced) 16-bit data. (C) 16-bit data converted to 8-bit, then normalised and (D) 16-bit data normalised then converted to 8-bit. Whilst quite similar, D is preferable to C as the shape of the histogram is not altered and data is not lost.

Equalising the histogram is more sophisticated than normalising as the stretching can be performed non-linearly or non-monotonically. A comparison of normalization and equalization is shown in Figure A.2. In ImageJ, the equalising method uses the square root of the histogram (Ferreira & Rasband, 2012) and produces greater contrast between the water and gravel phases than normalising the histogram whilst also entirely altering the shape of the histogram.

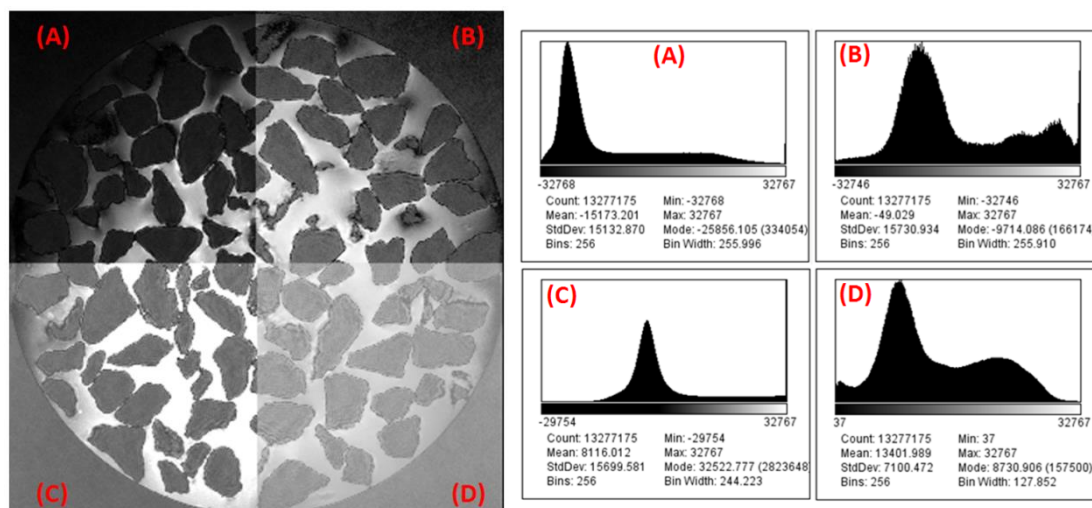


Figure A.2: contrast enhancement with (A) normalisation, (B) equalisation, (C) unsharp mask and (D) contrast limited adaptive histogram equalisation.

Unsharp masks are typically used in image processing to sharpen an image by amplifying the local contrast. By specifying a large local radius of 100 pixels and a high mask weight of 90%, the unsharp mask tool of ImageJ can be used to greatly increase the contrast over the entire image (Figure A.2).

The *local contrast enhancement* method used was contrast limited adaptive histogram equalisation (CLAHE) (Figure A.2). The method employed in ImageJ is 2D, however a 3D version has also been implemented in the open-source software ICY created by the Quantitative Image Analysis Unit of the Institut Pasteur (www.bioimageanalysis.org). In CLAHE, the image is first divided into a number of square contextual regions. The histogram of each contextual region is enhanced and then a bilinear interpolation scheme is used to avoid visibility of region boundaries. Finally, the increase in image noise associated with contrast enhancement is reduced by limiting contrast enhancement in homogenous areas (Zuiderveld, 1994).

Of the four contrast enhancement methods, three prove useful to gravel/water segmentation: equalisation, CLAHE and unsharp masks. These methods were selected for further investigation.

A.1.3 Noise Removal

Noise removal (low pass/smoothing) filters are commonly applied to x-ray data to reduce the effects of beam hardening (Iassonov & Tuller, 2010) and to other types of data to remove outliers and make a more homogenous image (Tarquis et al., 2009).

Mean filters replace the central pixel with the mean of its neighbours within a specified radius. Consequently mean filters remove noise, but also smooth the image, particularly at high contrast edges.

Median filters are commonly used to remove noise (Christensen, 2006; Luo et al., 2010; Keller et al., 2011; Reingruber et al., 2011; Bera et al., 2011) and do this by replacing the central pixel with the median value of its neighbours, therefore reducing ‘salt and pepper’ noise and resulting in less smoothing than mean filters. *Gaussian blur* works by convolving the image with a Gaussian function. This smooths the image and reduces noise. Gaussian blur is also a commonly used noise removal method (Iassonov et al., 2009; Tarquis et al., 2009; Elliot et al., 2010; Bera et al., 2011).

3D bandpass filtering is implemented in ImageJ as a Fourier transform. It can be used to enhance or remove objects of a particular size and is therefore useful in removing both noise and scanning artefacts such as horizontal or vertical stripes.

Outlier removal is similar to a median filter in that the value of a pixel is replaced by the median value of the neighbouring pixels. However, it is applied only if the pixel value deviates from the median by more than the threshold value. Outlier removal can therefore be used less invasively than a median filter and results in more discriminate smoothing of the image. A 3D implementation is not available in ImageJ.

Background subtraction can be used to remove a 2D smooth continuous variation in image intensity, such as might be produced by MR intensity inhomogeneity, using the ‘rolling ball’ algorithm (Sternberg, 1983).

A.1.4 Edge Modification

Edge modification can be used to restore edge detail that may be lost during noise removal.

Sharpening increases contrast, similar to an unsharp mask, and can partially restore edge detail lost by smoothing, but may also accentuate noise (Ferreira & Rasband, 2012).

Greyscale erode/dilate filters replaces each pixel with the minimum/maximum pixel within the defined neighbourhood. Greyscale erode/dilate can be used to create a higher/lower porosity final image or a series of erosion steps followed by dilation can be used to remove small structures (e.g. noise) from the image.

A.1.5 Edge Preserving Noise Removal

Edge preserving noise removal attempts to remove noise from the image without smoothing sharp transitions in image intensity such as the boundary between gravel and water. One such edge preserving noise removal technique is the *bilateral filter* implemented in ImageJ by Chaudhury et al. (2011) in which a Gaussian bilateral filter is applied to smooth the image. An additional range filter restricts the averaging effect of the Gaussian filter to neighbouring pixels with an intensity close to the pixel of interest.

Another technique is the *bi-exponential edge-preserving smoother* (BEEPS) implemented in ImageJ by Thévenaz et al. (2012) which uses a bi-exponential filter with adaptive weights. This filter is ‘edge-aware’ and is applied recursively so as to smooth the areas between edges whilst maintaining the edges themselves. Both methods can be implemented in 2D in ImageJ but not in 3D.

A.1.6 Pre-Processing Evaluation

Each pre-processing method stated above (and intuitive combinations of methods) were trialled and evaluated based on the shape of the resulting image histogram, the degree of preservation of the edges between gravel and water and their effect on the signal to noise ratio. The histogram shape (as shown in Figure A.3) was evaluated by eye: a bi-modal histogram with a clearly defined peak for gravel and a clearly defined peak for water is

preferable for image segmentation. Likewise a high signal to noise ratio and clearly defined edges are desirable. The edge definition was evaluated by comparing the pre-processed image with the gravel outline from a single slice manually segmented by tracing the outline of each gravel particle (see Section A.2.1 for details on manual segmentation). The signal to noise ratio (SNR) and peak signal to noise ratio (PSNR) were measured using an ImageJ plugin created by Daniel Sage (bigwww.epfl.ch/sage/soft/snr) according to the method of Gonzalez & Woods (2008) where the processed image is compared to a reference image (in this case the un-processed image) on a slice-by-slice basis with the difference expressed in decibels (dB).

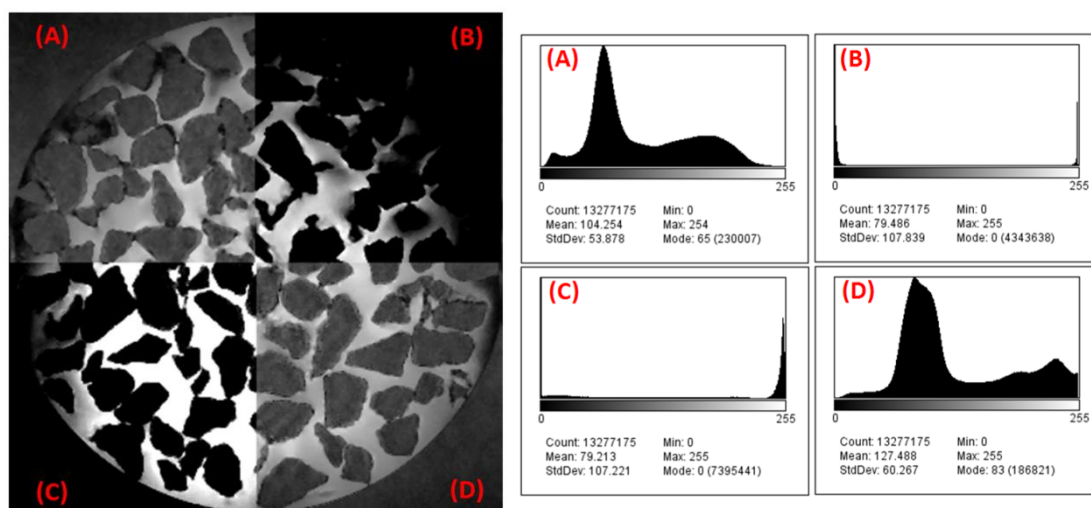


Figure A.3. contrast enhance with edge preserving noise removal. (A) CLAHE with bilateral filter, (B) unsharp mask with bilateral filter, (C) unsharp mask with BEEPS and (D) equalisation with bilateral filter.

Contrast enhancement can produce a bi-modal histogram, but, unfortunately, generally introduces noise. Noise removal can successfully remove noise but also causes blurring of the edges of gravel particles. Sharpening can restore some of the edge detail but can also enhance noise. Of the numerous combinations of pre-processing methods and parameters, the ten that best met the three criteria of creating a bi-modal histogram, increasing SNR and preserving edge details are outlined in Table A.1.

Table A.1. Pre-processing methods that improved the MRI data suitability for segmentation. Each method consists of cropping to the initial ROI, image alignment and contrast enhancement followed by either noise removal or edge preserving noise removal.

Step 1	Step 2	Step 3	Step 4
Cropping to Initial ROI 75mm x 130mm x 100mm. Slices 170-420	Image Alignment Translation Rotation Slice Number. (values determined for each scan)	2D CLAHE Block size = 127 Histogram bins = 256 Maximum slope = 10	2D outlier removal Radius = 1 Threshold = 1 Bright removed, then dark
			3D median filter Radius = 1
			2D bilateral filter Implementation = Fiji Spatial radius = 3 Range radius = 50
		2D Equalised Saturated pixels = 0.4%	2D outlier removal Radius = 1 Threshold = 1 Bright removed, then dark
			2D bilateral filter Implementation = Fiji Spatial radius = 3 Range radius = 50
			3D median filter Radius = 1
		2D Unsharp mask Radius (sigma) = 100 Mask weight = 90%	2D BEEPS Range filter = Gauss Photometric st dev = 1000 Spatial decay = 0.01 Iterations = 50
			2D bilateral filter Implementation = Fiji Spatial radius = 3 Range radius = 50
			3D median filter Radius = 1
		3D CLAHE XY block size = 127 Z block size = 63 Histogram bins = 256 Maximum slope = 10	2D bilateral filter Implementation = Fiji Spatial radius = 3 Range radius = 50

A.2 Image Segmentation (Binary Thresholding)

Image segmentation, also known as binary thresholding, consists of dividing a grey scale image into a binary black and white image. A great number of image segmentation techniques exist (over 100 according to Iassonov et al. (2009)). However, many of these were developed for purposes other than porous media research (such as optical character recognition of scanned documents or medical diagnosis from x-ray data).

The methods applicable to porous media research have been grouped by Iassonov et al. (2009) and very briefly stated below:

- Global thresholding – a single intensity value used to segregate areas of interest in the entire image.
- Locally adaptive thresholding – local characteristics used to calculate a threshold that varies spatially across the image.
- Region growing methods – initial “seed” regions are defined and a generic algorithm then iteratively adds neighbouring voxels to this region based on selection criteria such as similarity in intensity to the seed region.
- Deformable surfaces – an iterative shape based approach that requires seed points and in which the final shape is already known.
- Probabilistic fuzzy clustering – both voxel intensity and voxel connectedness within a cluster are used to segregate areas of interest.
- Bayesian methods – probabilistic methods based on Bayesian decision theory.
- Hybrid methods – a mixture of the other methods.
- Manual segmentation – an operator segments images using their own judgement.

Many studies use global thresholding and adjust the threshold value to match calculated and measured porosities whilst only a few more recent studies apply advanced segmentation techniques such as full 3D processing instead of 2D “slice-by-slice” processing (Iassonov et al., 2009).

Manual segmentation is time consuming, prone to user error, bias and inconsistencies. For that reason, automated segmentation programmes were used and manual segmentation was only used on a limited number of slices to verify the automated segmentation. Some of the segmentation tools available in ImageJ are given in Table A.2. Those methods investigated were *Auto Threshold*, *Auto Local Threshold*, *Adaptive 3D Threshold*, *3D Spot Segmentation* and *Connected Threshold Grower*.

Table A.2. Some automatic segmentation tools available in ImageJ.

Name	Domain	Description
Auto Threshold v1.14	2D (semi 3D)	Global threshold set with algorithms based on histogram shape, clustering, entropy or manual value for single slice or entire stack http://www.dentistry.bham.ac.uk/landinig/software/autothreshold/autothreshold.html
Auto Local Threshold v1.2	2D	Locally adaptive with several algorithms to choose from http://www.dentistry.bham.ac.uk/landinig/software/autothreshold/autothreshold.html
3D Spots Segmentation	3D	Hybrid region growing/ locally adaptive method http://imagejdocu.tudor.lu/doku.php?id=plugin:segmentation:3d_spots_segmentation:start
Adaptive 3D threshold v1.22	3D	Locally adaptive with user specified radius and weighting http://www.pvv.org/~perchrh/imagej/thresholding.html
BoneJ Optimize Threshold	2D	Hybrid global thresholding of entire stack to minimise connectivity between slices and hence minimise noise http://bonej.org/threshold
Multi Otsu Threshold	2D	Image histogram split into regions and global threshold set for each region using the Otsu clustering algorithm http://rsbweb.nih.gov/ij/plugins/multi-otsu-threshold.html
K-means Clustering	2D	Global threshold with clustering algorithm to assign each pixel into regions http://ij-plugins.sourceforge.net/plugins/segmentation/k-means.html
Seeded Region Growing	3D	Region growing http://ij-plugins.sourceforge.net/plugins/segmentation/Howto-Seeded-Region-Growing-Segmentation.pdf
Interactive 3D Segmentation	3D	Region growing with manual selection of seeding points and some manual control over region growth http://132.187.25.13/ij3d/?page=IntSeg_3D&category=Extensions
Watershed Segmentation	2D	Region growing with global threshold http://bigwww.epfl.ch/sage/soft/watershed/
Connected Threshold Grower	3D	Region growing where seed points and upper and lower global threshold for pixel intensity are manually specified http://ij-plugins.sourceforge.net/plugins/3d-toolkit/example-connected-threshold-growing.html
Advanced WEKA Segmentation	2D	Global threshold where the threshold value can be trained by manually selecting areas http://fiji.sc/wiki/index.php/Advanced_Weka_Segmentation

A.2.1 Manual Segmentation

To compare the performance, and ultimately to validate the choice of the segmentation method used, unprocessed slices from the Scan L1C (clean gravel) were manually segmented into gravel regions and water filled regions. First, the entire 211 slices were segmented automatically using *Auto Local Threshold* (Table A.2) with the threshold calculated from the mean intensity within a radius of 20 pixels. This method approximately reproduced the gravel structure and, after post processing by de-noising, yielded approximate average porosities for each slice. Nine slices from the 211 thick ROI were selected for manual segmentation: three slices of high porosity, three slices of low porosity and three slices of average porosity.

The nine slices were manually segmented using ArcGIS to trace around the gravel particles and then the area of gravel was divided by the total area of the slice and subtracted from one to yield the porosity. Manual segmentation was slow, tedious, prone to user bias in setting the threshold between gravel and water and prone to user error in applying that threshold consistently. However, it also utilises the pattern recognition capabilities of the human brain allowing the segmentation at the image edges (where the water signal varies from being lower than the gravel to being higher than the gravel), ignoring potential image artefacts and producing a segmented image that did not require post processing such as de-noising. Figure A.4 shows manual segmentation of a slice. Areas close to the column wall were difficult to threshold automatically as the signal from the water changes from being higher (lighter) than the gravel to lower (darker).

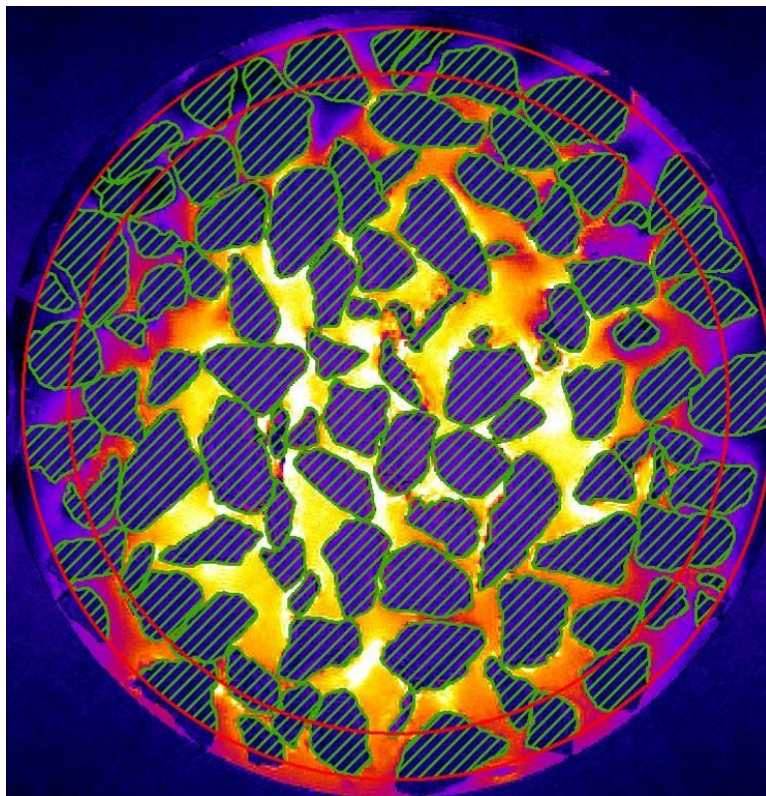


Figure A.4. manual segmentation of gravel (green hatched area) from water in an unprocessed MRI scan (Slice 155 of Scan 1 - Clean). Outer red ring is outer region of interest (ROI) and is the maximum extent of the image visible in all slices of the scan. Inner red ring is offset 25 pixels from the outer ring.

A.2.2 Automatic Segmentation

Analysis of the scan LIC intensity value histogram (Figure 3.3; histogram B) shows that the data is not distinctly bi-modal when considering the entire ROI. However, when looking at small regions of the image, the image is markedly bi-modal (Figure 3.3; histogram A) and it is possible for binary segmentation to split the image into gravel and water phases within these regions. This suggests that locally adaptive thresholding algorithms are more suitable for this data than global thresholding. Towards the edge of the image (around 25 pixels), the signal of the water drops and it is more difficult to distinguish water from gravel. For this reason, the area 25 pixels from the edge were not included further in the analysis reducing the ROI to 84.9mm diameter and 63.3mm length.

From the list of available automated segmentation methods (Table A.2), *Auto Threshold*, *Auto Local Threshold*, *Adaptive 3D Threshold*, *3D Spot Segmentation* and *Connected Threshold Grower* were selected for further analysis. Each of the segmentation method, in combination with the pre-processing methods detailed in Table A.1, were used to segment scan L1C. The merits and suitability of each segmentation method are discussed below.

A.2.3 Auto Threshold

As global thresholding has been used in so many previous studies (Cooper et al., 2003; Elliot & Heck, 2007; Tarquis et al., 2009; Munkholm et al., 2012), it has been used in this study as the baseline with which other segmentation methods are compared. Figure A.5 shows the raw data for Slice 155 together with a water/solid segmented image using the *ISOData* algorithm of *Auto Threshold*.

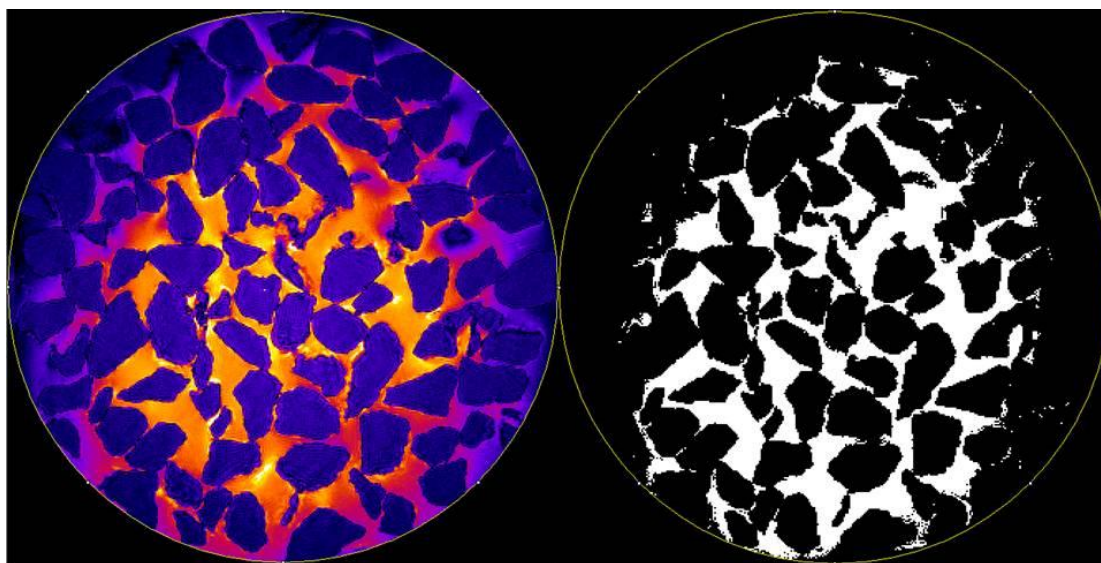


Figure A.5. Raw MRI data for slice 155 (left) compared with slice segmented using a global threshold (right). Raw data contrast was increased for display but not for segmentation. *ISOData* algorithm was used based on entire stack histogram (211 slices) resulting in a threshold value of 31 (on scale 0-255). No pre- or post-processing of images.

The *ISOData* algorithm developed by Ridler & Calvard (1978) sets an initial threshold that is used to divide the image into object and background (in this case, water and gravel). In this method, the initial threshold is varied incrementally until it is larger than the average

of the average background minus average objects (implemented in ImageJ as Equation). Out of the 16 algorithms available within *Auto Threshold*, the *ISOData* algorithm was chosen as it is relatively straightforward, was determined (by eye) to give an adequate result and gave the same threshold as other popular methods such as the Otsu thresholding clustering algorithm.

$$threshold = \left(\frac{average\ background - average\ objects}{2} \right) \quad \text{Equation A.1}$$

Global thresholds work well at the centre of the image, but it can be seen in Figure A.5 that they are inappropriate near the edge. This is because a single threshold value cannot be used over the entire range of intensities that represent water in this MRI scan.

A.2.4 Auto Local Threshold

To overcome the limitations of using a single global threshold, the 2D locally adaptive plugin *Auto Local Threshold* was investigated. This plugin allows selection from six algorithms that can be applied to set a global threshold within a user specified radius based on the histogram characteristics within that radius. In other words, every single pixel in the image is segmented based on a threshold determined from the pixels that surround it. This allows a very different threshold to be automatically set near the edges where the signal intensity of water is much lower than that at the centre.

In general, the *Bernsen* and *Niblack* algorithms gave the best results (Figure A.6). However, depending on what pre- and post-processing was used, *MidGrey* and *Mean* at times gave better results.

The *Bernsen* algorithm is based on the local contrast: if the local contrast is below the contrast threshold, the intensity threshold is set as the mean of the maximum and minimum intensities within the local search radius. In imageJ, the *Bernsen* algorithm is implemented according to the following equation (Sezgin & Sankur, 2004):

$$threshold(i, j) = 0.5 \{ \max_w [I(i+m, j+n)] + \min_w [I(i+m, j+n)] \} \quad \text{Equation A.2}$$

provided the contrast, C , meets the following criteria:

$$C(i, j) = I_{high}(i, j) - I_{low}(i, j) \geq 15 \quad \text{Equation A.3}$$

Where I = pixel intensity,

(i, j) = pixel coordinates

w = local search radius

m, n = pixel coordinates range (defined by w)

The *Niblack* algorithm is adapted from Niblack (1986) with the addition of an offset from the mean, c :

$$threshold(i, j) = m(i, j) + k \cdot \sigma(i, j) - c \quad \text{Equation A.4}$$

Where k = is a constant (by default 0.2)

σ = standard deviation

These algorithms perform similarly to the global threshold *ISOData* algorithm at the centre of the image, but perform far better at the edges where the contrast between gravel and water is much lower, as can be seen by comparing the right hand image in Figure A.5 with the right hand image in Figure A.6.

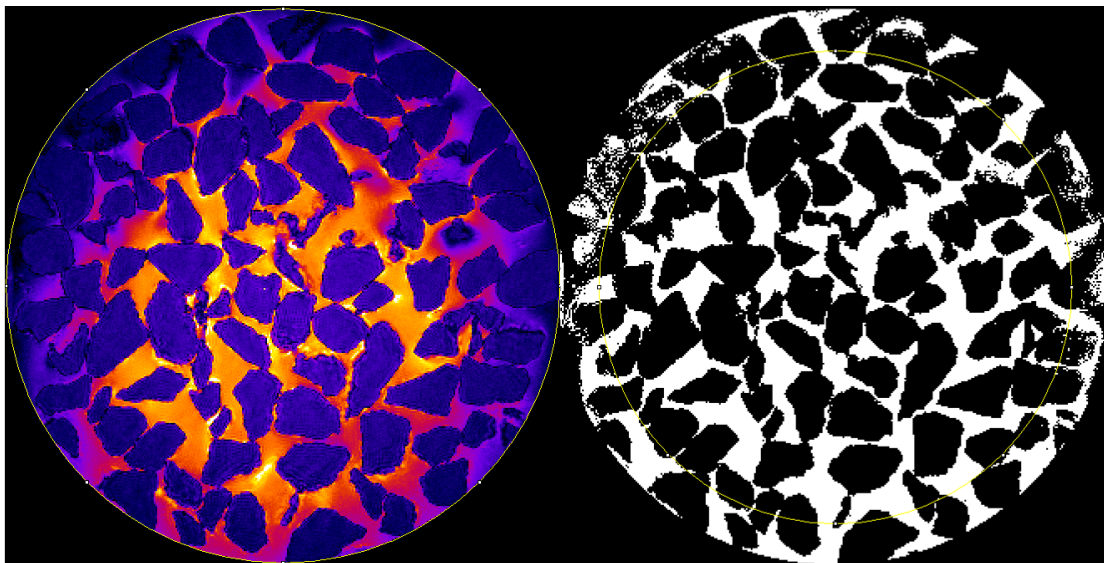


Figure A.6. Raw MRI data for slice 155 (left) compared with slice segmented using the locally adaptive *Bernsen* algorithm with a search radius of 30 pixels (right). Raw data contrast was increased for display but not for segmentation. No pre- or post-processing of images.

A.2.5 Adaptive 3D Threshold

2D adaptive segmentation is an improvement over global thresholding, however the MRI data is 3D and so should be segmented with a 3D algorithm in order to maintain the slice-to-slice features (Elliot & Heck, 2007). *Adaptive 3D Threshold* was the only 3D locally adaptive thresholding plugin found for ImageJ. The user sets a base threshold, a 3D search radius and a local weighting that determines the extent to which the local threshold can modify the base threshold. A search radius greater than 10 requires a huge amount of RAM to process the image stack (333x433x250 pixels) and, even with a local weighting factor of 99% applied to a base threshold of 31 (the threshold calculated by the *ISOData* global thresholding algorithm), the local weighting is not strong enough and so the resulting segmented image is virtually indistinguishable from the global thresholding method. This method did better preserve the 3D nature of the data but the segmentable volume was no larger than that for *Auto Threshold* and was smaller than for *Auto Local Threshold*.

A.2.6 Connected Threshold Grower & 3D Spot Segmentation

Connected Threshold Grower requires the selection of a single “seed point” and an upper and lower global threshold specified by the user (in this case specifying the upper and lower intensities of water in the MRI scan). Voxels adjacent to the seed point are evaluated and, if the intensity falls within the threshold band, those voxels are classed as water. If the intensity is outwith the threshold band, they are classed as part of the background. Voxels adjacent to the newly classed water voxels are then evaluated and segmented and the process repeats until the entire image has been segmented. Due to setting a global threshold, this method is not appropriate. Also, as only voxels that can be connected to the initial seed point are segmented, it would not be appropriate for analysing the clogged experiment results where some pore spaces were found to become entirely disconnected from the main pore network (and hence the initial seed point) after prolonged clogging.

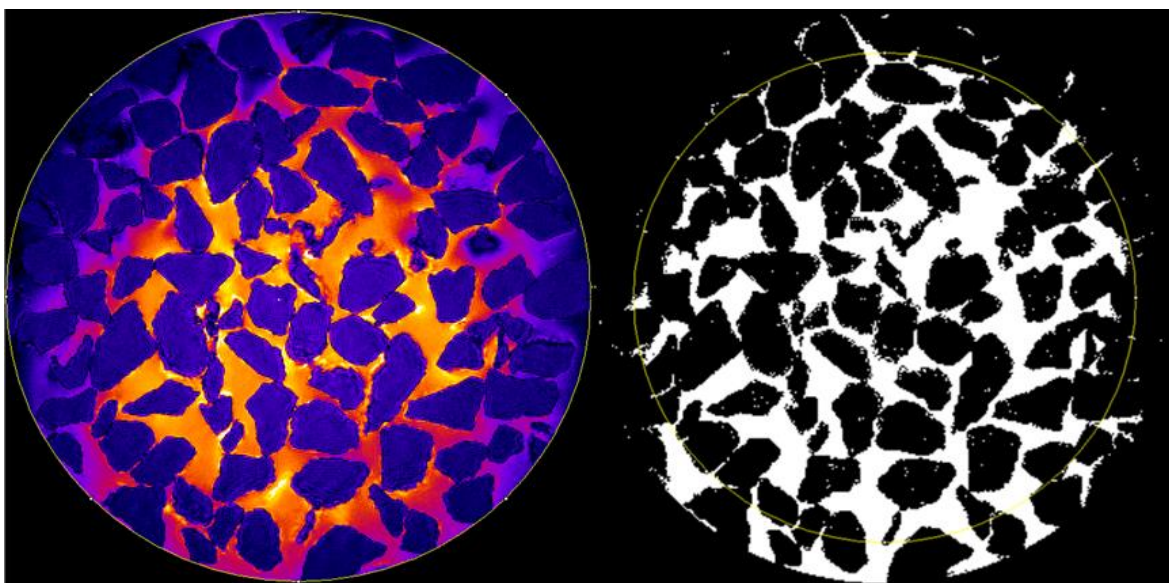


Figure A.7. Raw MRI data for slice 155 (left) compared with slice segmented using the 3D Spot Segmentation local mean algorithm with local search radii of 20, 21 and 22 pixels and local weighting of 50% (right). Raw data contrast was increased for display but not for segmentation. No pre- or post-processing of images.

3D Spot Segmentation uses multiple seed points. A local threshold is computed around each seed and voxels with values higher than this local threshold are classed as water. Three radii are set for the local weighting with the option of changing the weighting factor.

An initial background threshold is set (a global threshold) with the option of a local threshold calculated by the local mean method inside the local radii. This method is much slower than *2D Auto Local Threshold* but gives comparable results (as can be seen by comparing Figure A.7 with Figure A.6) and as it is a 3D method it should, in theory, better preserve the 3D data. The method used to obtain the seed points was to threshold the image using *Auto Local Threshold*, invert the intensity values, calculate a 3D distance map of the gravel and use a *3D Fast Filter* to extract the maximum points that roughly correspond to the centre of each grain of gravel. *3D Spot Segmentation* was then applied on the raw image using these seed points. This is a time consuming process and limits the area that can be segmented by *3D Spot Segmentation* to the area that can be segmented by *Auto Local Threshold*. It was found that the process of obtaining seed points and applying *3D Spot Segmentation* was sensitive to the direction in which the stack of images was processed: porosity varied by 1.2% depending on whether the stack was processed from top to bottom, left to right or front to back. Despite initially looking promising in its ability to reduce the 3D edge effects, the *3D Spot Segmentation* tool could not reliably be used to threshold the entire scan area and was not pursued further.

A.3 Post-segmentation Processing

Post-processing the segmented image consisted of removing noise, edge operations to fine tune the porosity and cropping to create the final 3D volume for analysis. Noise removal techniques used were 3D median filter (described in Section A.1), 3D isolated pixel removal which replaces only those voxels completely surrounded by those with a different value, and Despeckle, a form of 2D median filter. 3D region removal was used to remove regions of gravel smaller than 10 voxels as these must be the result of noise or incorrect segmentation (except at the image boundaries where 3D region removal was not applied).

The edge operations investigated were erode/dilate sequences to remove small structures and increase porosity and quasi-3D watershedding. Watershedding has the potential to separate particles of gravel that are touching allowing individual particles to be counted and their size measured as well as increasing the porosity of the image and ensuring that very small pore spaces (smaller than the MRI resolution) are re-introduced into the final image. The watershedding procedure developed is shown in Figure A.8 and consists of

taking the segmented image and inverting the intensities so that the gravel has a high intensity, calculating the 3D local thickness of the gravel then re-slicing this data so there is a stack of slices for each orthogonal plane. The grey-level watershed segmentation plugin developed by Tsukahara et al. (2008) is then applied to each orthogonal stack and the resulting watershed lines combined to give what we refer to here as quasi-3D watershed lines. These watershed lines can then be subtracted from the segmented image to give the separated gravel particles. The reason this method is referred to as quasi-3D is that each set of watershed lines was generated with 2D algorithms applied slice-by-slice to the 3D stack of images; but when combined, have properties more like a 3D watershedding algorithm. This method has some limitations as it results in over-segmentation of some gravel particles (resulting in the splitting of some particles) with concave sections and introduces some artefacts to the final image but also has the potential to compensate for an under-estimation of the pore volume during segmentation – particularly between gravel particles in close proximity – and so was evaluated as a post-processing tool.

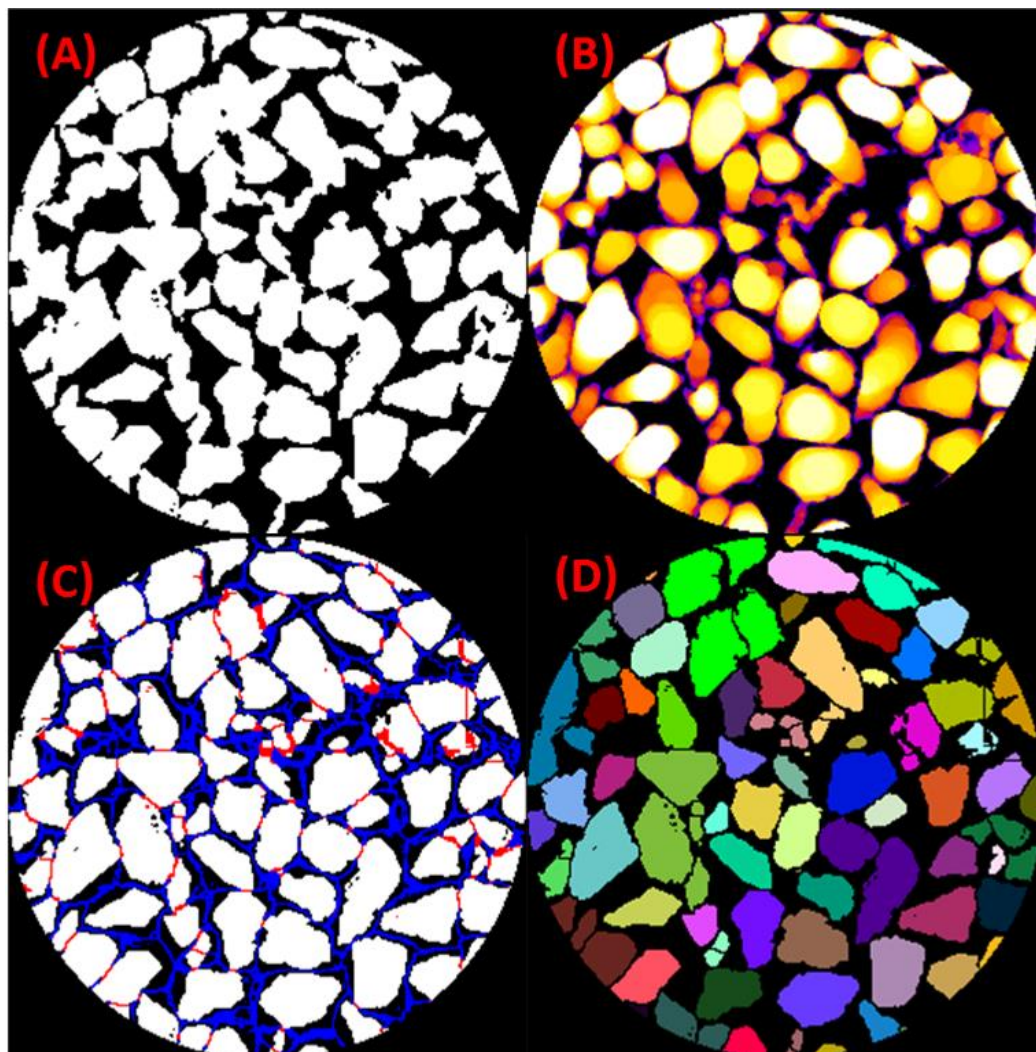


Figure A.8. 3D watershedding can be used to separate gravel particles to a certain extent. The individual particles can then be measured. (A) segmented gravel image, (B) gravel local thickness, (C) 3D watershed lines overlaid upon gravel showing where lines intersect the gravel in red and (D) the separated gravel particles.

A.4 Selection of Image Processing Method

Combinations of pre-processing, automatic segmentation and post-processing were evaluated as described in Section 3.5.1. The optimum image processing method is presented in Section 3.5.4.

Appendix B – Parametric Study Results

The aim of the parametric study was to evaluate the sensitivity of the model to 1) physical parameters of the gravel filter that could not be measured, and 2) elements of the modelling approach that needed to be tested. Both Eulerian (*simpleFoam*) and Lagrangian (*icoUncoupledKinematicParcelFoam*) parameters were evaluated.

The flow field for each Lagrangian case in Table B.2 was derived from the converged *simpleFoam* cases in Table B.1. Consistent numbering of cases is used to show whence the flow field originated. Lagrangian cases were suffixed with upper case letters to denote different Lagrangian solution parameters.

These parameters were assessed on the sub-volume geometry. An understanding of how these parameters affect the model solutions allowed a more informed choice of the most suitable parameter values for the full geometry simulations whilst increasing confidence in the modelling approach. It also allowed weaknesses and limitations of the adopted modelling approach to be identified.

The sensitivity of the sub-volume cases to each parameter were compared based on convergence time and velocity magnitude across the pore channel located in Figure B.1 and wall shear stress across the same pore channel. This channel was chosen because it is a typical channel with a medium flow rate. Visual inspection of the mesh was made to determine how well small diameter pores were represented for each mesh resolution and surface refinement level.

Table B.1. Euler FVM model runs for parametric study.

Case	Geometry	Scheme	Turbulence Model	Surface Roughness Model	Mesh			Parameter Tested	
					Name	Initial Mesh Size (mm)	Surface Refinement Levels (min, max)		Number of Cells
1	H1C	Limited	Laminar	None	Mesh 1	1.5	4, 4	2,153,316	Standard
2	H1C	Linear corrected	Laminar	None	Mesh 1	1.5	4, 4	2,153,316	Scheme
3	H1C	Limited	k- ϵ RASmodel, $k=1 \times 10^{-3}$, $\epsilon=0.1$	None	Mesh 1	1.5	4, 4	2,153,316	Turbulence, Scan 4
4	H3C	Limited	k- ϵ RASmodel, $k=1 \times 10^{-3}$, $\epsilon=0.1$	None	Mesh 1	1.5	4, 4	2,153,316	Turbulence, Scan 6
5	H3C	Linear corrected	k- ϵ RASmodel, $k=1 \times 10^{-3}$, $\epsilon=0.1$	None	Mesh 1	1.5	4, 4	2,153,316	Scheme with turbulence
6	H1C	Limited	Laminar	Rough wall. $C_s=0.5$, $k_s=1 \times 10^{-4}$	Mesh 1	1.5	4, 4	2,153,316	Roughness
7	H1C	Limited	Laminar	Rough wall. $C_s=0.5$, $k_s=1 \times 10^{-3}$	Mesh 1	1.5	4, 4	2,153,316	Roughness coefficients
8	H1C	Limited	k- ϵ RASmodel, $k=1 \times 10^{-3}$, $\epsilon=0.1$	Rough wall. $C_s=0.5$, $k_s=1 \times 10^{-4}$	Mesh 1	1.5	4, 4	2,153,316	Roughness with turbulence
9	H1C	Limited	k- ϵ RASmodel, $k=1 \times 10^{-6}$, $\epsilon=1 \times 10^{-4}$	Rough wall. $C_s=0.5$, $k_s=1 \times 10^{-4}$	Mesh 1	1.5	4, 4	2,153,316	Roughness with turbulence coefficients
10	H1C	Limited	Laminar	None	Mesh 2	1.5	2, 2	92,040	Initial mesh resolution
11	H1C	Limited	Laminar	None	Mesh 3	0.6	2, 2	823,441	Initial mesh resolution
12	H1C	Limited	Laminar	None	Mesh 4	0.3	2, 2	3,444,631	Initial mesh resolution
13	H1C	Limited	Laminar	None	Mesh 5	0.15	2, 2	15,235,272	Initial mesh resolution
14	H1C	Limited	k- ϵ RASmodel, $k=1 \times 10^{-3}$, $\epsilon=0.1$	None	Mesh 3	0.6	2, 2	823,441	Turbulence with surface refinement
15	H1C	Limited	Laminar	None	Mesh 6	1.5	3, 4	2,080,870	Surface refinement
16	H1C	Limited	Laminar	None	Mesh 7	1.5	1, 4	2,073,944	Surface refinement
17	H1C	Limited	Laminar	None	Mesh 8	0.6	1, 4	3,229,119	Surface refinement with initial block size
18	H3C	Limited	k- ϵ RASmodel, $k=1 \times 10^{-6}$, $\epsilon=1 \times 10^{-4}$	None	Mesh 1	1.5	4, 4	2,153,316	Turbulence coefficients
19	H3C	Limited	Laminar	None	Mesh 1	1.5	4, 4	2,153,316	Turbulence coefficients
20	H1C, smoothed	Limited	Laminar	None	Mesh 9	1.5	4, 4	2,089,939	STL generation
21	H1C	Limited	Laminar	None	Mesh 1	1.5	4, 4	2,153,316	Viscosity

Table B.2. Lagrangian model runs for parametric study.

Case	Turbulence Model	Roughness Model	Mesh Name	Particle Dispersion Model	Lagrangian Turbulence Model	Particle-Wall Interaction	Parameter Tested
1A	Laminar	None	Mesh 1	None	Laminar	Stick	Standard
1B	Laminar	None	Mesh 1	stochastic-DispersionRAS	Laminar	Stick	Dispersion
1C	Laminar	None	Mesh 1	None	Laminar	Rebound	Wall interaction
1D	Laminar	None	Mesh 1	None	Laminar	Rebound, $e=1$, $\mu=0$	Wall interaction coefficients
1E	Laminar	None	Mesh 1	stochastic-DispersionRAS	k- ϵ RASmodel, $k=1 \times 10^{-3}$, $\epsilon=0.1$	Stick	Dispersion with Lagrangian turbulence
3A	k- ϵ RASmodel, $k=1 \times 10^{-3}$, $\epsilon=0.1$	None	Mesh 1	None	Laminar	Stick	Turbulence
3B	k- ϵ RASmodel, $k=1 \times 10^{-3}$, $\epsilon=0.1$	None	Mesh 1	stochastic-DispersionRAS	k- ϵ RASmodel, $k=1 \times 10^{-3}$, $\epsilon=0.1$	Stick	Lagrangian turbulence
6	Laminar	Rough wall. $C_s=0.5$, $k_s=1 \times 10^{-4}$	Mesh 1	None	Laminar	Stick	Roughness
9A	k- ϵ RASmodel, $k=1 \times 10^{-6}$, $\epsilon=1 \times 10^{-4}$	Rough wall. $C_s=0.5$, $k_s=1 \times 10^{-4}$	Mesh 1	None	k- ϵ RASmodel, $k=1 \times 10^{-3}$, $\epsilon=0.1$	Stick	Lagrangian turbulence with roughness
9B	k- ϵ RASmodel, $k=1 \times 10^{-6}$, $\epsilon=1 \times 10^{-4}$	Rough wall. $C_s=0.5$, $k_s=1 \times 10^{-4}$	Mesh 1	None	Laminar	Stick	Turbulence with roughness
10	Laminar	None	Mesh 2	None	Laminar	Stick	Initial mesh resolution
11	Laminar	None	Mesh 3	None	Laminar	Stick	Initial mesh resolution
16	Laminar	None	Mesh 7	None	Laminar	Stick	Surface refinement
17	Laminar	None	Mesh 8	None	Laminar	Stick	Surface refinement with initial block size
20	Laminar	None	Mesh 9	None	Laminar	Stick	STL generation
21	Laminar	None	Mesh 1	None	Laminar	Stick	Viscosity

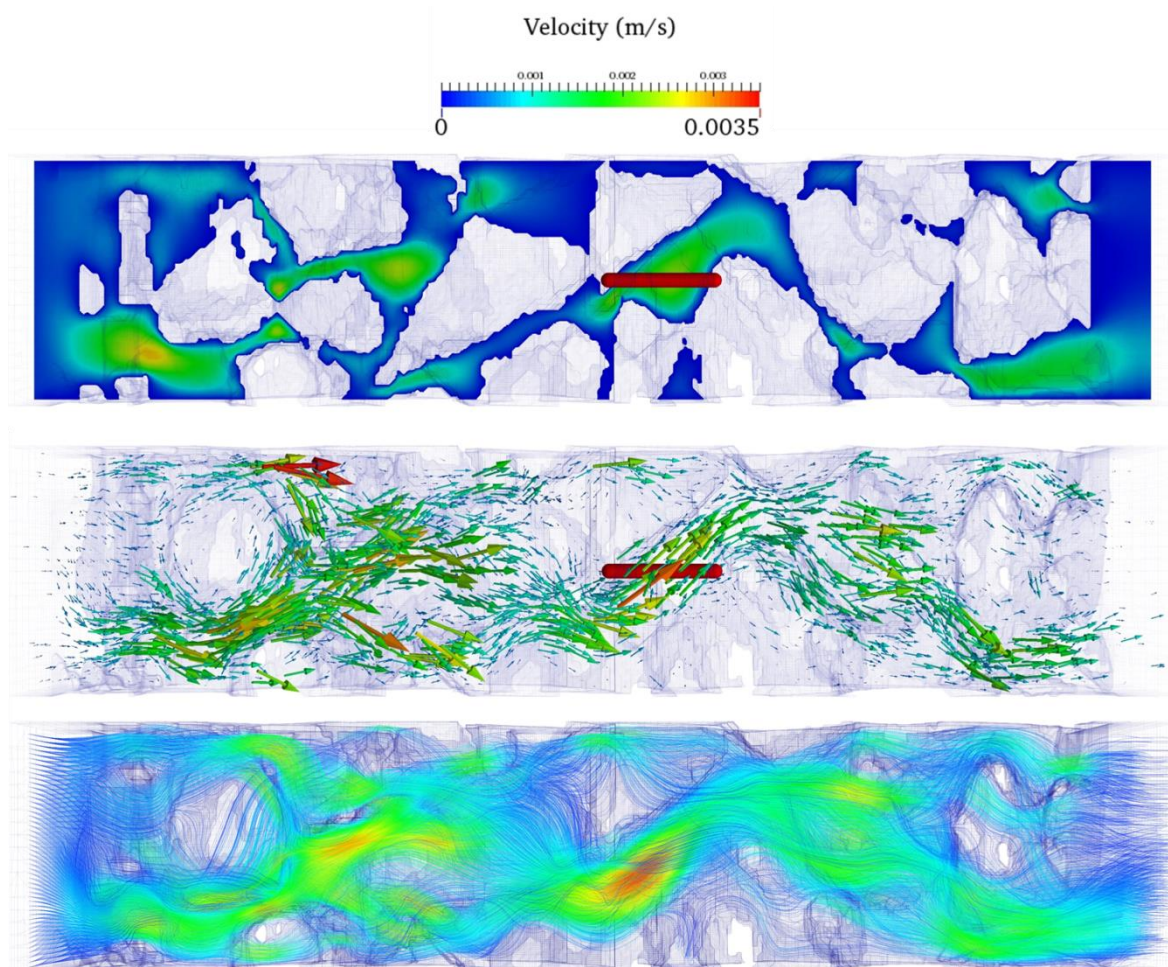


Figure B.1. Location of pore channel (red line) relative to Y-Z slice through computational domain showing pore velocities (top) and glyphs of entire 3D computational domain pore velocities (middle) derived from Case1. Lagrangian particle tracks with particle velocity are also shown (bottom) derived from Case1A.

Results for each parameter are presented in two stages: 1) Eulerian solution – the effect of the *simpleFoam* parameters (Table B.1) on the Eulerian flow field and, where appropriate, 2) Lagrangian particle tracking – the effect of the flow field, the *icoUncoupledKinematicParcelFoam* parameters and combined Eulerian/Lagrangian parameters (Table B.2) on the particle paths.

Those parameters that had little or no effect on the flow field or particle paths were identified whilst, for those that did, the magnitude of the effect was quantified. Finally, the optimum parameters for the full volume runs are selected in Section 5.3.7.

B.1 Solution Scheme

Number of steps and time to convergence are similar for each solution scheme (Table B.3).

Table B.3. Number of steps and time for convergence.

Case	Scan	Solver	Turbulence	Steps to Convergence	Convergence Time (mins)
1	H1C	Limited	Laminar	33	25.6
2		Linear corrected	Laminar	33	27.1
4	H3C	Limited	Turbulent	60	13.7
5		Linear corrected	Turbulent	56	12.8

The choice of solution scheme had no impact on flow velocity or wall shear stress (Case1 compared with Case2, Figure B.2, A and B) whilst solution scheme with turbulence produced a negligible increase of 0.18% for the maximum velocity (Case4 compared with Case5, Figure B.2, C and D).

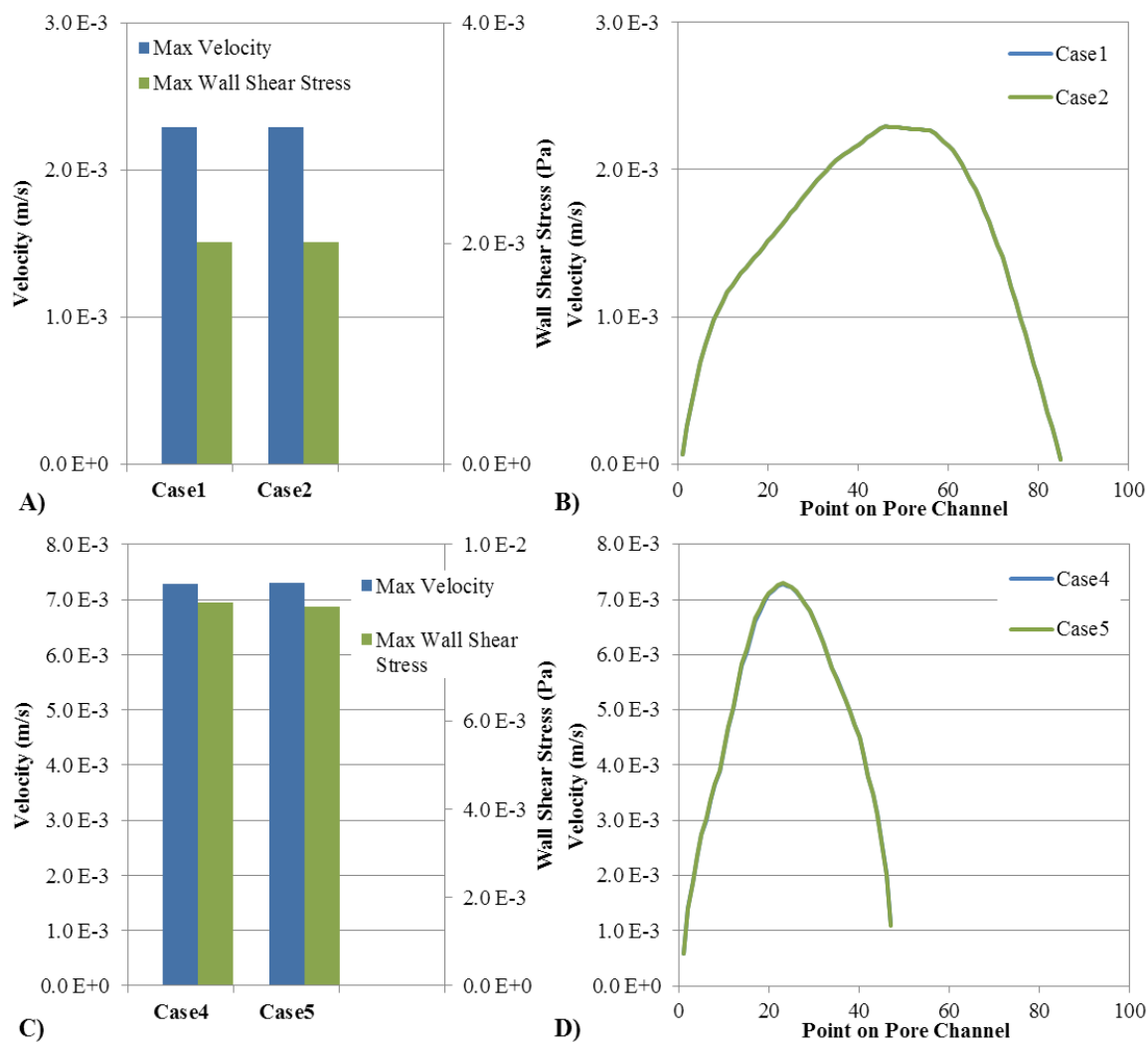


Figure B.2. Maximum velocities and wall shear stress across the pore. Note that Case1 and Case2 (A and B) are for the clean scan geometry whilst Case4 and Case5 (C and D) are for the clogged geometry. Details of each mesh can be cross-referenced with Table B.3. N.B. Curves on right overly each other hence only one is visible.

From this we can conclude that both the *linear corrected* and *limited* solution schemes provide an adequate solution; yet the *limited* solution scheme is preferable as it is more stable (see Section 5.3.3.1), allowing convergence of meshes with non-orthogonal elements.

B.2 Turbulence & Surface Roughness

B.2.1 Eulerian Solution

Number of steps and time to convergence were longest for runs with both turbulence and surface roughness (Table B.4) which could result in excessively long run times for the full volume cases.

Table B.4. Number of steps and time for convergence for turbulence, surface roughness and combined turbulence and surface roughness cases. Case parameters detailed in Table B.1.

Case	Scan	Turbulence	Surface Roughness	Steps to Convergence	Convergence Time (mins)
4	H3C	Turbulent, High Coefficients	None	60	13.7
18		Turbulent, Low Coefficients	None	33	11.7
19		Laminar	None	33	10.9
1	H1C	Laminar	None	33	25.6
6		Laminar	Rough, Low Coefficient	34	28.0
7		Laminar	Rough, High Coefficient	34	28.1
3	H1C	Turbulent, High Coefficients	None	102	59.6
8		Turbulent, High Coefficients	Rough, Low Coefficient	500	109
9		Turbulent, Low Coefficients	Rough, Low Coefficient	500	114

Turbulence with low k and ε coefficients had no impact on flow velocities compared with a laminar model of turbulence (Case18 compared with Case19, Figure B.) whilst high k and ε coefficients produced negligible change in velocities (Case4 compared with Case18, Figure B.). Likewise, wall shear stress was unaffected by turbulence model or turbulence coefficients.

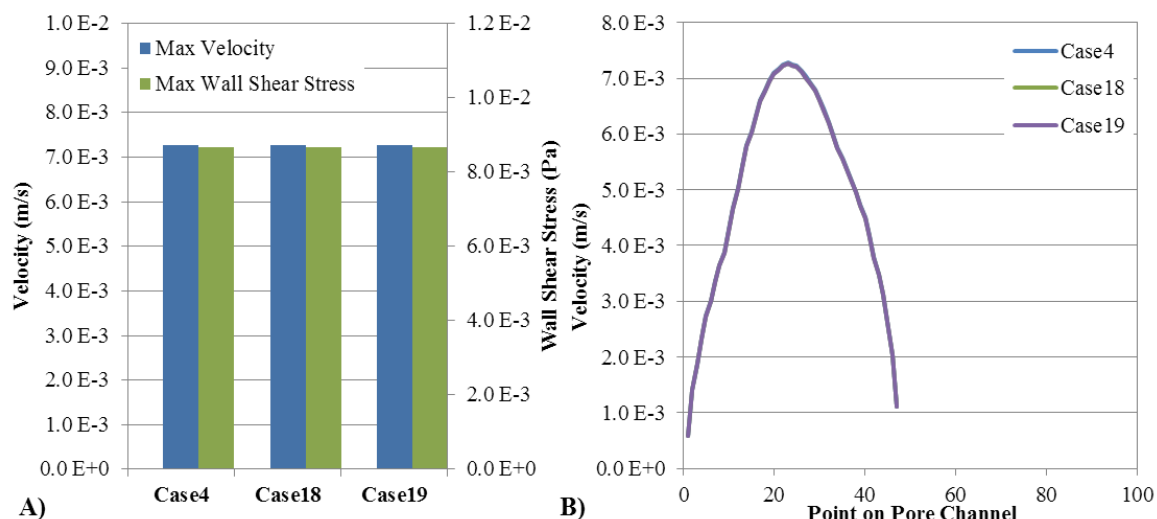


Figure B. For turbulent with high k and ε coefficients (Case4), low coefficients (Case18) and laminar (Case19): **A)** maximum pore velocity and wall shear stress and **B)** variation in velocity across pore channel. Details of each case can be cross-referenced with Table B.4. N.B. Curves on right overly each other hence only one is visible.

Surface roughness produced no change in flow velocities, regardless of the roughness coefficients, for a laminar turbulence model (cases 6 & 7 compared with Case1), as shown in Figure B.3.

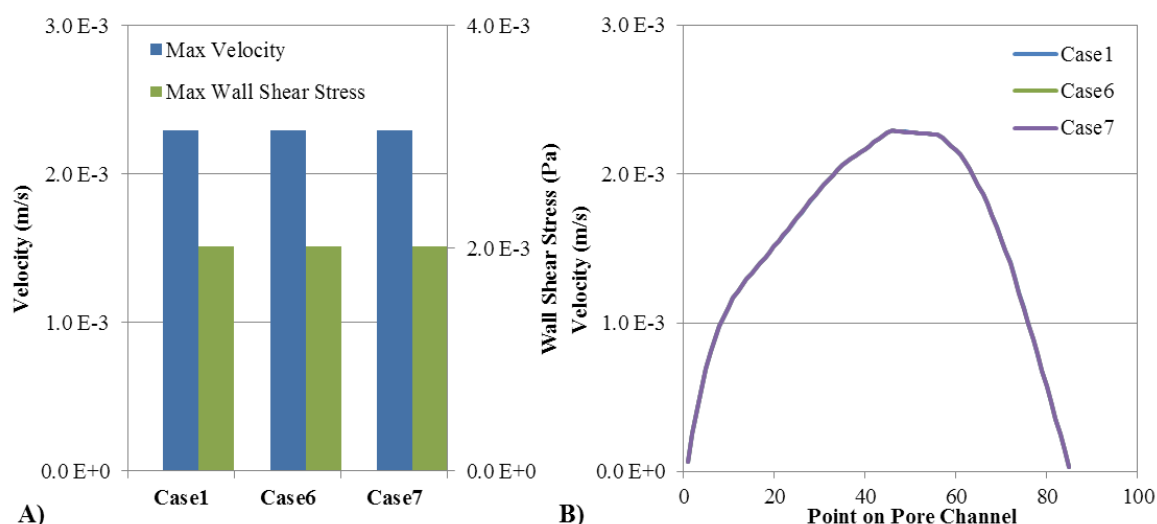


Figure B.3. For laminar model with no surface roughness (Case4), roughness with low coefficients (Case6) and with high coefficients (Case7): **A)** maximum pore velocity

and wall shear stress and B) variation in velocity across pore channel. Details of each case can be cross-referenced with Table B.4. N.B. Curves on right overly each other hence only one is visible.

With the $k-\varepsilon$ turbulence model, surface roughness did change the flow velocities resulting in a maximum velocity increase of 7.3% (Case8 compared with Case3, Figure B.4, A). The velocity distribution across the measurement pore channel is plotted in Figure B.4, B. The change in velocity was entirely due to the surface roughness as changing the turbulence coefficients resulted in no velocity change (Case9 compared with Case8). However, turbulence coefficients (when combined with surface roughness) did affect the maximum wall shear stress: the high coefficients resulted in a 1785% increase in wall shear stress compared to laminar model (Case8 compared with Case3) whilst the low coefficients resulted in a 989% increase (Case9 compared with Case3).

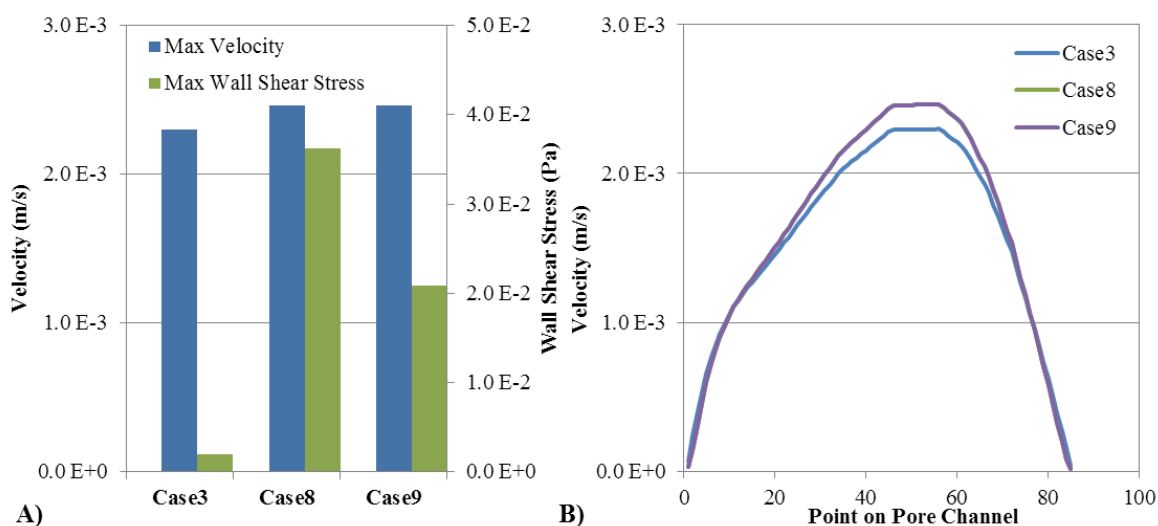


Figure B.4. For turbulent model with high coefficients and no surface roughness (Case3), turbulence with high coefficients and surface roughness (Case8) and turbulence with low coefficients and surface roughness (Case9): A) maximum pore velocity and wall shear stress and B) variation in velocity across pore channel. Details of each case can be cross-referenced with Table B.4.

B.2.2 Lagrangian Particle Tracking

Lagrangian particle tracking of 2500 tracer particles showed that Eulerian turbulence (Case3A) and Eulerian surface roughness (Case6) had a minimal impact on particle fate, travel time, distance travelled or tortuosity compared with the laminar model with no surface roughness (Case1A), as shown in Table B.5.

Combined Eulerian turbulence and surface roughness (Case9A) resulted in fewer particles sticking to surface patches and an increase in particles escaping from the model at the outlet patch or remaining in-transit after 400s run time - equivalent to 2.62 pore volumes passing through the filter. The distance and tortuosity of those particles that did escape increased by 0.85%, showing that they took a longer path through the filter as a result of the different flow field.

Including a $k-\varepsilon$ Lagrangian turbulence model with Eulerian turbulence and surface roughness resulted in no change in particle transport (Case9A compared with Case9B) but increased run times by 47%.

Table B.5. Lagrangian particle tracking transport characteristics.

		Case1A	Case3A	Case6	Case9A	Case9B
Fate	Number of particles	2500	2500	2500	2500	2500
	Number stick	326	338	340	87	87
	Number escape	2010	1974	1981	2176	2176
	Number in-transit	164	188	179	237	237
Time (s)	Average stick	98.90	97.26	98.06	91.64	91.64
	Average escape	124.11	120.52	123.11	121.76	121.76
	Average in-transit	400.00	400.00	400.00	400.00	400.00
	Average all	138.92	138.39	139.53	147.09	147.09
Distance (mm)	Average stick	38.6	38.1	39.0	30.4	30.4
	Average escape	84.3	84.4	84.3	85.0	85.0
	Average in-transit	37.4	40.6	40.4	45.9	45.9
	Average all	75.3	74.9	75.0	79.4	79.4
Tortuosity	Average stick	1.259	1.264	1.258	1.291	1.291
	Average escape	1.249	1.250	1.248	1.259	1.259
	Average in-transit	1.255	1.260	1.251	1.291	1.291
	Average all	1.250	1.253	1.250	1.263	1.263
Run Time/ Clock Time (mins)		19.6	19.4	19.6	29.7	19.7

To summarise:

- Eulerian turbulence and surface roughness have no effect on flow field velocity, wall shear stress or the transport of particles.
- Combined Eulerian turbulence and surface roughness increases peak velocity by 7.3%, decreases the number of particles that stick from 13.0% to 3.5% and increases wall shear stress by 989% to 1785%.
- Lagrangian turbulence had no effect on particle transport but increased run times.

From this we can conclude that surface roughness models are only implemented in conjunction with turbulence models. As turbulence alone does not affect flow velocities, wall shear stress or particle transport, flows in the model are laminar. Difficulties associated with accurately specifying surface roughness coefficients, and to a lesser extent the turbulence coefficients, can be circumvented by using a laminar model of turbulence.

B.3 Mesh Initial Resolution & Surface Refinement

Convergence time is highly dependent on the number of cells composing the computational domain and, as shown in Table B.6, does not scale linearly with the number of cells: Case13 has approximately 4.5 times more cells than Case12 and 18.5 times more than Case11, yet run times are 11.2 and 75.3 times greater respectively. For this reason, it is desirable to attain good representation of the flow velocity profile across the pore channel with a minimum number of cells.

Table B.6. Number of steps and time for convergence for initial mesh size (Cases 10, 11,12 and 13), surface refinement levels (Cases 1, 10, 15 and 16) and combined initial mesh size surface refinement (Cases 1, 10, 11 and 17). Case parameters detailed in Table B.1.

Case	Initial Mesh Size (mm)	Surface Refinement Levels (min, max)	Number of Cells	Steps to Convergence	Convergence Time (mins)
10	1.5	2, 2	92,040	22	0.2
11	0.6	2, 2	823,441	31	7.6
12	0.3	2, 2	3,444,631	42	51.0
13	0.15	2, 2	15,235,272	76	569.9
1	1.5	4, 4	2,153,316	33	25.6
10	1.5	2, 2	92,040	22	0.2
15	1.5	3, 4	2,080,870	34	27.8
16	1.5	1, 4	2,073,944	34	28.0
1	1.5	4, 4	2,153,316	33	25.6
10	1.5	1, 4	92,040	22	0.2
11	0.6	2, 2	823,441	31	7.6
17	0.6	1, 4	3,229,119	36	53.3

With respect to initial mesh size (cases 10, 11, 12 and 13), the velocity profile across the pore channel shows little change in maximum velocity (Figure B.5, A) between cases 11 and 12 (0.39% difference) and in the velocity profile as a whole (Figure B.5, B). Cases 10 and 13 differ from the case 11 and 12 average by 10.8% and 8.61% respectively suggesting that, outwith a certain range, initial mesh size can significantly affect velocities.

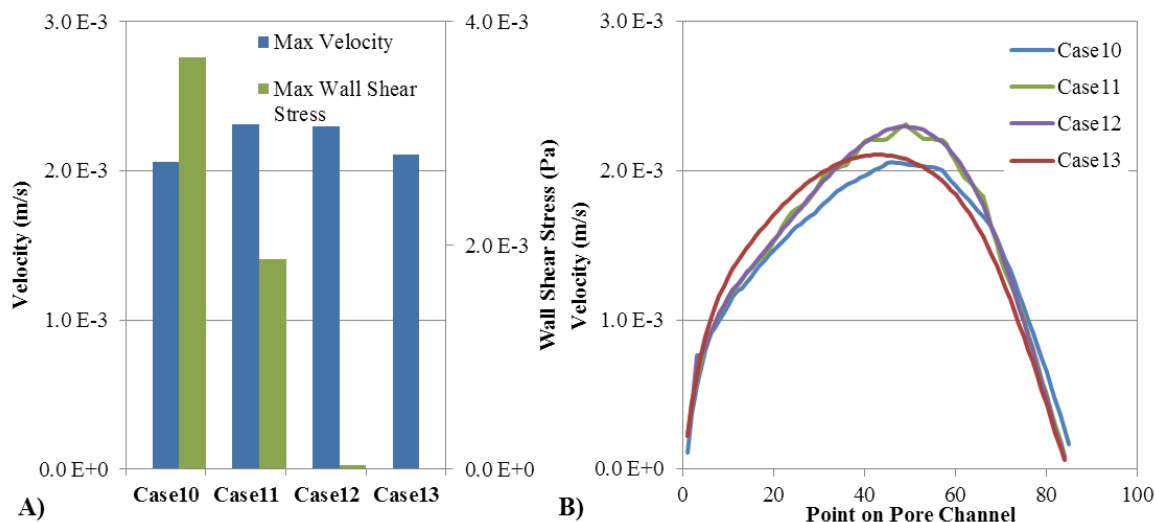


Figure B.5. For initial mesh size, A) Maximum pore velocity and wall shear stress and B) variation in velocity across pore channel. Details of each case can be cross-referenced with Table B.6.

Wall shear stress is greatly affected by initial mesh size with a large mesh size corresponding to high wall shear stress and a low size corresponding to a low wall shear stress. This is a consequence of the velocity in the cell adjacent to the surface: with a coarse mesh, the cell adjacent to a surface is an average velocity over an area that protrudes further from the surface into the pore channel than a fine mesh, and hence experiences a higher velocity. At the finest initial mesh size studied here (Case13), the average flow velocity in the cell adjacent to surface is lower than in all other cases resulting in the lowest wall shear stress, as shown in Figure B.6.

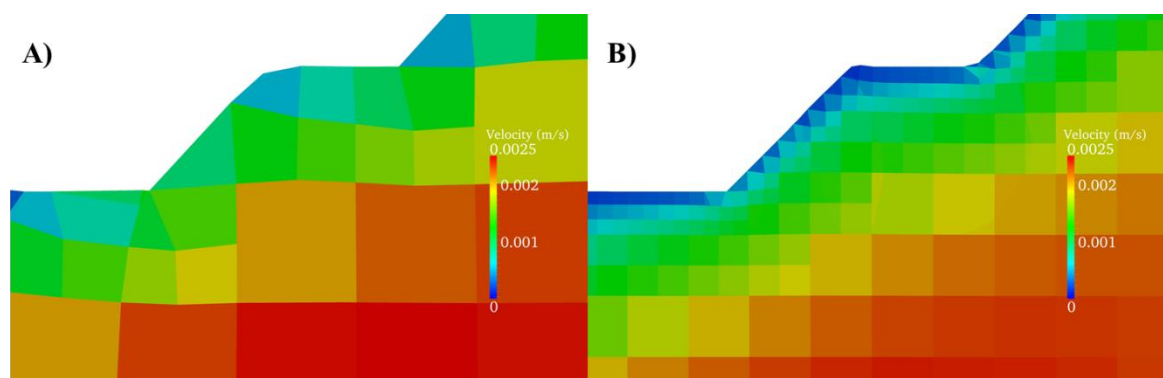


Figure B.6. Cell averaged velocities at gravel surface boundary for A) Case11, medium/coarse mesh and B) Case 13, fine mesh.

The minimum level of surface refinement has little effect on pore channel velocities with cases 1, 15 and 16 producing meshes with similar numbers of cells (between 2,073,944 and 2,153,316, Table B.6), similar convergence times and very similar pore channel velocities (Figure B.7). The maximum level of surface refinement does have a significant effect on pore velocity, as evinced by Case10 (in which the maximum surface refinement level was two) compared with cases 1, 15 and 16 (in which the maximum surface refinement level was 4). Wall shear stress is much greater for Case10 than for cases 1, 15 and 16 for the same reason wall shear stress was smaller for Case13: low surface refinement results in larger cells adjacent to the surface with a larger average velocity and hence larger shear stress.

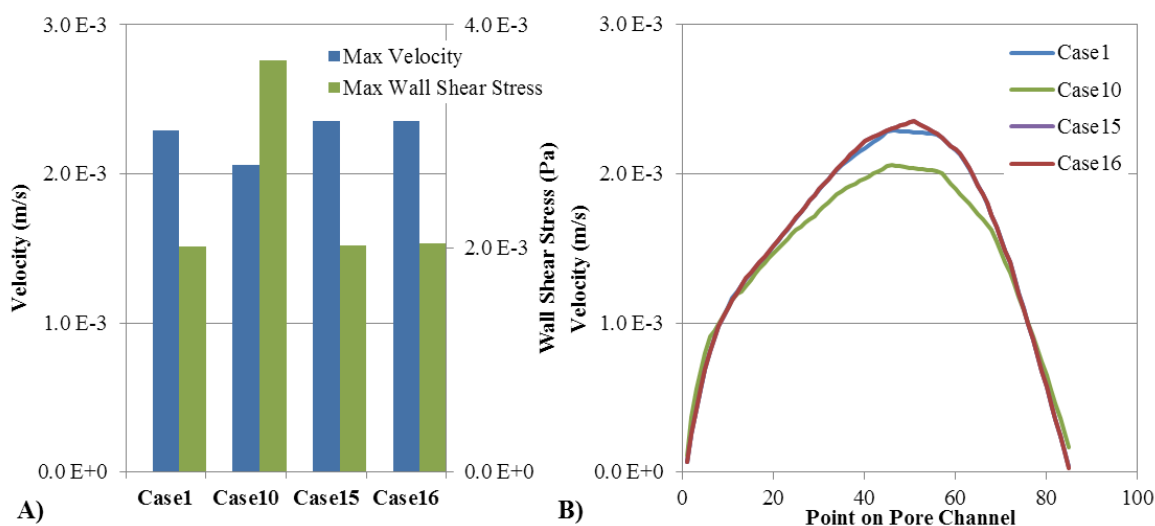


Figure B.7. For mesh surface refinement, A) Maximum pore velocity and wall shear stress and B) variation in velocity across pore channel. Details of each case can be cross-referenced with Table B.6.

With respect to combined initial mesh size and surface refinement level, comparing Case1 (low initial mesh size with high surface refinement levels) with Case11 (high initial mesh size with low surface refinement levels) results in a 0.72% difference in peak velocities (Figure B.8, A) and very little difference in pore velocity across the channel (Figure B.8B). As Case11 has 823,441 cells compared with the 2,153,316 cells of Case1, the time to convergence is 3.4 times shorter (Table B.6). A similar velocity profile can therefore be

obtained with a greatly reduced run time through the use of a high initial mesh size with low surface refinement.

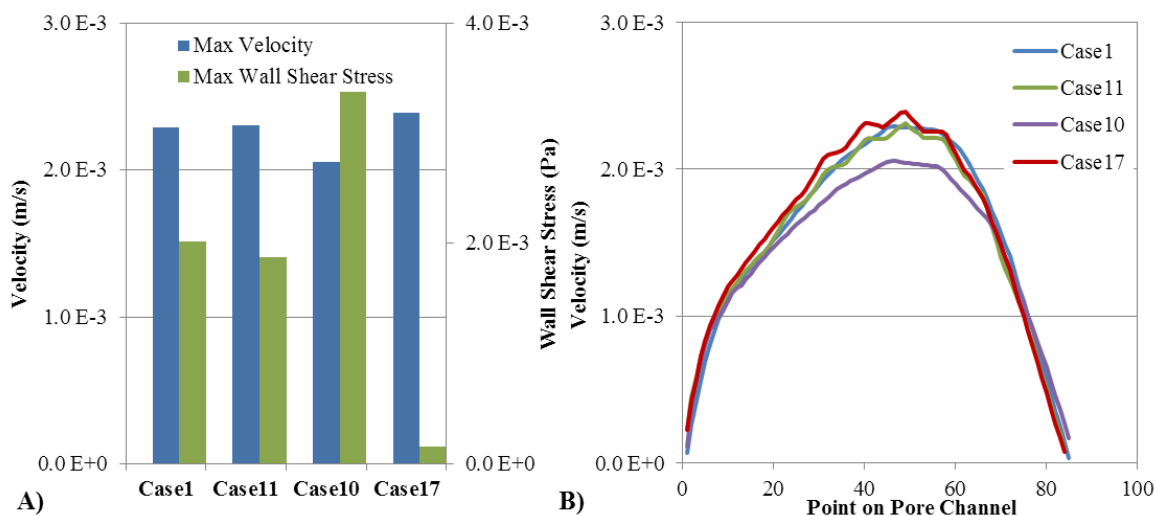


Figure B.8. For combined initial mesh size with mesh surface refinement, A) Maximum pore velocity and wall shear stress and B) variation in velocity across pore channel. Details of each case can be cross-referenced with Table B.6.

Comparing Case10 (low initial mesh size, low surface refinement) with Case17 (high initial mesh size, high surface refinement) shows that there is a significant difference in maximum velocity of 16.24%. In Figure B.9 it can be seen that the mesh generated for Case10 is too coarse to resolve narrow pore channels and hence the modelled flow paths velocities would not replicate true flow velocities. Wall shear stress is also markedly different between Case10 and Case17 and is due to the size of the cell adjacent to surface, as discussed above.

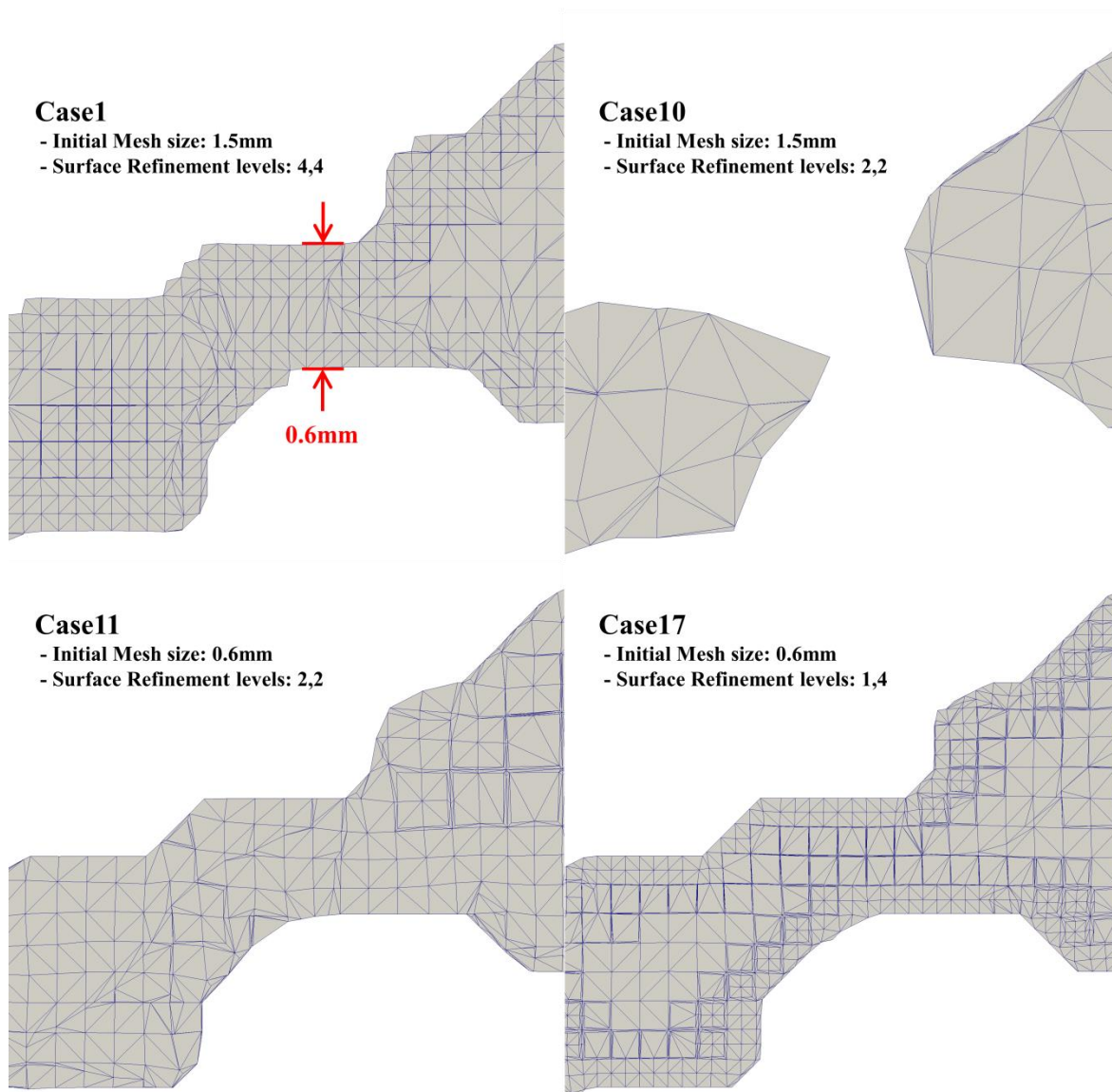


Figure B.9. Extent of computational domain for a very narrow pore throat 0.6mm wide at the narrowest point. Each combination of initial mesh size and surface refinement level represented by Case1, Case11 and Case17 accurately depict the pore throat and the overall computational domain. This is not true for Case10 in which the initial mesh size and refinement levels do not allow the pore throat to be meshed. Case10 therefore under predicts the volume of the computational domain and the connectivity provided by narrow pore throats.

In summary, initial mesh size and surface refinement affect flow velocities and wall shear stress throughout the model, as quantified by analysing a single chosen pore channel. The wall shear stress is dependent upon flow velocities in the cell adjacent to the wall surface and hence is very sensitive to the resolution of that cell. It is possible to obtain similar velocity profiles at a greatly reduced computational cost by utilising a high initial mesh

size with low surface refinement (Case11) in comparison to a low initial mesh resolution with high surface refinement (Case1). Figure B.9 shows that this is because Case1 produces more mesh cells adjacent to the surface. A high number of surface cells may be beneficial for models incorporating turbulence and surface roughness or in which the value of wall shear stress is critical; however, we have established that there is no turbulence in the model (Section B.2) and so the surface cells are superfluous. As such, model run time can be reduced and accurate flow velocities obtained by utilising a high initial mesh size (0.6mm) with low surface refinement levels (2, 2).

B.4 STL generation and Viscosity

As described in Section 5.3.2, the solid surface is created in STL format from the MRI data. The MRI data is composed of voxels 300 μ m to a side and so, when viewed at high resolution, the resulting solid surface consists of square blocks (see Figure B.10, A) whilst in reality the surface would be smoother. During STL creation, it is possible to smooth the surface (see Figure B.10, B) and this allows comparison between a smoothed mesh with an unsmoothed mesh. However, it must be noted that the smoothed surface is not necessarily a more accurate definition the pore space than the unsmoothed surface and this could only be settled with an MRI (or similar non-invasive scanning technique such as X-ray tomography) scan carried out at much higher resolution.

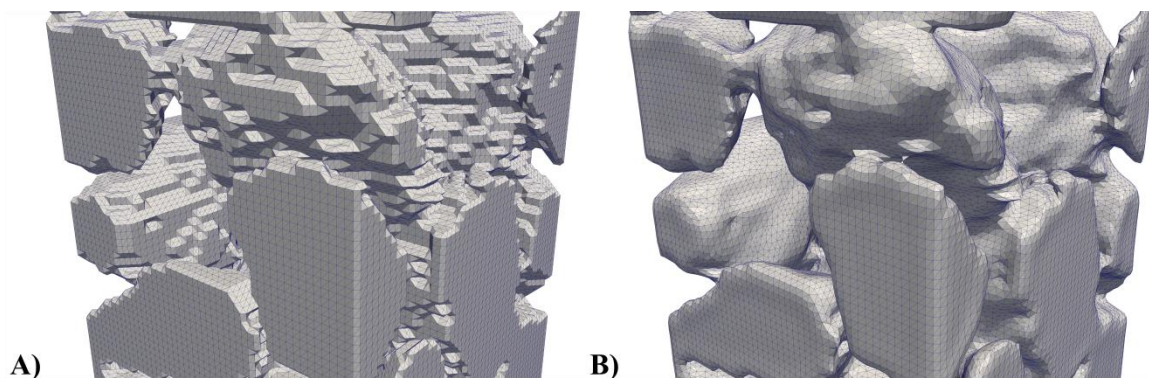


Figure B.10. Gravel surface derived from MRI data with A) the standard method of no smoothing and B) with smoothing. Smoothing creates a more natural looking mesh yet also alters the pore volume and pore network connectivity.

Kinematic viscosity is a function of the fluid, the temperature and the concentration of suspended kaolin particles. In the temperature controlled experiments of Chapter 2, the fluid and temperature remain constant yet the kaolin concentration varies spatially within the filter with a higher concentration at the inlet and a lower concentration at the outlet (due to removal along the filter length). Viscosity can therefore be expected to vary spatially within the filter and in time as the filter removal efficiency changes. To test the sensitivity of the model to viscosity, two kinematic viscosity values were used: $1.0\text{E-}6\text{ m}^2/\text{s}$ representing water at 20°C and, based on the measurements of Beazley (1972), $1.8\text{E-}6\text{ m}^2/\text{s}$ representing water at 20°C with 5% kaolin by volume. Water at 0°C (without any kaolin) has a kinematic viscosity approximately $1.8\text{E-}6\text{ m}^2/\text{s}$ and so this value serves to test the sensitivity of the model to viscosity change due to kaolin in suspension and due to the range in temperatures over which a gravel filter would be expected to operate.

B.4.1 Eulerian Solution

Table B.7. Number of steps and time for convergence for mesh generation method (Cases 1 and 20) and kinematic viscosity value (Cases 1 and 21). Case parameters detailed in Table B.1.

Case	STL Generation Method	Kinematic Viscosity	Steps to Convergence	Convergence Time (mins)
1	Standard	$1.00\text{E-}06$	33	25.6
20	Smoothed	$1.00\text{E-}06$	33	22.4
21	Standard	$1.80\text{E-}06$	34	25.5

Convergence time is 12.26% quicker for the smoothed mesh (Case20) compared with the standard mesh (Case1) whilst a higher viscosity reduces convergence time by only 0.18% (Case21 compared with Case1), as shown in Table B.7. The smoothed mesh results in a 6.00% decrease in maximum velocity across the pore channel (Figure B.11). This is thought to be caused by the change in geometry and connectivity of the computational domain as a result of smoothing, rather than due to an increase in velocity closer to the surface offsetting the reduction in peak velocity at the pore centre. No increase in velocity close to the surface is evident in Figure B.11.

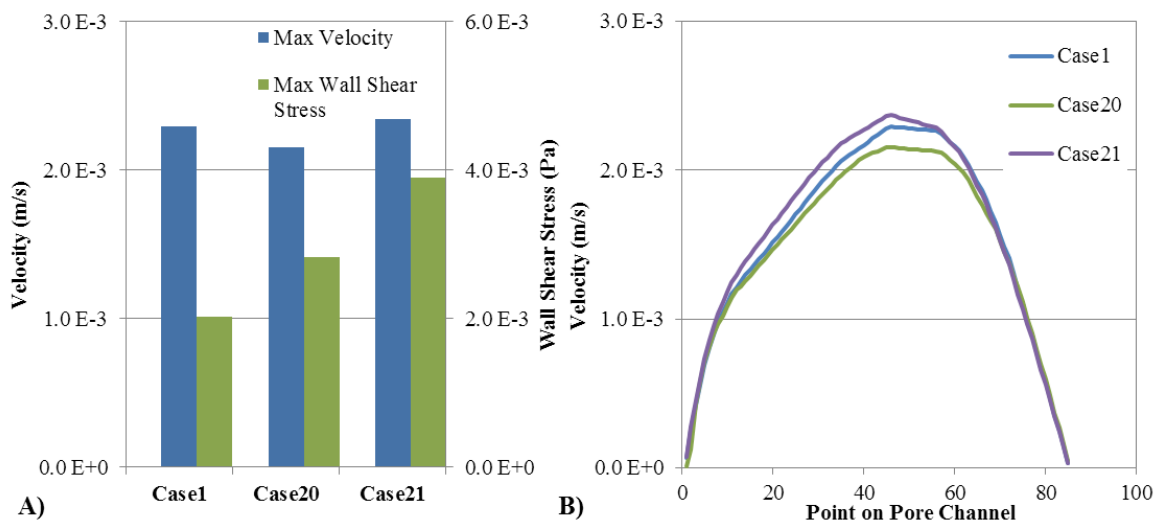


Figure B.11. For mesh generation method and viscosity, A) Maximum pore velocity and wall shear stress and B) variation in velocity across pore channel. Details of each case can be cross-referenced with Table B.7.

Increasing kinematic viscosity to account for a water/kaolin suspension increases maximum velocity by 3.40% and wall shear stress by 93.30%.

B.4.2 Lagrangian Solution

Smoothing the mesh decreased the number of sticking particles from 13.04% to 7.88% (Table B.8) and increased the average time to stick of these particles by 16.30% yet the distance they travelled increased by only 8.65%. This suggests that, on average, particles that did stick travelled at a lower velocity prior to reaching the surface. From this it is deduced that the smooth mesh provides fewer opportunities for particles to reach the surface and stick and only those travelling in the low velocity area close to the gravel surface were able to stick. Increasing the viscosity had little impact on the number of particles sticking, escaping or remaining in transit.

Table B.8. Lagrangian particle tracking transport characteristics for mesh generation method and viscosity.

		Case1A	Case20	Case21
Fate	Number of particles	2500	2500	2500
	Number stick	326	197	334
	Number escape	2010	2123	1973
	Number in-transit	164	180	193
Time (s)	Average stick	98.90	115.02	97.58
	Average escape	124.11	127.67	122.20
	Average in-transit	400.00	400.00	400.00
	Average all	138.92	146.28	140.36
Distance (mm)	Average stick	38.6	42.0	38.5
	Average escape	84.3	83.8	84.4
	Average in-transit	37.4	41.2	40.5
	Average all	75.3	77.4	74.8
Tortuosity	Average stick	1.259	1.252	1.255
	Average escape	1.249	1.240	1.249
	Average in-transit	1.255	1.269	1.272
	Average all	1.250	1.243	1.252
Run Time/ Clock Time (mins)		19.6	19.2	19.5

From this we can conclude that the smooth surface looks more like a real gravel surface than the unsmoothed surface and the surface generation method affects flow velocities as well as the transport of particles close to the surface. However, smoothing the surface means the pore volume and pore network connectivity are no longer the same as those assessed in Chapter 3 and Chapter 4. For this reason, comparing smoothed and unsmoothed surfaces is useful for understanding the implications of the MRI derived geometry resolution on the model results, yet the unsmoothed surface should be used in all simulations as this provides equivalent pore volume and pore network connectivity to those assessed in Chapter 3 and Chapter 4 respectively.

A further conclusion is that kinematic viscosity is an important parameter for both flow velocity and wall shear stress, but not Lagrangian particle transport. Quantifying the change in flow velocity due a change in kinematic viscosity, brought about by either a change in kaolin concentration or a change in temperature, helps to understand how the model can be applied to gravel filters operating outside of controlled laboratory conditions and the level of uncertainty associated with the results of the model.

B.5 Lagrangian Dispersion

In this section we determine if dispersion significantly affects the transport of Lagrangian particles and explore the necessity for a turbulent Lagrangian solution and turbulent Eulerian solution. Case1B compared with Case1A determines the effect of Lagrangian dispersion with no turbulence model: the results show no change (Table B.9). Case1E includes Lagrangian dispersion with Lagrangian turbulence and proves that a turbulence model is necessary for the implementation of the dispersion model. In Case1E, the dispersion model results in 97.32% of particles sticking to a surface, as opposed to 13.04% for Case1A without dispersion. The dispersion model is thought to enable the tracer particles to cross flow streamlines and thus come in to contact with the surface, resulting in the increase in sticking particles.

Table B.9. Lagrangian particle tracking transport characteristics for Lagrangian dispersion with turbulence.

		Case1A	Case1B	Case1E	Case3A	Case3B
Fate	Number of particles	2500	2500	2500	2500	2500
	Number stick	326	326	2433	338	2104
	Number escape	2010	2010	1	1974	285
	Number in-transit	164	164	66	188	106
Time (s)	Average stick	98.90	98.90	25.00	97.26	38.54
	Average escape	124.11	124.11	70.00	120.52	82.40
	Average in-transit	400.00	400.00	400.00	400.00	400.00
	Average all	138.92	138.92	34.91	138.39	58.91
Distance (mm)	Average stick	38.6	38.6	13.4	38.1	26.6
	Average escape	84.3	84.3	82.6	84.4	85.5
	Average in-transit	37.4	37.4	11.9	40.6	23.7
	Average all	75.3	75.3	13.4	74.9	33.2
Tortuosity	Average stick	1.259	1.259	1.268	1.264	1.334
	Average escape	1.249	1.249	1.216	1.250	1.290
	Average in-transit	1.255	1.255	1.253	1.260	1.383
	Average all	1.250	1.250	1.268	1.253	1.328
Run Time/ Clock Time (mins)		19.6	19.5	20.3	19.4	28.6

Case3B includes Lagrangian dispersion, Lagrangian turbulence and Eulerian turbulence. When compared with Case1E (Lagrangian dispersion and turbulence, no Eulerian turbulence), and Case3A (Eulerian turbulence, no Lagrangian dispersion or turbulence),

Case3B shows that Eulerian turbulence with Lagrangian dispersion has a significant impact on all aspects of particle transport.

B.6 Discussion

The significance of the parametric study results on model setup and reliability is discussed in Section 5.3.6.

Appendix C – OpenFOAM Model Files

```
    tolerance 1.0;
    nSolveIter 300;
    nRelaxIter 5;
    nFeatureSnapIter 10;
}

// Generic mesh quality settings.
meshQualityControls
{
    maxNonOrtho 65;
    maxBoundarySkewness 20;
    maxInternalSkewness 4;
    maxConcave 80;
    minVol 1e-13;
    minTetQuality 0.1;
    minArea 1e-13;
    minTwist 0.05;
    minDeterminant 0.001;
    minFaceWeight 0.05;
    minVolRatio 0.01;
    minTriangleTwist -1;
    nSmoothScale 4;
    errorReduction 0.75;

    relaxed
    {
        maxNonOrtho 75;
    }
}

debug 0;

mergeTolerance 1E-6;

// ***** //
```

```
    equations
    {
        U          0.7;
        k          0.7;
        epsilon    0.7;
    }
}

cache
{
    grad(U);
}

// ***** //
```



```

patchInteractionModel localInteraction;

heatTransferModel none;

surfaceFilmModel none;

collisionModel none;

radiation off;

manualInjectionCoeffs
{
    massTotal      0;
    parcelBasisType fixed;
    nParticle      1;
    SOI            0;
    positionsFile   "kinematicCloudPositions";
    U0             ( 0 0 0.0002165 );
    sizeDistribution
    {
        type      RosinRammler;
        RosinRammlerDistribution
        {
            minValue      1e-30;
            maxValue      1e-30;
            d              1e-30;
            n              1;
        }
    }
}

pairCollisionCoeffs
{
    // Maximum possible particle diameter expected at any time
    maxInteractionDistance 0.006;

    writeReferredParticleCloud no;

    pairModel pairSpringSliderDashpot;

    pairSpringSliderDashpotCoeffs
    {
        useEquivalentSize no;
        alpha             0.12;
        b                 1.5;
        mu                0.52;
        cohesionEnergyDensity 0;
        collisionResolutionSteps 12;
    };

    wallModel wallLocalSpringSliderDashpot;

    wallLocalSpringSliderDashpotCoeffs
    {
        useEquivalentSize no;
        collisionResolutionSteps 12;
        fixedWalls
        {
            youngsModulus 1e10;
            poissonsRatio 0.23;
            alpha         0.12;
            b             1.5;
            mu            0.43;
            cohesionEnergyDensity 0;
        }
        scan*
        {
            youngsModulus 1e10;
            poissonsRatio 0.23;
            alpha         0.12;
            b             1.5;
        }
    }
}

```

```
        mu          0.43;
        cohesionEnergyDensity 0;
    };
}

localInteractionCoeffs //available types are stick, rebound, escape
{
    patches
    (
        "scan*"
        { type      stick;
        }
        "inlet"
        { type      escape;
        }
        "outlet"
        { type      escape;
        }
        "fixedWalls"
        { type      stick;
        }
    );
}

}

// ***** //
```

C.5 Example Bash Script – Eulerian Model

```
#!/bin/sh
cd ${0%/*} || exit 1    # run from this directory

# Source tutorial run functions
. $WM_PROJECT_DIR/bin/tools/RunFunctions

runApplication blockMesh
runApplication surfaceFeatureExtract -includedAngle 140 constant/triSurface/scan4Surface.stl
scan4Surface
runApplication decomposePar
runParallel snappyHexMesh 4 -parallel
runApplication reconstructParMesh -latestTime
mv constant/polyMesh constant/polyMesh.org
mv 2/polyMesh constant/polyMesh
rm -r 2
rm -r proc*
rm -r log.blockMesh
rm -r log.surfaceFeatureExtract
rm -r log.decomposePar
rm -r log.reconstructParMesh

runApplication decomposePar
runParallel simpleFoam 4 -parallel
runApplication reconstructPar -latestTime
runApplication wallShearStress
foamToVTK -excludePatches '(inlet outlet fixedWalls scan*)' -noZero
runApplication foamLog log.simpleFoam
sample -latestTime
rm -r proc*
rm -r log.decomposePar
rm -r log.foamLog
rm -r log.wallShearStress
rm -r log.reconstructPar

# ----- end-of-file
```

C.6 Example Bash Script – Lagrangian Model

```
#!/bin/sh
cd ${0%/*} || exit 1    # run from this directory

# Source tutorial run functions
. $WM_PROJECT_DIR/bin/tools/RunFunctions

cp -au simpleFoamResults/constant/polyMesh constant
runApplication mapFields simpleFoamResults -sourceTime latestTime
runApplication decomposePar
runParallel icoUncoupledKinematicParcelFoam 4 -parallel
runApplication reconstructPar -fields '(Ux)'
foamToVTK -excludePatches '(inlet outlet fixedWalls scan*)' -noInternal -noZero
mv constant/particleTrackProperties.raw1 constant/particleTrackProperties
runApplication myExtendedParticleTracks
rm -r log.myExtendedParticleTracks
mv constant/particleTrackProperties constant/particleTrackProperties.raw1
mv constant/particleTrackProperties.vtk constant/particleTrackProperties
runApplication myExtendedParticleTracks
mv constant/particleTrackProperties constant/particleTrackProperties.vtk
rm -r proc*
rm -r log.mapFields
rm -r log.decomposePar
rm -r log.reconstructPar
grep -w 'stick' log.icoUncoupledKinematicParcelFoam > stick.txt
grep -w 'Time' log.icoUncoupledKinematicParcelFoam > time.txt
grep -w 'Current number' log.icoUncoupledKinematicParcelFoam > number.txt

# ----- end-of-file
```